Modeling, Analysis, and Experimental Investigation of a Variable Displacement Linkage Pump

A Dissertation

SUBMITTED TO THE FACULTY OF

UNIVERSITY OF MINNESOTA

BY

Shawn Wilhelm

IN PARTIAL FULFILLMENT OF THE REQUIREMENTS

FOR THE DEGREE OF

DOCTOR OF PHILOSOPHY

Advisor

James D. Van de Ven, PhD

July 2015

Acknowledgements

No one accomplishes anything on their own and I would like to acknowledge a few of the people who carried me as completed my degree. I would like to thank my lab mate Alex who helped me pull my thesis defense together and wouldn't let me give up. He saved me when I needed it most. To my friends who supported me and helped me through stressful times despite my neglect, I thank you. To my parents who made me who I am today, I am indebted. My mother always engaged my creativity and indulged my curiosity. She never directly answered my incessant childhood questions, but instead replied with her own to help me find the answers myself. My father always encouraged me to push myself to succeed. He never let me compare myself to anyone else and supported me as I attempted more and more challenging undertakings. Any success I achieve, I owe to them. I am forever grateful to my advisor, Jim Van de Ven. He has acted as a teacher, advisor, mentor, and friend. His guidance has brought me where I am today and I am in awe of his humility despite many accomplishments. I am honored to have worked with him and lucky to have had him as an advisor.

Dedication

This work is dedicated to my wife Jennifer, who moved across the country to be with me while I “finished up my thesis” two years ago. Without her love, support, and remarkable patience, I never would have been able to complete this work.

Abstract

Hydraulic power systems offer a robust, compact, and flexible method of power transmission and are used widely in both industrial and mobile applications. While 2% of the energy consumed in the US passes through hydraulic systems, less than half of it does any useful work largely due to the use of inefficient flow control valves. Variable displacement pumps offer a method of delivering the required flow to an actuator without suffering the losses associated with a flow control valve. However, current variable displacement pumps exhibit poor efficiency at low displacement because their primary sources of energy loss are largely independent of displacement. Here, a novel adjustable linkage is proposed as the driving mechanism of a variable displacement pump. The linkage is constructed such that the pumping piston returns to the same top-dead-center position at all displacement, and can also achieve zero displacement. As a result of these features, the pump displacement is infinitely variable, and the unswept volume is remains constant at all displacements. By using pinned joints rather than sliding joints, the majority of the energy losses scale with output power resulting in a pump that is efficient over a wide range of operating conditions.

In this thesis, a complete model of a variable displacement linkage pump is developed. A method of constructing the adjustable sixbar mechanism and the possible embodiments is presented. A new solution rectification technique is developed providing a robust method of generating valid linkages that is generally applicable to other mechanisms. The kinematics of the mechanism are then presented to describe the motion of the links and output piston. A kinetostatic model of the mechanism provides a means of determining the internal mechanical energy losses. A non-linear model of the bearing friction augments the model, but requires numerical methods to solve, and increases computational complexity. A dynamic model of the pumping cylinders and pump manifold provide a means of determining the fluid behavior of the pump including output flowrates and pressures. These models are coupled to create a complete understanding of the variable displacement linkage pump. The model is designed to be predictive and computationally inexpensive for use in multi-objective optimizations. As such, no experimentally determined performance coefficients are required. No model of this level of completeness exist for linkage driven pumps, variable displacement or otherwise.

Two prototype pumps are presented and used to validate the models. A single cylinder pump is used to validate the mechanical energy loss model but was limited to low pressure operation due to large torque variations. Close agreement is demonstrated between the model and experiment. The model predicts a pump efficiency greater than 90% at displacements as low as 15% if roller bearings are used in the pin joints. To validate this prediction, a multi-cylinder prototype which uses roller bearings in the joints is designed. The kinematic and mechanical energy loss models are coupled to a basic pumping model for use in a multi-objective genetic algorithm to optimize the mechanism. The resulting pump demonstrates close agreement between the model and experimentally measured shaft torque and mechanical energy loss at various pressures, displacements, and input shaft speeds. However, out-of-plane deflection of the mechanism reduced the piston displacement and altered the trajectory reducing pump output. The true temporal

piston position is measured and used as an input to the dynamic fluid model. The predicted and experimentally measured cylinder pressures demonstrate the effectiveness of the model at predicting the dynamic behavior of the fluid end of the pump.

It is shown that the models can accurately capture the physics of the pump without using tuning parameters or experimentally determined coefficients over a wide range of operating conditions. It is recommended that single shear linkage arrangements are avoided in future designs to increase the mechanism stiffness and improve performance. The variable displacement linkage pump offers the opportunity for high efficiency flow control at a wide range of operating conditions due to the nature of the energy loss mechanisms scaling with the output power. The flexibility of the driving sixbar mechanism allows for the optimization of the architecture for particular applications and the presented model provides a means of predicting performance.

Table of Contents

List of Tables

List of Figures

Nomenclature

Variable	Description	Units
$\boldsymbol{R_i}$	$Length\ of\ link\ i$	m
$\boldsymbol{\theta_i}$	$Global\ Angle\ of\ link\ i$	rad
$\boldsymbol{R_{1max}}$	$Maximum\ length\ of\ ground\ link$	m
$\boldsymbol{R_{1min}}$	$Minimum\ length\ of\ ground\ link$	m
$\boldsymbol{\theta_{min}}$	$Minimum\ transmission\ angle\ of\ fourbar$	rad
$\boldsymbol{\vec{r}_j}$	$Vector\ Describing\ Link\ j$	m
$\boldsymbol{\theta_{CTDC}}$	$Angle\ of\ vector\ to\ point\ coupler\ point\ associated\ with\ top\ dead\ center$	rad
$\boldsymbol{\vec{R}_C}$	$Vector\ from\ origin\ to\ coupler\ point\ associated\ with\ top\ dead\ center$	m
$\boldsymbol{\Upsilon}$	$Angle\ between\ \vec{r}_1\ and\ \vec{R}_C$	rad
$\boldsymbol{s}$	$Slider\ position$	m
$\boldsymbol{\omega_j}$	$Angular\ velocity\ of\ link\ j$	$\frac{rad}{s}$
$\boldsymbol{v_s}$	$Slider\ Velocity$	m/s
$\boldsymbol{\alpha_j}$	$Angular\ acceleration\ of\ link\ j$	$\frac{rad}{s^2}$
$\boldsymbol{A_s}$	$Linear\ Acceleration\ of\ Slider\ Link$	$\frac{m}{s^2}$
$\boldsymbol{\theta_s}$	$Angle\ of\ Axis\ of\ Slide$	rad
$\boldsymbol{h_s}$	$Distance\ to\ axis\ of\ slide\ from\ x\ axis$	m
$\boldsymbol{F_{ijx}}$	$Force\ of\ link\ j\ on\ link\ i\ in\ the\ x\ direction$	N
$\boldsymbol{F_{ijy}}$	$Force\ of\ link\ j\ on\ link\ i\ in\ the\ y\ direction$	N
$\boldsymbol{I_j}$	$Mass\ moment\ of\ inertia\ of\ link\ j\ about\ CG$	$\frac{kg}{m^2}$
$\boldsymbol{A_{gjx}}$	$Acceleration\ of\ the\ center\ of\ gravity\ of\ link\ j\ in\ x\ direction$	$\frac{m}{s^2}$
$\boldsymbol{A_{gjy}}$	$Acceleration\ of\ the\ center\ of\ gravity\ of\ link\ j\ in\ y\ direction$	$\frac{m}{s^2}$
$\boldsymbol{T_{12}}$	$Input\ shaft\ torque$	Nm
$\boldsymbol{M_{\mu_j}}$	$Friction\ moment\ at\ pin\ j$	Nm
$\boldsymbol{r_j}$	$The\ radius\ of\ pin\ j$	m
$\boldsymbol{\mu_j}$	$The\ coefficient\ of\ friction\ at\ joint\ j$	$unitless$
$\boldsymbol{F_v}$	$Viscous\ friction\ force$	N

d_p	$Piston\ diameter$	m
l_p	$Length\ of\ piston\ cylinder\ interface$	m
T_{ss}	$Shaft\ seal\ torque$	Nm
C_{ss}	$Shaft\ seal\ coefficient$	
D_{ss}	$Shaft\ seal\ ID$	m
h	$Piston\ cylinder\ clearance\ gap\ height$	m
μ_d	$Dynamic\ viscosity\ of\ pumping\ fluid$	$Pa\ s$
F_p	$Force\ applied\ to\ piston\ by\ cylinder\ pressure$	N
$F_{applied}$	$Total\ force\ applied\ to\ piston$	N
$F_{fr_{ext}}$	$Externally\ applied\ piston\ friction$	N
W_{in}	$input\ shaft\ work$	J
$E_{Cf_{crosshead}}$	$Crosshead\ friction\ energy\ loss$	J
$F_{Cf_{crosshead}}$	$Crosshead\ friction\ force$	N
μ_{k_c}	Coefficient of friction between the slider and bushing of the crosshead	$Unitless$
E_{cf_j}	$Coulomb\ friction\ energy\ loss\ at\ joint\ j$	J
E_v	$Energy\ loss\ due\ to\ viscous\ friction$	J
E_{ss}	$Shaft\ Seal\ friction\ energy\ loss$	J
V_D	$Volumetric\ pump\ displacement$	$\frac{m^3}{rev}$
m_j	$Mass\ of\ link\ j$	kg
C_{ij}	$Designation\ of\ joint\ between\ links\ i\ and\ j$	$unitless$
Q_{leak}	$Leakage\ flow\ rate$	$\frac{m^3}{s}$
ΔP	$Pressure\ drop$	Pa
ρ	$Density$	$\frac{kg}{m^2}$
A_v	$Valve\ orifice\ area$	m^3
Q_v	$Flow\ rate\ accross\ valve\ orifice\ area$	$\frac{m^3}{s}$
C_d	$Orifice\ discharge\ coefficient$	$unitless$
d_p	$Piston\backslash Plunger\ diameter$	m
E_{Ql}	$Energy\ loss\ to\ leakage\ flow$	J

E_{Loss}	Total energy loss of mechanism	J
E_p	Pin friction energy loss	J
L_{10}	Bearing life	unitless
L_h	Bearing life rating	hour
P_{eq}	Equivalent bearing load	N
C_0	Dynamic load rating of bearing	N
R_{ds}	Bore to stroke ratio	unitless
Q_o	Flowrate through orifice	$\frac{m^3}{s}$
A_o	Orifice area	m^2
β	Fluid Bulk Modulus	Pa
V	Volume	m^3
B_{eff}	Effective fluid bulk modulus	Pa
R_o	Volume fraction of entrained air in fluid	unitless
β_0	Bulk modulus of air free fluid at atmospheric pressure	Pa
γ	Polytropic gas constant	unitless
P_0	Atmospheric pressure	Pa
P	Current pressure of fluid	Pa
v_g	Gas volume	m^3
v_l	Liquid volume	m^3
x_p	Piston postion relative to top dead center	m
v_p	Piston velocity relative to top dead center	$\frac{m}{s}$
A_p	Piston acceleration relative to top dead center	$\frac{m}{s^2}$
Q_{in}	Flowrate into volume	$\frac{m^3}{s}$
Q_{out}	Flowrate of fluid exiting volume	$\frac{m^3}{s}$
P_c	Cylinder Pressure	Pa
V_c	Cylinder Volume	m^3
A_p	Piston area	m^2
V_{c0}	Unswept volume of cylinder	m^3
P_1	Check valve pressure at inlet	Pa
P_2	Check valve pressure at exhaust	Pa

$\boldsymbol{A_1}$	$Check\ valve\ area\ at\ inlet$	m^2
$\boldsymbol{A_2}$	$Check\ valve\ area\ at\ exhaust$	m^2
$\boldsymbol{F_t}$	$Transient\ flow\ force$	N
$\boldsymbol{F_{steady}}$	$Steady\ state\ flow\ forces$	N
$\boldsymbol{F_{Pr}}$	$Pressure\ force\ on\ poppet$	N
$\boldsymbol{m}$	$Poppet\ mass$	kg
$\boldsymbol{P_l}$	$Discharge\ line\ pressure$	Pa
$\boldsymbol{Q_{d,i}}$	$Dishcarge\ flowrate\ from\ cylinder\ i$	$\frac{m^3}{s}$
$\boldsymbol{Q_o}$	$Flowrate\ across\ load$	$\frac{m^3}{s}$
$\boldsymbol{V_l}$	$Volume\ of\ discharge\ line$	m^3
$\boldsymbol{\theta}$	$Check\ valve\ nose\ angle$	rad
$\boldsymbol{k}$	$Check\ valve\ spring\ rate$	N/m

Chapter 1 Background and Literature Review

1.1 Introduction

A 2012 study by Oak Ridge National Labs found that around 2% of the power consumption in the United States passes through hydraulic systems. They also found that the average efficiency for industrial and mobile hydraulic power systems is 50% and 21% respectively [1]. As a result, the inefficiencies of these systems contribute to the release of 120 to 171 million metric tons (MMT) of CO2 into the atmosphere at a cost of $16B to $28B annually. These losses are largely due to metering flow control, which throttles flow over a valve to control pressure and flowrate. There is a clear need for a more efficient flow control method from both an economic and environmental standpoint.

There are three common methods for controlling hydraulic flow: metering valves, speed control of an electric motor with a variable frequency drive, and variable displacement hydraulic pumps. Each of these methods has their own respective tradeoffs and are further discussed here.

Metering valve control uses a variable orifice valve to throttle the flow from a fixed displacement pump and is used in both mobile and industrial applications. It is the most popular solution due to the low cost, fast response, and ease of maintenance. However, it is also the most inefficient solution due to large amount of energy throttled across the control and relief valves.

Variable frequency drives (VFDs) are used to control the shaft speed of an electric drive motor that is coupled to a fixed displacement hydraulic pump. Due to the low power density of electric motors, their use is restricted to industrial applications

where space is available. While being the most efficient solution, VFDs are limited by the high cost associated with high power drives and the reduced motor life [2].

Variable displacement pumps are hydraulic pumps that can adjust the fluid delivered per revolution of the input shaft. They are used for applications that require a more efficient method of flow control than metering valves [3]. A variable displacement pump can deliver the power required by the system, rather than throttling unnecessary power across a valve, thus consuming less energy to complete the same task.

1.1.1 Current Variable Displacement Piston Machines

There are several types of positive displacement hydraulic pumps and motors including gear, screw, lobe, and piston machines. Of these machines, there are three main architectures that commonly have variable displacement: axial piston, bent axis, and vane. Much work has been done on improving the efficiency of these variable machines [4-9]. For the most part, these efforts have resulted in an increase in the maximum efficiency, but they have not significantly improved performance at low volumetric displacement.

The axial piston pump, shown in Figure 1.1, is the most widely used variable displacement machine due to its compact size and robust design [10]. This pump uses a non-rotating swash plate set at an angle to the rotational axis of a cylinder block. As the cylinder block rotates, the piston slippers slide along the swashplate on a hydrostatic bearing and the relative angle causes the pistons to reciprocate. The angle of the swashplate determines the displacement of the pistons and is varied to adjust the pump output.

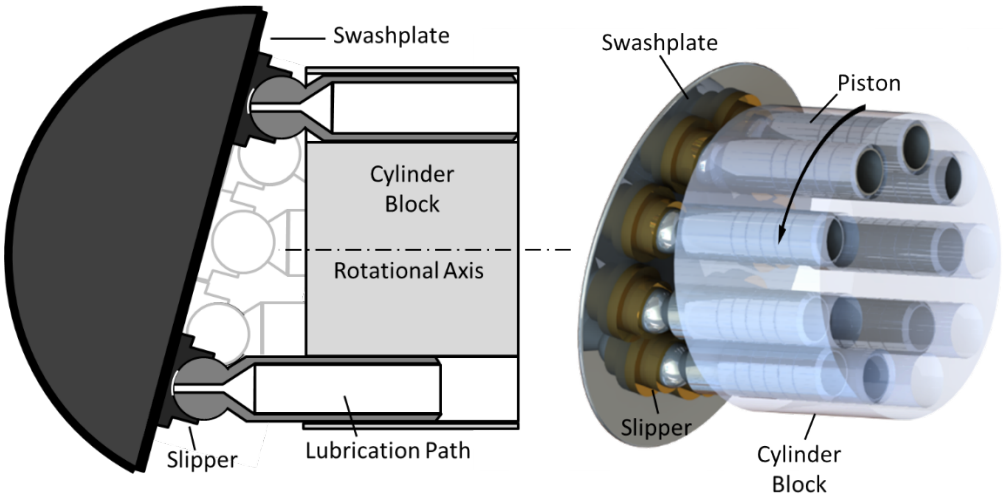

FIGURE 1.1 SCHEMATIC AND CAD RENDERING OF AXIAL PISTON PISTON PUMP SHOWN AT MAXIMUM DISPACEMENT

These pumps require a leakage path from the pumping cylinder to the swashplate in order to create a hydrostatic bearings in the piston-slipper and slipper-swashplate interfaces. Additionally, a valve plate is required at the other end of the cylinder block to direct flow to the high and low pressure ports. This interface, which both seals the pumping chambers and acts as a hydrostatic bearing surface, is the largest source of energy dissipation in the pump [11]. The frictional energy loss associated with these hydrodynamic surfaces is function of the square of the relative velocity between components and is relatively constant regardless of the volumetric displacement. Furthermore, there are three leakage paths per piston as a result of these bearing surfaces, with nine or eleven pistons used in a typical pump [12]. For a given operating pressure, the leakage energy loss is relatively constant with respect to displacement [13]. As a result, the efficiency of these pumps can be high at maximum output, but is significantly reduced at partial displacement when the output power decreases [13, 14].

A similar configuration to the axial piston pump is the bent axis type, depicted in Figure 1.2, which circumvents the high leakage and friction of the planar bearings by using spherical joints rather than a swash plate, but still requires a port plate. The rotation of the drive shaft and cylinder block are coupled and their relative angle causes the pistons to reciprocate. The displacement is varied by changing the relative angle between the drive shaft and cylinder block. These pumps have been shown to have high efficiency across a wide range of operating conditions[9, 15]. However, these pumps are not as widely used as swashplate type axial piston pumps because of their high costs, reliability issues, and their inability support a through-shaft design [10].

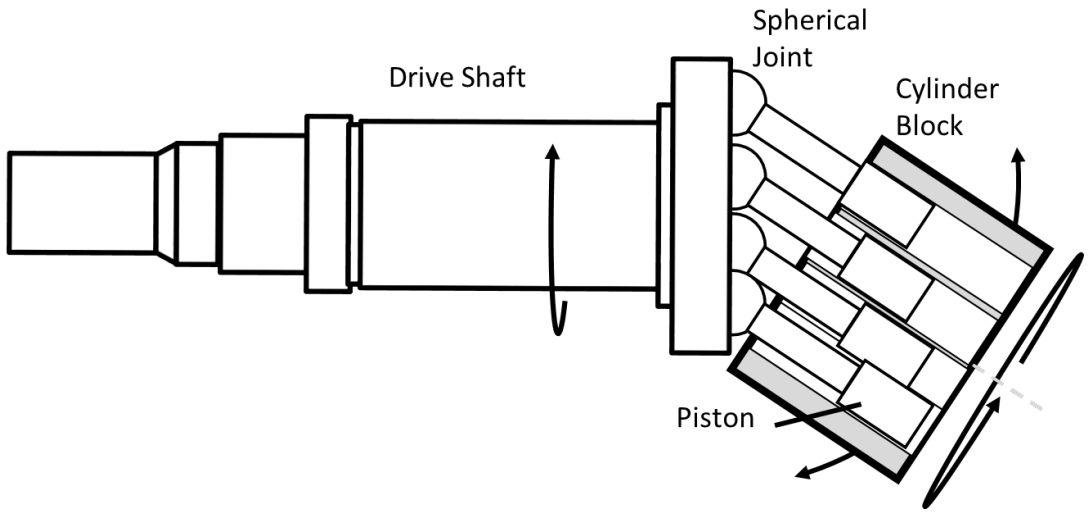

FIGURE 1.2 SCHEMATIC OF BENT AXIS PUMP

The vane pump, depicted in Figure 1.3, sweeps fluid from low pressure to high pressure by trapping the fluid between vanes that rotate with the rotor and seal against the outer ring. The displacement of this pump is varied by adjusting the eccentricity between the movable outer ring and the rotor. The vanes are shown here with return springs to

maintain contact with the outer ring but other methods are possible. These pumps have complex sealing surfaces and cannot achieve the same high pressures as piston pumps.

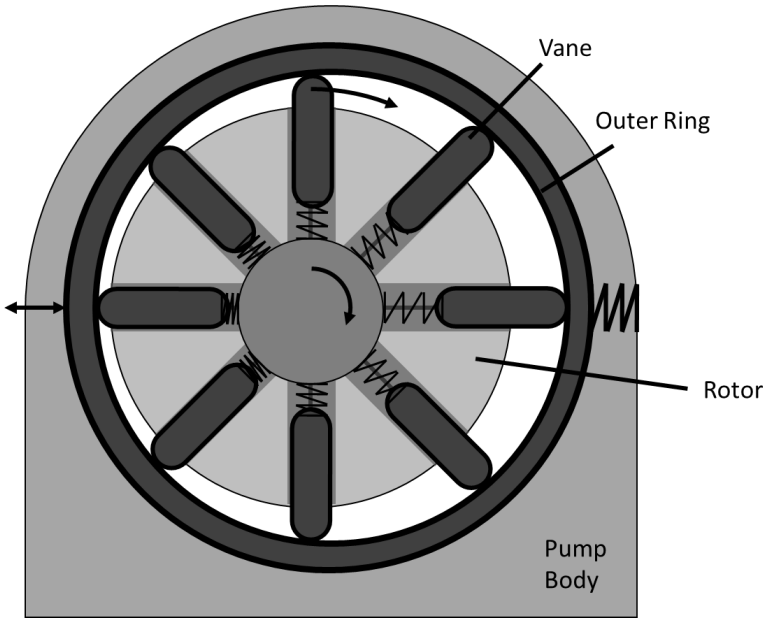

FIGURE 1.3 SCHEMATIC OF VANE PUMP

1.1.2 Linkage Solution

The crank-slider reciprocating piston pump is an architecture capable of the highest pressure operation and is insensitive to fluid contamination [16]. These pumps use pin joints, which are cheaper to manufacture, require less lubrication, and suffer smaller friction losses in comparison with the planar bearings used in other variable displacement architectures. Furthermore, if a crosshead bearing is used, the pumped fluid can be separated from the lubricating fluid, permitting the use of non-lubricating medium in the hydraulic system.

However, linkage pumps are not actively used for high power variable displacement. There are a number of variable stroke mechanisms for linkage-based

metering pumps, which are pumps that are used for precise flow control for low pressure hydraulic systems [17]. There are three primary methods in which these pumps control flow rate: stroke limitation, flow redirection, and adjustable mechanisms. The stroke limited pumps use a linear cam follower mechanism in which the return stroke of the slider is limited by an adjustable stop as depicted in Figure 1.4. Flow redirection metering pumps have internal leakage paths with adjustable opening periods to return fluid to the reservoir for a period of the pump stroke. Some also redirect fluid to an accumulator to prevent recirculation losses. Adjustable mechanism metering pumps vary some part of the drive mechanism to change the stroke of the pumping pistons. The majority of these mechanism vary the length of moving links and have multiple internal prismatic joints, limiting their operating speeds [17].

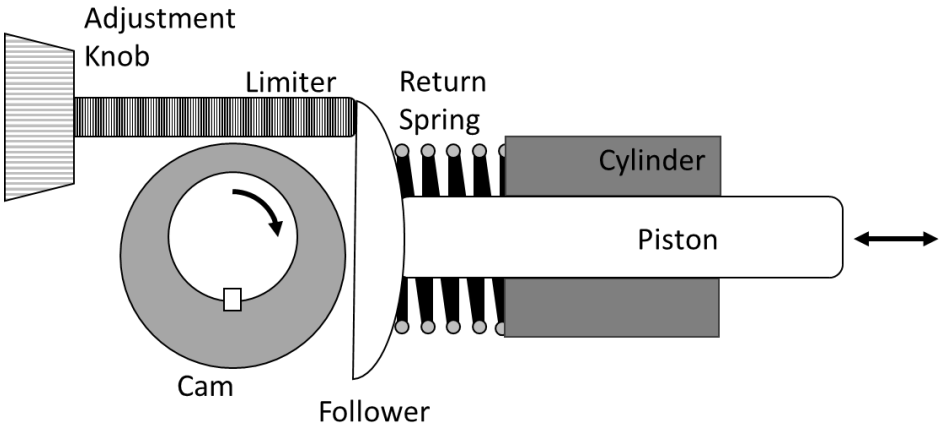

FIGURE 1.4 STROKE LIMITED METERING PUMP FLOW CONTROL

In this thesis, a novel adjustable mechanism, shown in Figure 1.5, is presented as the driving mechanism of a variable displacement pump. This adjustable sixbar mechanism can vary the stroke of the slider link as the input crank rotates without adjusting the position of the crankshaft or axis of slide. As the input crank rotates, the

coupler link causes the rocker link to oscillate. The connecting rod transfers this oscillating motion to the slider link. The ground pivot of the rocker link can be adjusted, causing a change in the oscillating motion, and thus the slider motion.

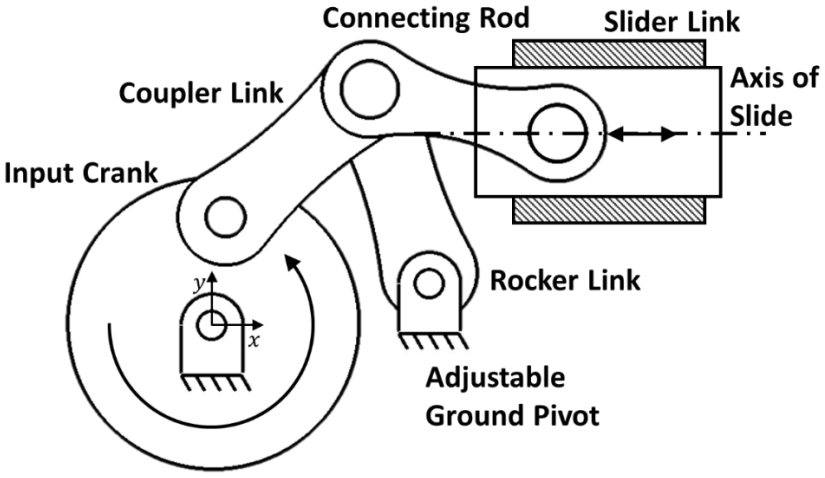

FIGURE 1.5 SCHEMATIC OF VARIABLE DISPLACEMENT LINKAGE PUMP MECHANISM

The mechanism is designed such that the slider link returns to the same position and the end of the travel, independent of stroke. Furthermore, the stroke is adjustable to zero travel of the slider. If a pumping piston is attached to the slider, the result is a variable displacement pump that achieves zero displacement and has a constant top dead center position of the piston. In contrast to other pump designs, the unswept volume of the proposed pumping chamber will remain constant independent of displacement.

1.2 Literature Review

Variable displacement mechanisms are not a new concept and have existed as long as there have been machines [18-20]. They have also been used for power transmission, such as variable displacement engines and compressors [9, 19, 21].

Rigorous study of adjustable mechanism synthesis did not begin until the 1960's as will be discussed in the following section.

1.2.1 Kinematic synthesis

Some of the first techniques of synthesizing adjustable mechanisms came from Tao and Amos, who developed graphical synthesis techniques for generating adjustable fourbar mechanisms for straight line motions and output velocities [22-24]. Bonnel and Coffer applied the complex number method of planar kinematic synthesis, developed by Sandor, to adjustable mechanisms [25]. McGovern and Sandor presented a complex number method to analytically synthesize adjustable mechanisms for variable function and path generation [26, 27]. Handra-Luca outlined a design procedure for six-bar mechanisms with adjustable oscillation angles [28]. Zhou and Ting present a method of generating adjustable slider-crank mechanisms for multiple paths by adjusting the distance between the slider axis and the crank [29]. Shoup developed a technique for the design of an adjustable spatial slider crank mechanism for use in pumps or compressors [30]. Freudenstein used the method of kinematic structure to identify 50 unique fourbar mechanisms suitable for both fixed and variable displacement axial piston pumps [31]. In a similar fashion, Freudenstein completed kinematic structure analysis to determine all of the feasible mechanisms to be used for a variable stroke internal combustion engine [32].

1.2.2 Variable Displacement Internal Combustion Engines

Much work has been done and several patents have been awarded for internal combustion engines that vary the displacement of a piston depending on the power demand [18, 32-36]. A study of one such mechanism was conducted by Pouliot with

Sandia Labs to determine the fuel consumption benefits of a mechanism, reproduced in Figure 1.6, similar to the one used in this thesis. A kinematic model and force analysis was proposed but the internal losses of the mechanism were not considered and no attempt was made to predict the engine performance from the model [34]. Work by Patton characterized the friction contributions of the majority of the running surfaces of an IC engine and this work was updated by Sandoval to reflect modern practices [37, 38]. These works are generally focused on the hydrodynamic bearings of the engine. To the author's knowledge, no model of a variable displacement linkage pump exists in the literature.

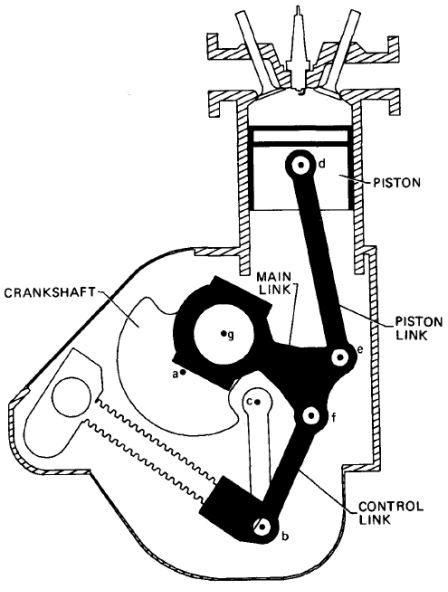

FIGURE 1.6 VARIABLE DISPLACMENT SPARK IGNITION ENGINE STUDIED BY POULLIOT [34]

1.2.3 Pump Models

There are a number of works that characterize the performance of positive displacement pumps and motors using coefficient models. These models use

experimental data to determine coefficients that describe the pump behavior [13, 14, 39-52]. A statistical analysis and comparison of these models was completed by Hall [53]. These models, however, are not predictive in nature and cannot be used during the design phase of a pump.

A number of detailed numerical models have been developed for axial piston, bent axis, and radial piston pumps to predict pump performance using ordinary differential equations to describe the system [4, 45, 52, 54-64]. The most complete modeling and simulation work done in recent years has been by the Maha Fluid Power Research Center at Purdue University with regards to the axial piston architecture. The simulation tool CASPAR, developed by Wieczoreck and Ivantysynova, provides a numerical model that considers the micro-motions of moving parts, predicting leakage flows, viscous friction forces, and applied moments and forces [4, 57]. The multi-physics model is predictive in nature and can be used as a design tool.

CASPAR has been developed through numerous stages to analyze fine details of the axial piston pump in an effort to improve the model, and was updated to include thermal effects in predicting gap heights, localized stresses, and pressure distribution [52]. More recently, the effects of micro surface texturing have been investigated as a method to reduce friction in the swashplate type axial piston machine [56, 65, 66]. Numerous other researchers have developed models of axial piston and other pump architectures, but these will not be discussed in detail as the focus of this work is on the linkage pump architecture

Linkage driven pumps have received far less study. The cylinder pressure dynamics, including the dynamic behavior of passive check valves have been studied, but they are primarily modeled to predict the behavior of the delivery line, and to predict cavitation at the pump inlet. The mechanical losses have not been considered.

In 1984, Edge introduced a computer model that solves the cylinder dynamics of a pump with passive valves [67], and in 1990 a cavitation model and some flow force effects were added [68]. This work found that the volumetric efficiency of a pump was strongly dependent on the performance of the inlet check valves. Later works are dedicated to determining check valve behavior [69, 70] and ultimately the focus was changed to pressure ripple in piping systems [16, 71, 72]

In 1987, Singh presented a model of triplex plunger pumps with self-acting valves, with a primary focus on determining pressure pulsations in the piping system [73]. The focus of the work then shifted to cavitation modeling and prediction [69]. Not much work has been done in the area until recently when CFD analyses have been applied to valve behavior and cavitation studies [65-68, 74, 75].

1.3 Contribution of Thesis

The primary contribution of this thesis is a complete model of a variable displacement linkage pump that considers the kinematic, mechanical, and volumetric characteristics for the purpose of designing such a machine. No model of this level of completeness exists for either fixed or variable displacement linkage pumps. Methods of synthesizing an adjustable mechanism for the application of a pump, as well as solution

rectification are introduced. A mechanical energy loss model is developed from first principles in addition to a dynamic cylinder model. The model is generally applicable to linkage pumps, predictive in nature, and intended to be useful during the design phase of a pump. Furthermore, the model developed in this thesis is applicable to multi-objective multi-parameter optimization where computation time is of key importance.

1.3.1 Overview of Thesis

The objective of this thesis to describe the operation of a variable displacement linkage pump and characterize its performance. Chapter two presents a method of synthesizing a mechanism which can achieve both constant top dead center and zero displacement, along with a kinematic analysis of the mechanism. Chapter three presents a new method of solution rectification that creates bounds on the linkage solution space, avoiding the synthesis of infeasible mechanisms. In chapter four, a kineto-static force analysis provides a method of determining internal forces and frictions in order to develop an energy loss model of the driving mechanism. Chapter five combines the kinematic, solution rectification, and energy loss models to develop a three cylinder demonstration prototype. In chapter six, a dynamic model of the fluid end of the pump predicts the pumping performance of the mechanism and provides realistic loading functions to the mechanical model. Chapter seven provides conclusions and recommendations for future work.

Attempts are made throughout the thesis to eliminate experimentally determined coefficients from the models, creating predictive models that can be applied during the design phase of a pump. Additionally, analytical solutions are used where appropriate to

reduce the computational expense of the analysis for the purpose of running the model a large number of times to optimize a solution. The combined models provide a complete characterization of the mechanism and the model development methodologies are generally applicable to other linkage topologies.

Chapter 2 Adjustable Linkage Mechanism: Construction, Kinematics and Single Cylinder Validation

2.1 Introduction

This chapter describes the design of an adjustable sixbar slider linkage that can drive a piston with a constant top dead center (TDC) and achieve zero displacement. The mechanism synthesis and construction method is presented in section two, followed by the equations of motion in section three. The fourth section describes the design and optimization of a prototype used for validation of the kinematic model. The fifth section presents the experimental validation of the kinematic model. The sixth section provides discussion and the final section contains concluding remarks.

2.2 Mechanism Synthesis and Construction

This section describes both the logical and numerical construction of the variable displacement mechanism with a crank input and a slider output. The described mechanism can achieve both constant top dead center positon and achieve true zero displacement of the slider, while only adjusting the ground link.

2.2.1 Task Specification and Type Synthesis

The operating principle of the variable displacement linkage is to adjust the position or length of one of the links such that there is a change in the displacement, or stroke, of a slider (the piston). Several requirements must be defined in order to guide the synthesis process of such a linkage. For simplicity, robustness, and minimization of moving mass, variability will be achieved by moving a ground pivot rather than changing the length of a moving link. The piston-cylinder axis and the input shaft should remain

fixed relative to each other to simplify the external interfaces with the mechanism. Therefore, at least a third movable ground pivot is required for a functioning variable linkage. A minimal number of links is favorable as it limits the linkage's complexity, moving-mass, and overall size. The three necessary ground pivot require at least a sixbar mechanism. The linkage options are therefore limited to either a Watt II or Stephenson III sixbar mechanism with a slider output. Of these 2 linkages, the Stephenson III seems more favorable because the adjustable ground pivot available for repositioning is attached to a binary link rather than a ternary link resulting in less moving mass to vary when the linkage is in motion.

With a linkage type selected, the next focus is on the task specifications. The first specification is that the output slider of the linkage must be able to reach a zero displacement condition while the input link rotates. This is important because it allows the pump to go to a zero flow state. In order to create a slider mechanism with zero displacement, it is necessary for the moving pivot of the link pinned to the slider link, referred to as the connecting link, to move in an arc about the pivot of the slider. As a result, the connecting link will not impart any translation on the slider. If a fourbar mechanism is constructed such that the coupler curve of any point on the coupler link is an arc, and the slider pivot is placed at the center of this arc, then the slider of the resultant sixbar linkage would have zero displacement. The topology of such a mechanism is depicted in Figure 2.1. If the ground pivot of the output link of the base fourbar is moved, the coupler curve deviates from the original arc and causes the slider to

move. It should be noted that the coupler curve of the mechanism in Figure 2.1.does not travel in a true circular arc, but is shown as doing so for illustrative purposes.

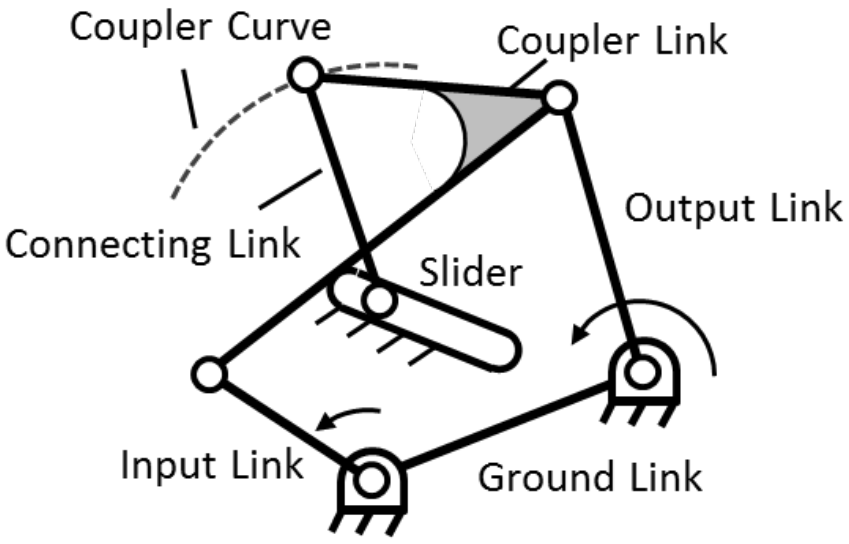

FIGURE 2.1 GENERIC MECHANISM HAVING ZERO SLIDER DISPLACEMENT

While it is challenging to achieve a circular arc by tracking the arbitrary point on the coupler, careful selection of the coupler point can guarantee a pure circular arc. With reference to Figure 2.2, the moving pivot, c, at the end of the output link, R_4, travels in a perfect arc about the ground pivot d. Thus, if the pin of the slider is located at point d, and this pin is connected to point c with an additional link of equal length to the output link, then the slider will exhibit zero displacement. In this arrangement, the output link will be collinear with the connecting link, R_5.

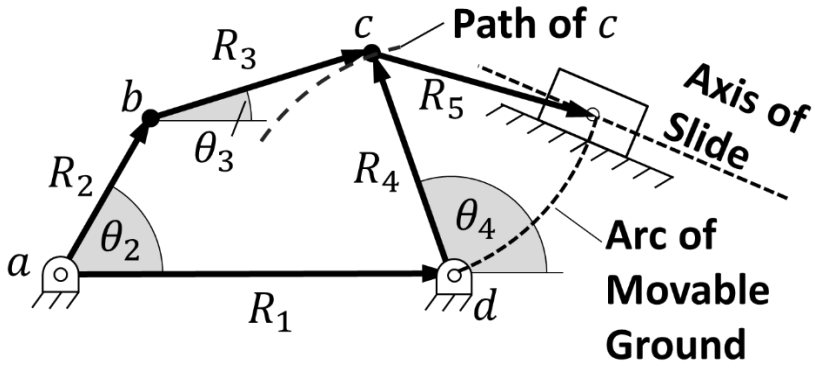

FIGURE 2.2 VARIABLE DISPLACMENT LINKAGE

The second task specification requires that the piston return the same position at the end of its stroke regardless of displacement. This position is referred to as top dead center (TDC). This is important because it minimizes the un-swept volume of the pump chamber at any displacement, which improves performance by reducing the compressible fluid volume.

Given the link lengths of a fourbar mechanisms, such as that in Figure 2.2, the position of the moving pivot c is defined at each angle of the input link, θ_2. If the ground pivot of the output link, d, is rotated about the moving pivot at a prescribed input link angle, then the moving pivot c will always return to this same position at the associated input link angle. The path created by d as it is rotated about the moving pivot is refered to as the arc of movable ground. In this figure, the prescribed input angle θ_2 is arbitrary. The process of determining θ_2 associated with the top dead center position of the slider is discussed in more detail in section 2.3

The two tasks are combined by creating a slider axis which passes through the arc of the movable ground pivot. When the ground pivot, d, is coincident with the axis of

slide, the slider will exhibit no motion. However, as the movable ground pivot travels away from the axis of slide along the specified arc, the slider will translate, and return to the same extreme position at the associated input angle. The methods of constructing a feasible mechanism for use in a pump are described in the next section

2.2.2 Dimensional Synthesis

With the type synthesis complete, and the method of achieving our task specifications known, dimensional synthesis is now presented to construct a feasible linkage solution. To represent this linkage mathematically, the input link is set to unity and all other lengths are a multiple of this value. The input link ground position, a is defined to be the origin of a global coordinate system. The linkage is constructed in five steps.

1) The adjustable base fourbar is synthesized

2) The input link angle associated with TDC is defined

3) The variable ground pivot locations are found

4) The location of zero displacement and axis of slide are defined

5) A resultant connecting rod-slider dyad is constructed

These steps are described in more detail in the next few sections.

2.2.2.1 Variable Fourbar Synthesis

In this section, the details of the base fourbar synthesis are described. In order for the mechanism to be usefully as a pump, a rotary input is required. A fourbar mechanism with an input link which can make a complete revolution with an oscillating output is

called a crank-rocker. The base fourbar must then be a crank-rocker where the input link, R_2, is the crank, the output link,R_4, is the rocker, R_3 is the coupler, and R_1 is the ground link. In order for the crank to make a full revolution the mechanism must meet the Grashof condition, defined as [76]:

$$S + L \leq P + Q \tag{2.1}$$

where S is the length of the smallest link, L is the length of the longest link, and P and Q are the lengths of the remaining links. Another requirement of a crank-rocker is that crank is the shortest link [76]. In this formulation, the crank length is set unity and the rest of the link lengths are a multiples of this value. The length of the coupler and rocker are free choices. With this information, the range of ground link lengths can be found. The Grashof requirement defines the minimum and maximum possible lengths of the ground link where:

$$R_{1max} = P + Q - R_2 \tag{2.2}$$

$$R_{1min} = R_2 + L - P \tag{2.3}$$

A transmission angle is defined as: *The acute angle between the relative velocity vectors of the output link and the coupler link*. [77] Force is best transmitted through these links when the transmission angle is 90º. Defining R_{1max} and R_{1min} according to Eqns. (2.2) and (2.3)guarantees that the coupler and rocker links will become collinear at R_{1max} and R_{1min}. This results in a transmission angle of zero which can cause binding of the linkage and the motion to be indeterminate. To avoid this, a minimum transmission angle, θ_{min}, is defined. From this transmission angle requirement, new values

for $R_{1\min}$ and $R_{1\max}$ are created with a narrower range. These values are solved for by using the law of cosines with the geometry shown in Figure 2.3 according to:

$$R_{1max} = \sqrt{R_3^2 + R_4^2 - 2R_3R_4\cos(\pi - \theta_{min})} - 1 \tag{2.4}$$

$$R_{1min} = \sqrt{R_3^2 + R_4^2 - 2R_3R_4\cos(\theta_{min})} + 1 \tag{2.5}$$

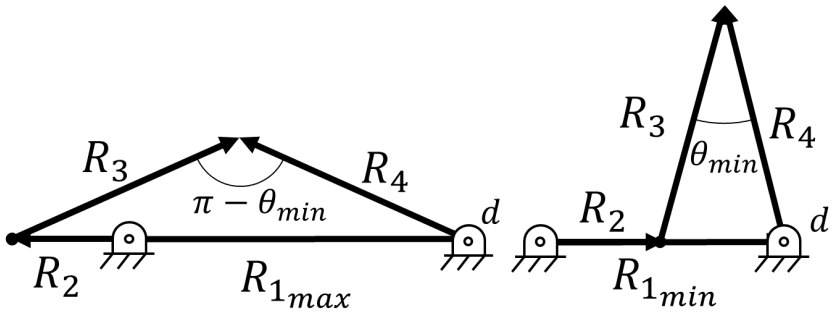

FIGURE 2.3. BASE TRIANGLES FOR DETERMING $R1_{min}$ AND $R1_{max}$

It is required that R_{1min} is less than R_{1max} in order for the transmission angle requirement to be satisfied. This is made apparent from Figure 2.3. If a value smaller than R_{1min} was used at the base of the acute triangle, than the resultant transmission angle would be less than θ_{min}.

Additionally, the variability of the mechanism is related to the difference between $R_{1_{min}}$ and $R_{1_{max}}$. As a result there is a constrained relationship between the link lengths of the coupler, rocker, and minimum transmission angle of the fourbar according to:

$$\sqrt{R_3^2 + R_4^2 - 2R_3R_4\cos(\pi - \theta_{min})} - 1 > \sqrt{R_3^2 + R_4^2 - 2R_3R_4\cos(\theta_{min})} + 1 \tag{2.6}$$

Solving the above inequality for θ_{min} yields:

$$\theta_{min} > \text{acos}\sqrt{\frac{R_3^2 + R_4^2 - 1}{R_3^2 R_4^2}} \tag{2.7}$$

Repeating this process for R_3 results in the inequality:

$$R_3 > \frac{\sqrt{R_4^2 - 1}}{\sqrt{R_4^2 \cos^2(\theta_{min}) - 1}} \tag{2.8}$$

The same relationship exists for R_4 where R_3 and R_4 are swapped in the previous equation. By satisfying these inequalities, the base fourbar can be guaranteed to be constructible and have a variable ground link length. Thus the fourbar is defined with the range of acceptable values for the length of the ground link being R_{1min} to R_{1max}.

2.2.2.2 Defining Top Dead Center

To create an arc of positions of the ground pivot d that can be associated with TDC, the moving pivot c must be located at either end of the coupler curve. This occurs when R_2 and R_3 are collinear in either the extended case or the overlapping case as seen in Figure 2.4. Selecting the extended or overlapped case is one of the free choices of the linkage synthesis. The collinear condition is required because the ends of the coupler curve represent the extreme positions of the rocker, which ultimately controls the slider position of TDC and bottom dead center (BDC).

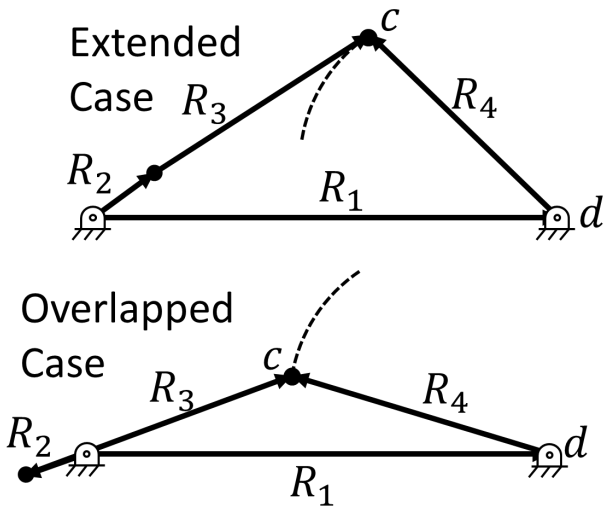

FIGURE 2.4 EXTENDED AND OVERLAPPED EXTREMES OF FOURBAR LINKAGE

2.2.2.3 Defining Variable Ground Pivot Locations

With R_{1min}, R_{1max}, and the location of TDC defined, the arc of acceptable ground pivot locations can be defined. The adjustable ground pivot must fall on a section of the arc of radius R_4 centered at c that falls between the circles of radius R_{1min} and R_{1max} centered at the origin. This construction method is satisfied by two arcs, as seen in Figure 2.5; both of which are valid as they result in a mirror image of the same linkage. Here the case where the input link is extended is shown, but the case where the input link and coupler link overlap is valid as well.

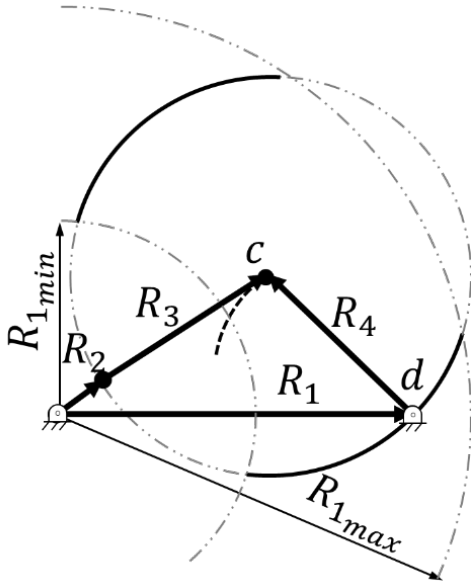

FIGURE 2.5. VARIABLE GROUND PIVOT LOCATIONS FOR EXTENDED CASE

2.2.2.4 Defining Location of Axis of Slide

The location of zero displacement can be placed anywhere along the arc of acceptable ground pivots. However, to maximize the displacement range, R_1 should be set to either R_{1min} or R_{1max} when determining the location of zero displacement. Doing so means that the position of d associated with zero displacement is located at an extreme of the arc of acceptable ground pivots. This allows maximum travel of d as it moves to the opposite extreme of the arc, creating maximum variability of the linkage.

The axis of slide is coincident with the location of the adjustable ground pivot that results in zero displacement. The angle of the axis of slide is a free choice, but the choice affects the maximum slider displacement and transmission angle. Because the axis of slide can be defined with the linkage in the extended case or the overlapped case and at R_{1max} or R_{1min}, there are four configurations in which the linkage can be constructed, as shown in Figure 2.6.

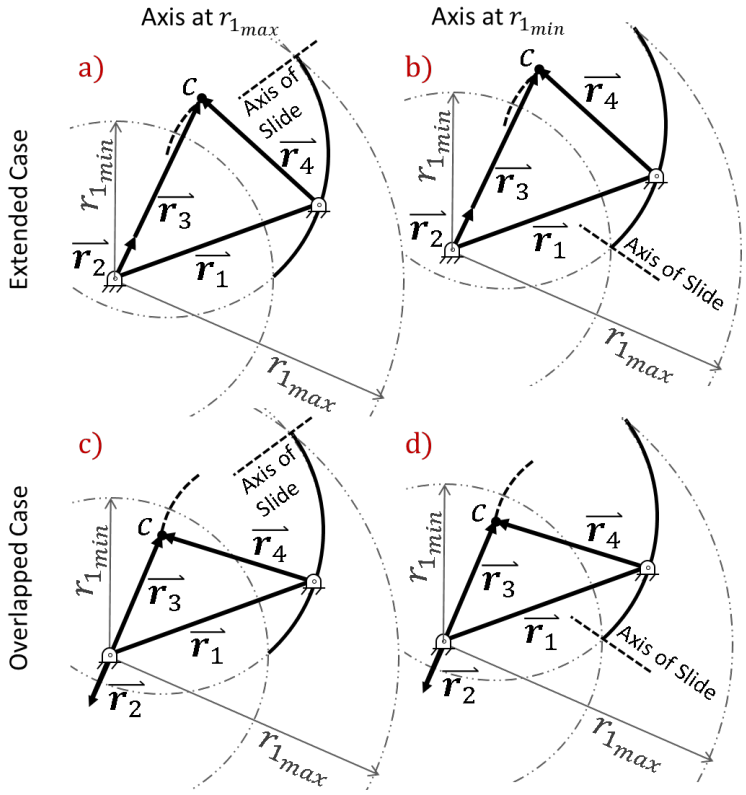

FIGURE 2.6. CONFIGURATIONS OF VARIABLE LINKAGE

Constructing the slider dyad is done by adding a link equal in length to R_4 called the connecting rod. One end of the connecting rod is pinned to the base fourbar at point c, and the other end is pinned to a slider which travels along the axis of slide. When d is coincident with the axis of slide, no translation is imparted to the slider because c travels in an arc about the slider. As d moves away from the axis of slide, the path of c varies. As a result, the slider is translated along the axis. The slider will always return to TDC at a specific value of θ_2.

2.3 Equations of Motion

The performance of the mechanism is determined by the position, velocity, and acceleration of the links. Analytically describing the linkage position is necessary to

predict the piston displacement, while the acceleration of the links is required for the force analysis. In this section, the motion analysis of the mechanism are presented.. For the sake of brevity the following section will focus on the geometry shown in Figure 2.6a, but the analysis of the other geometries is included in Appendix A. However, the position, velocity, and acceleration analyses are made general to apply to all of the geometries.

The linkage is described mathematically using complex number notation and rotation operators. The links are labeled with vector symbols which denote magnitude and direction of the link. The symbols are given by $\vec{\boldsymbol{r}}_j$ where j is the link number. As a point of clarification, r_j is equivalent to the length of link j and θ_j is the angle, counter clockwise positive, from the the x-axis of a non-rotating coordinate system, where $\vec{\boldsymbol{r}}_j = r_j e^{i\theta_j}$.

2.3.1 Vector Representation and Mechanism Definition

For ease of representation, $\vec{\boldsymbol{r}}_{1max}$ is set to be collinear with the x axis and then $\vec{\boldsymbol{r}}_1$ strays off this axis as the ground pivot is adjusted along the arc of acceptable ground pivots. The law of cosines is used to find the position of c associated with TDC, using the triangle with sides $r_{1_{max}}$, $r_2 + r_3$, and r_4, as seen in Figure 2.7.

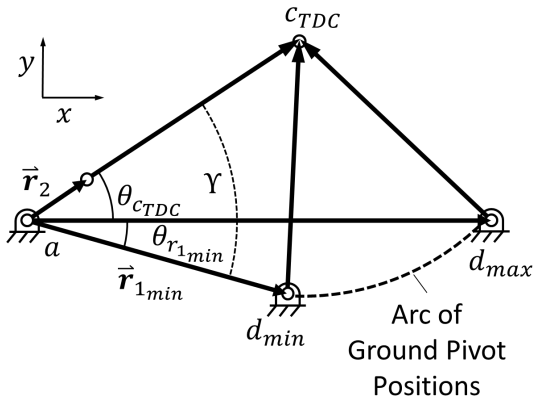

FIGURE 2.7 ASSOCIATED TRIANGLE FOR DETERMINING θ_c AND $\theta_{r_{1_{min}}}$

A vector from the origin to point c is defined as:

$$\vec{\boldsymbol{R}}_C = (\, r_2 + r_3) e^{i\theta_{c_{TDC}}} \tag{2.9}$$

With $\vec{\boldsymbol{R}}_C$ defined, the arc of acceptable ground pivots can be created. The angle of $\vec{\boldsymbol{r}}_{1_{min}}$ is determined by making another associated triangle, seen in Figure 2.7, with sides of $r_{1_{min}}$, $r_2 + r_3$, and r_4. The law of cosines can then be used to find ϒ. The angle of $\vec{\boldsymbol{r}}_{1_{min}}$ from the x axis is:

$$\theta_{r_{1_{min}}} = \theta_{c_{TDC}} - \Upsilon \tag{2.10}$$

As drawn in Figure 2.7, θ_{r1min} has a negative value.

Any point between $\vec{\boldsymbol{r}}_{1_{max}}$ and $\vec{\boldsymbol{r}}_{1_{min}}$ at distance of r_4 from point c is an acceptable ground pivot position of the rocker of the fourbar linkage. A more general form of Eqn. (2.10) is:

$$\theta_1 = \theta_{c_{TDC}} - \Upsilon_1 \tag{2.11}$$

where Υ_1 is found by the law of cosines using a triangle with sides of r_1, $r_2 + r_3$, and r_4. Values of r_1 are bounded by the domain $[r_{1_{min}}, r_{1_{max}}]$. By repeating this calculation over the full domain, the arc of ground pivot positions is found.

The axis of slide passes through d_{max} of Figure 2.7. The slider is joined to the base fourbar at the moving pivot of $\vec{\boldsymbol{r}}_4$ with a connecting link, $\vec{\boldsymbol{r}}_5$, of length equal to $\vec{\boldsymbol{r}}_4$. The angle of the axis of slide relative to the x axis is a free choice, but has a limited domain in which the mechanism can be assembled. A new solution rectification method has been developed to evaluate the domain and is described in full detail in the next chapter.

An example of an assembled linkage is shown in Figure 2.8. In the following section, the conventional vector loop equations are solved for the of the mechanism.

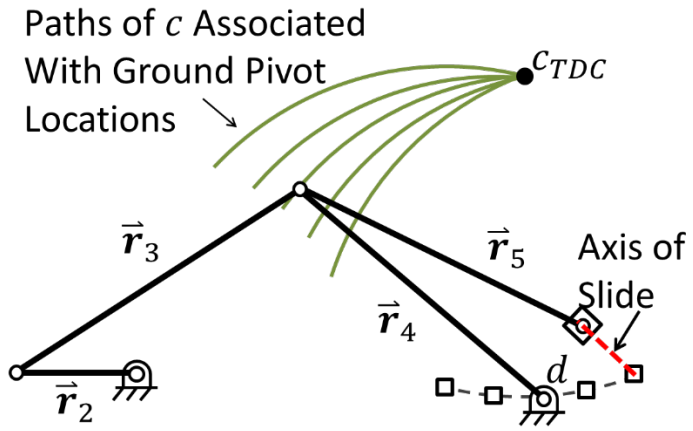

FIGURE 2.8. VARIABLE LINKAGE SHOWING FIVE GROUND PIVOT POSITIONS BETWEEN ZERO AND ONE-HUNDERED PERCENT DISPLACEMENT AND THE ASSOCIATED COUPLER CURVES

2.3.2 Position

The vector loop equations of the sixbar, with reference to Figure 2.9, are:

$$r_2 e^{i\theta_2} + r_3 e^{i\theta_3} - r_4 e^{i\theta_4} - r_1 e^{i\theta_1} = 0 \quad (2.\ 12)$$

$$r_4 e^{i\theta_4} + r_5 e^{i\theta_5} - r_7 \hat{\imath} - r_6 = 0 \quad (2.\ 13)$$

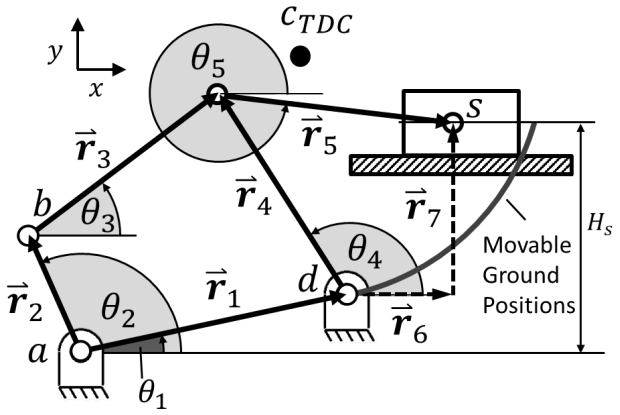

FIGURE 2.9 SIXBAR VECTOR LOOP DIAGRAM

Note that the mechanism has been rotated such that the axis of slide is parallel to the x axis.

In these two vector equations, the magnitudes r_1, r_2, r_3, r_4, r_5, and r_7 are known, as are the angle of the crank link, θ_2, the angle of the ground link, θ_1. The two equations are solved simultaneously for the four unknowns: $\theta_3, \theta_4, \theta_5,$ and s. This solution is now presented.

The position analysis follows the methodology presented by Norton [76] and is completed in two parts: The vector loop of Eqn. (2. 12) is solved to find the coupler and rocker angles, θ_3 and θ_4. Using θ_4 as an input, the vector loop of Eqn. (2. 13) can be solved to find θ_5 and s. The solution to the vector loop of Eqn. (2. 12) is found by the following calculations:

$$K_1 = \frac{r_1}{r_2} \tag{2. 14}$$

$$K_2 = \frac{r_1}{r_4} \tag{2. 15}$$

$$K_3 = \frac{r_2^2 - r_3^2 + r_4^2 + r_1^2}{2r_2 r_4} \tag{2. 16}$$

$$K_4 = \frac{r_1}{r_3} \tag{2. 17}$$

$$K_5 = \frac{r_4^2 - r_1^2 - r_2^2 - r_3^2}{2r_2 r_3} \tag{2. 18}$$

$$A = \cos(\theta_2 - \theta_1) \ - K_1 + K_2 \cos(\theta_2 - \theta_1) \ + K_3 \tag{2. 19}$$

$$B = -2\sin(\theta_2 - \theta_1) \tag{2. 20}$$

$$C = K_1 - (K_2 + 1)\cos(\theta_2 - \theta_1) + K_3 \tag{2. 21}$$

$$\mathrm{D} = \cos(\theta_2 - \theta_1) - K_1 + K_4 \cos(\theta_2 - \theta_1) \ + K_5 \tag{2. 22}$$

$$E = -2sin(\theta_2 - \theta_1) \tag{2. 23}$$

$$F = K_1 + (K_4 1)\cos(\theta_2 - \theta_1) + K_5 \tag{2. 24}$$

$$\theta_3 = 2\tan^{-1}\left(\frac{-E - \sqrt{E^2 - 4DF}}{2D}\right) + \theta_1 \tag{2. 25}$$

$$\theta_4 = 2\tan^{-1}\left(\frac{-B - \sqrt{B^2 - 4AC}}{2A}\right) + \theta_1 \tag{2. 26}$$

with θ_4 known, the slider dyad position can be evaluated.

$$r_7 = H_s - r_1 cos\theta_1 \tag{2. 27}$$

$$\theta_5 = \sin^{-1}\left(\frac{r_7 \ - \ r_4 \sin\theta_4}{r_5}\right) \tag{2. 28}$$

$$s = r_1 e^{1i\theta_1} + r_4 e^{1i\theta_4} + r_5 e^{1i\theta_5} \quad (2.29)$$

where s is the position of the slider.

2.3.3 Velocity Analysis

Assuming that the crankshaft is rotating at some known angular velocity, the angular velocity of the other links and the linear velocity of the slider can be found. The angular velocity of a link is denoted by ω_j where j is the link number. The closed form solution is:

$$\omega_3 = \frac{r_2 \omega_2 \sin(\theta_4 - \theta_2)}{r_3 \sin(\theta_3 - \theta_4)} \quad (2.30)$$

$$\omega_4 = \frac{r_2 \omega_2 \sin(\theta_2 - \theta_3)}{r_4 \sin(\theta_4 - \theta_3)} \quad (2.31)$$

$$\omega_5 = \frac{-r_4 \omega_4 \cos\theta_4}{r_5 \cos\theta_5} \quad (2.32)$$

$$v_S = -r_4 \omega_4 sin\theta_4 - r_5 \omega_5 sin\theta_5 \quad (2.33)$$

where v_s is the piston velocity. With the angular velocity of the links known and the velocity of the piston known, the resultant accelerations can be found.

2.3.4 Acceleration

The angular acceleration of a link is denoted by α_j where j is the number of the link. It is assumed that α_2 is known as with ω_2 in the previous section.The close form solution is:

$$G = r_4 sin\theta_4 \tag{2. 34}$$

$$H = r_3 \sin\theta_3 \tag{2. 35}$$

$$I = r_2\alpha_2 sin\theta_2 + r_2\omega_2^2 cos\theta_2 + r_3\omega_3^2 cos\theta_3 - r_4\omega_4^2 cos\theta_4 \tag{2. 36}$$

$$J = r_4 cos\theta_4 \tag{2. 37}$$

$$K = r_3 cos\theta_3 \tag{2. 38}$$

$$L = r_2\alpha_2 cos\theta_2 - r_2\omega_2^2 cos\theta_2 - r_3\omega_3^2 cos\theta_3 + r_4\omega_4^2 cos\theta_4 \tag{2. 39}$$

$$\alpha_3 = \frac{IJ - GL}{GK - HJ} \tag{2. 40}$$

$$\alpha_4 = \frac{IK - HL}{GK - HJ} \tag{2. 41}$$

$$M = r_4\alpha_4 cos\theta_4 - r_4\omega_4^2 sin\theta_4 - r_5\omega_5^2 sin\theta_5 \tag{2. 42}$$

$$\alpha_5 = \frac{-M}{r_5 cos\theta_5} \tag{2. 43}$$

$$A_s = -r_4\alpha_4 sin\theta_4 - r_4\omega_4^2 cos\theta_4 - r_5\alpha_5 \sin\theta_5 - r_5\omega_5^2 cos\theta_5 \tag{2. 44}$$

where A_s is the acceleration of the slider. With the angular acceleration of the links and acceleration of the slider known, the equations of motion are complete. Using these

values, the position, velocity, and acceleration of any point on the mechanism can be determined.

2.4 Prototype Design for Kinematic Validation

In order to verify the kinematic model and demonstrate the mechanism, a single cylinder prototype was constructed. In this section, the design of the prototype and experimental methods for evaluating the kinematic model are presented.

2.4.1 Design Criteria

Before a prototype linkage was built, the link lengths were chosen and the links then sized. A set of performance metrics were developed to evaluate the linkage solutions. These metrics include: minimum transmission angle of the base fourbar and slider, maximum displacement of the slider, and footprint area of mechanism. An optimal linkage would have maximum transmission angles, maximum displacement, and minimum mechanism footprint. These performance metrics are now discussed in more detail.

2.4.1.1 Transmission angle

There are two transmission angles of interest in this linkage, the angle between the coupler and rocker links and the angle between the connecting rod and the slider. The minimum transmission angle between the coupler and rocker was defined earlier in the synthesis by setting the minimum and maximum lengths of the ground link, R_1. The connecting rod to slider transmission angle is dependent on the angle of the axis of slide.

As previously described, a new solution rectification technique for this slider dyad has been developed and is explained in the next chapter.

At the time of the design of this prototype, the aforementioned rectification method did not exist. A simple relationship was used to define the angle of the axis of slide. With reference to Figure 2.10, in the zero displacement configuration of the linkage, the connecting rod travels in an arc about the slider, defined by the swept angle θ_{4s}. To maximize the slider transmission angle at zero displacement, the angle of the sliding axis bisects θ_{4s} and can be defined as:

$$\theta_s = \pi - \theta_{4_{max}} - \frac{\theta_{4_{max}} - \theta_{4_{min}}}{2} \tag{2.45}$$

where $\theta_{4_{max}}$ occurs at the overlapped condition and $\theta_{4_{min}}$ occurs at the extended condition of the crank and coupler links.

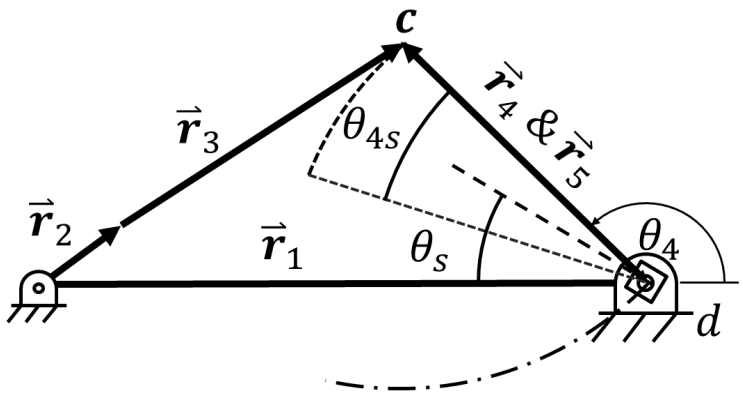

FIGURE 2.10 DEFINING THE ANGLE OF AXIS OF SLIDE

As a result, the transmission angle of the connecting rod and slider is maximized at zero displacement. As the ground pivot moves away from the zero displacement position, this is not the case. As a result, the transmission angle of the slider reaches its minimum value at maximum displacement. The axis of slide angle can be optimized for any displacement however by finding the associated θ_{4s} at the appropriate position of the movable ground d and solving Eqn. (2.45) accordingly.

2.4.1.2 Slider Displacement

The slider displacement is defined as the distance traveled by the slider along the axis of slide from TDC to BDC. The maximum displacement of the slider is calculated when the adjustable ground pivot, d, is located at the farthest position from the axis of slide.

2.4.1.3 Footprint Area of Linkage

The footprint of the linkage is defined as the two-dimensional area occupied by the linkage throughout the range of motion and includes the entirety of the linkage. This area is found by setting the extents of the linkage to a polygon and calculating the internal area. The footprint is guaranteed to be a convex polygon for all cases because the arc of ground pivots extends away from the moving pivot c. The units of the footprint are unit length squared.

2.4.2 Kinematic Optimization

The prototype was optimized with regards to the kinematic characteristics described in the previous section. The solution space for the linkage involves any of the

four configurations in Figure 2.6, each with any lengths of the coupler and rocker. The minimum transmission angle, $\theta_{\min}$, for the revolute joint was set to 30°, as suggested by Alt for maintaining good force transmission[78]. Thus, there are two parameters, r_3 and r_4, for each of the four configuration of the prototype, which are optimized separately.

A grid search optimization study was completed by varying r_3 and r_4 through reasonable bounds to determine the linkage metrics described in the previous section. This study indicated that the minimum slider transmission angle was generally around 60°.. Because of this, the footprint and maximum displacement became the primary optimization metrics of interest. The mechanism was optimized for maximum stroke to footprint ratio as follows:

$$\max_{r_3,r_4} \frac{stroke(r_3,r_4)}{footprint(r_3,r_4)}$$
$$subject\ to: \theta_{min}(r_3,r_4) > 30° \tag{2. 46}$$

Figure 2.11 shows a plot of the Stroke/Footprint for the extended case with the axis of slide located at $r_{1_{max}}$. The peak of this plot shows the location of the optimum lengths of links 3 and 4 at 2.6 and 2.3 unit lengths respectively. This study was completed with the other 3 possible linkage configurations as well. The data for the four optimized linkages are presented in Table 2.1. Based on these data, the overlapped $r_{1_{max}}$ was selected as it has a superior stroke to footprint ratio and a reasonable minimum slider

transmission angle. The optimal length of links 3 and 4 were both found to be 1.8 unit lengths.

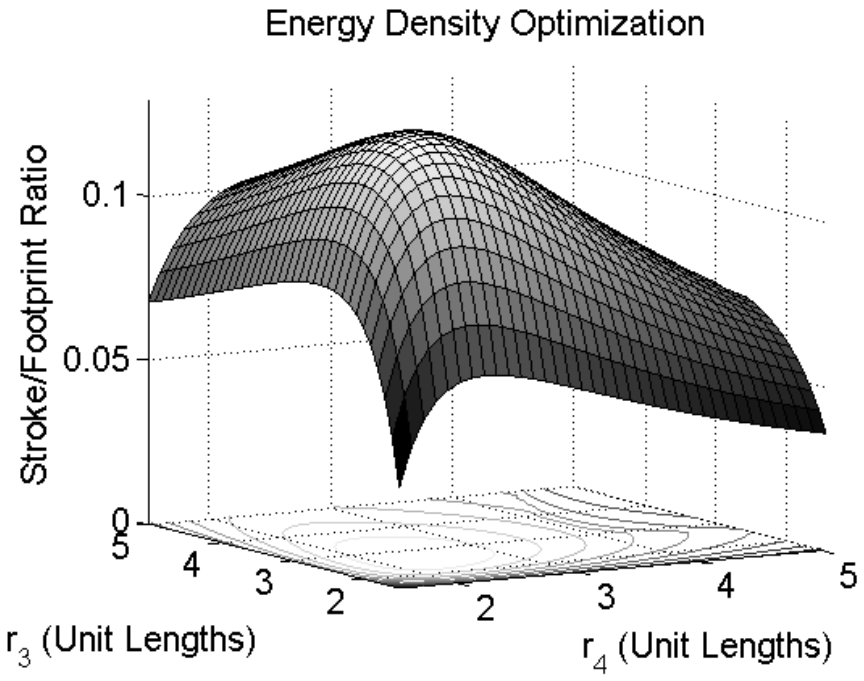

FIGURE 2.11 SURFACE PLOT OF STROKE/FOOTPRINT OF CASE "A" LINKAGE AS FUNCTION OF LINK LENGTHS r_3 AND r_4

TABLE 2.1. LINKAGE OPTIMIZATION RESULTS

Configuration	**Maximum Stroke**	**Footprint**	$\frac{Stroke}{Footprint}$	**Minimum Slider Transmission Angle**
Extended $R_{1\max}$ Figure 2.6a	1.28	9.95	0.13	63°
Extended $R_{1\min}$ Figure 2.6b	1.55	8.6	0.18	58°
Overlapped R_{1max} Figure 2.6c	2.1	8.83	0.24	56°
Overlapped R_{1min} Figure 2.6d	1.35	8.74	0.15	52°

2.4.3 Prototype Sizing

A prototype linkage was designed and fabricated to demonstrate the kinematics of the adjustable linkage. The prototype was also intended to be adapted to a pumping mechanism to accommodate a pressure of 5 MPa with a maximum volumetric displacement of 8.7 cm^3/rev. This requirement drove the link sizing. The resulting design variables are listed in Table 2.2

TABLE 2.2 DESIGN TABLE OF PROTOTYPE VALUES FOR MODELING

PROTOTYPE DESIGN TABLE

Symbol	Description	Value	Unit
$\boldsymbol{r_2}$	Length of Link 2	0.0089	$[m]$
$\boldsymbol{r_3}$	Length of Link 3	0.016	$[m]$
$\boldsymbol{r_4}$	Length of Link 4	0.016	$[m]$
$\boldsymbol{r_5}$	Length of Link 5	0.016	$[m]$
$\boldsymbol{\theta_{min}}$	Minumum Transmission angle of Fourbar	30	$[degree]$
$\boldsymbol{h_s}$	Distance to axis of slide from x axis	0.0158	$[m]$

Plain bronze bushings were used in the joints for design simplicity. A hydraulic cylinder controls the displacement by actuating the displacement adjustment link, causing the adjustable ground pivot to rotate about the adjustment point, $\vec{\boldsymbol{R}}_c$. Figure 2.12 *s*hows a CAD model and line diagram of the fabricated mechanism. Dimensional drawings can be found in Appendix B. The line diagram shows the mechanism at maximum displacement close to BDC.

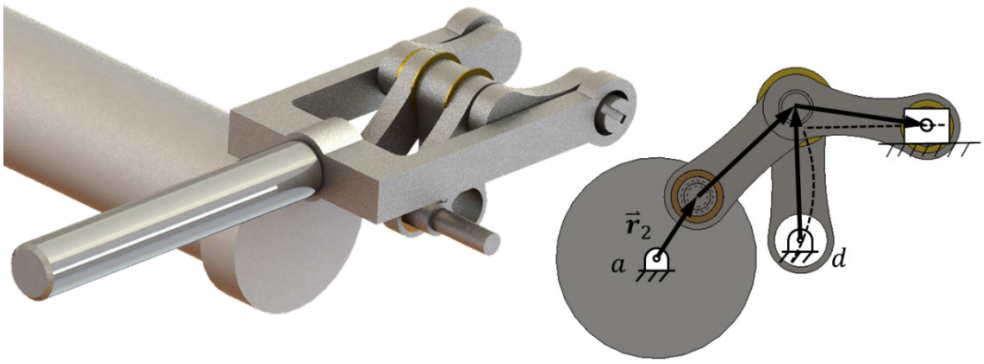

FIGURE 2.12 PROTOTYPE VARIABLE DISPLACEMENT LINKAGE USED FOR EXPERIMENTAL VALIDATION OF KINEMATICS

2.5 Experimental Validation

In order to validate the kinematic model, experiments were conducted to measure the piston position as a function of input crank angle. The measurements were then compared to the kinematic model for validation. To measure the piston position, a precision spring with an experimentally determined spring constant was placed between the piston and a force sensor. The measured spring force was used to determine the piston position. The input shaft speed was measured using an optical quadrature encoder.

The mechanism was driven by a 200W DC electric motor powered directly by a DC power supply, using open loop voltage control. The kinematic model accounts for variations in shaft speed so only the shaft speed measurement was required for validation.

For the experiment, the angular velocity of the input shaft was limited to 8-10 Hz, which allowed for more points of measurement per revolution. Displacement was varied using a hydraulic actuator shown Figure 2.13 and Figure 2.14. The percent displacement was determined by dividing the measured piston displacement by the maximum design

displacement. Each experiment was run for 5 seconds and a single crank rotation from TDC position to the next TDC position was selected at random for analysis. It should be noted that the variation from rotation to rotation was minimal.

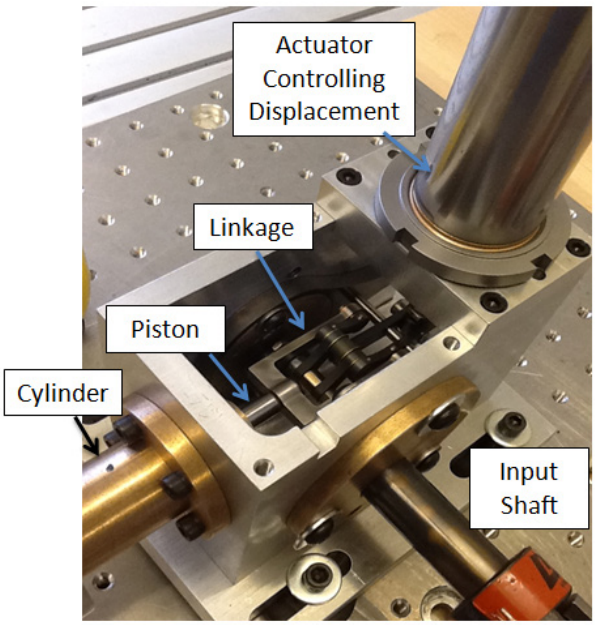

FIGURE 2.13 PROTOTYPE VARIABLE DISPLACEMENT LINKAGE

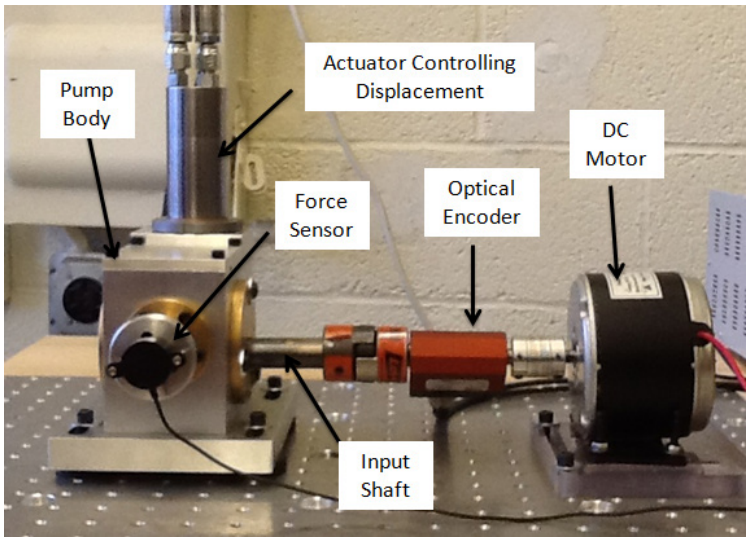

FIGURE 2.14 EXPERIMENTAL SETUP FOR EVALUATING KINEMATIC MODEL

2.5.1 Results

The angular velocity of the input shaft, seen in Figure 2.15, varies between ~340 and 500 RPM through each complete rotation due to the low inertia of the input shaft, the kinetic energy stored in the linkage, and potential energy stored in the spring. The data were filtered digitally using a low pass filter with a cutoff frequency of 50 Hz to remove unwanted 60Hz noise generated by ac electronics in the room. Since the mechanism was running at 8-10Hz this cutoff frequency was deemed acceptable. This filtered crank speed data was then used as an input to the model for an accurate comparison of the position, velocity, and acceleration profiles.

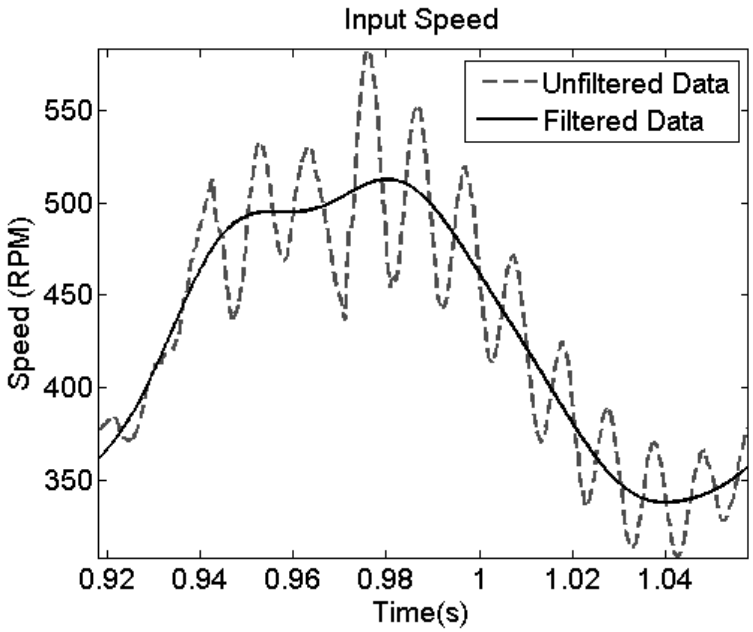

FIGURE 2.15 INPUT SHAFT VELOCITY

Figure 2.16 compares the predicted and experimentally measured piston position through one revolution of the input shaft. The BDC position is defined as zero point and

the peak displacement, 0.0185m, is TDC which corresponds to 93 percent of maximum displacement. The x-axis is the time across one revolution of the input shaft.

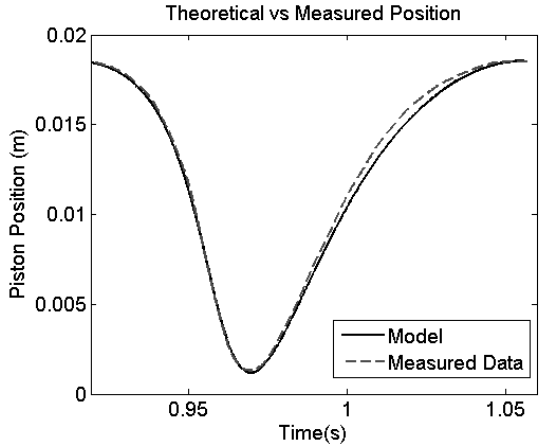

FIGURE 2.16 PISTON POSITION

Figure 2.17 and Figure 2.18 show the piston velocity and acceleration respectively, which were created by differentiating the position data. A zero-phase 50 point moving average filter was used to remove the noise created by differentiating experimental data.

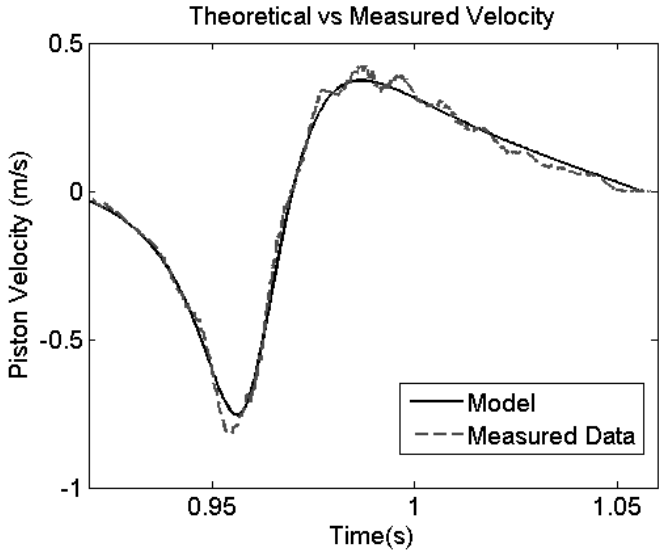

FIGURE 2.17 PISTON VELOCITY

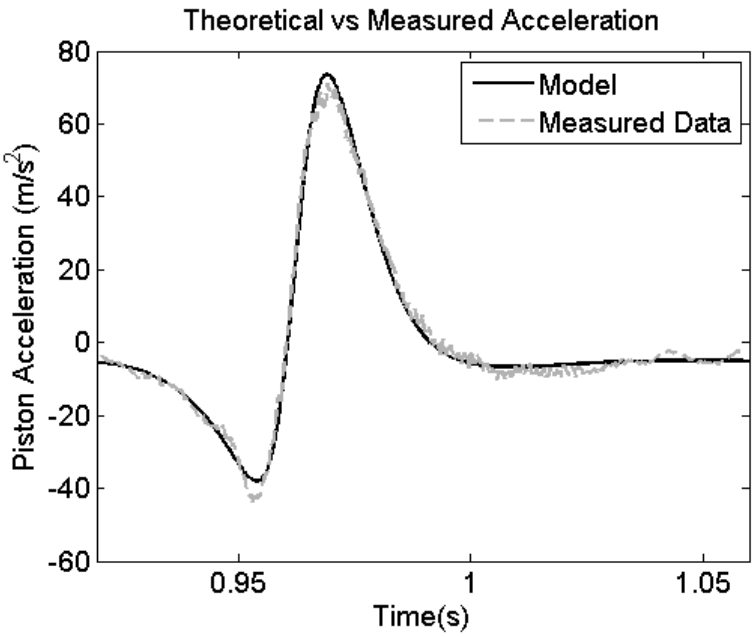

FIGURE 2.18 PISTON ACCELERATION

2.6 Discussion

Figure 2.19 and Figure 2.20 show the theoretical piston velocity and acceleration at 100%, 50%, and 25% of the prototype adjustable linkage. These values are compared with those of a comparable inline fourbar crank slider mechanism having a crank and coupler length equal to those of the prototype. . The Zero-displacement values are not shown as the result is a flat line along the x-axis. These plots show that while the velocity and acceleration profile of the adjustable linkage differs from that of a fourbar crank-slider mechanism, the values are on the same order of magnitude.

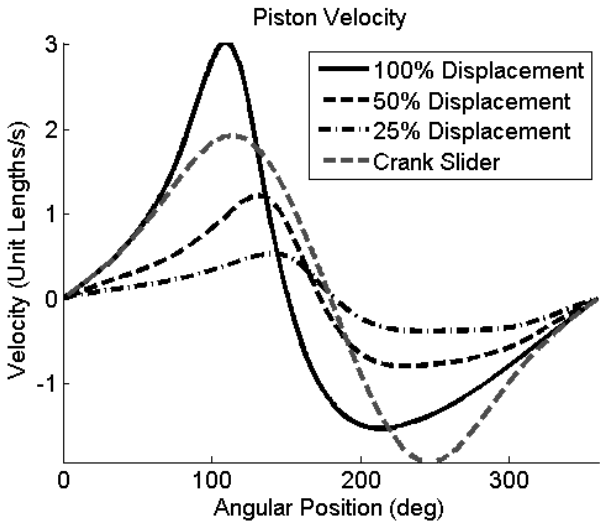

FIGURE 2.19 THEORETICAL VELOCITY PROFILE OF PROTOTYPE LINKAGE WITH INPUT SHAFT SPEED OF 1800RPM AT VARIOUS DISPLACEMENTS COMPARED TO A REFERENCE CRANK SLIDER

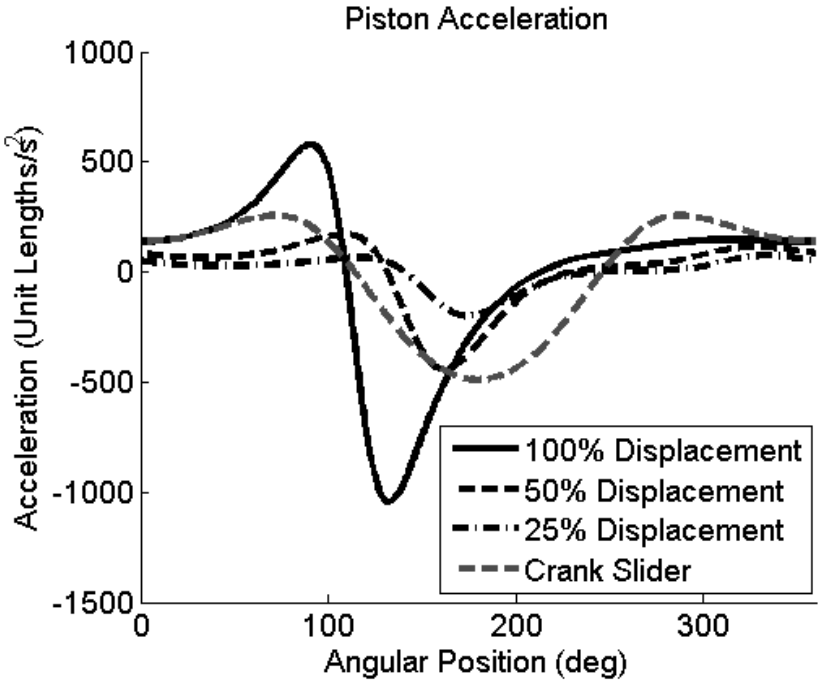

FIGURE 2.20 THEORETICAL ACCELERATION PROFILE OF PROTOTYPE LINKAGE WITH INPUT SHAFT SPEED OF 1800RPM AT VARIOUS DISPLACEMENTS COMPARED TO A REFERENCE CRANK SLIDER

The timing ratio is defined as the ratio of time of working stroke to time of return stroke [76]. When the timing ratio is greater than one, the working stroke is longer than the return stroke which is desirable because it is related to an increased mechanical advantage. When the timing ratio is less than one, the working stroke is shorter than the return stroke resulting in a lower mechanical advantage. When the timing ratio is equal to one, the working stroke is equal to the return stroke and the linkage timing is balanced. A timing ratio close to 1 is desirable because it minimizes piston velocities and accelerations.

The timing ratio of the mechanism varies with displacement as shown in Figure 2.21. At 33% displacement the timing ratio is 1 and deviates by 15% at zero displacement. At maximum displacement, the timing ratio deviates by 28% from 1.When used in a pumping application, the variable timing ratio is not critical because check valves can be used to control the fluid flow into and out of the pumping chamber. However, when used in motoring applications, active valves with variable timing are required to synchronize the fluid flow with the varying BDC position.

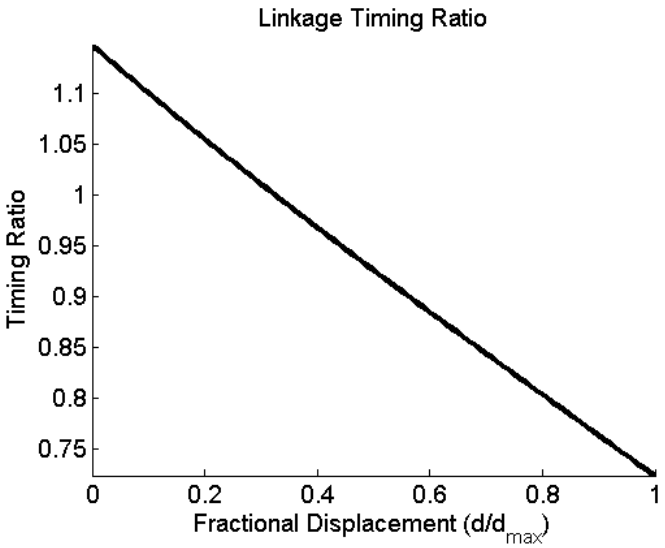

FIGURE 2.21 MECHANISM TIMING RATIO AS A FUNCTION OF FRACTIONAL DISPLACEMENT

The variations in the input shaft velocity, seen in Figure 2.15, are due to the kinetic and potential energy storage in the linkage and spring respectively. When the piston is traveling from TDC to BDC, the spring is extending which applies torque to the shaft, aiding its rotation, thus increasing its speed. When the piston is returning from BDC to TDC, the spring is compressing and storing energy, requiring additional torque, slowing the DC motor speed. Additionally, the figure shows that the variations in shaft velocity don't correspond exactly to TDC and BDC position. This can be attributed to the kinetic energy change as the links are changing velocity through the cycle.

The experimental kinematic data exhibits excellent agreement with the model predictions. The slight variations observed can be attributed to machining tolerances and measurement accuracy. The choice to display the results from a high displacement was based on a desire to show the largest travel, velocity, and acceleration. While not shown, experiments run at other displacements exhibited similar results.

2.7 Conclusions

This chapter describes the synthesis and experimental validation of an adjustable linkage for use as a variable displacement piston pump/motor that can go to zero displacement and has a constant top dead center. The linkage is made by synthesizing a base fourbar with a crank input and a rocker output, and then attaching a connecting link, of equal length to the rocker, and slider link dyad to the moving pivot of the rocker link. When the ground pivot of the rocker link is placed on the axis of slide, the slider will exhibit zero displacement. When the ground pivot of the rocker link is moved along an arc about $\vec{\boldsymbol{R}}_C$, the displacement of the slider varies, while returning to a constant TDC. There are four feasible configurations of the presented mechanism which exhibit these characteristics and an optimization showed that the overlapped $R_{1_{max}}$ configuration was the most compact for a given stroke.

A prototype mechanism was designed to validate the kinematic model. The mechanism was optimized for a maximum stroke to footprint ratio, and the resulting linkage had a minimum base fourbar transmission angle of 30°, and a minimum slider transmission angle of 52°. The optimization showed that the footprint of variable linkages is approximately twice as large as that of a comparable fixed displacement crank-slider, but the increase in size can be expected with the added capability of variable displacement. The model showed good agreement with the experimentally measured piston position, velocity, and acceleration at maximum displacement. Additionally, the velocities and accelerations of the piston are on the same order of magnitude as those of inline crank slider mechanisms which are actively used in fixed displacement pumps.

It can be expected that this mechanism will result in a highly efficient pump due to the low friction revolute joints, lack of hydrodynamic bearings, lack of piston side-loading due to the cross-head bearing, and low un-swept volume at all displacements. The validated kinematic model allows more detailed analysis of the mechanism performance for pumping applications. In chapter four, an energy loss model is developed of the pumping mechanism, and this prototype is modified to act as a pump to validate that model.

Chapter 3 Solution Rectification of Fourbar Mechanisms Including a Prismatic Joint with Transmission Angle Control

3.1 Introduction

In mechanism synthesis, defects occur that often result in unusable solutions and wasted computational effort. Solution rectification is a method of detecting and preventing such defects during synthesis and has been studied for numerous linkage topologies. This approach eliminates areas of the solution space that would result in linkages containing branch defects, circuit defects, order defects, or low transmission angles. Bali and Chand provide a comprehensive literature review of solution rectification, including transmission angle control in mechanisms [79]. In this chapter, a method of solution rectification for planar fourbar mechanisms having a prismatic joint is presented that includes transmission angle control.

Traditionally, the transmission angle is used to evaluate the quality of force and torque transmission through a fourbar linkage. Additionally, a number of authors have developed transmission quality indices to predict linkage performance such as the joint-force index analysis defined by Holte and Chase and more recently the force transmission index [80, 81]. In this chapter, the context of linkage optimization is considered where the energy loss due to joint friction is an optimization objective as seen in [82-84]. This method proves useful for high-speed mechanisms, where the transmission angle is not a direct indicator of performance. When applied to an optimization problem, solution rectification reduces the time to an optimal solution by eliminating computation time for

invalid solutions and, for an evolutionary optimizations, increasing the number of valid solutions in the population.[85-87]

While the transmission angle rectification of four-bar mechanisms is well studied [78, 88], four-bars with prismatic joints have received less attention. Since the output of the variable displacement linkage is a rocker-slider mechanism, it is necessary to develop a method of rectification. Previous works have shown transmission angle control of offset crank-slider mechanisms [89, 90]. However, a solution for an offset rocker-slider mechanisms has not yet been presented. Without the crank constraint, in which the input link completes a full revolution, the problem becomes more complex as more variables are introduced.

In this chapter, a method is presented to determine the valid positions of rocker-slider mechanisms, given a set of link lengths, a minimum transmission angle, and assuming a horizontal slider axis. The solution applies to both non-Grashof rocker-sliders and Grashof crank-rockers where the crank link is constrained to prevent full rotation. Because the Grashof condition is not specified, the term rocker and crank are equivalent and the link pinned to ground is referred to as the pinned link. In section one, an overview of the linkage is provided and the method of defining the rectified solution space is presented. In section two, an example is given to demonstrate the method and provide clarification to the reader. In section three, the solution is discussed in context of the variable displacement linkage pump. Finally, concluding remarks are drawn about the applicability of this method.

3.2 Methods

In this section, the linkage geometry is defined and then the solution rectification method is described for pinned link drive, slider driven, and then switch mode linkages. While the variable displacement linkage pump is a pinned link driven mechanism, the general solution includes slider driven mechanisms and is presented here for completeness.

3.2.1 Linkage Geometry Definition

In this section, the linkage geometry by which the solution is formulated is presented. With reference to Figure 3.1, the linkage geometry is defined by the length of the pinned link, r, the coupler link length, l, and the slider offset distance, H. The slider is assumed to travel parallel to the x-axis. The position of the mechanism is defined by the piston position, X, and the angle of the pinned link, θ. Here the mechanism is parameterized by θ, but could equally be defined by X.

In this system, there are two transmission angle constraints to be specified depending on how the linkage is driven. If the slider is the input to the mechanism, the transmission angle between the pinned link and coupler link, γ, is to be specified. If the pinned link is the input, the transmission angle between the slider and coupler link, γ_s, is specified. If there is a reversal of driver and driven link, both angles are specified in order to control the effectiveness of the mechanism. To provide a more intuitive representation of the transmission quality at the slider joint, the pressure angle, α, which is equal to $\left|\frac{\pi}{2} - \gamma_s\right|$ is used in the derivation.

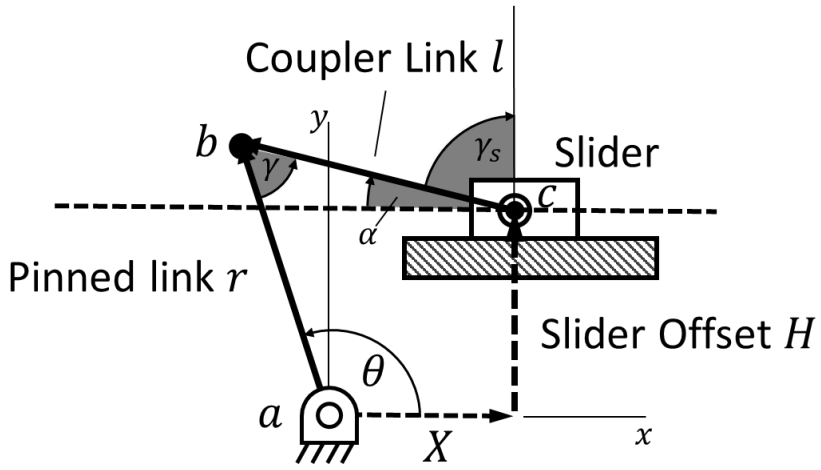

FIGURE 3.1 LINKAGE GEOMETRY

The formulation presented in this chapter assumes that α and γ are acute and positive. Since the transmission angle γ is the acute angle between the pinned link and coupler link, there are two equivalent angles which are used in the derivation where $\gamma_{min} = \gamma$ and $\gamma_{max} = \pi - \gamma$. There is no such equivalency for the pressure angle, α. It is assumed and that the slider is on the right side of the pinned link r and $H \geq 0$. Any other situation is realizable by reflection over the y and/or x axes.

Bounds on θ are determined with regards to the γ and α constraints independently. If both constraints are to be considered simultaneously, these bounds are then compared to determine which values are limiting.

3.2.2 Slider Driven Mechanism

The transmission angle is measured with reference to the output link of a mechanism. In the case of a slider driven mechanism, such as a hydraulic motor, the angle γ is constrained. This section describes the solution rectification of a slider driven mechanism. From the defined linkage geometry and transmission angle requirements, a

solution space of valid slider positions is created. When considering the maximum and minimum values of γ, an annulus, seen in Figure 3.2, can be created with interior radius k_{min} and exterior radius k_{max}, defined by:

$$k = \sqrt{r^2 + l^2 - 2rl\cos(\gamma)} \tag{3. 1}$$

where k_{min} and k_{max} are found using γ_{min} and γ_{max} respectively.

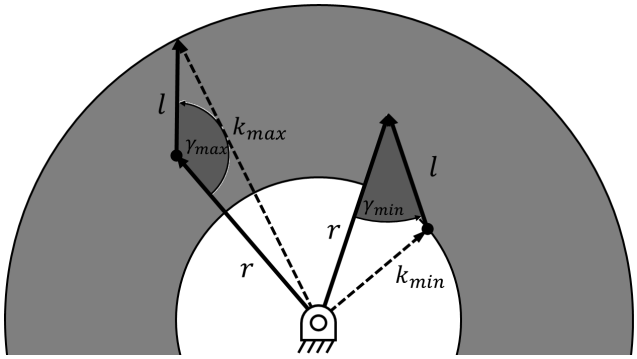

FIGURE 3.2 ANNULUS DEFINING SOLUTION SPACE DEFINED BY PINNED DYAD TRANSMISSION ANGLE γ

The slider offset distance, H must be defined such that the resulting axis of slide passes through this annulus. There are three possible outcomes for a given value of H:

Case A: If $H \geq k_{max}$, the intersection is empty or at a single point, resulting in no useful linkages.

Case B: If $k_{min} \leq H < k_{max}$, the intersection is a continuous segment.

Case C: If $H < k_{min}$, the intersection is a pair of line segments.

Case C, depicted in Figure 3.3, is the most general case and is used to define the solution space for slider driven mechanisms. The two segments are mirrored about the

y axis resulting in a right and left segment solution space. This nomenclature is used throughout to differentiate these two spaces. Using the k values found previously, the points of intersection between the segments and annulus can be found. These slider segment lengths are defined by the right triangle ΔkHX yielding the equation:

$$X = \sqrt{k^2 - H^2} \tag{3. 2}$$

where k is either k_{min} or k_{max}. X defines the right side segment while $-X$ defines the left.

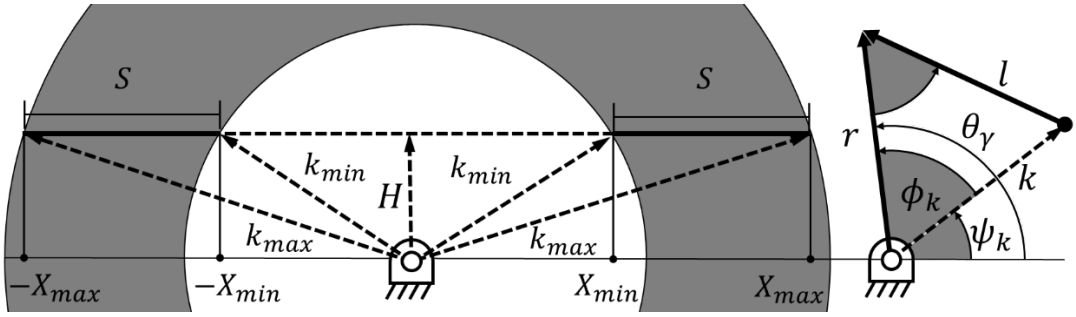

FIGURE 3.3 DEFINING VALID SLIDER POSITIONS CONSIDERING γ CONSTRAINTS

The slider segment length is defined as:

$$S = X_{max} - X_{min} \tag{3. 3}$$

Assuming the slider is to the right side of the link pinned to ground, the open and crossed configurations are defined by right and left segments respectively.

For each of the bounding points, there is an associated angle between the x-axis and the k line defined by:

$$\psi_k = \text{atan2}(H, X) \tag{3. 4}$$

where a unique value is found for each of the four *X* points and atan2 is the four quadrant inverse tangent function.

The angle between each k line and the pinned link is described by:

$$\phi_k = \text{acos}\left(\frac{r^2 + k^2 - l^2}{2rk}\right) \tag{3. 5}$$

The bounding angles of the pinned link are expressed as:

$$\theta_\gamma = \psi_k \pm \phi_k \tag{3. 6}$$

where ϕ_k is added to ψ_k for the right segment and subtracted for the left segment. These calculations result in a total of 4 bounding angles defining the right and left segment solution spaces. These four bounding values of θ_γ are depicted in Figure 3.4 for an arbitrary linkage.

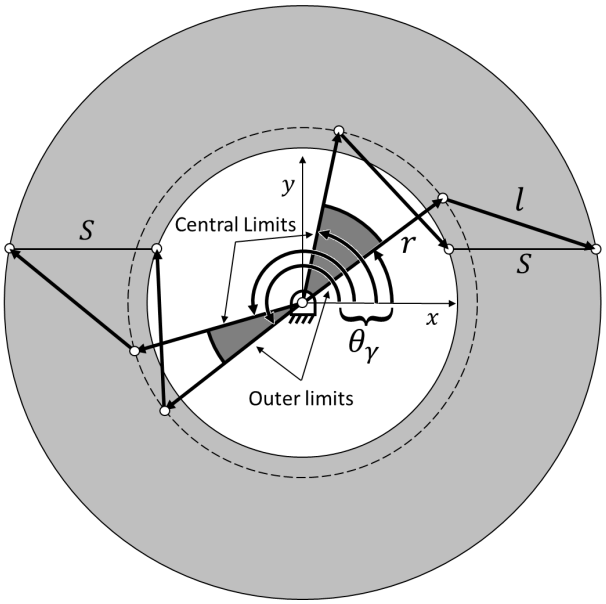

FIGURE 3.4 DIAGRAM SHOWING FOUR VALUES OF θ_γ FOR AN ARBITRARY LINKAGE OF CASE C

For Case B, k_{min} is not considered because $H \geq k_{min}$ resulting in a continuous slider segment. In this case the segment length is found by:

$$S = 2X_{max} \tag{3. 7}$$

There is only one unique linkage solution associated with this condition. The mechanism transitions between the open and crossed configurations as the slider passed the y axis. As a result, a single solution embodies both the crossed and open configurations. To find the point at which the slider crosses the y-axis and the linkage transitions between the crossed and open condition, X is set equal to zero in Eqns. (3. 4) to (3. 6).

3.2.2.1 Transition between crossed and open configuration

For both Cases B and C, it is possible for the linkage to transfer between the open and crossed configurations in positions other than when the piston passes the y-axis. This is because the slider dyad has no constraint on the pressure angle α, which is allowed to pass 90°. As a result, the pinned link angle, θ, as a function of X, can be multivalued. If a single valued result is required, these transition positions must be identified. This transition only occurs if the following conditions are met:

For the right side, open configuration

$$H > rcos(\gamma) - l \tag{3. 8}$$

For the left side, crossed configuration

$$H < r\cos(\gamma) + l \tag{3. 9}$$

If either of those conditions are met the position at which the transition occurs can be found by:

$$X_0 = \pm\sqrt{r^2 - (H \pm l)^2} \tag{3. 10}$$

$$\theta_0 = atan2(H \pm l, X_0) \tag{3. 11}$$

where using the + and – in Eqns (2.2) and (2.3) corresponds to the right and left segments respectively.

Figure 3.5 shows Cases B and C where the linkage transitions between the crossed and open condition. For Case B, the right and left segment solutions are identified with grey and black vectors respectively. Positions 1-4 correspond to the points of minimum transmission angle. Note that in this figure, X_0 occurs before the fourth position of the mechanism demonstrating that the pinned link angle, θ, is not always increasing as the slider moves from right to left. For Case C, the left and right segments are part of the same mechanism. Since the slider can pass freely between the left and right sides, the interior points 2 and 3 are coincident and are numbered this way for consistency with Case B.

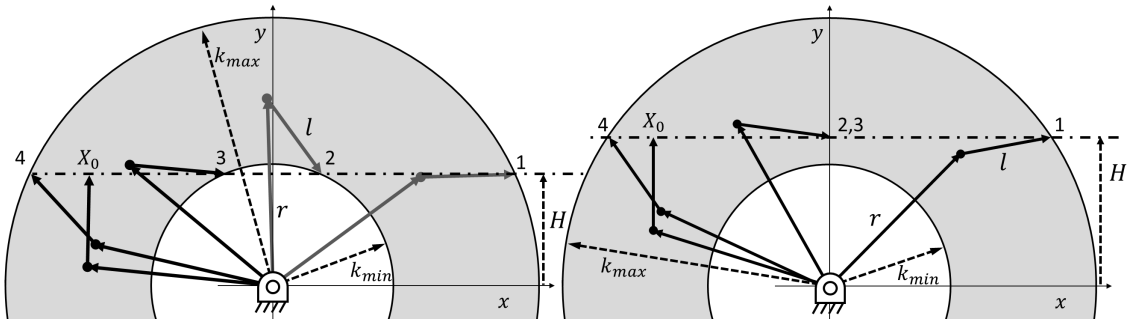

FIGURE 3.5 CRITICAL POSITIONS OF SLIDER DRIVEN MECHANISM FOR CASE B AND C DEPICTING THE MINIMUM TRANSMISION ANGLES OF THE PINNED LINK DYAD AND THE TRANSITIONS BETWEEN CROSSED AND OPEN CONDITION

3.2.3 Pinned Link Driven Mechanism

In this section, the solution rectification of a pinned link driven mechanism is described in which the pressure angle α is constrained. A new variable, Y, is introduced which is the distance between the axis of slide and the joint connecting r and l. The offset, Y, can be above or below the axis of slide. As seen in Figure 3.6, this offset is a function of α according to:

$$Y = l\sin(\alpha) \tag{3. 12}$$

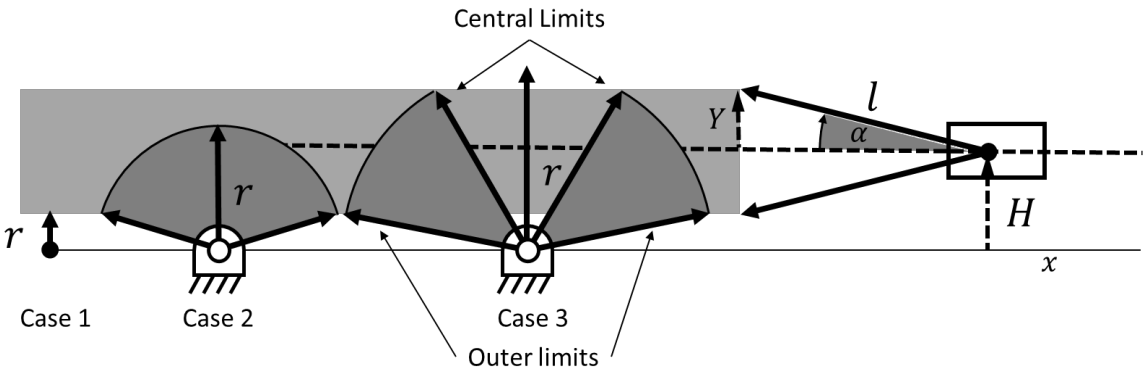

FIGURE 3.6 DEFINING THE VALID SLIDER POSITIONS CONSIDERING α CONSTRAINTS

The constraints on α result in four distinct solution spaces:

Case 1: If $r < (H - Y)$, the pinned link is too short and the constraint cannot be satisfied and no useful solution exists.

Case 2: If $(H - Y) < r \leq (H + Y)$, a continuous range of θ is possible.

Case 3: If $r > (H + Y)$, the valid range of θ is split by a region which does not satisfy the constraint resulting in two segments similar to the γ limited Case.

Case 4: If $r < (Y - H)$, α is non-constraining and need not be considered further. This is equivalent to a Grashof crank-slider mechanism with transmission angle control as the pinned link is allowed to make a complete revolution without breaking the constraint.

Case 3 represents the most general solution space as it has 2 separate regions, a right and a left, defined by four angles of the pinned link. These right and left regions are not to be confused with the right and left segments of the slider driven mechanism. The four defining angles are categorized into central and outer limits. The solution space is depicted in Figure 3.6.

Figure 3.7 depicts the geometry used to determine the valid angles of the pinned link for Cases 2 and 3, which are both valid and constrained. The variable m is introduced to

define the right triangle $\measuredangle r(H \pm Y)m$. This value can then be used to determine the bounds on the angle of the pinned link θ_α:

$$m = \sqrt{r^2 - (H \pm Y)^2} \tag{3. 13}$$

$$\theta_\alpha = atan2\big((H \pm Y), \pm m\big) \tag{3. 14}$$

where $(H + Y)$ in Eqns (3. 13) and (3. 14) results in the central limits and $(H - Y)$ results in the outer limits of the valid range of θ_α. The evaluation of Eqn (3. 14) with + or - m results in the values for the right and left regions respectively.

For Case 2 the central limit is not considered resulting in a continuous range of θ, with the mechanism only bounded by the two outer limit values of θ_α. For Case 3, the central limits are defined by evaluating Eqns (3. 13) and (3. 14) with $(H + Y)$. There are four values of θ_α which define the bounds of the valid regions of the pinned link angles θ of both the left and right region respectively.

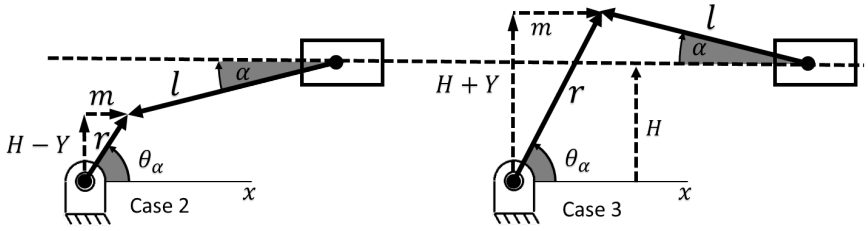

FIGURE 3.7 DEFINING α LIMITED OSCILLATOR ANGLE θ FOR TWO DIFFERENT CASES OF PINNED LINK LENGTH r

3.2.4 Switched Input Mechanisms

For some mechanisms, the slider or the pinned link can be the driver link depending on the mode of the linkage. For example, in an IC engine, the crank (pinned

link) is the driver during the compression stroke, but the piston is the driver during the power stroke. In these cases, both γ and α should be specified.

If both of the transmission angle constraints must be satisfied simultaneously, the slider driven and pinned link driven solution spaces must be compared. Each of the two solution spaces result in a set of four angles that bound the valid pinned link angles: the outer-left, central-left, central-right, and outer-right bounding angles. For Case 2, Case 4, and Case B, the central limits are null. These two sets of four angles must then be compared to find the limiting values. Because there is a constraint on α, θ_0 of Eqn. (2.3) need not be considered.

For each bounding angle comparison, there are three feasible results:

Case I: If there is no overlap, then there are no valid regions of linkage motion.

Case II: If there is overlap and all for central angles are null, the result is a continuous segment. This occurs when both Case B and Case 2 true or when both Case B and Case 4 are true.

Case III: Otherwise, there will be a left side and right side range in which the mechanism can operate but cannot transfer between the two with acceptable transmission angles, forming different transmission-angle-limited pseudo-circuits of the linkage. These are not true circuits because the linkage could potentially pass from one to the other without taking the linkage apart, but this cannot occur while satisfying the transmission angle constraints.

Figure 3.8 shows a sample of the overlapped solution space for an arbitrary linkage limited by both the γ and α constraints. Only the open configuration is shown, but a similar graphic could be made for the crossed configuration as well. Note how the overlap is contained interior to both sets of limits.

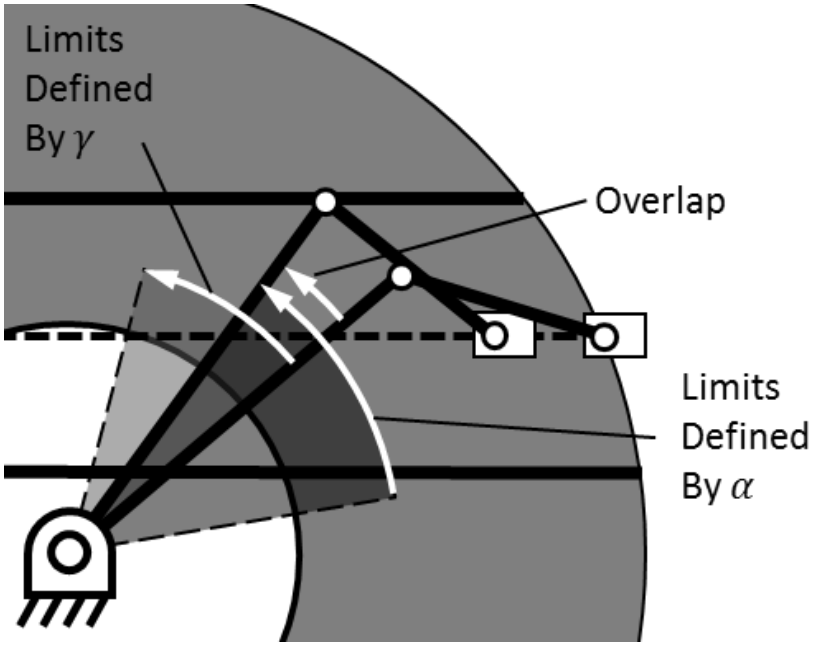

FIGURE 3.8 OVERLAP OF THE RIGHT SIDE α AND γ LIMITS FOR AN ARBITRARY LINKAGE

3.3 Example Mechanism

A Watt-II sixbar with a slider output for application in a pump is used as an example for clarification and to demonstrate the method. As seen in Figure 3.9, the base fourbar of the Watt II is a Grashof crank-rocker where the pinned link travels through a 39.5° arc. The dimensions of this linkage are given in Table 3.1. As the slider is the output link, only the pressure angle of the slider, α, must be considered. However, for

demonstration purposes a minimum transmission angle requirement of 20° is added for γ; this would represent this linkage operating as a motor. In this example, the values of the slider offset distance, H, that satisfy these constraints will be determined.

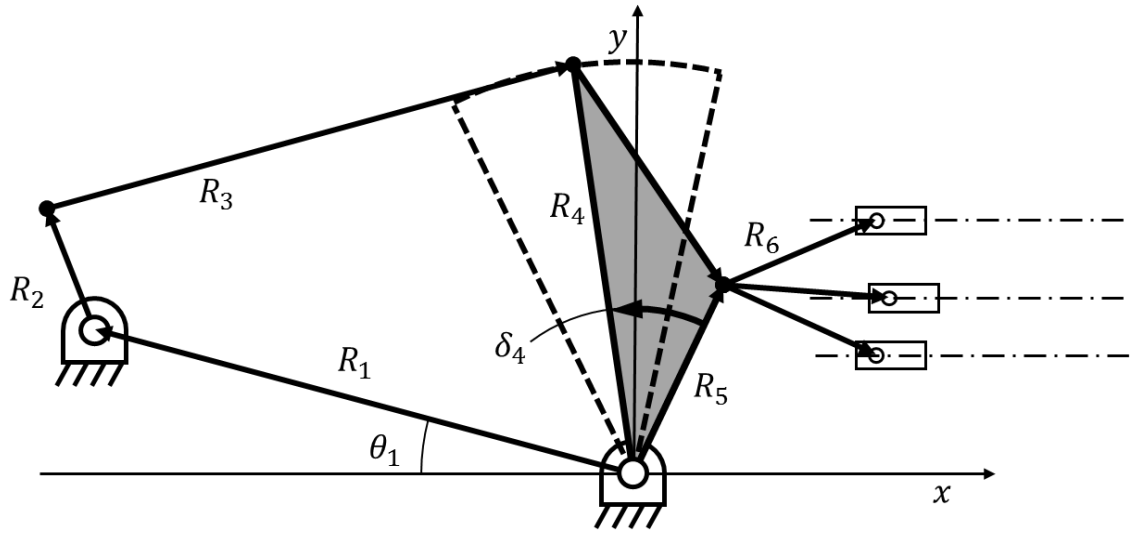

FIGURE 3.9 PROBLEM STATEMENT FOR EX2 DEFINING CANDIDATE LINKAGE

TABLE 3.1 PARAMETERS OF LINKAGE IN EX. 2

Parameter	R_1	R_2	R_3	R_4	R_5	R_6	θ_1	δ_4
Value	4.38	1	4.3	3.13	1.6	1.3	165.7°	30°

Step 1: Define Slider Dyad

The rocker-slider output of the Watt II is defined by the rocker length R_5, the coupler length R_6, and the rocker swept angle from θ_{5_0} to θ_{5_1}. Due to the rocker path generated by the crank-rocker input, the swept angle does not cross the y-axis so the right side solution for the pinned dyad limited space is considered. It would be impractical to

build the pump with the piston on the left side of the coupler link so only the configuration shown is considered.

Step 2: Determine Valid Slider Axis Heights

The limits on the slider offset due to the γ transmission angle is found by, first, solving for k_{max}, k_{min}, and ϕ_k from Eqns (2.1) and (3. 5). Next, ψ_k is found from Eqn (3. 4) with θ_γ set equal to either θ_{5_0} or θ_{5_1}. The slider offset is described by:

$$H = k\sin\theta \tag{3. 15}$$

where H has four values associated with θ_{5_0} and θ_{5_1}, using both k_{min} and k_{max}. The limiting values are selected (minimum of the k_{max} value and maximum of the k_{min} value). The calculated slider offset values and resulting limits are presented in Table 3.2 and the resulting solution space is shown in Figure 3.10a.

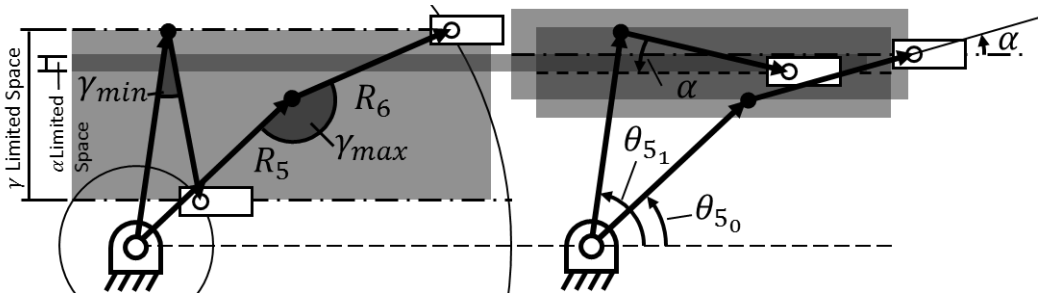

FIGURE 3.10. SLIDER HEIGHT SOLUTION SPACE FOR THE OPEN LINKAGE

TABLE 3.2 CALCULATED VALUES OF γ LIMITED VALUES OF H

	k_{min}	k_{max}
θ_{5_0}	$H = 0.073$	$H = 1.572$
θ_{5_1}	$H = 0.311$	$H = 2.79$
Limiting Value	$H = 0.311$	$H = 1.572$

A similar process is completed to solve for the α limited space. By computing Y from Eqn. (3. 12) the slider offset is described by:

$$H = R_5 \sin\theta_\alpha \pm Y \tag{3. 16}$$

where θ_α is set equal to either θ_{5_0} or θ_{5_1} resulting in 4 values for H from which the limiting values must be selected. The resulting solution space is shown in Figure 3.10b. The results from the γ and α limited cases must be compared to determine the most limiting values of H, as shown in Table 3.3.

TABLE 3.3 CALCULATED VALUES OF α LIMITED VALUES OF H

H	Min	Max
α	1.247	1.414
γ	0.311	1.572
Limiting Value	1.247	1.414

Step 3: Select a Slider Axis Height

From the range of acceptable slider offset distances, H can be selected freely. If, for example, α were to be minimized and if H is limited by α alone, the average of the limits of H would be selected. In general, the transmission angle is smaller as the slider axis height approaches the limits. In order to maximize the transmission angle, the distance between the axis of slide and the limits is maximized. For this problem, H is selected such that γ is maximized. This corresponds to an H of 1.247 in the example.

Step 5: Build Solution Linkage

The resulting sixbar mechanism is shown in Figure 3.11 at both ends of the slider displacement and the mid-point. This solution has the largest minimum transmission angle between links R_5 and R_6 of the open linkage.

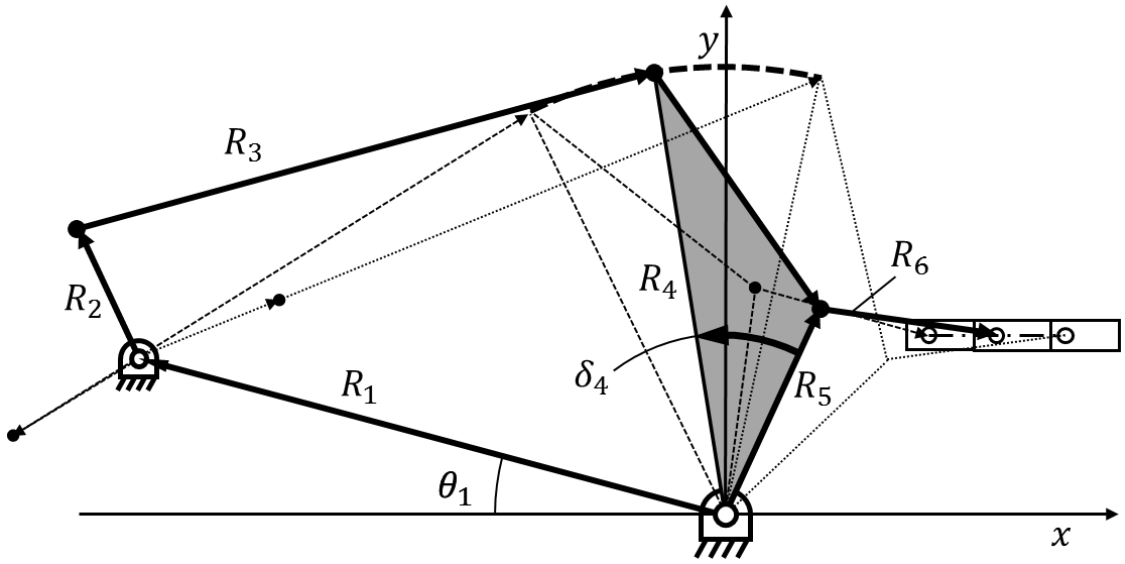

FIGURE 3.11 SOLUTION LINKAGE WITH MAXIMIZED MINUMUM TRANSMISSION ANGLE FOR THE OPEN LINKAGE OF EX2

3.4 Discussion

In this section, the application of the solution rectification method to the variable displacement linkage pump is discussed. In the context of the adjustable mechanism, the example of the previous section directly applies. However, the solution space must be expanded to accommodate the varying ground pivot location of the pinned link.

Additionally, the output of the variable displacement linkage pump is always the slider so only constraints on α are considered for the rocker slider dyad.

In the synthesis of the linkage pump mechanism, the crank-rocker base four-bar is defined according to the methods described in the chapter 2. The solution rectification method is then used to create a range of feasible slider offset distances as a function of R_1, which define the location of the adjustable ground pivot, and a maximum pressure angle, α. This range is then further refined to a solution space that satisfies all ground pivot locations simultaneously. As a result, only feasible mechanisms which satisfy the user defined constraint are considered during the design and optimization process.

3.5 Conclusions

A method of controlling the transmission angles of a four-bar mechanism with a pinned link and a slider has been presented, which can be used to prevent defects in mechanisms. Methods for both pinned link driven and slider driven were presented along with a combination of the two for mechanisms which reverse the driver and driven links. A Watt-II linkage pump mechanism was provided as an example to show how the method can be used to limit the solution space. The example also demonstrated how different aspects of the linkage definition can be used to parameterize the linkage solution space. Furthermore, the solution was discussed in context of the variable displacement linkage pump mechanism.

Solution rectification can be especially useful when applied to optimization problems. Typically, the inputs to an optimization are meant to be as general and un-constraining as possible. When optimizing a mechanism, the majority of evaluated

linkages have defects and are unusable as a result of this generality. Using these new techniques, the evaluation of defective slider mechanisms can be avoided without unnecessarily constraining the problem, thus preventing wasted computational effort and speeding up optimizations.

Chapter 4 Mechanism Force Analysis and Energy Loss Modeling

4.1 Introduction

The crank-slider reciprocating piston pump is an architecture that is not actively used for variable displacement. These pumps use pin joints, which require less lubrication and suffer smaller friction losses in comparison with the prismatic joints used in other variable displacement architectures. Both plain and roller bearings can be modeled using Coulomb friction, and as a result, the losses in the pin joints of a mechanism scale linearly with applied load and angular displacement. Other works and patents have presented the use of adjustable linkages for stroke variation of internal combustion engines [18, 31-36], but little can be found with regards to an adjustable linkage-based variable hydraulic pump.

The presented adjustable mechanism, shown in Figure 1.5, is being proposed as the driving mechanism of a variable displacement pump. This mechanism is of the overlapped R_{1max}configuration presented in chapter two.

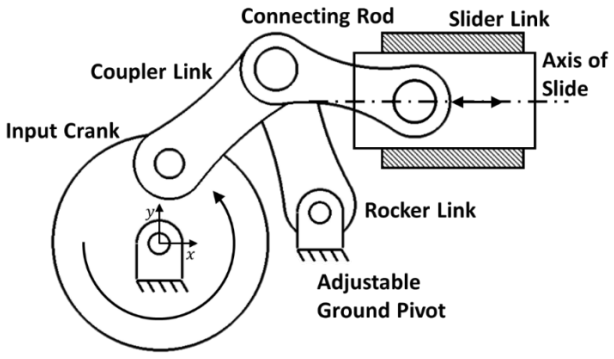

FIGURE 4.1 SCHEMATIC OF VARAIBLE DISPLACEMENT LINKAGE PUMP MECHANISM

If a pumping piston is attached to the slider, the result is a variable displacement pump which can achieve zero displacement and have a constant top dead center position of the piston. In contrast to other pump designs, the unswept volume of the proposed pumping chamber will remain constant independent of displacement improving pumping performance at low displacement.

However, an energy loss model is required to predict the performance and viability of the mechanism as a pumping machine. The model should be as simple as possible while capturing the physics of the system for use in a design optimization. In the context of an optimization, the model should be predictive without using experimentally determined coefficients.

Previous chapters have developed the kinematic model including position, velocity, and acceleration analysis as well as solution rectification methods for both the base crank-rocker fourbar, and the output slider dyad. This chapter develops a kinetostatic force analysis of the mechanism and energy loss model for determining the performance of the mechanism. The second section describes the force analysis of the proposed mechanism. The third section develops the energy loss model. The fourth section presents an experimental validation of the model using a single cylinder pump. The fifth section presents the results. Conclusions are provided in the sixth section.

4.2 Force Analysis

In chapter two, the kinematic model of the linkage was presented and validated. In this section, the force analysis of the mechanism is presented. The model is

demonstrated with regards to the prototype mechanism presented in Chapter 2. In this section, a complete force analysis of the mechanism will be performed. A line diagram of this mechanism is shown in Figure 4.2 for reference.

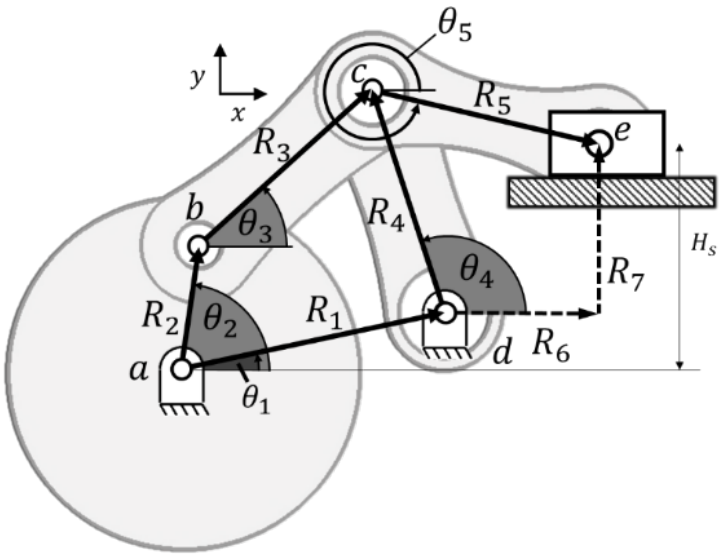

FIGURE 4.2 LINE DIAGRAM AND SCHEMATIC OF LINKAGE USED FOR DEVELOPMENT OF FORCE ANALYSIS

4.2.1 Mechanism Internal Forces

From the kinematic analysis, the position velocity and accelerations of the mechanism can be found. Due to their mass and accelerations, the links themselves apply load to the joints in addition to any applied load. To resolve the loading at the mechanism joints, a force analysis is required.

A kineto-static force analysis is completed by applying Newtons second law to balance the forces and moments of each link at each angular steps of the input crank angle θ_2. The quasi-static method assumes that the position, angular velocity, and angular acceleration of any of the links are known at each time step. The forces and torques found

are those required to cause the mechanism to achieve these kinetics. This method is used because it provides detailed information of the internal forces of the mechanism required to estimate the internal losses and design the links of a physical mechanism, and requires no differential equations resulting in a computationally lightweight solution.

Figure 4.3 shows the physical system with labeled forces and locations of the center of mass of each link.

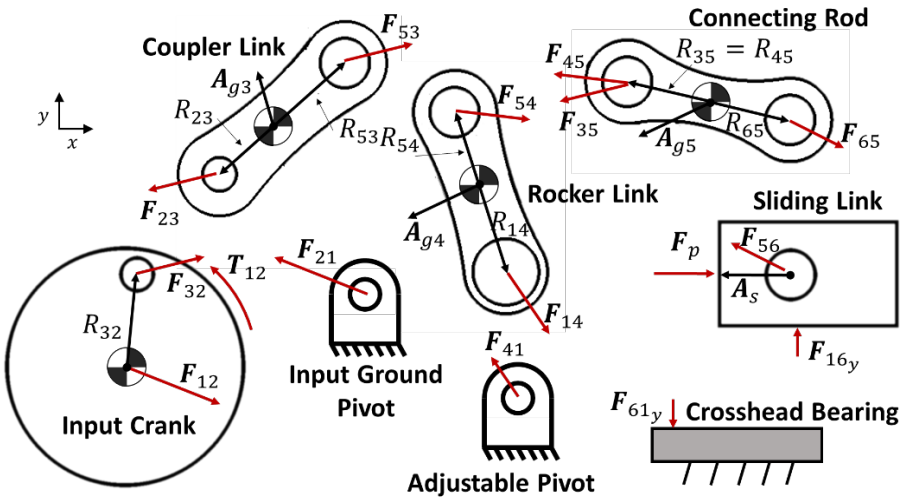

FIGURE 4.3 FREE BODY DIAGRAM OF THE MOVING COMPONENTS OF THE LINKAGE SHOWING FORCES AND CENTRES OF MASS

Notice that the external force acting on the slider, $\boldsymbol{F}_p$ is drawn in the positive x direction. For different configurations of the pump, the piston will be attached to different sides of the slider and the sign of this force will change. This is a result of the location of the TDC position of the mechanism. In this configuration, the TDC positon is on the left side of the slider displacement path. As a result, the pumping piston is loaded from the left side and the force is positive. In other configurations, the TDC positon is on

the right side of the slider displacement path, so the pumping piston would be loaded from the right side and the force would be negative.

With reference to Figure 4.2, the pin at *c* is fixed to the connecting rod, and is loaded by the rocker and coupler links which share this joint. The pin can be fixed to any of the three links at this joint, but the system of equations must be adjusted accordingly. If the pin is not physically fixed to a link, it can be assumed to be fixed to any of one the links to complete the force analysis, but friction torques, discussed later, cannot be calculated. To solve the system, a simultaneous solution is required. Links 2-5 each provide three equations, and the slider produces two additional equations to resolve the force and moment balance. In total there are fourteen equations and fourteen unknowns: the twelve pin forces, the slider reaction force, and the input torque. Since the slider has no angular velocity, there is no moment to balance, and solving for the location of the center of mass is unnecessary. Additionally, the input crank is considered balanced about its rotational axis. The analysis assumes that the internal friction of the mechanism is negligible compared to the applied load and that the links are inelastic rigid bodies. The applicability of these assumption, however, greatly depends on the loading, operating frequency, and mechanism design and should be evaluated on a case by case bases. The internal friction is considered later in section 4.2.2.3.

4.2.1.1 System of Equations

The set of dynamic force balance equations for each link are now presented with respect to Figure 4.3.

For Link 2

$$F_{32x} - F_{12x} = 0 \tag{4.1}$$

$$F_{32y} - F_{12y} = 0 \tag{4.2}$$

$$\boldsymbol{T}_{12} + R_{32}(cos\,\theta_2 F_{32y} - sin\theta_2 F_{32x}) = I_2\alpha_2 \tag{4.3}$$

where I_j is the moment of inertia of link j.

For Link 3

$$F_{53x} - F_{32x} = m_3 A_{g3x} \tag{4.4}$$

$$F_{53y} - F_{32y} = m_3 A_{g3y} \tag{4.5}$$

$$R_{23}\left(cos\theta_3 F_{32y} - sin\theta_3 F_{32x}\right) + R_{53}(cos\theta_3 F_{53y} - sin\theta_3 F_{53x}) = I_3\alpha_3 \tag{4.6}$$

where A_{gjx} and A_{gjy} are the x and y components of the acceleration of the center of gravity of link j.

For Link 4

$$-\mathrm{F_{14x}} + \mathrm{F_{54x}} = \mathrm{m_4 A_{g4x}} \tag{4.7}$$

$$-\mathrm{F_{14y}} + \mathrm{F_{54y}} = \mathrm{m_4 A_{g4y}} \tag{4.8}$$

$$\mathrm{R_{14}}\left(\cos\theta_4 \mathrm{F_{14y}} - \sin\theta_4 \mathrm{F_{14x}}\right) + \mathrm{R_{54}}(\cos\theta_4 \mathrm{F_{54y}} - \sin\theta_4 \mathrm{F_{54x}}) = \mathrm{I_4}\alpha_4 \tag{4.9}$$

For Link 5

$$\mathrm{F_{65x}} - \mathrm{F_{54x}} - \mathrm{F_{53x}} = \mathrm{m_5 A_{g5x}} \tag{4.10}$$

$$\mathrm{F_{65y}} - \mathrm{F_{54y}} - \mathrm{F_{53y}} = \mathrm{m_5 A_{g5y}} \tag{4.11}$$

$$R_{65}\left(cos\theta_5 F_{65y} - sin\theta_5 F_{65x}\right) + R_{35}\left(cos\theta_5\left(F_{54y} + F_{53y}\right) - sin\theta_5\ \left(F_{54x} + F_{53x}\right)\ \right) = I_5\alpha_5 \tag{4.12}$$

The slider provides 2 additional equations.

$$F_p - F_{65x} = m_s A_s \tag{4.13}$$

$$F_{16y} - F_{65y} = 0 \tag{4.14}$$

This system of equations can be solved simultaneously or combined to find the solution explicitly.

4.2.2 Internal Friction of the Mechanism

Due to the loading and the relative motion of the links, there are friction forces at each joint and the slider that oppose motion. The friction forces are considered internal to the mechanism because they are a function of the joint forces and also contribute to the joint forces themselves. While there may be other external frictions, they are considered separately because they are not inherent to the design. In this section, the internal forms of friction are modeled and discussed in further detail.

4.2.2.1 Crosshead Bearing Friction

In the pumping head of a reciprocating pump there are four primary components: The slider, the crosshead bearing, the cylinder, and the piston or plunger. Figure 4.4 provides clarification between the various components. The slider is the link attached to the mechanism as depicted in Figure 4.1. The crosshead is the linear bearing which reacts the slider side load and centers the piston. The piston is the pumping element used to displace fluid in the cylinder and the cylinder is the chamber which contains the piston.

The piston cylinder interface is shown here as having a gap between the cylinder wall with seals to prevent leakage, but many arrangements are possible such as a small clearance seal. If the seal is fixed to the cylinder, the pumping element is called a plunger. If the seals are fixed to the pumping element, it is referred to as a piston.

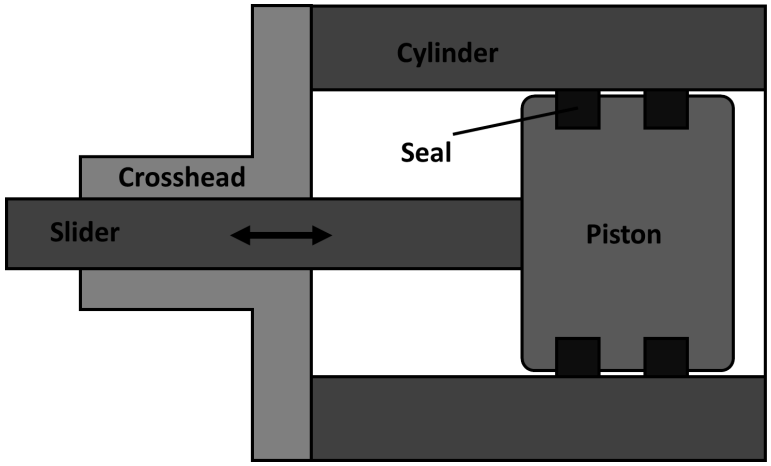

FIGURE 4.4 SCHEMATIC OF GENERIC PUMPING HEAD DEPICTING PRIMARY COMPONENTS

Depending on the type of lubrication at the interface of the slider and the crosshead bearing, different types of friction may be exhibited. Viscous friction is caused by the shearing of a film of fluid which may exist between the slider and the bearing due to the relative motion. Coulomb friction is caused by direct contact between the slider and the bushing.

If there is forced lubrication or hydrodynamic lubrication that prevents contact, only viscous friction exists in the crosshead bearing. If insufficient lubrication is provided, mixed boundary lubrication occurs. If no forced lubrication is used, Coulomb friction can be assumed.

This model does not consider viscous friction in the crosshead because splash lubrication is used. Viscous friction is modeled later for the piston-cylinder interface. The magnitude of the Coulomb friction force in the crosshead bearing is found by:

$$F_{cf_{crosshead}} = -\mu_{k_c}|F_{16y}|sign(v_s) \tag{4.15}$$

where μ_{k_c} is the coefficient of friction between the slider and bushing of the crosshead, and F_{16}, shown in Figure 4.3, is the normal force. The negative sign denotes that the force opposes the motion of the slider.

4.2.2.2 Friction Torque at Pin Joints

The present mechanism is modeled as having plain bearings in the revolute pin joints. These bearings consist of a cylinder which provides a running surface for a pin, as shown in Figure 4.5**.** The interface between the pin and bearing is modeled by Coulomb friction. The figure shows the loading and relative motion between two links. The pin is fixed to Link B and the bearing surface is fixed to Link A. The relative motion is denoted by the curved arrow direction and the normal force is shown as applied to the pin. The friction force F_{cf} acts at a distance from the center of the pin and opposes the relative motion resulting in a friction torque applied to the joint. This torque can be taken with respect to the pin or the bushing

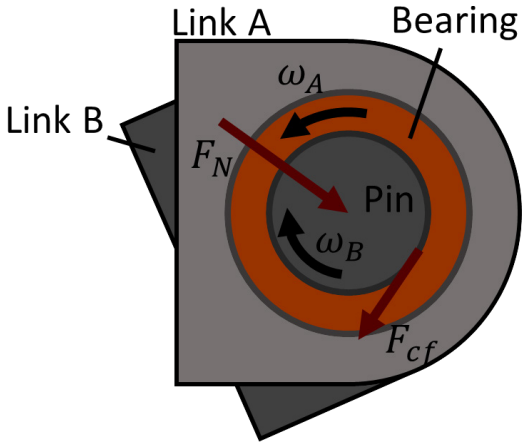

FIGURE 4.5 SCHEMATIC OF LINKAGE JOINT FOR DETERMINATION FRICTION FRICTION TORQUE

The friction torque is found by:

$$M_{\mu_j} = -\mu_{k_j} F_N \frac{d_j}{2} \, sign(\omega_A - \omega_B) \tag{4.16}$$

where μ_{k_j} is the coefficient of friction between the pin and bearing of the joint,d_j is the nominal diameter of the pin, ω_B is the angular velocity of the pin, and ω_A is the angular velocity of the bushing. Roller bearings can also be modeled with Coulomb friction and have an equivalent coefficient of friction two orders of magnitude lower than plane bearings[91] but aren't used here to provide a simpler design.

4.2.2.3 System of Equations Including Friction

Because the friction forces and torques are a function of the applied load, they must be included in the simultaneous solution. Each of the pin joints and the crosshead provide one additional equation and one unknown. Furthermore, the friction force on the piston does not act along the axis of slider and therefore imparts a moment on the piston

which must be reacted by the crosshead bearing. As a result, the system of equations consists of 21 equations and 21 unknowns. Note that there are only 14 unknowns in the system that neglects friction. A free body diagram showing the friction torques and forces is provided in Figure 4.6. The friction torques and moments are in addition to forces in the free body diagram of Figure 4.3.

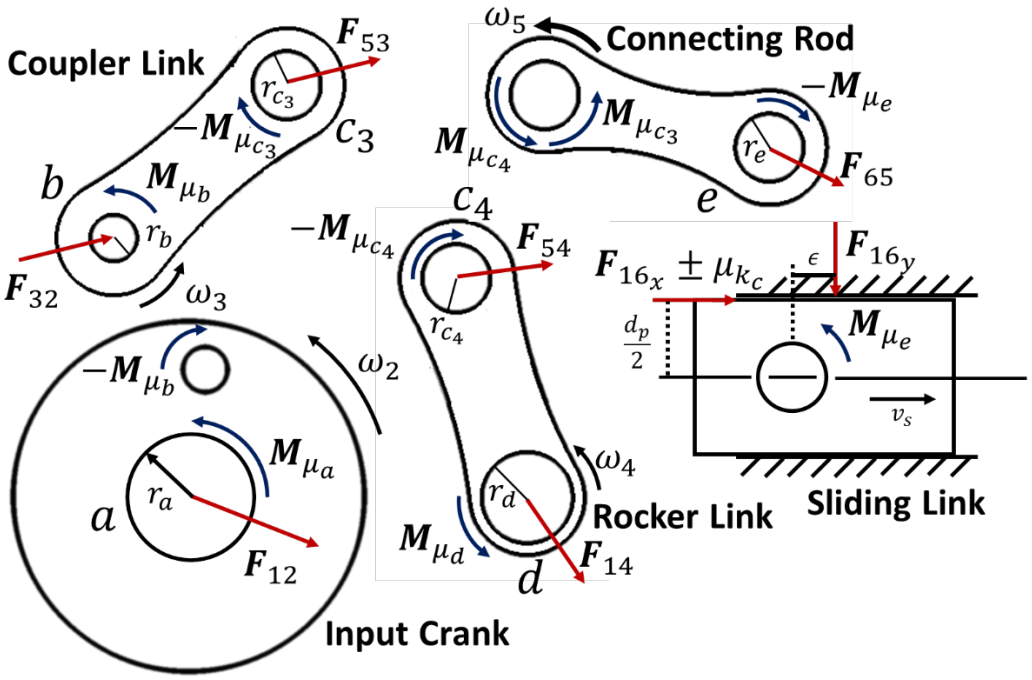

FIGURE 4.6 FREE BODY DIAGRAM OF MECHANISM SHOWING FRICTION TORQUES AND FORCES

For Link 2

$$F_{32x} - F_{12x} = 0 \tag{4.17}$$

$$F_{32y} - F_{12y} = 0 \tag{4.18}$$

$$\boldsymbol{M}_{\mu_a} = -\sqrt{F_{12_x}^2 + F_{12_y}^2}\, r_a \mu_a sign(\omega_2) \tag{4.19}$$

$$\boldsymbol{M}_{\mu_b} = -\sqrt{F_{32_x}^2 + F_{32_y}^2}\, r_b \mu_b sign(\omega_3 - \omega_2) \tag{4.20}$$

$$\boldsymbol{T}_{12} + R_{32}(cos\,\theta_2 F_{32y} - sin\theta_2 F_{32x}) + \boldsymbol{M}_{\mu_a} - \boldsymbol{M}_{\mu_b} = I_2\alpha_2 \tag{4.21}$$

where $M_{\mu_j}$is the friction moment at pin j, r_j, is the radius of pin j, and μ_j is the coefficient of friction at joint j.

For Link 3

$$F_{53x} - F_{32x} = m_3 A_{g3x} \tag{4.22}$$

$$F_{53y} - F_{32y} = m_3 A_{g3y} \tag{4.23}$$

$$\boldsymbol{M}_{\mu_{c_3}} = -\sqrt{F_{53_x}^2 + F_{53_y}^2}\, r_{c_3} \mu_{c_3} sign(\omega_5 - \omega_3) \tag{4.24}$$

$$\begin{gathered} R_{23}\left(cos\theta_3 F_{32y} - sin\theta_3 F_{32x}\right) + R_{53}\left(cos\theta_3 F_{53y} - sin\theta_3 F_{53x}\right) \\ -\mathbf{M}_{\mu_{c_3}} + \mathbf{M}_{\mu_B} = I_3\alpha_3 \end{gathered} \tag{4.25}$$

For Link 4

$$-\mathrm{F}_{14x} + \mathrm{F}_{54x} = \mathrm{m}_4 \mathrm{A}_{g4x} \tag{4.26}$$

$$-\mathrm{F}_{14y} + \mathrm{F}_{54y} = \mathrm{m}_4 \mathrm{A}_{g4y} \tag{4.27}$$

$$\boldsymbol{M}_{\mu_{c_4}} = -\sqrt{F_{54_x}^2 + F_{54_y}^2}\, r_{c_4} \mu_{c_4} sign(\omega_5 - \omega_4) \tag{4.28}$$

$$\boldsymbol{M}_{\mu_d} = -\sqrt{F_{14_x}^2 + F_{14_y}^2}\, r_d \mu_d sign(\omega_4) \tag{4.29}$$

$$\begin{gathered} \mathrm{R}_{14}\left(\cos\theta_4 \mathrm{F}_{14y} - \sin\theta_4 \mathrm{F}_{14x}\right) + \mathrm{R}_{54}\left(\cos\theta_4 \mathrm{F}_{54y} - \sin\theta_4 \mathrm{F}_{54x}\right) \\ +\mathbf{M}_{\mu_d} - \mathbf{M}_{\mu_{c_4}} = \mathrm{I}_4\alpha_4 \end{gathered} \tag{4.30}$$

For Link 5

$$\mathrm{F_{65x}} - \mathrm{F_{54x}} - \mathrm{F_{53x}} = \mathrm{m_5 A_{g5x}} \tag{4.31}$$

$$\mathrm{F_{65y}} - \mathrm{F_{54y}} - \mathrm{F_{53y}} = \mathrm{m_5 A_{g5y}} \tag{4.32}$$

$$\boldsymbol{M}_{\mu_e} = \sqrt{F_{65_x}^2 + F_{65_y}^2}\, r_e \mu_e sign(\omega_5) \tag{4.33}$$

$$\begin{gathered} R_{65}\left(cos\theta_5 F_{65y} - sin\theta_5 F_{65x}\right) + \\ R_{35}\left(cos\theta_5 F_{54y} - sin\theta_5 F_{54x} + \cos\theta_5 \mathrm{F_{53y}} - \sin\theta_5 \mathrm{F_{53x}}\right) \\ -\boldsymbol{M}_{\mu_e} + \boldsymbol{M}_{\mu_{c_3}} + \boldsymbol{M}_{\mu_{c_4}} = I_5 \alpha_5 \end{gathered} \tag{4.34}$$

And the final equations come from the slider

$$\mathrm{F_p} - \mathrm{F_{65x}} - |\mathrm{F_{16_y}}|\mu_{\mathrm{k_c}} sign\left(v_{s_x}\right) = \mathrm{m_s A_s} \tag{4.35}$$

$$F_{16y} - F_{65y} = 0 \tag{4.36}$$

$$F_{16_y}\left(-\epsilon - \frac{\mu_{k_c} d_p}{2} sign\left(v_{s_x}\right)\right) + \boldsymbol{M}_{\mu_e} = 0 \tag{4.37}$$

where ϵ is the required moment arm to balance the moment at the slider as shown in Figure 4.6.

The magnitudes of the forces are required to determine the friction torque in the joints. This magnitude of a force at a joint is $\sqrt{F_x^2 + F_y^2}$ resulting in 6 non-linear equations requiring an iterative solver. Quickly it becomes apparent that including friction torque in the system of equations increases the complexity of the solution method.

4.2.3 External Friction

Friction which is not inherent to the mechanism design is considered external. In a pumping application, these external friction loads are introduced by seals. Depending on

the application, different seals will be used. The section gives the friction forces introduced by the piston-cylinder interface, piston seals, and input shaft seals.

4.2.3.1 Piston-Cylinder Interface

The friction in piston-cylinder interface are similar to those of the crosshead bearing. However, if a linear crosshead bearing is used to center the piston in the cylinder, no contact occurs, resulting in fluid film lubrication. The piston-cylinder interface of Figure 4.4 had positive seals to prevent leakage. Positive seals introduce friction which can be avoided with a clearance seal that limits leakage due to the very small channel created by the gap between the piston and cylinder. The leakage past the piston results in a consistent lubrication gap. Viscous friction is caused by the shearing of the fluid in this gap due to the relative motion. The viscous friction of the piston is a function only of the piston velocity which can be calculated independently and added to the piston force in the model.

The modeled pump uses a crosshead bearing and clearance seal so only viscous friction is considered for the piston cylinder interface. From Newton's law of viscosity, the viscous friction force in the piston-cylinder gap can be expressed as:

$$F_v = -\pi d_p l_p \frac{\mu_d}{h} v_s \tag{4.38}$$

where d_p is the piston diameter, l_p is the piston length, μ_d is the dynamic viscosity of the fluid, h is the radial piston clearance, and v_s is the relative velocity of the piston and cylinder. The negative sign denotes that the force opposes the motion.

4.2.3.2 Piston Seals

When pumping corrosive or non-lubricating fluids, pumps employ positive seals that make contact with the reciprocating piston to prevent fluid from leaking into the pump case. Typically these seals are charged, meaning that the load on the piston surface increases with pressure allowing them to maintain a positive seal. The friction of positive seals is not modeled here as clearance seals are used in the prototypes, and the model depends greatly on the type of seal used.

4.2.3.3 Shaft Seal

The pump case of a reciprocating pump is flooded with lubricating fluid which is distributed to the joints by splash lubrication. Shaft seals prevent lubrication fluid from leaking out of a pump case. These low pressure lip seals are fixed to the pump body and maintain contact with the input shaft as it rotates. As a result there is a friction torque introduced. This shaft seal torque is largely considered negligible but an estimate is provided by [92]:

$$T_{SS} = 15.095\, D_s^2 \omega_2^{\frac{1}{3}} \tag{4.39}$$

where D_s is the input shaft diameter in meters and ω is the shaft speed in radians per second. The coefficient 15.095 is an empirical value provided but a seal manufacturer[92]. The above equation has been adapted from the source to return the torque in Nm and assumes no pressure differential across the seal. For a 25mm input shaft operating at 1800rpm, the model predicts a shaft torque of .056Nm which can be neglected.

4.3 Energy Loss Modeling

With the internal and external forces and frictions determined, the energy losses in the mechanism can be calculated. The external piston forces, such as the viscous friction force and piston seal friction, are added to the piston pressure force input to the internal friction model according to:

$$F_{applied} = F_p + \sum F_{fr_{ext}} \tag{4.40}$$

where F_p is the pressure force applied to the piston and $\sum F_{fr_{ext}}$ is the sum of external friction forces acting on the piston.

All of the internal frictions are then solved simultaneously using the nonlinear system of equations. The shaft seal torque can then be added to the input shaft torque. The total input work can then be calculated by:

$$W_{in} = \int (T_{12} + T_{ss})\omega_2 \, dt \tag{4.41}$$

where T_{12} is the shaft torque which accounts for all of the modeled losses, and ω_2 is the input shaft speed. To determine the contributions of the individual loss mechanisms, their energy losses must be integrated separately, as described next.

4.3.1 Coulomb Friction Energy Loss

In general, the Coulomb friction energy loss of a linear bearing can be estimated by:

$$E_{Coulomb} = \int F_{Coulomb} v_{surface} dt \tag{4.42}$$

where $F_{coulomb}$ is the friction force found by Eqn (4.15) and $v_{surface}$ is the relative velocity between the friction surfaces. For the crosshead bearing the Eqn. becomes:

$$E_{Cf_{crosshead}} = \int F_{Cf_{crosshead}} v_s dt \tag{4.43}$$

The energy loss in the pin joints is found by integrating the friction moments with the respect to the relative velocities between the shared links. For example, pin b is fixed to the crank link, and the bearing is fixed to the coupler link. The relative angular velocity between the pin and the bearing is $\omega_2 - \omega_3$. The energy loss at a revolute joint can be found by:

$$E_{cf_j} = \int \boldsymbol{M_{\mu j}} d\theta = \int \boldsymbol{M_{\mu j}} \omega dt \tag{4.44}$$

where $d\theta$ is the relative change in angle between the link joint and the pin, and ω is the relative angular velocity between the link joint and the pin. Any change in direction of relative velocity is accounted for in Eqn (4.16). The energy loss at each joint can be calculated separately allowing for rapid identification of high loss pin joints. The pin losses can also be summed for comparison to other loss mechanisms.

4.3.2 Viscous Friction

The energy loss due to viscous friction is expressed as:

$$E_v = \int F_v dx = \int F_v v_s dt \tag{4.45}$$

Inserting (4.38) into (4.45) yields:

$$E_v = -\pi d_p l_p \frac{\mu_d}{h} \int v_s^2 dt \tag{4.46}$$

This result demonstrates that the viscous friction energy loss is a function of the square of the relative velocity between the piston and cylinder. If speed is doubled, the viscous friction energy loss is quadrupled.

4.3.3 Seal Friction

Energy loss at the shaft seal is found by:

$$E_{ss} = \int T_{ss} d\theta_2 = \int T_{ss} \omega_2 dt \tag{4.47}$$

where T_{ss} is the shaft seal torque from Eqn. (4.39) and ω_2 is the input shaft speed.

4.4 Single Cylinder Validation

To evaluate the mechanical energy loss model, the mechanism presented in Chapter 2 was modified to act as a low power prototype pump and an experimental validation of the model was conducted. The primary objective of the pump was to validate the model and the pumping capabilities were used as a method of creating a load for comparison. This section introduces the prototype, the experimental methods, and the model validation.

4.4.1 Prototype Pumping Machine

The prototype was designed to accommodate a pressure of 5 MPa with a maximum volumetric displacement of 8.7 cm^3/rev. The optimization of the linkage kinematics presented in Chapter 2 was used to determine the link length ratios. The

mechanism was then scaled to meet the displacement requirement and handle the applied forces.

The volumetric displacement is a function of the piston area and the maximum stroke of the pump according to:

$$V_D = \frac{\pi d_p^2}{4} s_{max} \tag{4.48}$$

where s_{max} is the maximum piston stroke, and d_p is the piston diameter. Displacement can be increased by increasing either the piston diameter, or stroke length. The piston force is a function of the piston cross-sectional area of the piston, while the mechanism size and dynamic velocities and accelerations are a function of the stroke, resulting in a tradeoff. In the case of the prototype, the peak piston forces drove the design. The crosshead bearing used in the pump limited the peak velocity of the slider to 3 m/s . The mechanism was scaled to achieve this peak velocity at 30Hz operating frequency.

The links and pins were designed to have a static loading safety factor of 5. Fatigue loading was not considered due to the low number of cycles intended for the mechanism. Plain bronze bushings were used in the joints due to the limiting size of the link lengths. Roller bearing were incorporated into the pump body for the crank shaft. The mechanism was hand lubricated and no shaft seal was used.

Inline check valves on the hydraulic manifold provide passive flow control to create a pumping action as the piston reciprocates. A hydraulic cylinder controls the displacement by actuating the displacement adjustment link, causing the adjustable

ground pivot to rotate about the adjustment point. Figure 4.7 shows a cross sectional view of the mechanism and a model rendering is provided in Figure 4.8. The resultant design variables used in the analysis are listed in Table 4.1.

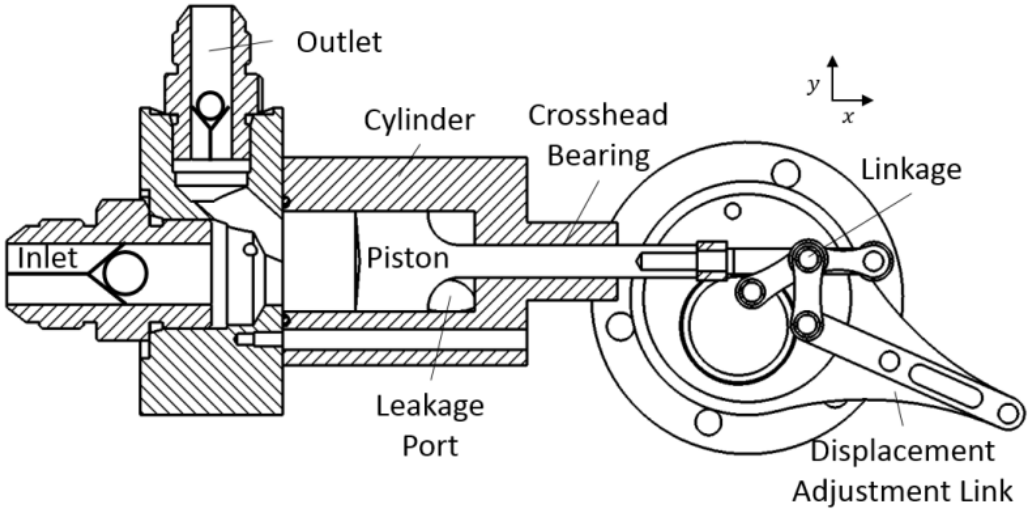

FIGURE 4.7 PROTOTYPE VARIABLE DISPLACEMENT LINKAGE PUMP USED FOR LOW POWER EXPERIMENTAL VALIDATION

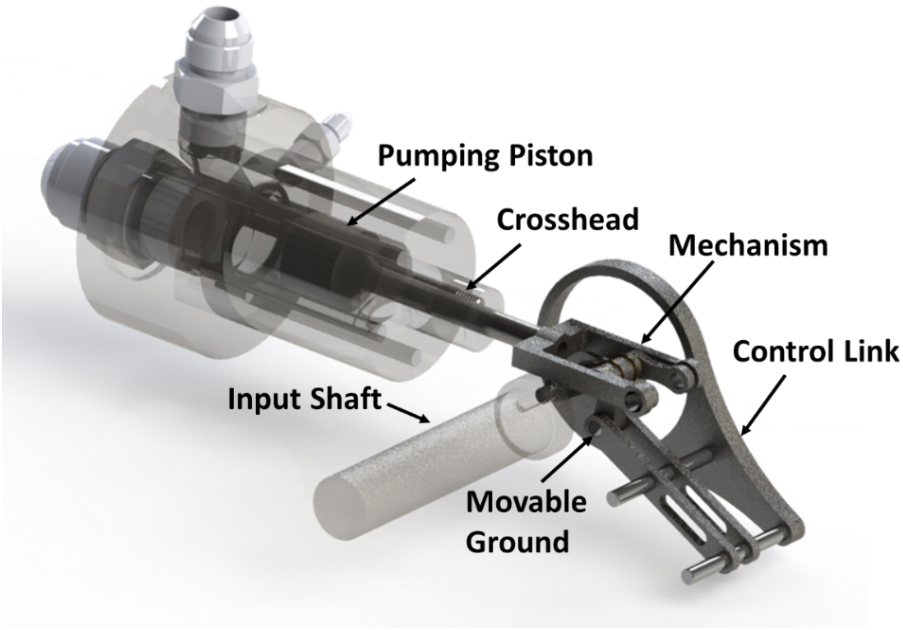

FIGURE 4.8 MODEL RENDERING OF PUMPING MECHANISM

TABLE 4.1 DESIGN TABLE OF PROTOTYPE VALUES FOR MODELING

PROTOTYPE DESIGN TABLE

Symbol	Description	Value	Unit
$\boldsymbol{d_p}$	Piston Diameter	0.0246	$[m]$
$\boldsymbol{h}$	Piston Cylinder Gap Height	4.00	$[\mu m]$
$\boldsymbol{r_2}$	Length of Link 2	8.9	$[mm]$
$\boldsymbol{r_3}$	Length of Link 3	15.98	$[mm]$
$\boldsymbol{r_4}$	Length of Link 4	15.98	$[mm]$
$\boldsymbol{r_5}$	Length of Link 5	15.98	$[mm]$
$\boldsymbol{r_{g3}}$	Distance to Cg of Link 3	3.56	$[mm]$
$\boldsymbol{r_{g4}}$	Distance to Cg of Link 4	7.99	$[mm]$
$\boldsymbol{r_{g5}}$	Distance to Cg of Link 5	5.37	$[mm]$
$\boldsymbol{m_3}$	Mass of link 3	11.17	$[gram]$
$\boldsymbol{m_4}$	Mass of link 4	4.44	$[gram]$
$\boldsymbol{m_5}$	Mass of link 5	8.12	$[gram]$
$\boldsymbol{m_s}$	Mass of slider link	112.4	$[gram]$
$\boldsymbol{l_p}$	Length of Piston Sealing Surface	17.8	$[mm]$
$\boldsymbol{P}$	Location of Pivot Point	$2.1 + 6.8i$	$[mm]$
$\boldsymbol{h_{s_x}}$	Distance to axis of slide from x axis	15.8	$[mm]$
$\boldsymbol{r}$	Pin radius	2.4	$[mm]$
$\boldsymbol{\mu_d}$	Coefficient of dynamic viscosity*	0.061	$[Pa\ s]$
$\boldsymbol{\mu_k}$	Coefficient of friction for pins [91]	0.173	$[unitless]$
$\boldsymbol{\mu_{k_c}}$	Coefficient of friction for crosshead bearing [91]	0.12	$[unitless]$

$\boldsymbol{\mu_{k_{rb}}}$	Coefficient of friction for input shaft bearing [91]	.005	$[unitless]$
$\boldsymbol{\gamma_{min}}$	Minimum linkage transmission angle	30	$[deg]$

*Based on ISO grade 46 Hydraulic Oil at 30°C

4.4.2 Experimental Setup

With the objective of validating the force and energy loss model, an experimental setup was developed. The pressure on the piston provided a measurable varying input load on the mechanism, and the shaft torque provided a measurable output of the mechanism for model comparison. A non-contact torque transducer and optical encoder measured the torque and angular velocity of the input shaft and allowed for the calculation of the input work. A pressure transducer in the cylinder is used to evaluate the piston force, F_p. A hydraulic accumulator is included to maintain the set pressure and smooth pressure pulsations.

The variable linkage pump is driven by an electric motor. The angular velocity of the AC motor is controlled using a variable frequency drive. For certain experiments, a gear reducer with a ratio of 10:1 was used to prevent large angular velocity fluctuations at low shaft speeds. A schematic of the experimental setup is provided in Figure 4.9.

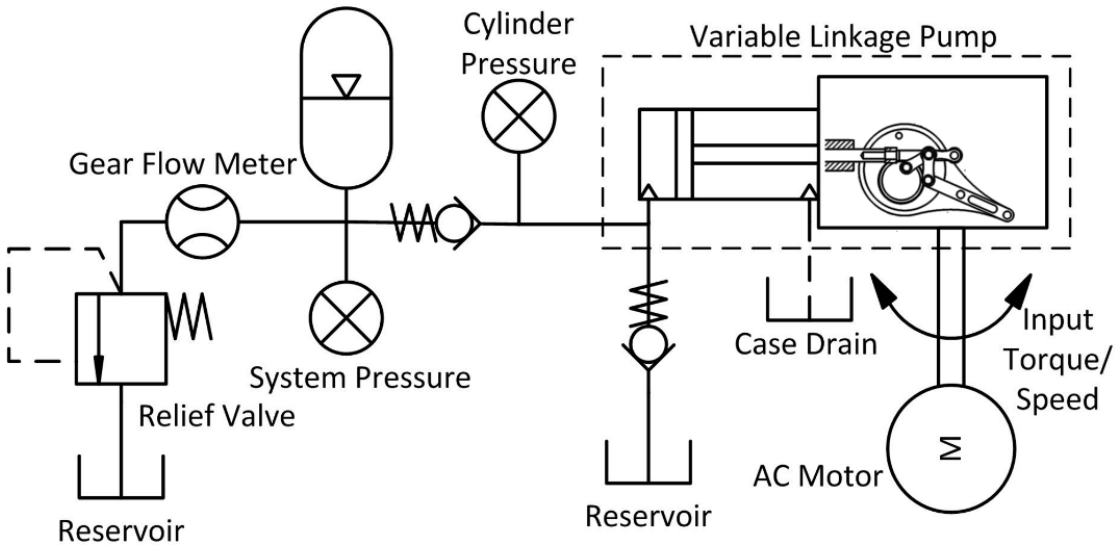

FIGURE 4.9 HYDRAULIC CIRCUIT DIAGRAM DISPLAYING THE EXPERIMENTAL SETUP

A series of 6 experiments were conducted with the pressure varying between 1.2 MPa and 3.45 MPa at input speeds between 3 Hz and 9 Hz. The shaft speeds were kept low to minimize fluid dynamic effects, which are not modeled here. Data were collected for a total of 5 seconds per experiment at a sample rate of 10 kHz. A digital low-pass filter with a pass band of 1kHz was applied to the data to remove high frequency noise associated with the AC drive and other electronic devices in the lab.

For a given experiment, the displacement was set with the hydraulic cylinder acting on the control link. A set of machined pins were constructed to limit the travel of the control link with reference to the pump body. The cylinders lengths determined the displacement. Next, the shaft speed was then set using the variable frequency drive for control. The pressure was then set by adjusting the relief valve. The pump ran in this condition for 30 seconds allowing it to reach cyclic steady state. Data from the sensors was then collected for 5 seconds to capture multiple cycles of pumping action.

The experimentally measured cylinder pressure and input crank angle data are inserted into the model to predict the shaft work. The validated kinematics model is used to predict the velocities, and accelerations of the links and piston for use in the mechanism model. These predicted values are then compared to the measured shaft work.

4.5 Results

In total, 64 conditions were measured to validate the mechanical energy loss model. Sample data from the 2.4MPa, 6Hz, and 100% displacement experiment is presented to demonstrate detailed results as a representative condition and a compilation of the data sets provide a large scale comparison of the measured and predicted shaft energy work.

The experimentally measured cylinder pressure and shaft speed are used as inputs to the model and a single cycle of each are shown in Figure 4.10 and Figure 4.11 respectively. The x axis of both plots is the crank angle of the input shaft where 0° is aligned with the top dead center position of the piston. These data are input into the model to predict shaft torque and energy input.

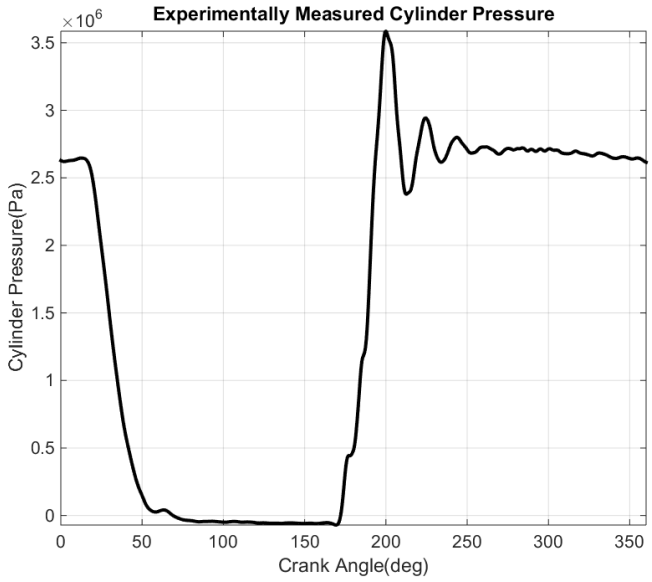

FIGURE 4.10 EXPERIEMNTALLY MEAURED CYLINDER PRESSURE TAKEN AT 2.4 MPA, 6HZ AND 100% DISPLACEMCENT OPERATING CONDITIONS

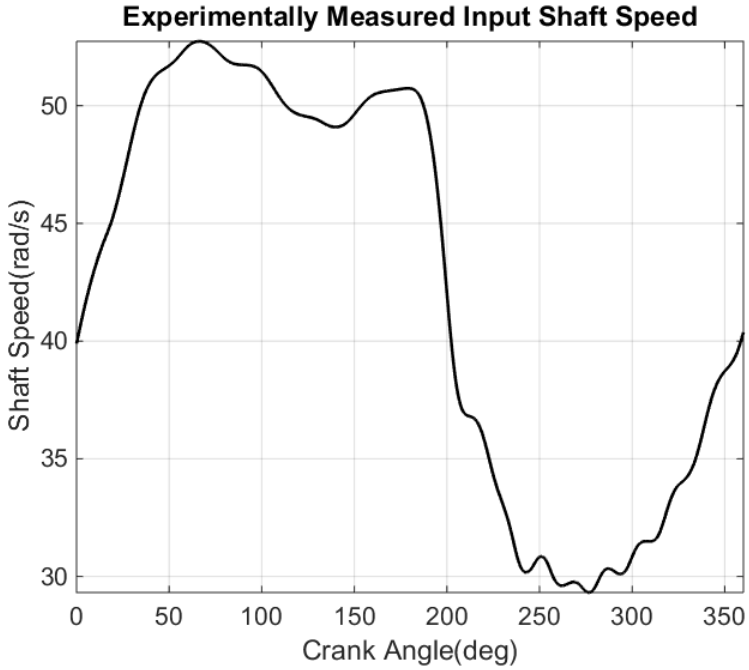

FIGURE 4.11 EXPERIEMNTALLY MEAURED SHAFT SPEED TAKEN AT 2.4 MPA, 6HZ AND 100% DISPLACEMCENT OPERATING CONDITIONS

Figure 4.12 shows the modeled and experimentally measured shaft torque from the same experiment as above.

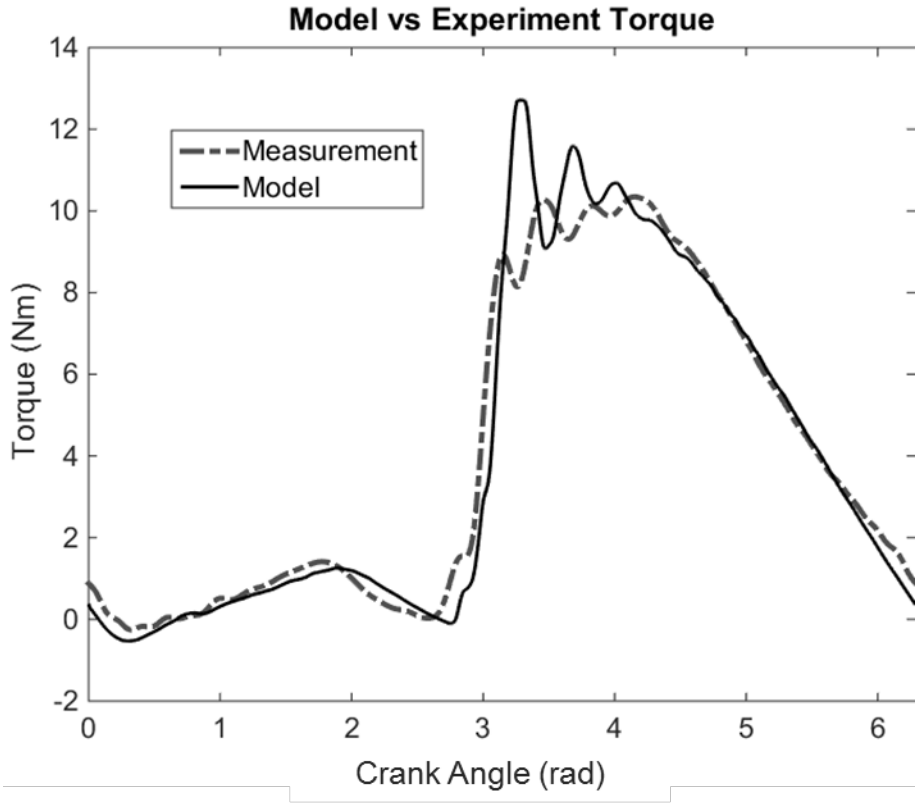

FIGURE 4.12 MODEL AND EXPERMINETAL TORQUE VALUES MEASURED AT 100 % DISPLACMENT 2.4MPa AND 6HZ

Figure 4.13 compares the experimentally measured work input per input shaft revolution, as measured by the input shaft speed and torque, to that predicted by the model for various pressures and frequencies. The model results are for the experimentally measured operating speed and pressure at each experimental data point.

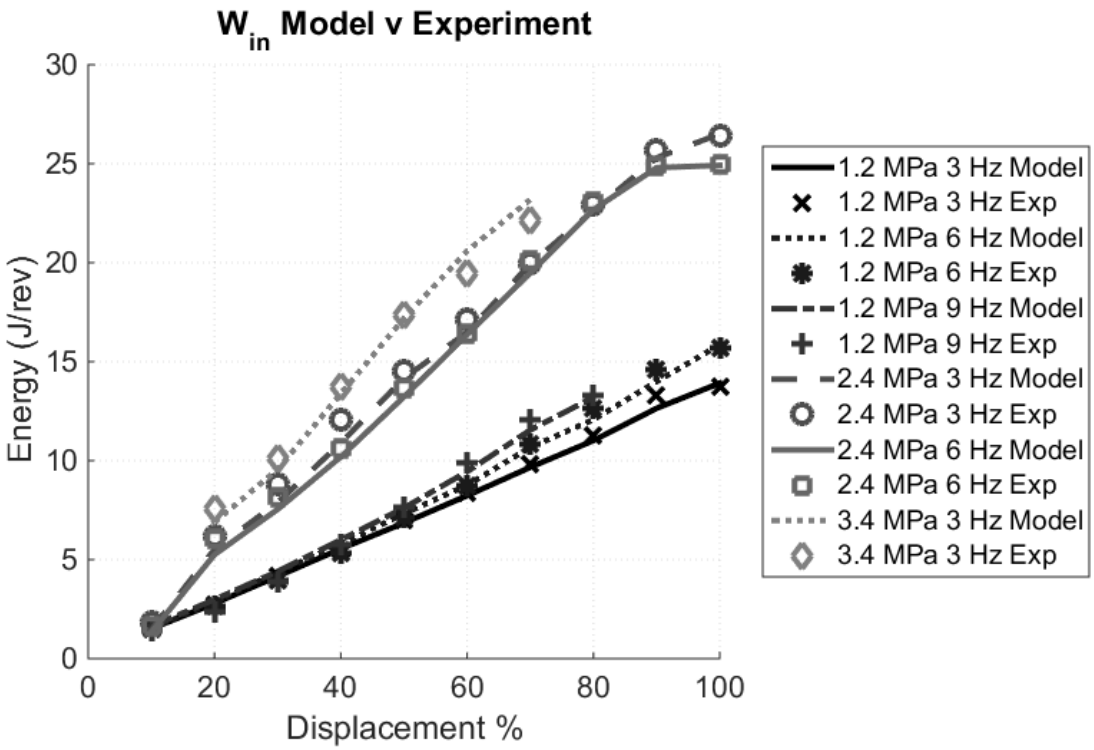

FIGURE 4.13 WORK INPUT EXPERIMENTAL DATA PLOTTED AGAINST MODEL AT VARIOUS FREQUENCIES AND PRESSURES

4.6 Discussion

The pressure trace of Figure 4.10 lags the pistons return to bottom dead center due to the slow response of the inlet and outlet check valves, which is a result of the fluid dynamics. The pump acts as a motor for a short time period as the piston retracts and the cylinder pressure stays high. The negative shaft torques measured during this period verifies this motoring effect as is shown in Figure 4.12. The pressure dynamics effects and check valve behavior are discussed further in Chapter 6.

The shaft speed oscillation, shown in Figure 4.11, is due to the large torque fluctuations at the crank shaft demonstrated in Figure 4.12. The shaft torque varies from

1Nm to ~ 10Nm over the course of a single cycle. A multi-cylinder design would reduce these large fluctuations in shaft torque.

Figure 4.13 and Figure 4.12 show excellent agreement between the model and experimental results for both work input and the shaft torque prediction. The model is able to predict the input shaft work using only the pressure signal of the pump and the input shaft speed over a wide range of displacements and operating frequencies. The model uses no experimentally measured values to predict performance. All coefficients used are readily available in literature and have been provided for reference. The linear nature of the work input vs displacement of Figure 4.13 show that the losses scale with displacement as predicted.

With the model generally validated, it is used to determine the energy loss contributions of the various loss mechanism. Figure 4.16 shows the relative contributions of the energy loss mechanisms as a function of displacement from the 2.4MPa and 3Hz experiment as predicted by the model. The dominant loss mechanism the prototype is the pin friction, and the viscous friction increases quadratically with displacement as expected.

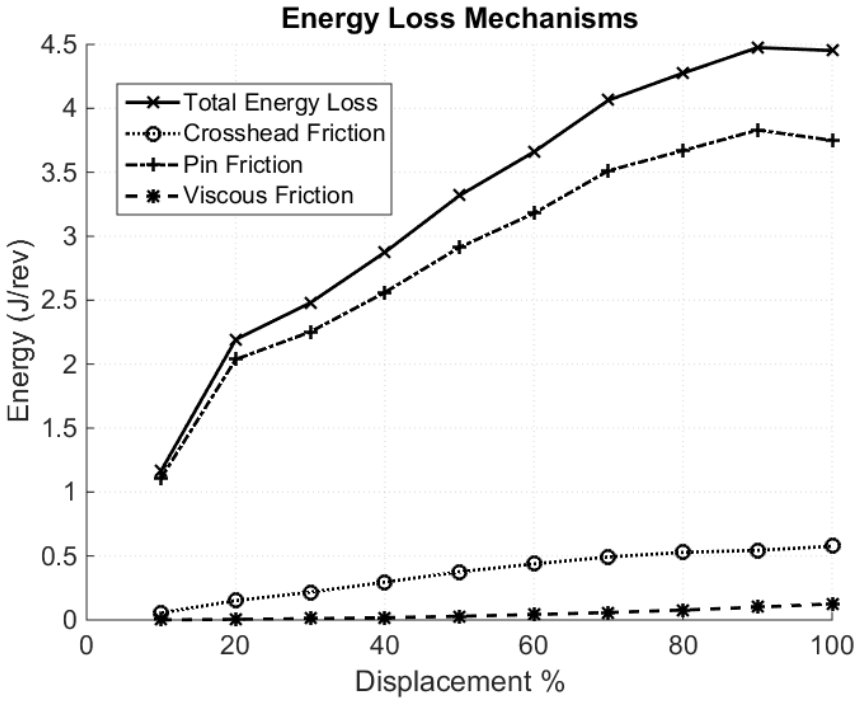

FIGURE 4.14 COMPARISON OF THE MODELED MECHANICAL ENERGY LOSS MECHANISMS

The slope of the crosshead friction and pin friction energy losses decrease with increased displacement. As the displacement is increased, the crosshead peak forces become shifted from the peak velocities, as demonstrated in Figure 4.15, a plot of the slider velocity and crosshead normal force through a cycle. 0 and 2π radians are associated with the top dead center position of the piston and the point at which the velocity curve crosses the x axis is associated with bottom dead center. The transmission angles of the rocker-slider dyad vary with displacement. For this mechanism, the transmission angles are favorable at bottom dead center causing reduced normal force on the slider. At top dead center however, the transmission angle of the rocker-slider dyad is constant independent of displacement. The peak normal forces occur as the piston approaches TDC and are similar due to the constant transmission angle.

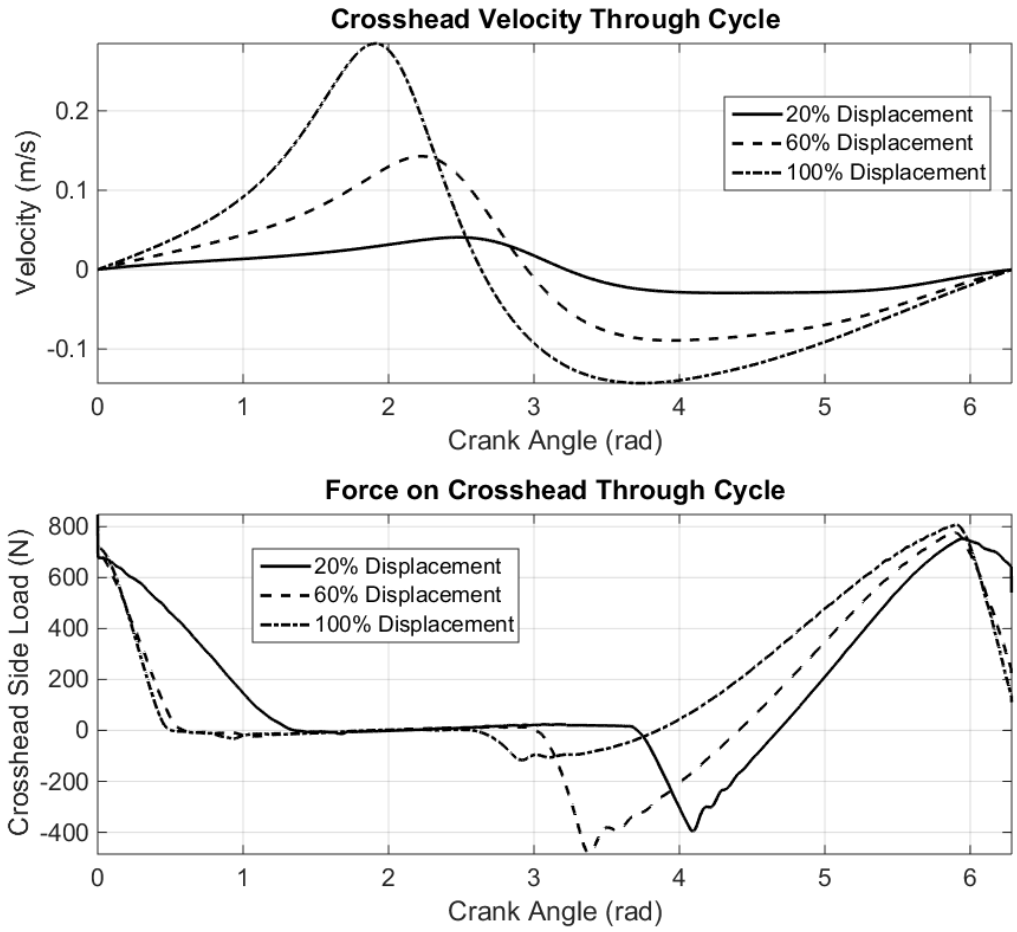

FIGURE 4.15 COMPARISON OF MODELED CROSSHEAD VELOCITY AND SIDE LOAD OVER A CYCLE AT VARIOUS DISPLACEMENTS

Table 4.2 shows the model predicted energy loss contributions of the experimental conditions discussed above at 100% displacement. The shaft seal energy loss was less than 0.1%, so was not included. The viscous friction of the piston and Coulomb friction of the crosshead hearing were similar in magnitude, accounting for a quarter of the energy losses at maximum displacement. The rest of the mechanical losses were generated by the revolute joints.

TABLE 4.2 ENERGY LOSS MECHANISMS AND THEIR CONTRIBUTIONS TO FRICTION IN THE MECHANISM MODELED FROM EXPERIMENTAL DATA

Symbol	***Loss Mechanism***	***Bearing Type***	***Energy Lost Over Cycle***	***% of Total Losses***
$M\_(\mu\_a)$	Friction torque at pin a	Roller	$0.04\ J$	01.1%
$M\_(\mu\_b)$	Friction torque at pin b	Bushing	$1.20\ J$	33.3%
$M\_(\mu\_c3)$	Friction torque at pin c_3	Bushing	$0.42\ J$	11.6%
$M\_(\mu\_c4)$	Friction torque at pin c_4	Bushing	$0.13\ J$	03.6%
$M\_(\mu\_d)$	Friction torque at pin d	Bushing	$0.52\ J$	14.4%
$M\_(\mu\_e)$	Friction torque at pin e	Bushing	$0.31\ J$	08.5%
$F\_(fr\_s)$	Crosshead Friction	Linear Bushing	$0.60\ J$	16.6%
$F\_(f\_v)$	Viscous Friction	N/A	$0.39\ J$	10.8%

The pin between the connecting rod and the rocker contributed the least energy loss of the joints having plain bearings. This is because the relative angular velocity between these two links is small. Their relative velocity goes to zero at zero displacement when these links are collinear. In this mechanism, the pin at c is fixed to the connecting rod, but the model could be used to determine to which link the pin should be fixed to minimize friction torque energy loss.

Of the revolute joints, pin b contributed the most energy loss. This is because the joint rotates with the input shaft and is the connection between the input shaft and the rest of the mechanism. As a result, it is heavily loaded and has large angular velocities. The

input shaft bearing also rotates constantly yet had the lowest friction torque energy loss. This is expected as it used a roller bearing having an equivalent coefficient of friction of 0.005 versus 0.174 for the plain bearings. If roller bearings are used in all the joints, the friction loss can be reduced greatly, as will be explored in Chapter 5.

Figure 4.16 shows a comparison of the work input data from the 2.4MPa and 3Hz experiment as well as modeled data for both the mechanism with plain bearings and with roller bearings. The work output data, which is the modeled piston work per revolution, is given for reference. Because roller bearings have an equivalent coefficient of friction of .001-.005[91], the energy loss in the joints can be significantly reduced. As a result, the work input can be reduced from the dashed line with 'x' markers, which represents the current state of the prototype, to the solid line, which represents a prediction of the same mechanism with roller bearings having a coefficient of friction of .005.

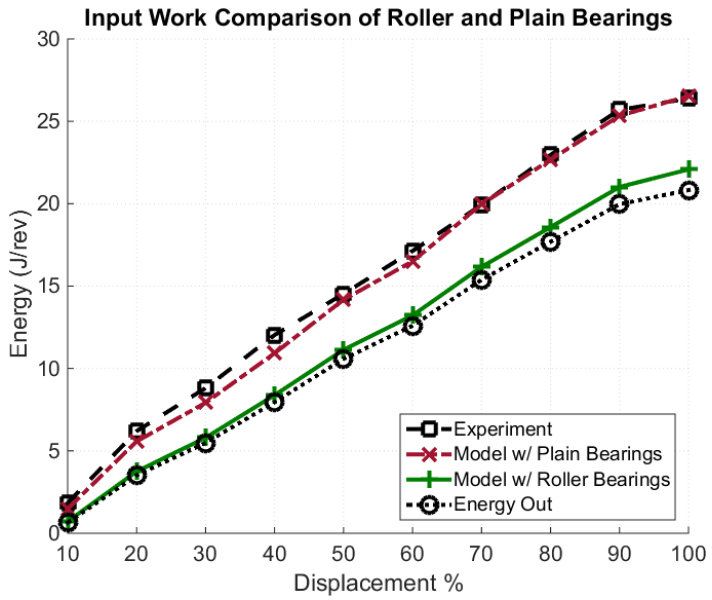

FIGURE 4.16COMPARISON OF THE ENERGY INPUT OF THE MECHANSIM WITH PLAIN AND ROLLER BEARINGS

The potential gains in efficiency offered by roller bearings are shown in Figure 4.17 with mechanism efficiency defined according to:

$$\eta_{mech} = \frac{W_{out}}{W_{in}} = \frac{\int F_p v_s dt}{\int T_{12}\omega_2 dt} \tag{4.49}$$

These data are derived from experimentally measured shaft speed and torque for the work input. The work output is calculated from the experimentally measured cylinder pressure, and the inferred slider velocity from the validated kinematic model.

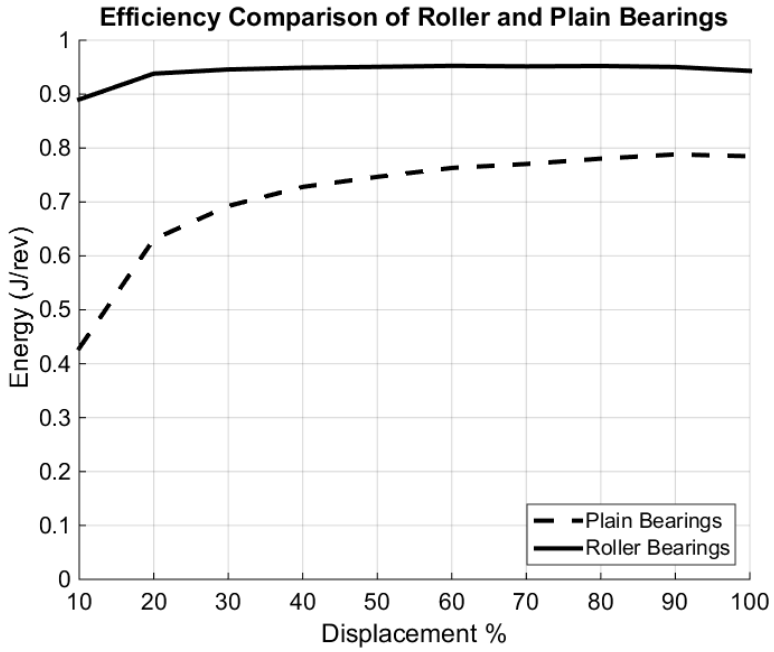

FIGURE 4.17 POTENTIAL EFFICIENCY IMPROVEMENT BY USING ROLLER BEARINGS IN PROTOTYPE

There are tradeoff associated with rolling element bearings. Roller bearings are larger, heavier, and more expensive than plain bushings. However, the potential significant gains in improvement makes roller bearings an attractive method of improving efficiency despite the potential tradeoffs.

Eqn. (4.38) shows that the viscous friction force is inversely proportional to the gap height. The measured radial gap height for this pumping cylinder was four microns. If the gap height is increased, the viscous friction component quickly becomes negligible at the expense of increased leakage flow.

The work input could be further reduced by using forced lubrication or linear roller bearings in the crosshead. Forced lubrication prevents Coulomb friction and wear in the linear bearing, but requires parasitic losses associated with pumping lubricating fluid into the bearing. Linear roller bearings have very low friction but must be large to handle the side loads.

4.7 Conclusions

A method of determining the forces and friction in the mechanism has been presented. Excellent agreement was shown between predicted and measured work input with experimentally measured shaft speed and piston pressure as inputs to the model. No experimentally determined coefficients were required to achieve agreement, adding confidence that the model accurately predicts the mechanism behavior.

The input work scaled linearly with displacement, resulting in a relatively flat efficiency curve. It was shown that the plain bearings used in the mechanism contributed the most energy loss, but roller bearings can significantly improve the mechanism efficiency.

All these data are presented at low power outputs with a peak of 150W. The fluid dynamics of the pump prevented higher speed operation as the high piston velocities

resulted in cavitation in the pump cylinder. Furthermore, large torque variations of the single cylinder pump resulted in large variations in shaft speed at higher pressures. A mechanism more suited to pumping applications is required to further validate the model at higher power levels.

Despite these limitations, the presented prototype was used to successfully demonstrate the effectiveness of both the kinematic and mechanical energy loss models. The proof of concept device demonstrates that the mechanical losses scale with displacement, validating the hypothesis that the mechanical efficiency should remain relatively constant independent of displacement. These losses can be further reduced by incorporating roller bearings in the joints as demonstrated in Figure 4.17. Finally, the methodology of mechanism loss analysis is generally applicable to other linkage topologies and can be used to generate predictive models.

Chapter 5 Design and Testing of a Multi-Cylinder Variable Displacement Linkage Pump

5.1 Introduction

The single cylinder, 8.75 cc/rev prototype pump presented in the previous chapter demonstrated that the energy loss model of the mechanism was accurate. It was shown that the energy losses of the mechanism could be reduced by five times if roller bearings were used and the mechanical efficiency could be greater than 90% at displacements as low as 10% of maximum. The experimental validation of the mechanical energy loss model was limited to low power due to large piston velocities during intake, creating cavitation as speeds were increased. Also, large torque variation due to the nature of a single cylinder operation prevented operation at higher pressures.

In this chapter, the validated kinematic and mechanical energy loss models are coupled with the solution rectification method to optimize a mechanism for a second generation prototype. The purpose of the prototype is to validate the mechanical energy loss model at higher power levels, and to provide a test bed for the development of a dynamic pumping end model presented in the next chapter. The optimization considers the pumping behavior of the mechanism by incorporating basic pressure drop and leakage flow calculations to prevent the cavitation and torque fluctuation problems of the first generation prototype. A detailed fluid dynamic model is developed in chapter six and the prototype presented in this chapter is used to validate the fluid dynamics model.

The conceptual design of the mechanism, presented in the second section, creates a basic structure to guide the model development. Section three presents the mechanism

optimization including modeling and methods. The fourth section describes the detailed prototype design resulting from the optimization. Section five presents the prototype including validation of the mechanical model at higher power levels. Discussion is provided in the sixth section, and concluding remarks are given in section seven.

5.2 Conceptual Design

There are four main components required to make a working reciprocating piston pump: The mechanism to drive reciprocation, the piston-cylinder chamber, the check-valve manifold, and the pump body. There are a number of ways to assemble these components so a conceptual design is provided to demonstrate the design process leading to the optimization.

5.2.1 Design Specifications

A set of design specification define the operating conditions of the prototype. In addition to providing a test bed for model development and validation, the prototype acts as a proof of concept demonstration of the technology at real world operating pressures and displacements. The peak operating pressure of the pump was set to 21MPa (3000 psi), a common industry standard. The testing facility had a variable frequency drive capable of 5kW, and typical electric drive motors have an operating speed of 30Hz. From the power and pressure requirements, a peak flowrate of 14.3 $\frac{l}{min}$ was calculated assuming no losses. The 30Hz requirement dictates that the maximum volumetric displacement of the pump is 7.9$\frac{cc}{rev}$. The working fluid is hydraulic oil to prevent sealing complications with pumping non-lubricating fluids.

5.2.2 Prototype Embodiment

The prototype of Chapter 4 suffered from large torque fluctuations due to the single cylinder design. A multi-cylinder pump design both reduces the shaft torque variation and improves pumping performance by reducing flow pulsations. Hydraulic pumps typically have an odd number of cylinders because the effective number of flow pulses per crank-shaft is twice the number of pumping pistons. Pumps having an even number of cylinders produce as many flow pulses per revolution as there are pistons as demonstrated in Figure 5.5. The upper figure shows the normalized output flowrate of an idealized three cylinder pump including each cylinder and their summation. The lower plot show that of a four cylinder pump. Even though the three cylinder pump has 1 less cylinder, it produces more pulses per revolution reducing the amplitude of the pulsation as compared to the four cylinder pump.

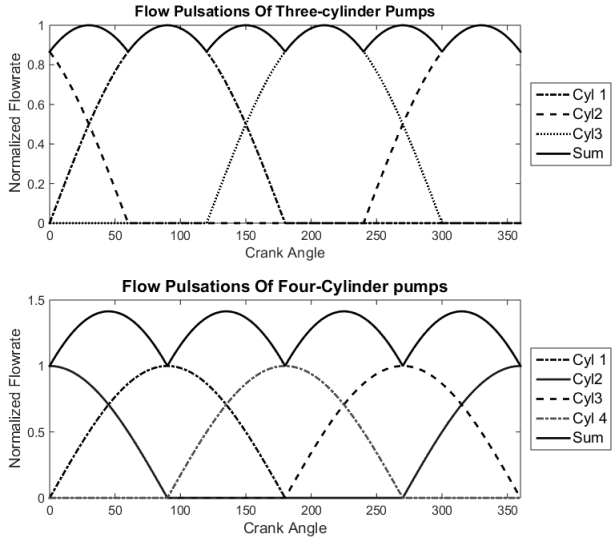

FIGURE 5.1 NORMALIZED FLOW PULSATIONS OF IDEAL THREE AND FOUR CYLINDER PUMPS

The doubling affect does not occur for a single cylinder so at least three are required. To reduce the number of moving parts and prevent an overly complicated design, five or more cylinders were not considered. Furthermore, to simplify both the input crank shaft and the manifold design, an inline configuration is used. The inline three-cylinder design is common to reciprocating plunger and piston pumps which have fixed displacement crank slider mechanisms to drive the pumping pistons.

5.2.3 Manifold Arrangement

The pump manifold is used to deliver fluid to the pumping cylinders during intake and recombine the flow from the cylinders during exhaust to the discharge line. It also houses the check valves for flow control. A diagram is given in Figure 5.2 for clarification. The outlet check valves are positioned at the top of the cylinders to aid in the exhaust of any air that is trapped in the pumping cylinder. Fluid flow and the buoyancy of the air work in the same direction in this orientation to flush trapped air out of the cylinder.

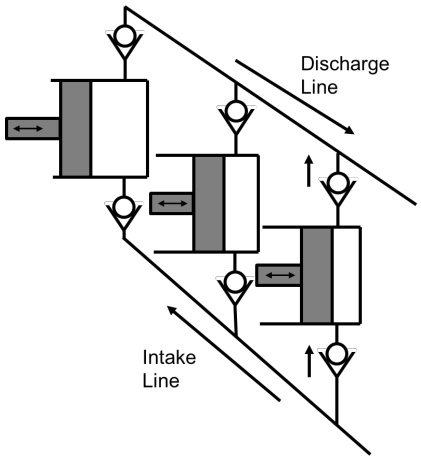

FIGURE 5.2 DIAGRAM OF MANIFOLD FUNCTION OPERATION

A manifold block houses all of the lines, valves and the pumping chamber. The discharge and exhaust lines are created by boring two channels along the length of the manifold. The pumping chambers are bores on the face of the block between the tank and pressure lines. From the top of the manifold a single bore per cylinder creates a cavity for housing the check valves that separate the lines from the pumping chamber. Disk style check valves were donated by Cat Pumps from their 5CP3120 three cylinder pump, which has similar specifications as those prescribed for the prototype.

5.2.4 Pumping Piston Arrangement

In the first generation single-cylinder pump, a crosshead bearing was used to react the slider side loads and center the pumping piston, which has a clearance seal with the cylinder. To reduce the number of precision parts in the prototype described in this chapter, the crosshead bearing also acts as the sealing cylinder and the slider acts as the piston. To prevent confusion with the cylinder and crosshead of the previous chapter, the combined purpose interface with the piston is referred to as the bore.

The piston and bore were constructed from commercially available drill rod and drill bushings due to their tight tolerances, desired hardness, and low costs. The drill bushing were honed to create a smooth surface finish. The combined tolerances of the rod and bushing result in a radial clearance between 3-25μm.

5.2.5 Configuration Selection

The linkage configuration of the previous prototype required a link that crossed over the mechanism to join the connecting rod to the slider, as seen in Figure 5.3. This additional member interferes with other links and adds moving parts. The extended r_{1min}

and overlapped r_{1max} require a crossover link because the slider moves towards the linkage as it approaches top dead center.

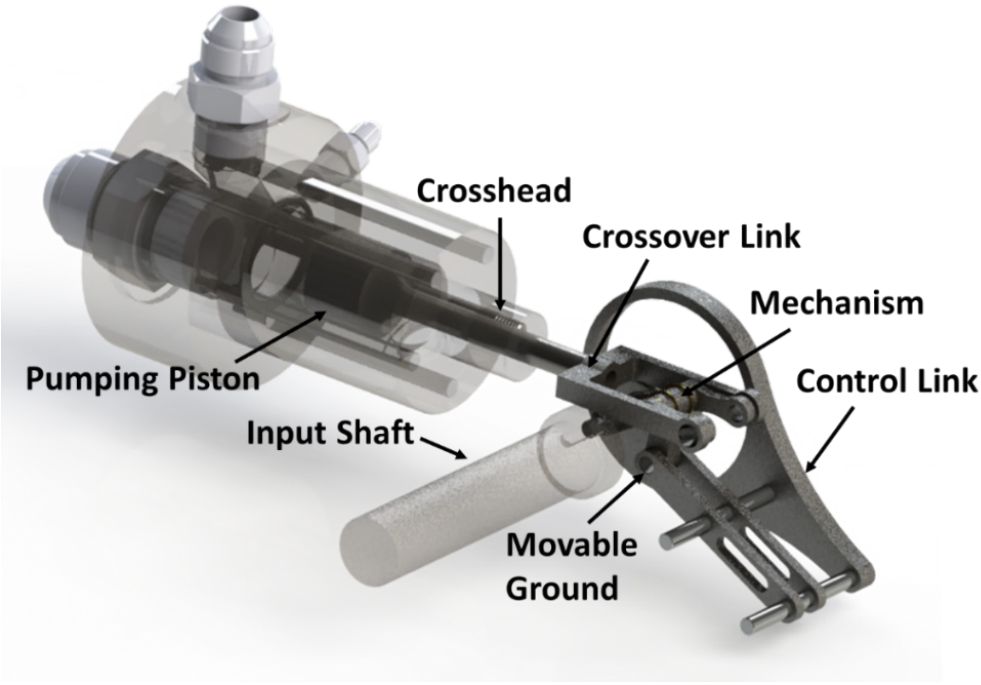

FIGURE 5.3 RENDERING OF FIRST GENERATION SINGLE CYLINDER PUMP SHOWING THE CROSSOVER LINK

For the extended r_{1max} and overlapped r_{1min} configurations, the slider moves away from the mechanism as it approaches top dead center. The optimization of chapter two showed that the extended r_{1max} configuration tended to be the smaller of the two and was selected for this reason. A line drawing of this configuration is given in Figure 5.4 showing the mechanism at top and bottom dead center positions.

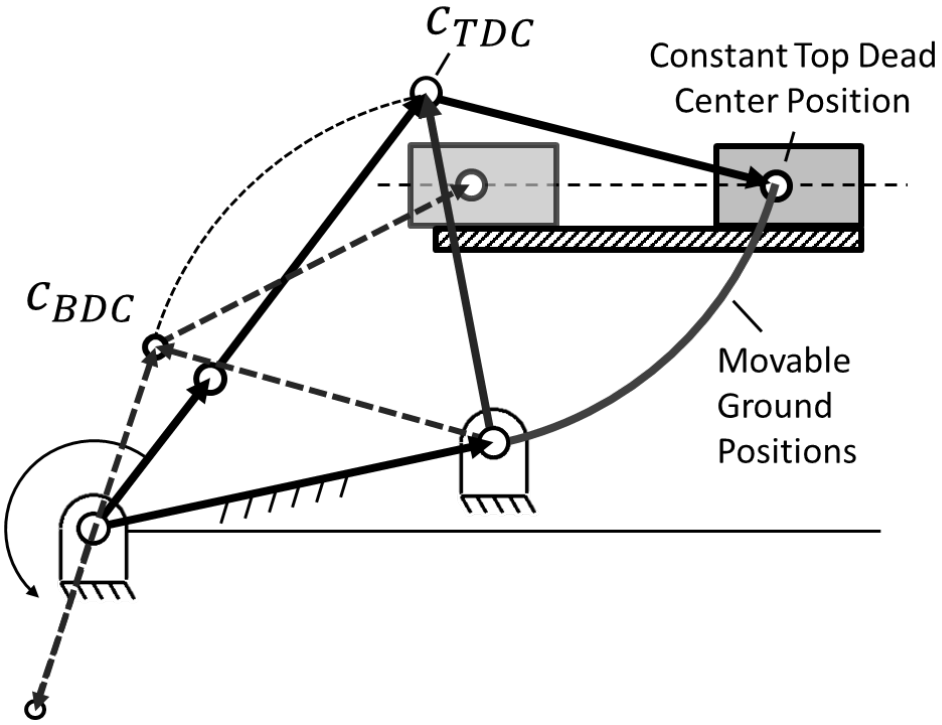

FIGURE 5.4 LINE DRAWING OF EXTENDED R1MAX MECHANISM SHOWN AT TOP DEAD CENTER AND BOTTOM DEAD CENTER

5.2.6 Mechanism Arrangement

This six-bar mechanism consists of 5 moving links with 6 unique joints requiring bearings, and a control link. Figure 5.5 provides a diagram for reference. The control link is fixed to the pump body at one end and the other end acts as the movable ground pivot. The control link is actuated to cause the adjustable pivot to move through the dashed arc.

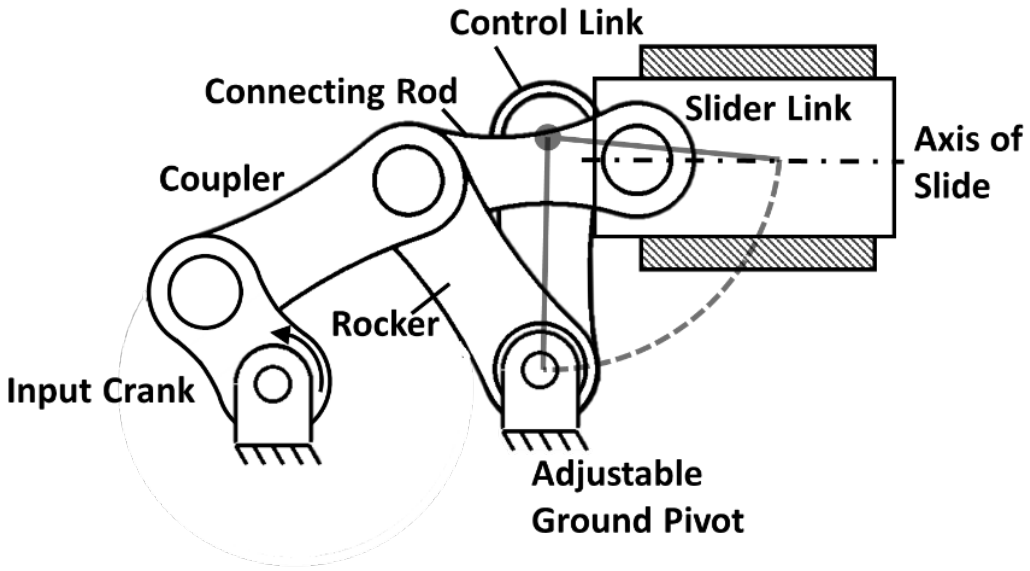

FIGURE 5.5 DIAGRAM OF MECHANISM LINKS SHOWING CONTROL LINK AND ADJUSTABLE GROUND PIVOT

The validation of the mechanical model showed that replacing the plain bearings with low friction roller element bearings in the revolute joints could significantly reduce the energy losses of the mechanism. However, roller bearings are larger for the same load rating as a plain bearing. To reduce both the number of bearings and the axial length of the pump, one bearing is used per unique joint. As a result, some links are loaded in single shear. There are a number of ways to setup the mechanism so a systematic approach is used to determine the arrangement.

To describe the mechanism assembly, links are numbered 1-6 with the assignments given in Table 5.1 and the joints are labeled as C_{ij} where i and j denote the links which share the joint, with C_{ij} being equivalent to C_{ji}.

TABLE 5.1 LINK ASSIGNMENTS

Link Name	**Assignment**	**Shared Joints**
Ground Link*	1	C_{12}, C_{14}, C_{16}
Input Crank	2	C_{12}, C_{32}
Coupler	3	C_{32}, C_{34}, C_{35}
Rocker	4	C_{41}, C_{34}
Connecting Rod	5	C_{35}, C_{65}
Slider	6	C_{65}, C_{16}
*Includes the Control Link, Input Shaft, and Slider Axis		

The inline arrangement of the cylinders requires a common crankshaft. C_{12} , the joint between the input crank and coupler link, was therefore duplicated. Additionally, the piston center was prescribed to pass through the central plane of the connecting rod as is common practice.

To reduce moments, links with shared joints were located adjacent to each other. As such, it is beneficial to for the control link to be adjacent to the rocker link, as C_{14} constitutes the movable ground pivot. Because link 3 has a common joint with both links 4 and 5, it was located between the two.

As a result of these constraints, there are 2 unique linkage arrangements which are depicted in Figure 5.6. Here, the various links are labeled by their assignment, and represented by two dimensional top view cross sections with holes present at pin locations. Because arrangement “b” resulted in interference between the control link (1) and the coupler (3), arrangement “a” was selected for the design.

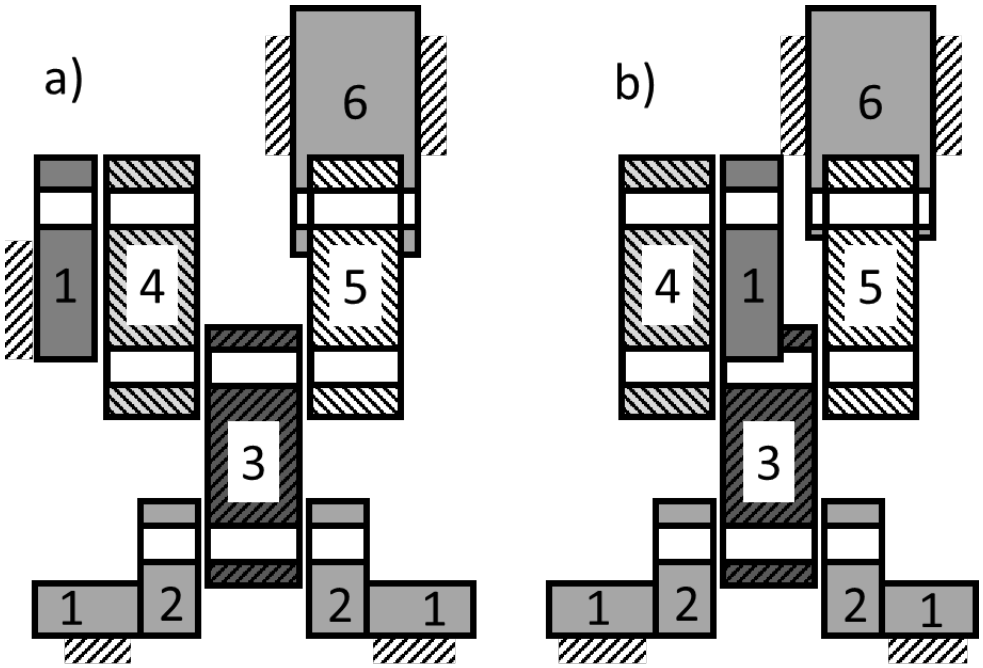

FIGURE 5.6 UNIQUE LINKAGE ARRANGEMENTS

5.2.7 Bearing Locations

For each of the 6 joints, a bearing is to be mounted in one of the associated links. The bearings for joints C_{32} and C_{65} were mounted in links 3 and 5 respectively as to reduce the moving mass of the material required to support the bearing and thus shaking forces. Additionally, joint C_{12} is the crank shaft bearing and was mounted to the crank case.

Joints C_{34} and C_{35} share a common pin and therefore the bearings for these pins are concentric. To prevent large pin moments, it is better for the common pin to be mounted in link 3, which is in between the other links. Therefore, the bearings for joints C_{34} and C_{35} were located in links 4 and 5 respectively.

Joint C_{41} is the movable ground pivot and the location of the associated bearing was not as readily deduced as with the other joints. Ultimately, the bearing was mounted in link 4 for convenience of design and assembly.

5.2.8 Bearing Selection

Needle roller bearings are the least expensive, most radially compact, and lightweight type of rolling element bearing. However they are axially longer than other types of bearings. Cylindrical rollers are the most axially compact type for a given load. To limit the axial length of the mechanism, cylindrical rollers were used where size permits. Needle rollers are used elsewhere. In order to reduce manufacturing costs, the number of hardened precision surfaces was minimized by selecting bearings which have inner and outer races. Therefore caged roller and drawn cup needle rollers were not considered.

5.3 Optimization

The first generation prototype was optimized with only the kinematics in mind, requiring only two optimization parameters and a single objective. As such, a grid search method was sufficient. The second generation pump optimization considers the kinematics, mechanical energy loss model, and pumping characteristics. A more targeted approach is required. This section presents the optimization of the mechanism for the three cylinder variable displacement linkage pump prototype.

5.3.1 Modeling

The conceptual mechanism design and linkage arrangement provide a framework around which to build a model for simulating the pump behavior. The model is required to be robust as to handle a large variation in input parameters, and computationally inexpensive to permit the evaluation of a large number of candidate solutions.

The solution rectification methods described in chapters two and three augments the kinematic model preventing the optimization from considering invalid linkage solutions and wasting computational effort. The mechanical energy loss model of chapter four, and the pumping behavior presented in this section, provide an estimation of the performance of a candidate mechanism. These models are coupled in a simulation of the prototype.

5.3.1.1 Simple Pump Model

The model assumes that the working fluid is incompressible, inviscid, and that the flow through the pumping cylinder is fully-developed and laminar. The volumetric flow rate is considered to be equal to the piston velocity times area. The inlet and outlet check valves are also assumed to open and close instantly depending on piston direction. While these assumptions are not strictly valid, they qualitatively insert the influence of piston velocity and diameter on viscous drag and provide a means of estimating leakage flow rate.

5.3.1.1.1 Leakage flow rate

The piston is side loaded in the crosshead bearing which also provides a clearance seal. As a result, the piston is eccentrically located in the bore. The leakage flow rate for an eccentric piston in a bore is found by[93]:

$$Q_{leak} = \frac{\pi d_p h^3 (1 + 1.5e^2)}{12 \mu_d l_p} \Delta P_s \tag{5.1}$$

where d_p is the piston diameter, h is the nominal piston bore radial clearance, l_p is the effective length of the piston-bore interface, ΔP_s is the pressure drop across the piston bore, μ_d is the dynamic viscosity of the working fluid, and e is the eccentricity ratio. The piston is longer than the bore so the effective length does not change with stroke and l_p is equal to the bore length, l_b.

For the sake of this optimization, the piston is assumed to be concentric with the crosshead bore so the eccentricity is taken as zero resulting in an under prediction of the leakage flowrate. However, the gap height is on the order of microns. The tolerance of the cylinder bore and piston are on the order of tens of microns. The leakage flow rate is a function of the cube of the gap height. As a result, the maximum under prediction of the model due to the concentric assumption is within the uncertainty introduced by the tolerance of the machined clearance gap height.

Eqn. (5.1) shows that the leakage flow rate increases with the cube of the gap height, while the viscous friction force decreases linearly with gap height. The gap height is therefore minimized as the leakage dominates the friction term. The tolerance of the

piston and bore resulted in a minimum gap height range from 3-25μm. A gap height of 10μm was assumed for the optimization.

5.3.1.1.2 Pressure Drop

Pressure drops across the inlet and outlet check valves are described by the orifice flow equation according to:

$$\Delta P_v = \frac{\rho}{2}\left(\frac{Q_v}{A_v C_d}\right)^2 \tag{5.2}$$

where A_v is the valve opening area, C_d is the discharge coefficient, ρ is the density of the fluid, and Q_v is the flowrate across the valve. The discharge coefficient C_d is assumed to be 0.62 as suggested by Manring[94] and the density is that of the hydraulic oil used. The flow rate is estimated from the piston velocity as described above. The valve area is assumed to be the maximum opening area of the donated check valves.

5.3.1.2 Mechanical Energy Loss Model

In chapter four, the mechanical energy loss model was discussed. The complete model requires in iterative solver to converge a system of 21 equations for 21 unknowns. However, by assuming the influence of the roller bearing friction torque on the pin forces is negligible, the need for an iterative solver is eliminated. The bearing energy loss is calculated from the joint forces and relative angular velocities according to the equations of the previous chapter. The equivalent Coulomb friction coefficient of roller bearings varies between 0.0011 and .0025 depending on the type used[95]. Because the bearing type is unknown at each joint, .0025 is assumed.

5.3.2 Parameters

There are six optimized design variables required to describe the functional operation of the mechanism. The linkage is initially normalized by the length of the input link, r_2, so only two normalized link lengths, r_3 and r_4, and two angles, θ_{as} and γ_{min}, are required to describe the kinematics as outlined in chapter two. In this optimization, the presented solution rectification method was used to create limits on the axis of slide to prevent unfeasible slider mechanisms.

The kinematic model provides a normalized stroke length. The piston diameter,d_p, determines the required stroke of the mechanism from the pump displacement specified in the second section of this chapter. The normalized linkage is then scaled to have the required stroke. The bore length, l_b, is then used to calculate the viscous friction and leakage flow rate losses.

5.3.3 Objective functions

The six objectives used to optimize the linkage are: minimize cylinder pressure drop, maximize mechanical efficiency, minimize cross head bearing side load, minimize roller bearing load rating, minimize timing ratio variation, and maximize power density,. Each of these will now be defined.

5.3.3.1 Pressure Drop

The peak pressure drop across the inlet valve was minimized to prevent cavitation which results in partial filling and prevents wear of precision surfaces during collapse of the cavitation bubbles. With reference to Eqn (5.2), the only independent variable for calculating the pressure drop is the flow rate across the valve. This term is determined by

the kinematics of the mechanism. By minimizing the peak piston velocity, the pressure drop across the inlet is minimized.

5.3.3.2 Efficiency

The fluid model and mechanical model are coupled by the bore length parameter which determines the viscous friction energy loss and leakage losses. The leakage energy loss is found by:

$$\mathrm{E}_{\mathrm{Q_l}} = \Delta P \int Q_{leak} dt \tag{5.3}$$

Because a clearance seal is used in the bore, forced lubrication is assumed so only viscous friction is considered. The efficiency of the mechanism is maximized by minimizing the sum of the energy loss components according to

$$\mathrm{E}_{Loss} = \mathrm{E}_{\mathrm{Q_l}} + E_v + E_p \tag{5.4}$$

where E_v and E_p are the viscous friction energy loss and pin friction energy loss defined in the previous chapter.

5.3.3.3 Piston side load

In order for the forced lubrication assumption to be valid, the side load of the piston must be kept low to prevent contact. However, there are no penalizations on the piston side load in the efficiency calculation because only viscous friction is assumed. The normal force on the piston F_{16y} is minimized to prevent piston cylinder contact.

5.3.3.4 Bearing load rating

The bearing life is a function of the relative motion between the bearing and its pin and the applied load. Minimizing this value results in smaller bearings and thus reduced mechanism size and weight.

Figure 5.7 shows a schematic of two representative links who share a common joint and are rotating relative to each other. F_{AB} is the joint load and ω angular velocity of the links. In order to determine their relative rotation, θ_{AB}, the angular velocity difference between the two links is integrated over a cycle as shown in equation (5.5). From these values and the desired life rating, a bearing load rating was determined.

$$\theta_{AB} = \int abs(\omega_A - \omega_B)dt \tag{5.5}$$

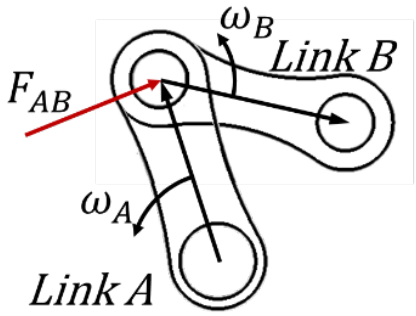

FIGURE 5.7 RELATIVE ANGULAR VELOCITY OF TWO LINKS WITH A SHARED JOINT

The bearing life calculation is based off the L10 designation, which means that 90% of bearings will survive for the prescribed period. The bearing life is determined by:

$$L_{10} = \frac{\theta_{AB}}{2\pi}\omega_{sys}\frac{3600s}{Hr}L_h \tag{5.6}$$

where ω_{sys} is the system frequency, and L_h is the desired life in hours.

The equivalent load for a fluctuating load and required dynamic load rating C are found by:[91]

$$P_{eq} = \frac{2}{3}\max(F_{AB}) \tag{5.7}$$

$$C = \sqrt[\frac{3}{10}]{L_{10}}P_{eq} \tag{5.8))}$$

5.3.3.5 Timing Ratio

The timing ratio is defined as the ratio of time of the pumping stroke to the time of return stroke. If the timing is not equal, the piston velocity will be higher for one part of the cycle. Timing ratio variation is the maximum difference between 1 and the timing ratio across all displacements. The pressure drop objective function only considers peak velocities during the return stroke so the timing ratio variation is used to consider the entire pumping cycle.

5.3.3.6 Power Density

The linkage was designed for a prescribed power output, so the power density is a function of the linkage area which was defined by the area of a bounding box, parallel to the axis of slide, enclosing the entirety of the linkage. It should be noted that the linkage area is based on the vector lengths and does not take into account link widths or bearings. It is not a measure of the physical mechanism, but rather a comparison metric between candidates based on the assumption that candidates with similar vector areas will have

similar true areas when a linkage is constructed. Minimizing this area maximizes power density and minimizes the mechanism size.

5.3.4 Optimization Technique

Due to the large number of objective functions, design variables, and the coupled kinematic and pumping behavior of this problem, a robust global optimization technique was required. The Elitist non-dominated sorting genetic algorithm (NSGA-II) has been shown to be effective in solving non-linear multi-objective problems and was selected to optimize the pump [96]. The algorithm was completed with 10,000 individuals per generation for 100 generations with a mutation probability of 0.9 for a total computation time of 1hr 24 min on a single core of a 2.7GHz AMD processor.

The output of a multi-objective optimization is not a single optimized solution, but rather an *N*-dimensional optimal surface where *N* is the number of objective functions. This optimal surface is called the Pareto front and contains all of the non-dominated solutions found. A solution is considered non-dominated if no other solution is better than the current one in some objective function without being worse in some other objective.

5.3.5 Results

Figure 5.8 shows the six-dimensional Pareto front projected on a two-dimensional plane to show the design trade-off between linkage area and bearing load rating. Each point represents a candidate mechanism plotted by its objective values. When the linkage area decreases towards zero, there is an exponential increase in bearing load rating. As the bearing load rating approaches it minimum, the size of the linkage becomes greater.

Tradeoffs exist between each of the objective functions and it is the job of the designer to select the appropriate solution for the given application.

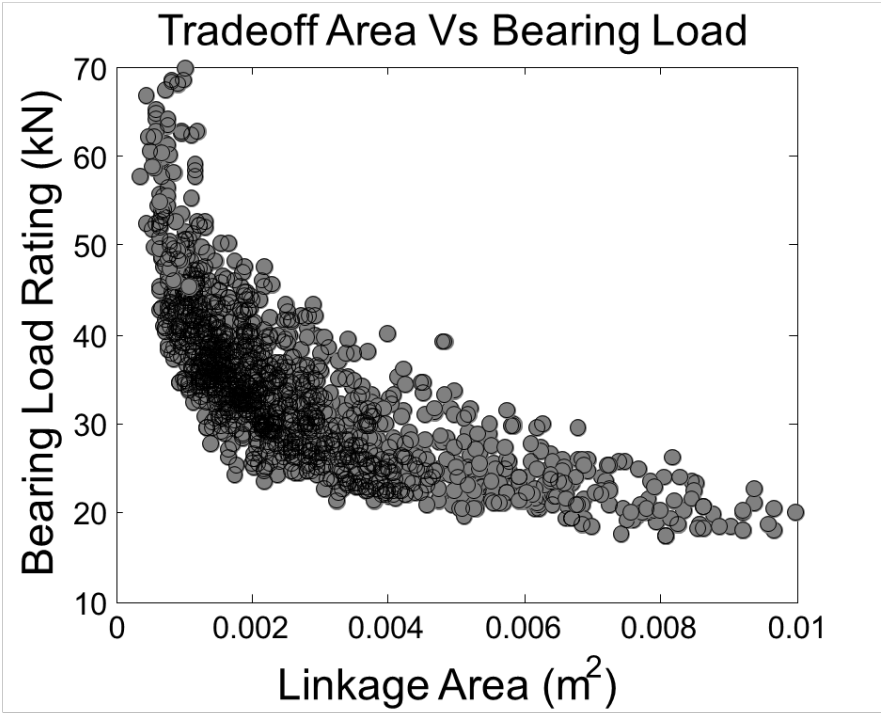

FIGURE 5.8 TWO DIMENSIONAL PROJECTION OF PARETO-FRONT REPRESENTING DESIGN TRADE-OFFS OF OPTIMAL SOLUTIONS

As seen in Figure 5.8, there can be a large number of Pareto-optimal candidate solutions. In this problem, there are on the order of 2000. In order to reduce the number of solutions, a set of threshold values are applied to act as a filter. These values were chosen as to disqualify candidates which were not viable. Table 5.2 shows the thresholds used for each objective. These values where developed to reduce the list of candidate solutions to those which would perform reasonably well from both a performance and practical standpoint.

TABLE 5.2 USER DEFINED THRESHOLD VALUES AND THE OBJECTIVE FUNCTION VALUES OF THE SELECTED SOLUTION

Objective	Threshold	Solution Value
Efficiency at 50% Displacement (min)	92%	94.7%
Linkage Area (max)	45 cm^2	42 cm^2
Timing Ratio Variation (max)	.07	.055
Bearing Load Rating (max)	32 kN	25.4kN
Crosshead Side Load (max)	2 kN	0.85 kN
Pressure Drop (max)	$7kPa$ $(\sim 1psi)$	6.6 kPa

After filtering the initial large solution space, there were multiple candidate solutions. These solutions were further evaluated to select a single candidate. For this application, the timing ratio variation is the most important constraint due to its coupling with peak shaft torques and flow rates. Therefore, the solution which met the criteria listed in Table 5.2 with the smallest timing ratio variation was selected.

Figure 5.9 shows the energy loss contributions of the selected solution including Coulomb friction in the pin joints, viscous friction in the piston cylinder interface, and leakage at 10 Hz and 21 MPa operating pressure. The pin friction still dominates, but is on the same order as the viscous friction and leakage, while it was an order of magnitude higher for the earlier prototype with bronze bushings. The energy loss is not reduced to the same degree as predicted in the previous chapter because the diameter of a roller bearing is larger for the same load than a plain bearing. In this case, the bearing diameters are ~20 mm whereas the previous prototype had 6 mm diameter bearings.

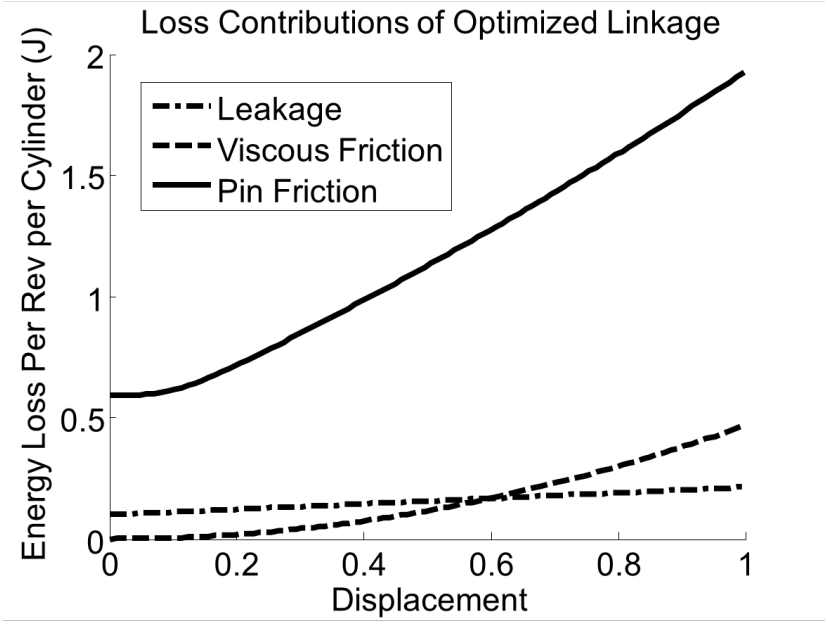

FIGURE 5.9 ENERGY LOSS CONTRIBUTIONS AT 30HZ AND 21MPa OPERATION AS A FUNCTION OF FRACTIONAL DISPLACEMENT

As shown in Eqns. (5.1), the leakage flow rate is a function of the pressure drop across the clearance seal. Additionally, Eqn (5.3) shows that the energy loss is a function of the pressure drop with respect to time, so the overall leakage energy loss is therefore a function of the pressure drop across the piston, and the amount of time the seal is exposed to that pressure. As a result of the cylinder pressure assumptions, the leakage is a function of the timing ratio variation. While the assumptions of the cylinder model make this result inexact, it illustrates and additional reason the timing ratio variation is important to the performance of the mechanism.

The reduction in timing ratio variation is demonstrated by Figure 5.10, where the performance of the optimized linkage is compared to the first generation prototype and a timing ratio variation of zero for reference.

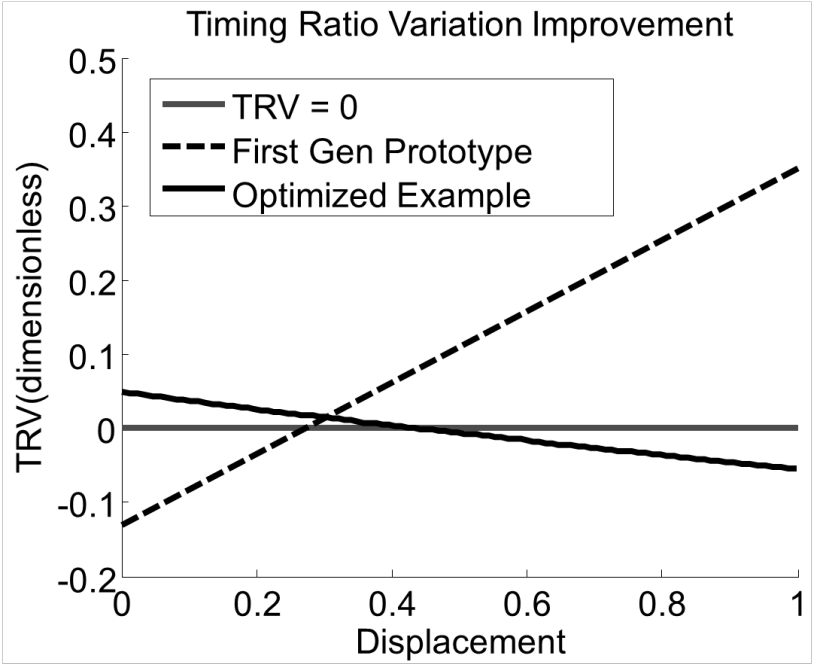

FIGURE 5.10 TIMING RATIO VARIATION AS A FUNCTION OF FRACTIONAL DISPLACEMENT

The mechanical efficiency of the mechanism is predicted to be greater than 90% for the majority of the operating conditions as shown in Figure 5.11. An average total efficiency of 92% is expected between 10 % and 100% displacement at 30Hz and 21MPa operating conditions. The volumetric efficiency is not predicted at this point as the model assumptions would not produce realistic values.

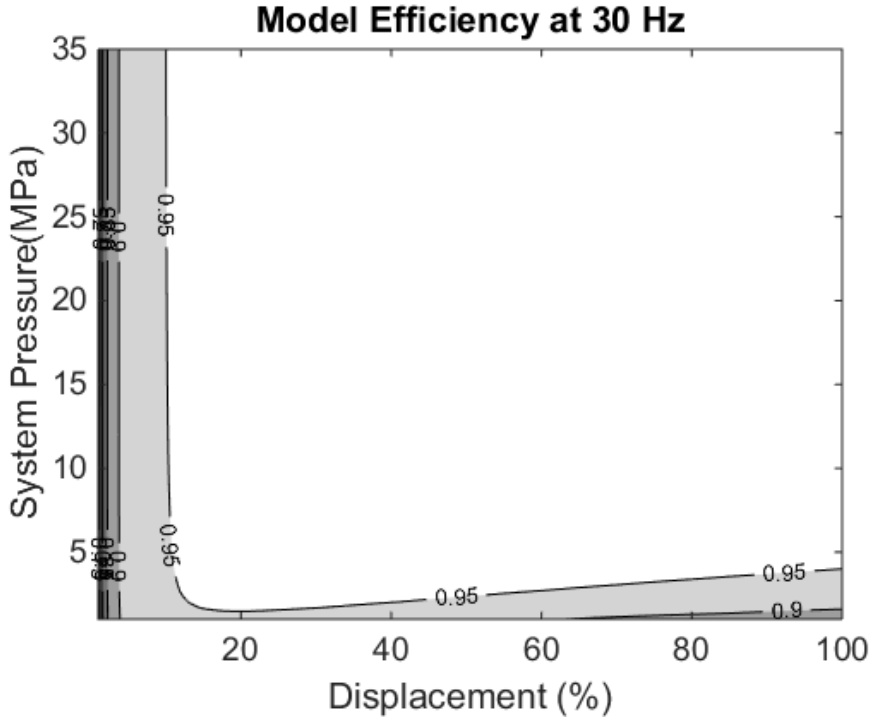

FIGURE 5.11 CONTOUR PLOT SHOWING PREDICTED PERFORMANCE OF PUMP AT VARIOUS OPERATING CONDITIONS

5.4 Final Design

The optimization in the previous section produced a set link length and angles that define the kinematics and the piston diameter and bore length that describe the pumping head. From the bore and the required displaced volume, the required stroke is found and the normalized mechanism is scaled to meet this requirement. The final link lengths of the optimization are presented in Table 5.3.

The results of the optimization provided design guidelines, which were altered where convenient. For example, the optimization resulted in a piston diameter of 17.4 mm. However, precision ground rod is readily available in 16 mm diameter. Reducing the diameter reduces the displacement of the pump, but the displaced volume is not critical to

the purpose of the prototype. Additionally, the drill bushings used as the cylinder bore are readily available in 28mm lengths rather than the optimal 77mm length for the piston cylinder interface. To account for this reduced length, the drill bushing was honed such that the matching piston had just a 6 μm radial clearance rather than the 10 μm assumed by the optimization.

TABLE 5.3 RESULTS OF OPTIMIZATION

Parameter	Description	Optimized Value
r_3	Normalized Coupler Length	13.87
r_4	Normalized Rocker Length	5.48
θ_s	Angle Axis of Slide	133.64°
θ_{min}	Minimum Transmission Angle of Base Fourbar	47.75°
R_{ds}	Bore to Stroke Ratio	1.4307
l_p	Length of Piston Cylinder Interface	$77mm$

The moving links, were designed to accommodate their bearings and the applied load with a design life of 10^9 cycles. The link forces were first estimated with a massless and frictionless assumption, and then the minimum link dimensions were evaluated considering axial load, bearing size, and bearing tear-out failure. The bearing size requirements however dominated the link dimensions creating oversized links from a stress perspective.

The pin dimensions were restricted by the inner diameter of the selected bearings. A Von Mises combined bending and shear stress calculation was used to calculate an equivalent stress to determine if the pins would be able to survive the required life. The moment load was reduced whenever possible by minimizing the gap between the applied

load and the furthest point from the pin. In general, the inner diameter of a bearings require a pin that is greatly oversized for the applied loads.

Figure 5.12 shows a 2-D rendering of the final linkage design. The coupler used cylindrical roller bearings at the crank shaft, while the rocker and connecting rod use machined ring needle rollers at both ends.

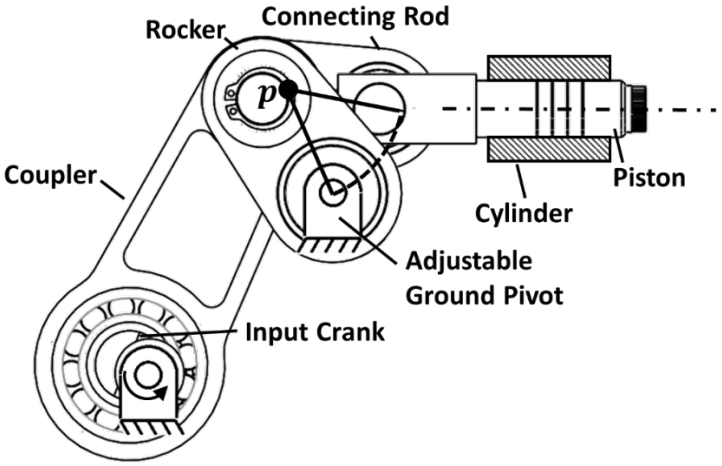

FIGURE 5.12 RENDERING OF THE FINAL LINKAGE DESIGN AINCLUDING ROLLER ELEMENT BEARINGS

A split input crank-shaft is required to accommodate a rolling element bearing between the input link and the coupler. To accomplish this, a novel modular crankshaft was designed. The crankshaft is formed by machining flats into the crank pin and input shaft to create eccentric centers when mated. After the crank pin is installed inside of its roller bearing, it is clamped to the input shaft to create a rigid structure. A counter mass is built into the clamp to balance the crankshaft and crank-pin bearings. Figure 5.13 shows an exploded view of a partial crankshaft assembly and Figure 5.14 shows the fully assembled crankshaft for clarification.

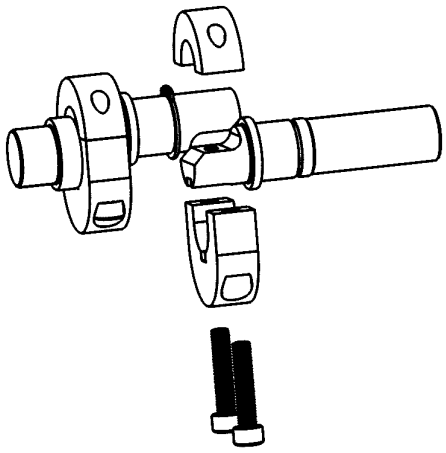

FIGURE 5.13 EXPLODED VIEW OF SPLIT CRANKSHAFT DESIGN

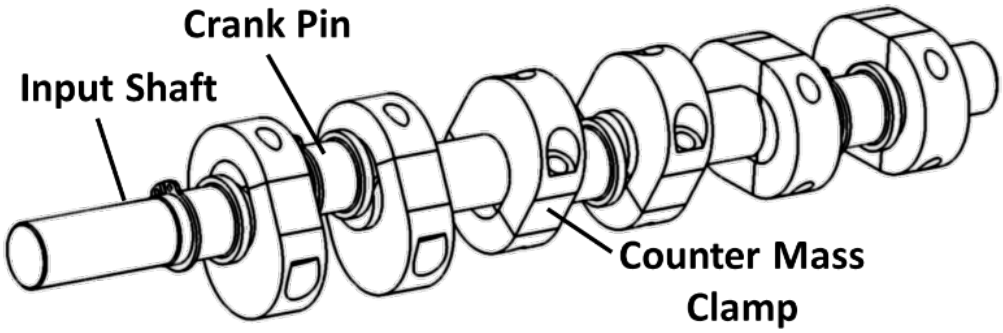

FIGURE 5.14 SPLIT CRANK-SHAFT WITH COUNTER MASS CLAMPS

Figure 5.15 shows a CAD rendering of the triplex pump design. Some of the bearings and mounting frame have been excluded for clarity. The adjustment cylinder is used to actuate the central control link, which is coupled to the other two control links with a common pin. This pin synchronizes the displacement control of the three pistons.

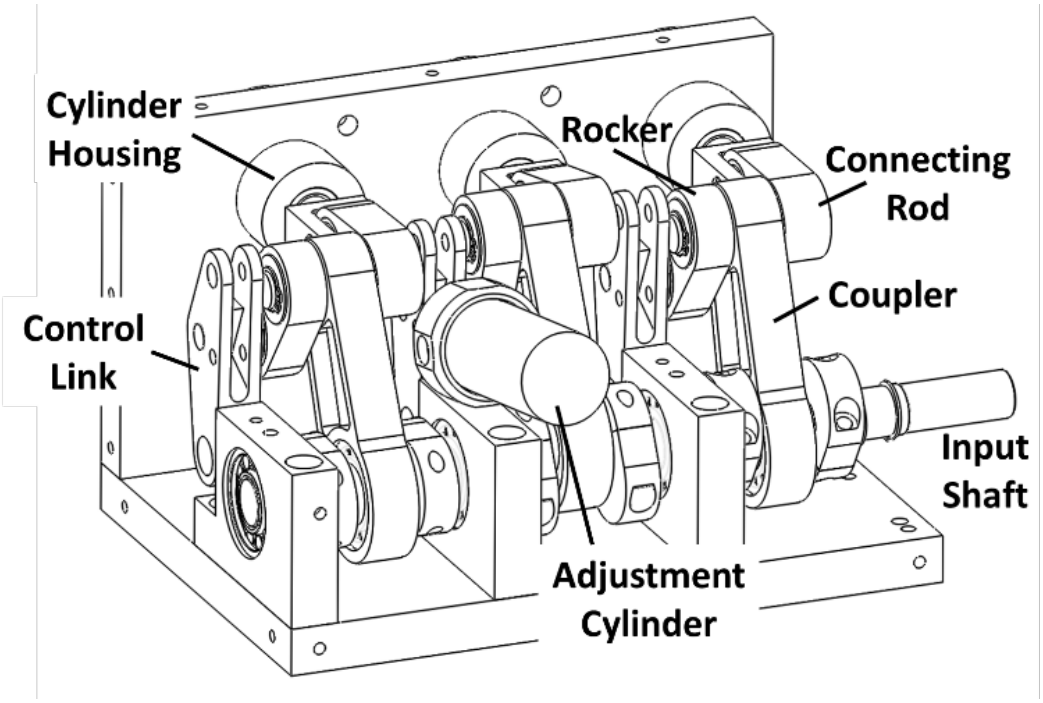

FIGURE 5.15 CAD RENDERING OF THREE CYLINDER PRORTOTYPE PUMP

Detailed drawing of the components are provided in Appendix C Additionally, the various parameters required for the full model, such as link masses, center of mass locations, mass moments of inertia, etc. are included in Appendix D for reference. All of the mass properties are evaluated from the CAD model.

5.5 Prototype Evaluation

The optimization provided design parameters and the prototype is an embodiment of that design. In this section, experimental tests are described that determine if the model is valid and if the roller bearings were effective in reducing the friction torque as expected.

5.5.1 Experimental Setup

The prototype performance was determined using the experimental setup depicted in Figure 5.16. The pump was driven by a 3-phase electric motor with a variable frequency drive to control shaft speed. The pumping head was connected to a hydraulic circuit to create a load. A pilot-operated relief valve provides pressure control.

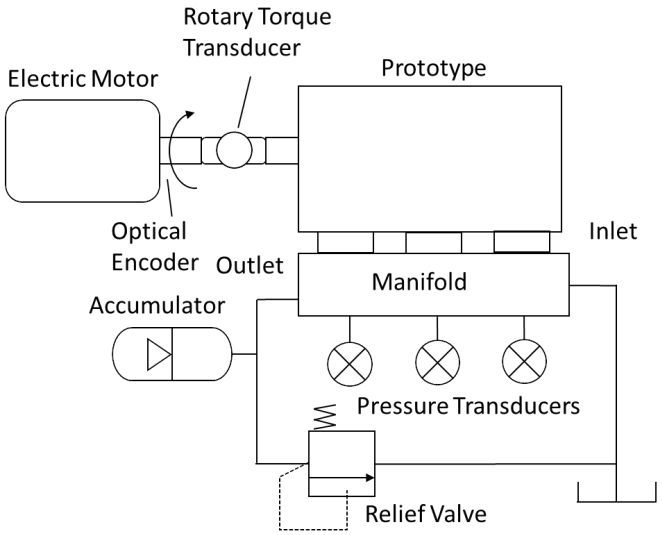

FIGURE 5.16 SCHEMATIC OF THE EXPERIMENTAL TEST SETUP

The displacement of the pistons was measured with a magnetic absolute encoder, which measures the relative angle of a magnet placed on the control link. A hydraulic actuator was used to vary the pump displacement, and was powered by the output flow of the pump through a directional control valve. An optical encoder measured the input shaft position, which is used as an input to the model. The shaft speed was calculated from the position data and an inline rotary torque transducer provided shaft torque data for input work calculations. Pressure transducers were included in each pumping chamber and provide input to the model to calculate piston loads for model comparison.

A 1 liter accumulator pre-charged to 1.7 MPa was connected to the outlet of the pump. The reservoir was pre-charged to 35 kPa to prevent cavitation through the inlet check valve. The working fluid was ISO grade 46 hydraulic fluid with the temperature maintained at 22-25° C. Figure 5.17 provides a photograph of the test setup and the primary components.

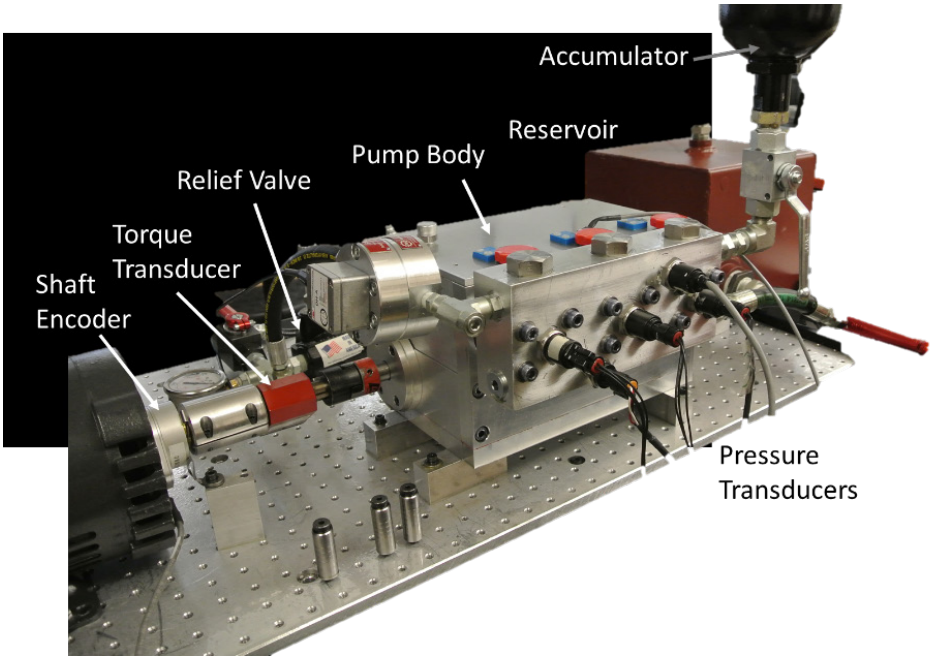

FIGURE 5.17 PHOTOGRAPH OF TEST SETUP AND PROTOTYPE PUMP SHOWING PRIMARY SENSORS USED FOR VALIDATION

Here, the experimental procedure is described. In a given set of experiments, the shaft speed was set, followed by pressure. Then the pump displacement was increased to maximum. For each test, the system was given 30 seconds to reach cyclic steady state. Data is collected for five seconds and then the displacement was reduced to the next set point. Ten displacements were measured per pressure and speed setting.

The pressure in the three cylinders and the shaft speed and were used as inputs to the mechanical energy loss mode. The model outputs the predicted shaft torque and energy losses. In the optimization, the bearing friction torque was assumed to be negligible to the pin force analysis. However, the data presented in the next section were generated without this assumption and the iterative solver was used.

5.6 Experimental Results

The experimentally measured cylinder pressure and shaft speed from a 7 MPa 10 Hz and 100% displacement experiment are shown in Figure 5.18 and Figure 5.19 respectively, as a demonstration of the model inputs. The data are presented with respect to a single rotation of the input shaft. From these measurements the shaft torque can be predicted and compared with the model as seen in Figure 5.20.

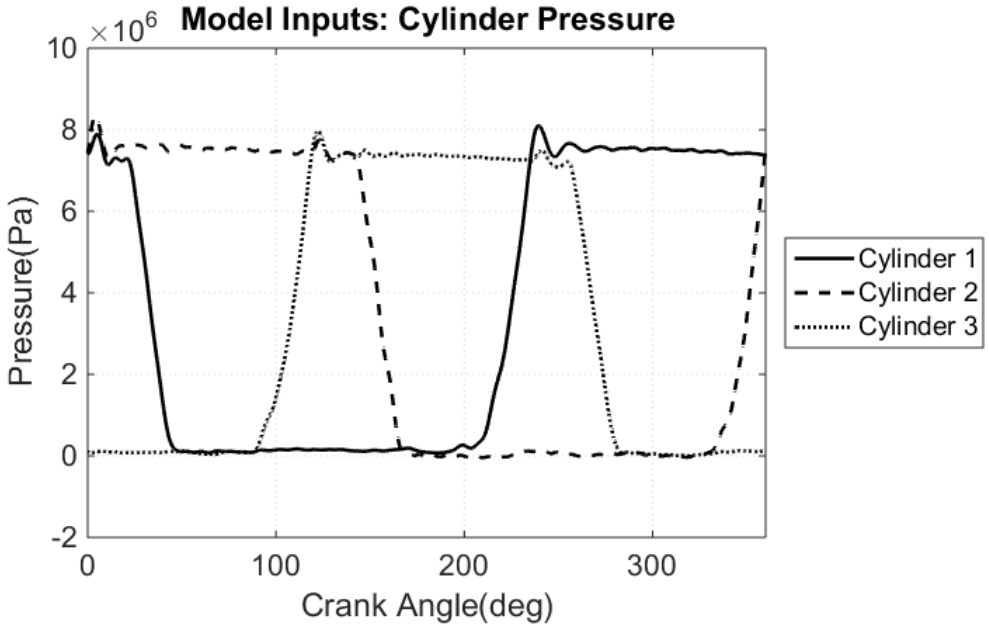

FIGURE 5.18 MEASURED CYLINDER PRESSURE INPUT TO MODEL FOR 7MPA 100% DISPLACEMENT EXPERIMENT

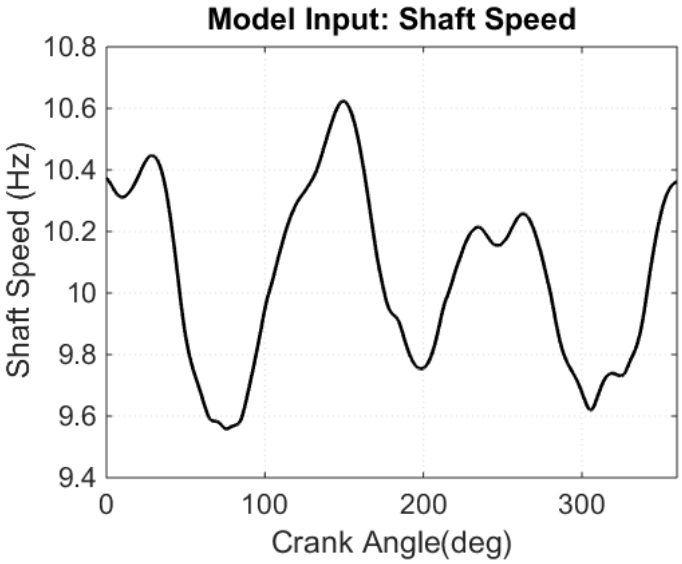

FIGURE 5.19 MEASURED SHAFT SPEED INPUT TO MODEL FOR 7MPA 100% DISPLACEMENT EXPERIMENT

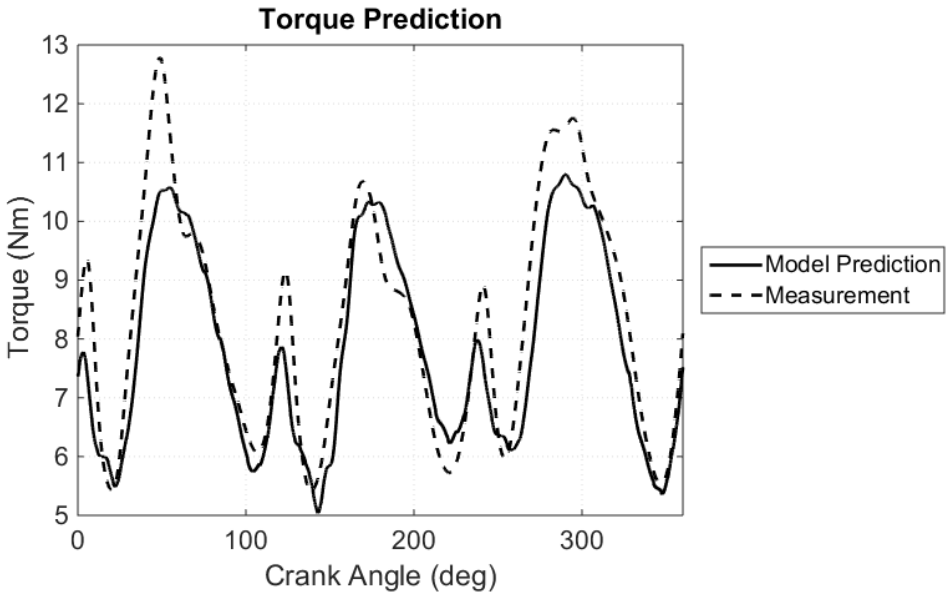

FIGURE 5.20 MEASURED AND AND PREDICTED INPUT SHAFT TORQUE FOR 7 MPA 100% DISPLACEMENT EXPERIMENT

With the assumption that the agreement between the predicted and measured shaft torque is an indication of the accuracy of the model, it can be used to evaluate the individual contributions to energy loss as shown in Figure 5.21. In the previous chapter,

the shaft seal energy loss was considered negligible, but due to the reduced energy losses of the bearings, the shaft seal torque is considered and is shown in the figure.

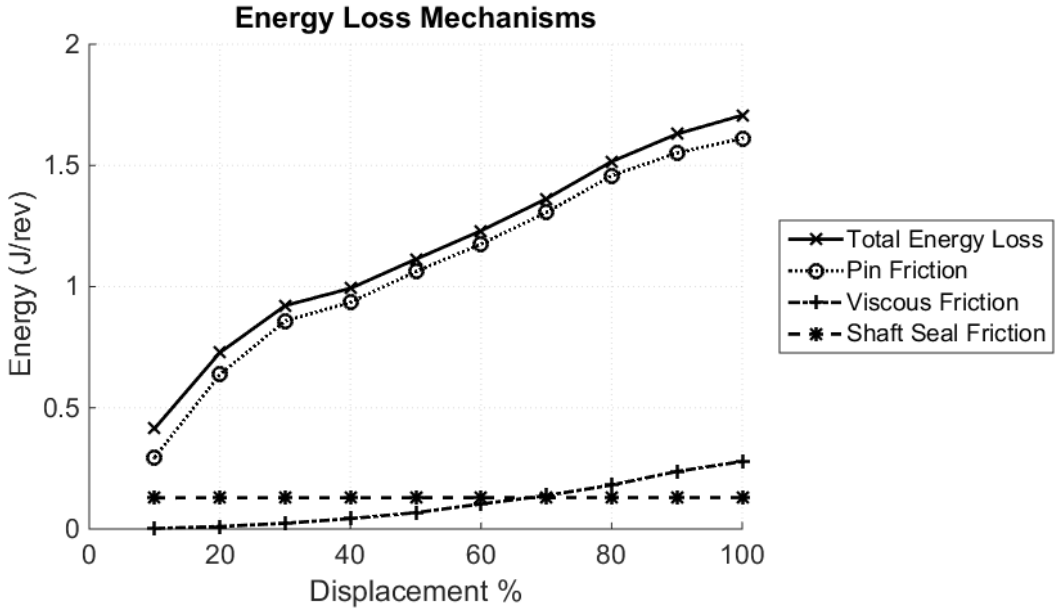

FIGURE 5.21 MODELED CONTRIBUTIONS TO ENERGY LOSS FOR 7MPA 100% DISPLACEMENT EXPERIMENT

The measured and predicted shaft work provides a demonstration of the model performance over a broader range of data. The data is presented in two figures, a low power comparison and a high power comparison. The low power comparison includes experiments at 3 and 5 Hz shaft speeds at pressures between two and 4 MPa for 10 displacements, covering a power range of 6-150 W. The high power measurements are all taken at 10 Hz operating speeds at pressures between 2 and 14 MPa, covering a power range of 20-900W. The wide range of data points is used to demonstrate the versatility of the model to predict the pump performance.

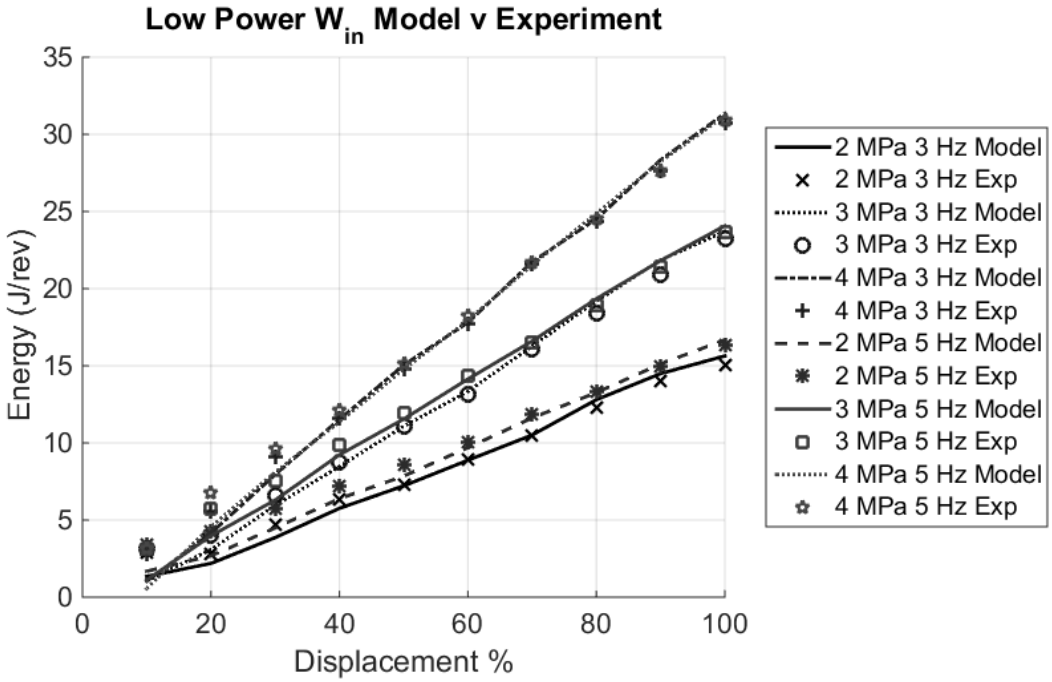

FIGURE 5.22 LOW POWER DATA SHOWING WORK INPUT AT 3 AND 5 HZ AND PRESSURES FROM 2-4 MPA

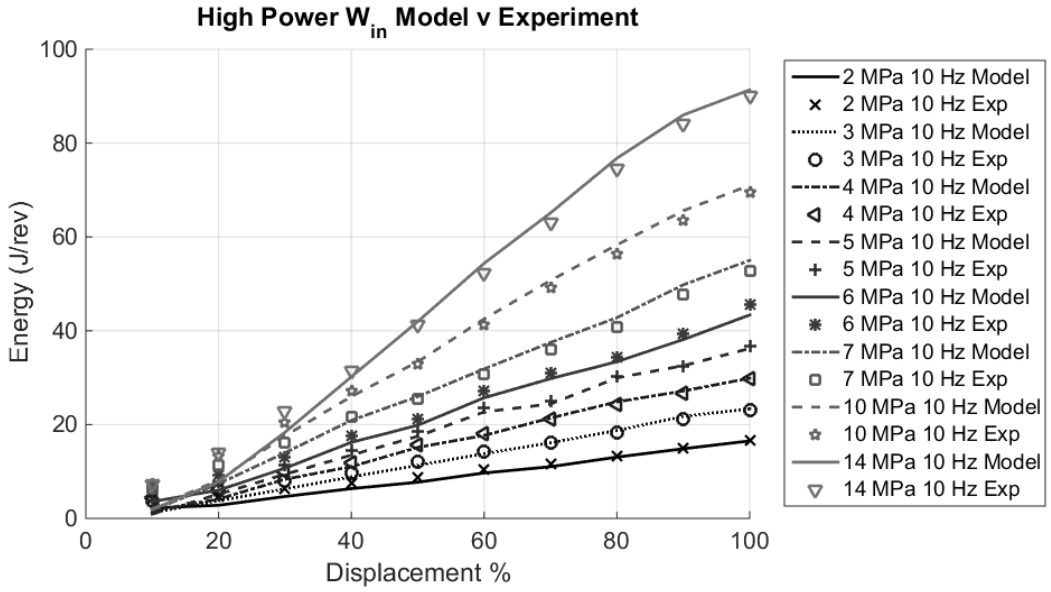

FIGURE 5.23 HIGH POWER DATA SHOWING WORK INPUT AT 10 HZ AND PRESSURES FROM 2-14 MPA

5.7 Discussion

The model prediction and experimental measurements show good agreement. over a wide range of operating conditions. Comparisons include input powers from 6W through 900W demonstrating the versatility of the model. The new design accommodated pressure measurements up to 14 MPa (2200 psi) and operating speeds up to 10 Hz. Figure 5.20 gives the shaft torque at 100% displacement under the same operating conditions. The figure demonstrates the models ability to predict the shaft torque despite the complexity of solving the system of equations simultaneously for each of the three cylinders and combing results.

Figure 5.22 presents low power data, on the order of the first generation prototype, and Figure 5.23 demonstrates the models performance at 10 Hz operating speed over a broad range of pressures and displacements. Without changing any constants or parameters, the model was able to predict the input work of the pump at each operating point. However, deviation of the model prediction and measurement can be seen at displacements below 40%. Furthermore, the model tends to under-predict the work input as displacement increases.

Upon further investigation, out of plane deflection of the mechanism was observed. A study was completed to determine the severity of the deflection by measuring the piston displacement with a linear variable differential transformer (LVDT) at various displacements. Piston displacements are measured both with and without pressure applied to the manifold. The difference between these measurements determines the deflection of a single piston. The results of this study are shown in Figure 5.24. The

measured deflection is normalized by the displacement set point. Trend lines are given for the each pressure set point as a visual aid.

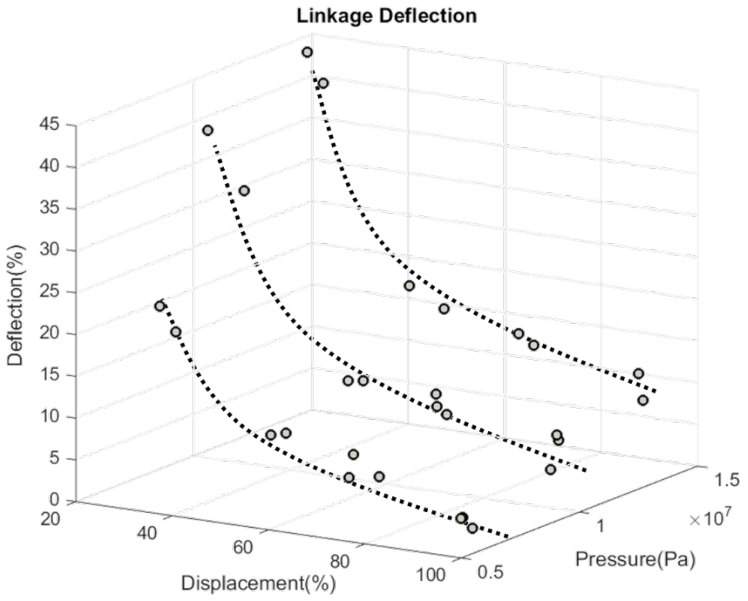

FIGURE 5.24 NORMALIZED PISTON DEFELCTION MEASUREMENT AS A FUNCTION OF DISPLACEMENT SET POINT AND SYSTEM PRESSURE INCLUDING TREND LINES

The deflection of the piston increases with pressure as would be expected. However the deflection as a fraction of piston stroke increases rapidly as the displacement decreases below 40%. The rapid increase in deflection fraction correlates with the deviation of the model prediction from the experimental measurements.

It is believed that the deflection is a function of the out of plane loading on the mechanism induced by the single shear arrangement of the links, shown in Figure 5.24. The forces shown are with reference to the coordinate system depicted and the force analysis presented in the previous chapter. These forces create moments about the x and y axes, which are reacted at the planar interface of the joints, as well as z direction forces

on the coupler link. This results in a deflection of the coupler link which reduces the piston displacement. In addition, this out-of-plane deflection causes the links to contact, generating additional joint friction due to the sliding of the aluminum link and steel bearing surfaces, which have a coefficient of friction of 0.3[97]. As a result, the model does not capture the energy losses as well at lower displacement. These effects were not observed for the first generation prototype which had duplicated links to prevent single shear loading.

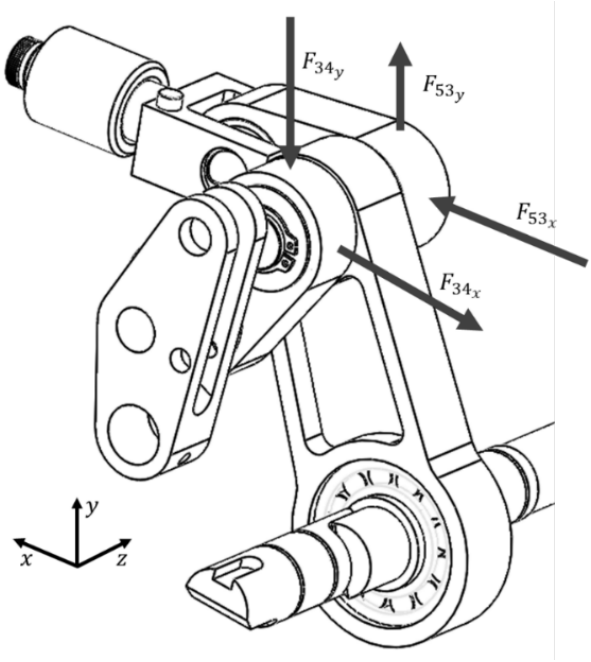

FIGURE 5.25 SCHEMATIC OF LINKAGE ASSEMBLY SHOWING OUT OF PLANE FORCES RESULTING IN MECHANISM DEFLECTION

In addition to the deflection study, the shaft seal model was evaluated to determine the validity of the presented model. The shaft torque was evaluated by running the pump under no-load conditions both with and without a shaft seal at various shaft speeds. The difference between the averages of these measurements is the shaft seal

contribution to shaft torque. As seen in Figure 5.26, the manufacturer model significantly under predicts the shaft seal torque.

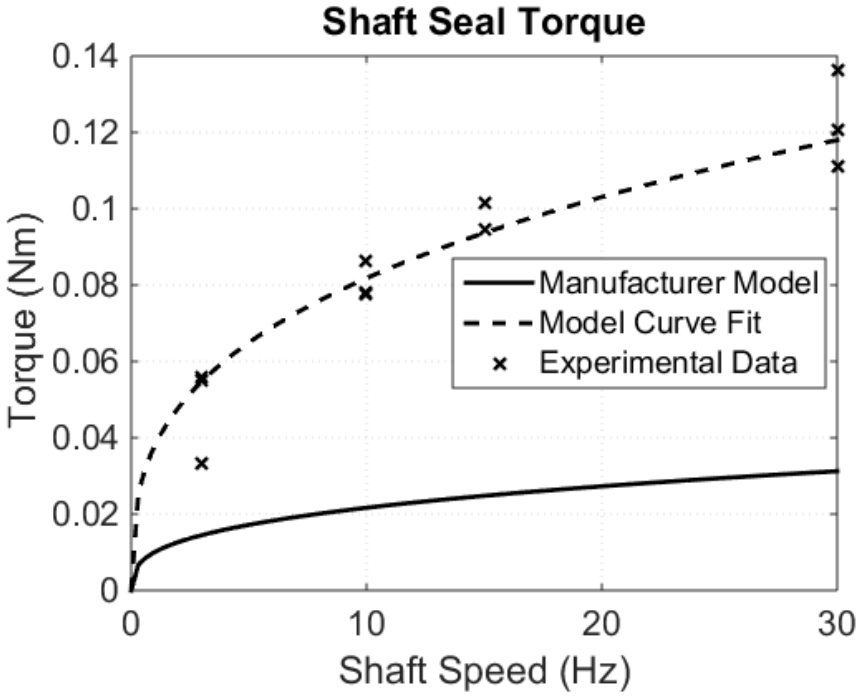

FIGURE 5.26 MEASURED SHAFT SEEL TORQUE MEASUREMENTS COMPARED TO MODELS

In order to obtain a more realistic estimate of the shaft seal torque, the data is curve fit to the original model to determine a new coefficient for the shaft torque model reproduced from chapter four below:

$$T_{SS} = C_{ss} D_s^2 \omega^{\frac{1}{3}} \tag{5.9}$$

where C_{ss} is the shaft seat coefficient. The manufacturer provided a C_{ss} of 15 [92]. A curve fit of the experimental data was used to determine a new coefficient. The resulting curve can be seen in the figure with a C_{ss} of 57. This is approximately a four times increase in shaft seal torque. However, the shaft seal torque is on the order of 0.1 Nm at

10 Hz, which is only around 1% of the overall shaft torque at 7 MPa. The energy loss contributions of the previous section are reproduced in Figure 5.27 below including the increase in shaft seal torque energy loss. As a result of this increase in shaft seal torque, this energy loss dominates the viscous friction energy loss at all displacements and the pin friction at low displacements.

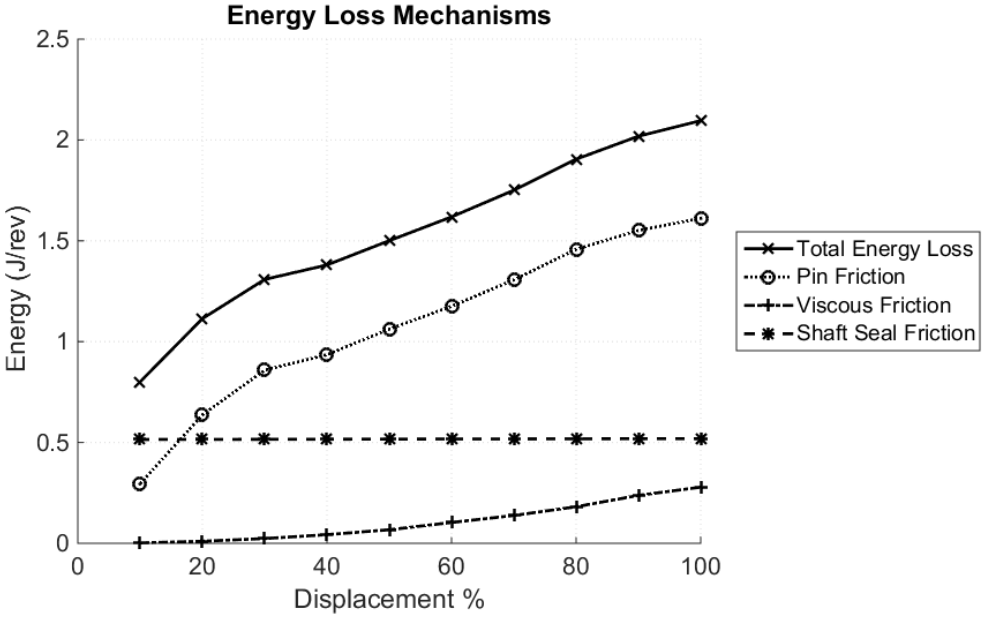

FIGURE 5.27 MODELED CONTRIBUTIONS TO ENERGY LOSS FOR 7MPA 100% DISPLACEMENT EXPERIMENT INCLUDEING SHAFT SEAL TORQUE

5.8 Conclusions

A three cylinder variable displacement linkage pump has been designed, optimized and constructed to evaluate the mechanical energy loss model presented in the previous chapter. A simple pump model was developed for capturing fluid end effects to prevent cavitation and large leakage rates. This simple model was coupled to the mechanical energy loss model as well as the kinematic model of chapters four and two. The solution rectification model of chapter three was used to prevent the evaluation of

infeasible mechanisms. These coupled models were implemented in a multi-objective evolutionary algorithm which optimized six pump parameters for six objective functions.

The optimization results were used to create a detailed design of the multi-cylinder prototype pump that was used to perform an experimental validation of the energy loss model. The model was able to accurately predict both the shaft torque and the input shaft work between 6W and 900W input power. Discrepancies were shown at low displacements.

Due to the single shear arrangement of the mechanism, out of plane forces caused deflection of coupler link and ultimately reduced the piston displacement. It was found that the fractional deflection increases rapidly as displacement was reduced below 40%. This ultimately results in a reduction of mechanism output and efficiency. Furthermore, these out of plane forces cause side loading at the joints which are reacted by aluminum bearing surfaces introducing increased frictional losses. These deflections were not observed in the single cylinder prototype. It is suggested that single shear designs be avoided for future variable displacement linkage pumps.

The model provided by the shaft seal manufacturer under predicted the shaft seal torque by approximately four times. A new torque coefficient was determined experimentally to accurately portray the energy loss associated with seal. The updated shaft seal energy loss was on the same order as the bearing friction and dominated the viscous friction energy loss. The shaft seal coefficient is the only experimentally determined parameter of the model. However, the associated loss is small, on the order of 1% if the shaft torque at 7MPa operating pressure, and is considered external to the

mechanism. As a result the shaft seal torque does not greatly affect the usefulness of the model during the design phase of the pump.

The pin friction energy loss was shown to be reduced by an order of magnitude by incorporating roller bearings as predicted giving the pump potential for high efficiency at low piston displacements. .

Chapter 6 Pressure Dynamics and Cylinder Modeling

6.1 Introduction

During a pumping cycle of a piston pump with passive valves, a piston is retracted to draw fluid into the pumping chamber through an inlet check valve, then, after the piston has fully retracted, its direction is reversed to discharge this fluid from the cylinder through an outlet check valve and into the pressurized system. The fluid that enters the system from the piston-cylinder is applied to a load and is then returned to the reservoir.

Over a single revolution of the input shaft, this process occurs for each pumping cylinder and their flows are combined at the outlet of the pump. Ideally, the amount of fluid drawn into a cylinder and subsequently discharged into the system is equal to volume swept by the piston. However, due to the compressibility of the fluid, leakage past the pumping piston, and valve dynamics, this is not the case.

Figure 6.1 is a depiction of the difference between the pressure-volume curve of a typical pumping cycle and the ideal case. The dashed line represents the pressure in the pumping chamber as a function of volume and the square box represents the ideal case. The difference between the two are the solid shapes whose combined area represents the volumetric energy potential lost over a pumping cycle. Much of this energy is recoverable through the pumping mechanism, but the energy output delivered to the load is reduced. The arrows around the curve show the cycle show the pumping cycle direction and the processes are labeled.

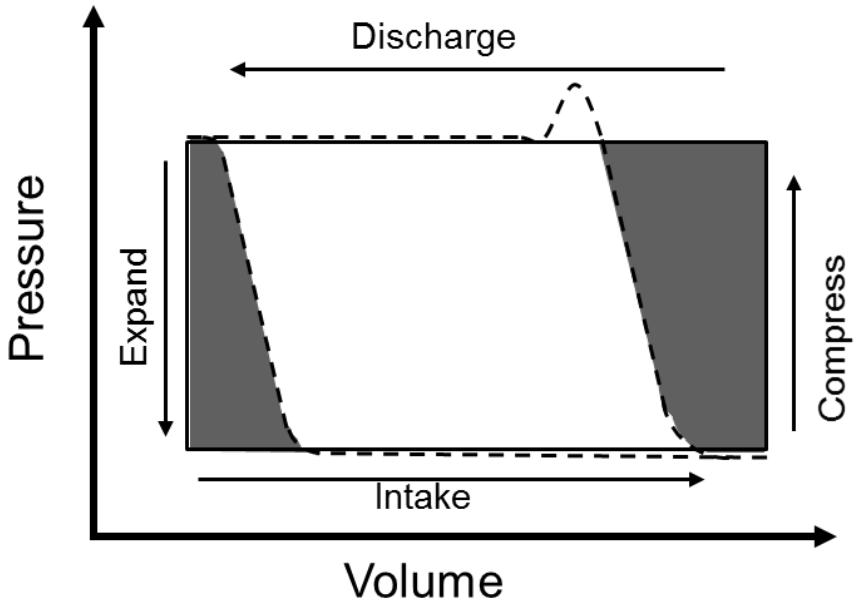

FIGURE 6.1 A TYPICAL PV CURVE FOR A PUMPING CHAMBER COMPARED TO THE IDEAL CASE

Additionally, the combined flows from the various pumping chambers do not result in a constant total flow. This variation in flowrate as fluid exits the pump is referred to as flow ripple. As a consequence of this varying flow, there is also a pressure pulsation in the system. It is generally desirable to minimize this ripple effect due to the resulting fluctuation of power at the load. The magnitude of this ripple is a direct result of the dynamics of the hydraulic pumping chamber. In order to predict and characterize the behavior of the linkage pump, these dynamics must be modeled.

In the previous chapter, a three cylinder prototype pump was designed, optimized, fabricated, and used for experimental validation of the mechanical models at higher pressure than the first prototype. The simple fluid mechanics model used to optimize the prototype assumed ideal behavior of both the valves and the working fluid. The

motivation of this chapter is to develop a model that captures the dynamics of the fluid in the piston chambers, the check valves, and the discharge line of the pump. In combination with the kinematic and mechanical models of chapters two and four, the models represent a complete understanding of the variable displacement linkage pump.

Much attention has been given to the pressure pulsations of gear, vane, and axial piston type pumps with active valves [62, 72, 98-102]. These models aren't readily applicable to the linkage pump as the dynamics created by active valves are different from those introduced by passive check valves.

A number of works have described the fluid behavior of triplex pumps including check valve dynamics. Johnston developed a lumped parameter model of a fixed displacement, three-cylinder crank-slider type pump with passive valves [103]. Singh and Madavan present a thorough analysis of reciprocating pump behavior that including check valve dynamics[73]. Shu Burrows and Edge developed a distributed parameter model of the transmission lines to predict pressure pulsations and suction line cavitation and compared the results to the lumped parameter model of Johnston [67, 71]. In all cases, a simple kinematic model of the pump is used as an input to the model. Additionally, none provide a model of the pressure dependent effective bulk modulus of the fluid volumes, and all rely on experimentally determined coefficients to describe flow forces on the valves. The primary objective of these works was to characterize the inlet and discharge line models of pumping systems employing reciprocating pumps, whereas the objective of this work is to characterize the pump itself.

Johnston and Edge go on further to describe check valve dynamics of poppet and disk type check valves[69, 70] however, only steady state flow forces are considered. Thorley gives a review of check valve behavior under transient conditions, but the work is limited to check valves in the hydraulic piping system [104]. Again, the majority of these works are dedicated to experimentally determining flow force coefficients. The purpose of this work is to develop a lumped parameter model of the pump having an arbitrary piston trajectory using no experimentally determined coefficients as to be more generally applicable.

In this chapter, the dynamic behavior of the various hydraulic flows are modeled and experimentally validated. In the second section, models of the pump control volumes and valves are developed and the third section describes experimental methods to validate the model. The fourth section presents the experimental results with the fifth section providing discussion. Finally, conclusions are given in the sixth section.

6.2 Modeling

The pumping head consists of the pumping cylinders, passive directional flow control valves (check valves), and a manifold that combines the flows from the cylinders and supplies them to the hydraulic circuit. A diagram of the modeled system is shown in Figure 6.2 with the modeled system enclosed in the dashed lines. Before modeling the components, two fundamental equations of fluid dynamics are discussed: orifice flow, and fluid compressibility.

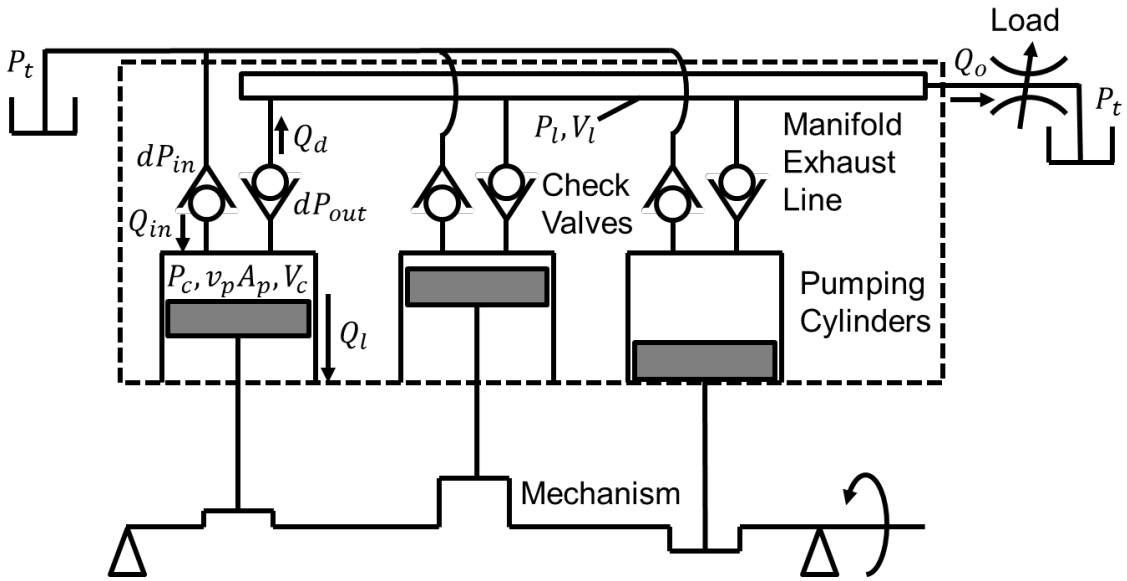

FIGURE 6.2 PUMP SCHEMATIC OUTLINING MODELED ELEMENTS

Orifice Flow

The flow across an orifice is dictated by the classic orifice equation:

$$Q_o = A_o C_d \sqrt{\frac{2}{\rho} \Delta P_o} \tag{6. 1}$$

Where Q_o is the flow through the orifice, A_o is the orifice area, C_d is the characteristic discharge coefficient, ρ is the fluid density, and ΔP_o is the pressure drop across the orifice. Typically, the discharge coefficient is experimentally determined. However, as a first estimate, the C_d of a sharp plate orifice (0.62) is used. The orifice equation is based on the Bernoulli equation which assumes steady, inviscid, incompressible, laminar flow. While this is not generally the case for hydraulic systems, these assumptions are regularly ignored in hydraulic circuit modeling in order to reduce computational complexity of system models [94].

Bulk Modulus

The compressibility of a hydraulic fluid is often described in terms of its reciprocal property, bulk modulus which is defined according to:

$$\beta = -V\frac{dP}{dV} \tag{6. 2}$$

The bulk modulus of liquids is pressure dependent. Additionally, if there is air in the hydraulic oil, an effective bulk modulus, B_{eff}, must be used which accounts for the air in the fluid.

Air exists in hydraulic systems in three main forms:

- ***Free Air*** – large pockets of air in the system.
- ***Entrained Air*** - Air in the form of tiny bubbles dispersed through the fluid itself
- ***Dissolved Air*** -Air stored in the empty molecular space of the fluid. As the air is in the intermolecular spaces, it does not have an effect on the effective bulk modulus of the fluid[39].

At a given pressure, air will dissolve into hydraulic fluid until a saturation point is met, as described by Henry's law[105]. If the pressure of this fluid drops below the saturation pressure, air will come out of solution and become entrained. This occurs regularly in pumping cylinders due to the drop in pressure as the fluid is drawn in. According to work by Zhou and Vacca [106], the rate of absorption of air in hydraulic oil is 20,000 times slower than the rate of dissolution. As a result, air that comes out of solution does not typically re-dissolve within the hydraulic circuit. Typically, free air can

be discharged from the system by bleeding the lines and cylinders and is not considered further.

There are a number of works that attempt to characterize the effective bulk modulus of hydraulic fluid with entrained air. Manring and Merrit present a model that sums the compressibility of the fluid, gas volume, and cylinder wall but does not account for the change in volume of the air as it is compressed [93, 94]. A number of more recent works account for these affects. An overview of these models and subsequent model comparison is given by Burton in [107] and [108] respectively. These works found that the models presented by Yu et. al.[109], Cho [110], and Nykanen [111] all collapsed to the same solution when all of the variables where made consistent. However, Yu et al. adds a "bubble variation" coefficient which has been shown to add considerable sensitivity to the model [112]. Ultimately, Burton and Van de Ven suggest the following model be used for the effective bulk modulus of hydraulic fluid undergoing compression:

$$\beta_{eff} = \frac{\left(\frac{P_0}{P}\right)^{\frac{1}{\gamma}} R_0 + (1 - R_0)}{\frac{R_0}{\gamma P}\left(\frac{P_o}{P}\right)^{\frac{1}{\gamma}} + \frac{1 - R_0}{\beta_0}} \tag{6. 3}$$

where R_0 is the volume fraction of entrained air $\left(\frac{v_g}{v_g + v_l}\right)$, β_0 is the bulk modulus of the pure liquid at atmospheric pressure, P_0, P is the current pressure of the fluid, and γ is the polytropic gas constant. The pumping process is considered adiabatic due to the fast

rate of compression, so γ is set equal to 1.4. It is not suggested that this model be used for expansion of the fluid because it does not account for air coming out of solution.

However, the dissolution of air can be prevented by maintaining the fluid pressure above the saturation pressure. This is accomplished by reducing the reservoir pressure as to draw air out of solution, exhausting the released air, sealing the reservoir, and re-pressurizing the degassed volume. If the pressure in the suction line does not drop below the pressure at which the fluid was degassed, more air will not come out of solution and the above model can be used for both compression and expansion of the fluid.

6.2.1 Cylinder Dynamics

In the pumping cylinder, a piston is retracted to draw fluid into the cylinder from the reservoir, and then the piston extends and discharges the fluid from the cylinder into the high outlet. The behavior of the fluid in the pumping cylinder, shown in Figure 6.3, is modeled as a compressible volume having a moving boundary, and multiple flow paths.

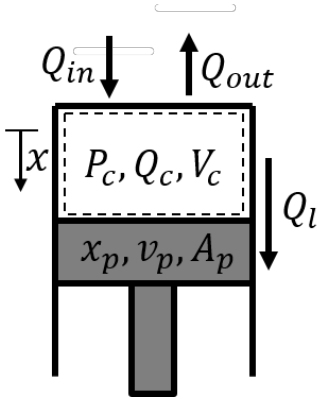

FIGURE 6.3 SCHEMATIC OF A PUMPING CYLINDER

The control volume is denoted by the dashed lines. Flow can pass into or out of the control volume through both the inlet valve, Q_{in}, and the outlet valve, Q_{out}.

Additionally, there is a leakage path between the piston and cylinder resulting in fluid exiting the control volume, Q_l. The moving boundary and cylinder volume is dictated by the piston position, x_p, and area, A_p. The piston position is referenced from the TDC position when the pumping chamber volume is at a minimum, V_{c_0}. This minimum volume of the pumping chamber is the unswept volume, commonly referred to as dead volume. From the definition of bulk modulus, the rate of change of pressure of the pumping cylinder can be described by:

$$\frac{dP_c}{dt} = \frac{\beta_{eff}}{V_c}\left(Q_{in} - Q_{out} - Q_l - v_p A_p\right) \tag{6. 4}$$

The cylinder volume, V_c, is found by:

$$V_c = A_p x_p + \mathrm{V_{c_0}} \tag{6. 5}$$

The piston cylinder leakage rate is found by assuming laminar Couette flow in the piston-cylinder clearance seal according to:

$$\mathrm{Q_l} = \frac{\pi d_p (P_c - P_0) h^3}{12 \mu_d l_p} \tag{6. 6}$$

where d_p is the piston diameter, P_0 is the pump case pressure which is vented to atmosphere, h is the piston cylinder gap height, μ_d is the dynamic viscosity of the fluid, and l_p is the length of the piston cylinder interface. In some pumps, l_p is a function of piston position. However, for the pump used here, l_p is constant. Note that the leakage rate is a function of the cube of the gap height. As a result, this dimension is critical to

performance. The cylinder pressure is found by numerical integration of Eqn. (6. 4) according to:

$$P_c = P_{c0} + \frac{dP_c}{dt}\Delta t \tag{6. 7}$$

The only unknowns in this system of equations are the flow rates through the check valves: Q_{in} and Q_{out}. In order to determine these values, the check valve model is now presented.

6.2.2 Check Valves Dynamics

A check valve is flow control device which allows fluid to pass in one direction but prevents flow in the reverse direction. This is accomplished by using a spring to seat a sealing element, a poppet in this case, against an orifice. If there is a force differential across the poppet that acts to open the valve and overcomes the spring force, the poppet will unseat, allowing flow to travel through the valve.

Typically, this initial opening is created by a pressure differential across the poppet. The valve is held open by a combination of flow forces and the pressure differential created as fluid passes through the valve orifice. If these forces cannot overcome the spring force acting on the poppet, it will begin to reseat. This occurs when the flow reduces to some low level or changes direction. When the valve is completely seated, reverse flow is prevented. However, as the valve transitions from open to closed, reverse flow can occur.

Typically this reversing through the valve is unwanted. In the pumping cylinder, reverse flow through the check valves results in reduced volumetric efficiency. It is therefore critical to characterize the check valves to determine the pumps performance. In this section the check valve motion and dynamic behavior are modeled. First, the equations of motion are described, then the steady and transient flow forces are modeled, and finally the complete force balance equations are presented.

6.2.2.1 Dynamic System

The check valves are modeled as a spring mass damper system where the poppet is a mass acted on by external forces as seen in Figure 6.4.

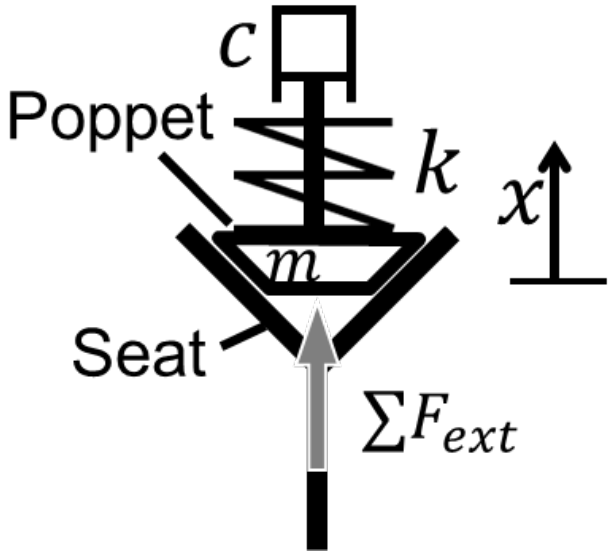

FIGURE 6.4 CHECK VALVE SPRING MASS DAMPER SYSTEM

The poppet motion is derived from Newton's second law. The forces on the poppet are described by:

$$\sum F_{ext} = m\ddot{x} + c\dot{x} + k(x + x_{pre}) \tag{6. 8}$$

where $\sum F_{ext}$ is the sum of the external forces applied to the poppet, c is the damping coefficient, k is the spring rate, m is the poppet mass, and x_{pre} is the preload compression length of the spring. By rearranging Eqn (6. 8) the poppet acceleration can be found by:

$$\ddot{x} = \frac{\sum F_{ext} - c\dot{x} - kx}{m} \tag{6. 9}$$

In the physical system, the poppet position is limited by the valve seat ($x = 0$) and a hard stop setting the maximum opening position ($x = x_{max}$). The model neglects poppet bounce and assumes these surfaces have infinite damping. The limits are imposed according to:

$$\begin{aligned} x < x_0, \quad & (x = x_0, v = 0) \\ x > x_{max}, \quad & (x = x_{max}, v = 0) \end{aligned} \tag{6. 10}$$

Using these equations, the poppet motion can be found as a function of the external forces. In the next section, the external flow forces acting on the poppet are found.

6.2.2.2 Flow and Pressure Forces

As fluid passes through the valve, the flow changes both speed and direction as a result of the valve geometry. Because the fluid has mass, there is a change in momentum, which results in net force acting on the poppet. These forces are referred to as flow forces. Additionally, the fluid experiences a pressure drop as it passes through the valve orifice area, resulting in a pressure differential across the valve, and thus a net force. These forces are referred to as pressure forces. The flow and pressure forces as they are applied disk style check are now described.

The valve used in the pump is a disk style check valve having a nose cone angle. The critical dimensions of the valve, shown in Figure 6.5 are described here:

A_1 and D_1 are the area and diameter of the valve inlet, L is the inertial length of the valve inlet, θ is the poppet nose cone angle, A_2 and D_2 are the overall area and diameter of the poppet itself. The pressure drop across the valve, ΔP is the inlet pressure minus the outlet pressure, $P_1 - P_2$. Note that ΔP is always positive for the calculations in this section. The sign convention of the flow and force direction will be discussed later in this section. The flow forces model in this section follows the general approach outlined by Manring for poppet valves [94].

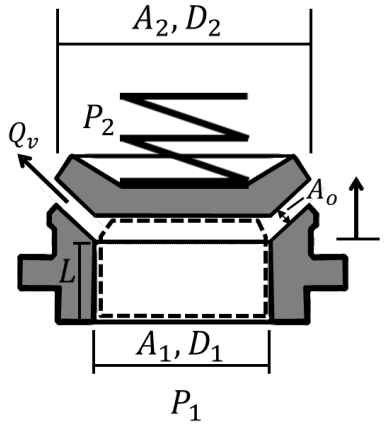

FIGURE 6.5 DIAGRAM OF DISK STYLE CHECK VALVE USED IN THE PUMPING CHAMBER SHOWING CRITICAL DIMENSIONS

The Reynolds transport theorem is used to derive the flow forces with regards to the valve control volume shown in Figure 6.6 where F_x and F_y are the forces as they are applied to the control volume, and Q_v is the flow passing through the volume.

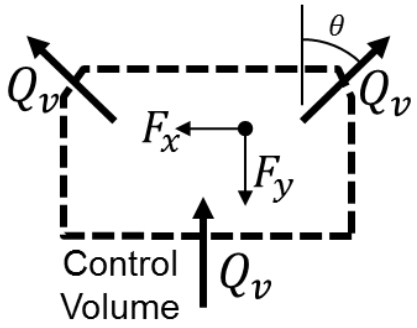

FIGURE 6.6 CONTROL VOLUME FOR DETERMINING POPPET FLOW FORCES

Conservation of momentum for the control volume is described by:

$$\boldsymbol{F} = \frac{\partial}{\partial t}\int_{cv} \rho \boldsymbol{u} dV + \int_{cs} \rho \mathbf{u}(\boldsymbol{u} \cdot \hat{\boldsymbol{n}}) dA \tag{6. 11}$$

where $\boldsymbol{F}$ is the force vector acting on the control volume, ρ is the fluid density, $\boldsymbol{u}$ is the fluid velocity vector, and $\hat{\boldsymbol{n}}$ is a unit vector pointing normally outward from the dashed control surface. It can be shown that the flow forces in the x direction are balanced, so only forces in the vertical, y, direction will be considered further.

The first integral of Eqn. (6. 11) describes the fluid moment effects inside the control volume itself, whereas the second integral describes the momentum crossing the control surface. These terms are referred to as the transient and steady state flow forces respectively which are now derived.

Integrating the transient flow force term of Eqn. (6. 11), the following is obtained:

$$F_t = \frac{\partial}{\partial t}\int_{cv} \rho u dV = \rho L \frac{\partial Q}{\partial t} \tag{6. 12}$$

where F_t is the transient flow force in the y direction. Doing the same for the steady state term, the following is obtained:

$$F_{steady} = \int_{cs} \rho u(u \cdot \hat{\boldsymbol{j}}) dA = \rho \frac{Q_v^2}{A_o} \cos(\theta) + \rho \frac{Q_v^2}{A_1} \tag{6.13}$$

The sum of the forces in the y direction are then:

$$F_y = \rho L \frac{\partial Q}{\partial t} + \rho \frac{Q_v^2}{A_o} \cos(\theta) + \rho \frac{Q_v^2}{A_1} \tag{6.14}$$

The flow through the valve, Q_v, is dictated by the orifice equation presented earlier and is reproduced for the valve here for convenience:

$$Q_v = A_o C_d \sqrt{\frac{2}{\rho} \Delta P} \tag{6.15}$$

The orifice area, A_0, is the area of a cone as a function of D_1 and x. This area is developed from geometry and is described as:

$$A_o = \pi [D_1 \sin(\theta)\, x - \cos(\theta) \sin^2(\theta) x^2] \tag{6.16}$$

In the case of the check valves used for the pump, $x_{max} \approx .001m$ resulting in x being at least 1000 times greater than x^2, allowing the area to be approximated by:

$$A_o = \pi D_1 \sin(\theta)\, x \tag{6.17}$$

Now by inserting Eqn. (6.17) into (6.15) and subsequently into Eqn. (6.13), the steady state flow force can be solved explicitly as shown in Eqn. (6.18).

$$F_{steady} = \frac{2\rho A_o^2 C_d^2 \Delta P}{\rho A_o}\cos(\theta) + \frac{2\rho A_o^2 C_d^2 \Delta P}{\rho A_1} \tag{6.18}$$

Combining terms and simplifying results in the following:

$$\begin{aligned} F_{steady} &= 2A_o C_d^2 \Delta P cos(\theta) + \frac{2A_o^2 C_d^2 \Delta P}{A_1} \\ &= 2A_o C_d^2 \left(\frac{A_o}{A_1} + \cos(\theta)\right)\Delta P \end{aligned} \tag{6.19}$$

In order to solve the transient flow forces, the partial derivative of the flow rate Q_v with respect to time must be evaluated. Because the poppet position and pressure drop across the valve are a function of time, the product rule is used to solve the derivative as shown in Eqns. (6.20) and (6.21).

$$\frac{\partial Q}{\partial t} = \frac{\partial}{\partial t}\left(\pi D_1 \sin\theta \, x C_d \sqrt{\frac{2}{rho}\Delta P}\right) = \frac{\partial Q}{\partial x}\frac{\partial x}{\partial t} + \frac{\partial Q}{\partial P}\frac{\partial P}{\partial t} \tag{6.20}$$

$$\frac{\partial Q}{\partial x}\frac{\partial x}{\partial t} + \frac{\partial Q}{\partial P}\frac{\partial P}{\partial t} = \pi D_1 \sin\theta \, C_d \sqrt{\frac{2}{rho}\Delta P}\,\dot{x} + \frac{\pi D_1 \sin(\theta)\, x C_d}{\sqrt{2\rho\Delta P}}\dot{P} \tag{6.21}$$

In order to simplify presentation, the constants of the two terms of Egn (6.21) are lumped together as the constants K_q and K_c respectively according to the following:

$$K_q = \pi D_1 \sin(\theta)\, C_d \sqrt{\frac{2}{rho}\Delta P} \tag{6.22}$$

$$K_c = \frac{\pi D_1 \sin(\theta)\, x C_d}{\sqrt{2\rho\Delta P}} \tag{6.23}$$

Where K_q is referred to as the flow gain and K_c is the pressure flow coefficient. The transient flow force F_t is then:

$$F_t = \rho L \frac{\partial Q}{\partial t} = \rho L K_q \dot{x} + \rho L K_c \dot{P} \tag{6.24}$$

The pressure force on the poppet is simply:

$$F_{Pr} = A_2 \Delta P \tag{6.25}$$

Note that when the valve is fully closed there is an area differential between the base of the poppet exposed to A_1 and the top of the poppet, A_2. However, this difference is small and has no effect the instant the valve opens so is neglected here.

6.2.2.2.1 Sign Convention

As mentioned earlier in the chapter, all of the pressure and flow force equations take ΔP to be a positive value as to prevent taking the square root of a negative value. The flow direction of the orifice equation is found by multiplying Q_o by $sign(\Delta P)$. In

this convention, positive flow is considered flow from the inlet to the outlet. The pressure force acting on the poppet is the same direction as the flow.

Conservation of momentum dictates that the steady state flow force F_{steady} always acts to close the valve regardless of the flow direction. While this may seem counterintuitive the following explanation is given with reference to Figure 6.7. Here the flow lines though the valve are represented by the double sided arrow. The arrow points in either direction so show that flow can occur in either direction. F_x and F_y are the steady state flow forces as they act on the poppet. From this figure, it can be seen that the direction of these forces does not change depending on flow direction. In order to conserve momentum, the reaction force of the poppet onto the control volume is in the negative direction acting to close the valve. As mentioned previously, the force in the x direction is balanced by the mirrored force on the opposite side of the poppet.

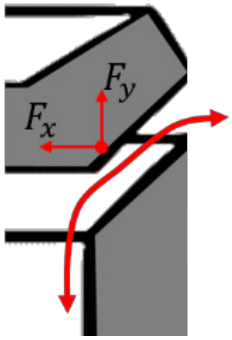

FIGURE 6.7 STEADY STATE FLOW FORCES AS THEY ACT ON THE CONTROL VOLUME

In contrast, the transient flow force, F_t, can act to either close or open the valve because it is a function of the rate of change of momentum. To conserve the direction, the transient flow force is multiplied by the sign(Δ P).Total External Forces

The sum of the external forces on the poppet can now be found by:

$$\sum F_{ext} = -F_t sign(\Delta P) - F_{steady} + F_{Pr} sign(\Delta P) \tag{6.26}$$

By substituting this result into Egn (6. 9), the poppet acceleration can be found according to:

$$\ddot{x} = \frac{-F_t sign(\Delta P) - F_{steady} + F_{Pr} sign(\Delta P) - c\dot{x} - k(x_{pre} + x)}{m} \tag{6. 27}$$

However, the spring damping term, c, can be considered negligible compared to the damping term of the transient force, $\rho L K_q$, and is neglected here resulting in the following:

$$\ddot{x} = \frac{-F_t sign(\Delta P) - F_{steady} + F_{Pr} sign(\Delta P) - kx}{m} \tag{6.28}$$

Finally, the total flow through the valve, as applied to the pumping cylinder in Eqn. (6. 4) or manifold discharge line, can be found summing the flow through the valve and the poppet displacement itself according to:

$$Q = Q_v + vA_2 \tag{6.29}$$

where v is the poppet velocity found by integration of Eqn. (6.28). Over a course of a pumping cycle, the poppet flow term integrates to zero, but has an effect on the instantaneous state of the system.

6.2.3 Manifold

The manifold is where the flow from each of the pumping cylinders are combined and then delivered to a load. The control volume has a fixed boundary with flows entering through the outlet check valves, Q_d, and exiting through the load, Q_o, which, in this case, is a relief valve. The inertial effects of the manifold are neglected as they are a function of the fluid channel length over the area, and the manifold is relatively short for the cross-sectional area. This is a similar system to the pumping cylinder but is simpler in that the control volume boundaries are constant. Figure 6.8 depicts the modeled system with the control volume depicted as the solid outlined tube.

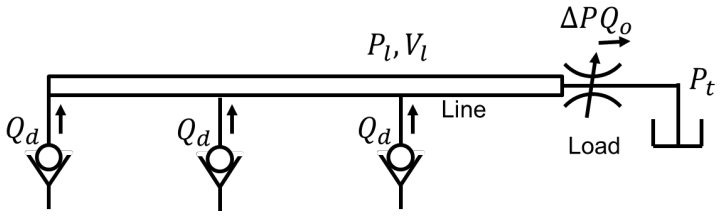

FIGURE 6.8 HYDRAULIC MANIFOLD OUTLET LINE CONNECTED TO SYSTEM

The flow exiting the control volume is dictated by the orifice equation reproduced here:

$$Q_0 = C_d A_r \sqrt{\frac{(P_l - P_t)\rho}{2}} \tag{6.30}$$

The rate of change of pressure in the line can then be found according to:

$$\frac{dP_l}{dt} = \frac{\beta_{eff}}{V_l}\left(\sum_{1}^{n} \sum Q_{d,i} - Q_o\right)dt \tag{6.31}$$

where P_l is the line pressure, V_l, is the constant line volume, n, is the number of cylinders, and $Q_{d,i}$ is the flow through the outlet check valve of cylinder i according to Eqn. (6.29). Note that this value can be positive or negative depending on the valve dynamics.

With the manifold pressure and flowrate found, the model of the fluid end of the pump is complete. In the next section, the experimental system is used to validate the model.

6.3 Experimental Validation

The fluid end model is validated using the three cylinder variable displacement linkage pump described in chapter five. The pump is driven by a variable speed electric motor and draws hydraulic oil from a pressurized reservoir, and exhausts it to a pressurized system. The discharge pressure is controlled using a relief valve which acts as a load. A diagram of the experimental circuit is provided in Figure 6.9.

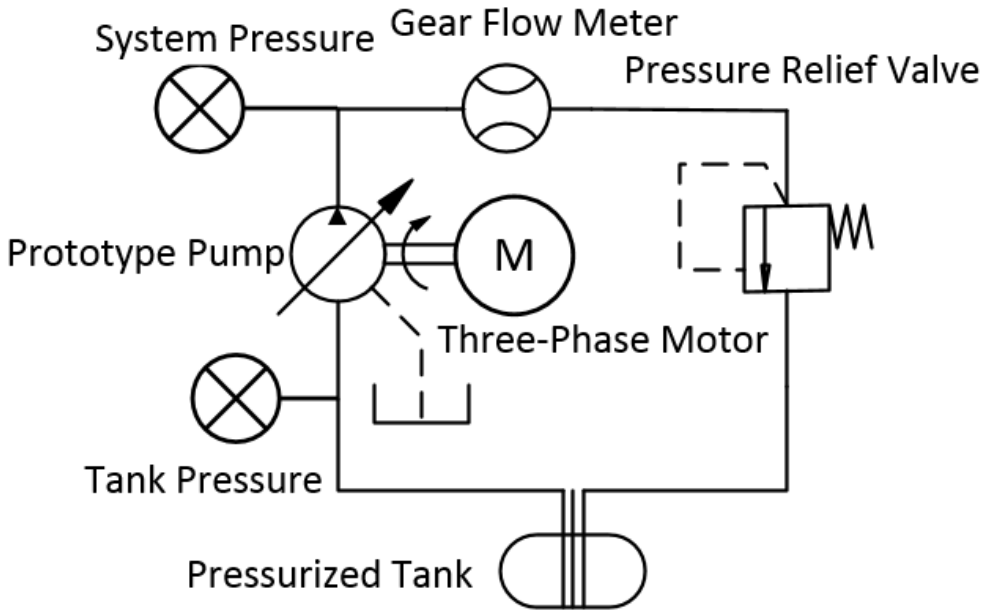

FIGURE 6.9 HYDRAULIC CIRCUIT DEPICTING THE EXPERIMENTAL SETUP USED FOR MODEL VALIDATION AND THE PRIMARY COMPONENTS USED

The pump provides a variable piston trajectory. The electric motor allows variation in operating frequency, and the relief valve allows for variation in operating pressure. The reservoir is pre-charged to 220 kPa (30psi) as to prevent cavitation in the suction line.

The piston position is measured by placing a magnet on the piston and using a linear field sensor to determine the field strength. The sensor output is then a function of relative position. This allows for the simultaneous measurement of the three piston trajectories. The pressure of each cylinder, the reservoir, and system are measured with sealed gauge pressure transducers. Additionally, a gear flow meter is used to measure the flow rate from the pump. However, this meter can only provide an average flow rate

rather than an instantaneous measurement. The reservoir pressure, measured at the manifold, and the piston trajectories are used as inputs to the model. The load is estimated from the measured mean system pressure and flowrate. The cylinder pressure, and system pressure time histories are used for model validation.

6.3.1 Test Conditions

In order to demonstrate the generality of the model, the performance is evaluated for three test conditions: 7 MPa at 25% displacement, 10 MPa at 50% displacement, and 15 MPa at 100% displacement. This provides a wide range of input parameters to the model. The measured piston trajectories, used as an input to the model, and are shown in Figure 6.10. The piston trajectory is presented as the piston position normalized by the maximum stroke of 11.2mm. All experiments are conducted at a pump operating frequency of 10 Hz.

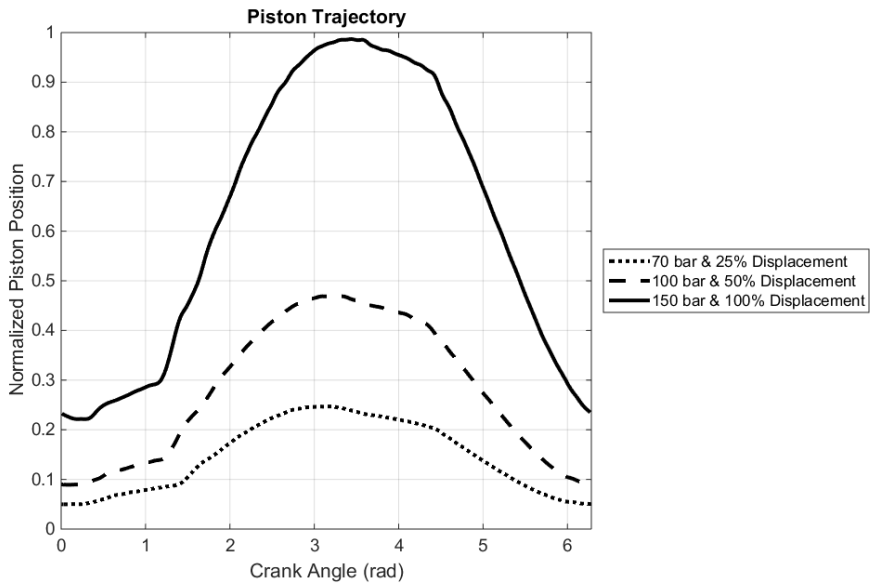

FIGURE 6.10 PISTON TRAJECTORIES USED FOR MODEL VALIDATION

A model representation of the actual pumping head is depicted in Figure 6.11 for reference. The control volume is outlined by the dashed lines. Here, the piston is shown at top dead center with the discharge valve open and intake valve closed. The valves are installed from the top of the manifold which is then sealed using a plug. The sealing cylinder is to the far left of the image. Since the cylinder in this design is also used as a crosshead bearing, a pocket is included in the manifold for lubrication purposes. Since the clearance between the manifold and the piston is large, these pockets are included in the unswept volume estimate. Critical dimensions of the pumping chamber, valves, and manifold are included in Table 6.1.

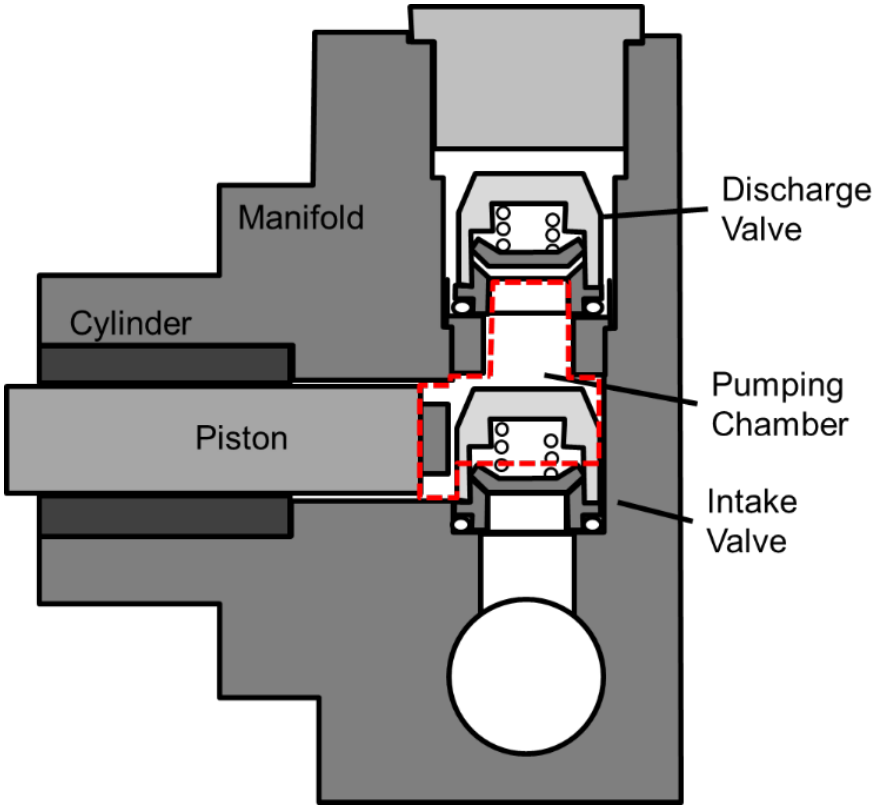

FIGURE 6.11 SCHEMATIC REPRESENTATION OF THE PUMPING CYLINDER DEPICTING ACTUAL GEOMETRY FROM MACHINED PARTS

TABLE 6.1 CRITICAL DIMENTIONS OF PHYSICAL COMPONENTS IN MODEL

Variable	Description	Value
d_p	Piston diameter (mm)	16 (measured)
l_p	Piston cylinder interface length (mm)	28 (measured)
h	Piston cylinder gap height (micron)	6.4 (measured)
D_1	Check valve inlet diameter (mm)	10.5 (measured)
D_2	Check valve disk diameter (mm)	15.1 (measured)
θ	Check valve nose angle (degree)	45 (measured)
m	Check valve disk mass (gram)	02 (measured)
x_{pre}	Check valve preload compression length (mm)	3.02 (measured)
x_{max}	Check valve maximum disk displacement (mm)	1.03 (measured)
k	Check valve spring rate (N/m)	121.3 (measured)
L	Check valve inertial length (mm)	5.25 (measured)
V_l	Manifold line volume (cm^3)	140 (from CAD)
V_{c_0}	Unswept pumping chamber volume (cm^3)	14 (from CAD)

In these experiments, the working fluid is Mobile DTE 25 hydraulic fluid. All coefficients used in the model are either fluid properties available from the manufacturer, or measured values readily available in literature. Table 6.2 gives the coefficients used in the model for comparison to the experiment.

The only coefficient in the table which is derived from empirical data is the orifice discharge coefficient. However, this value is regularly assumed to be equivalent to the value for a sharp edged orifice when empirical data is unavailable. Additionally, this assumption has been validated for poppet valves with a nose cone angle of 45° by Stone [113].

TABLE 6.2 COEFFICENTS USED FOR MODEL COMPARISON TO EXPERIMENT

Coefficient	Description	Value
$\boldsymbol{\beta_0}$	Bulk Modulus of pure hydraulic fluid (Pa)	1.8e9
$\boldsymbol{\rho}$	Density of pure hydraulic fluid (kg/m^3)	870
$\boldsymbol{\mu_d}$	Dynamic viscosity of hydraulic fluid at 22°C (Pa s)	.087
$\boldsymbol{\gamma}$	Polytropic gas constant (adiabatic)	1.4
$\boldsymbol{R_0}$	Volumetric fraction of entrained air	.002
$\boldsymbol{C_d}$	Orifice discharge coefficient	0.62
$\boldsymbol{P_0}$	Atmospheric pressure (Pa)	101e3

6.3.2 Procedure

Data is collecting according to the following procedure:

1) The pump shaft speed is set to 10 Hz using the variable frequency drive controller.
2) The system pressure is set to 3MPa using the adjustment on the pressure relief valve
3) The displacement is set to the desired value using the manual control.
4) The system pressure is set to the desired value using the adjustment on the pressure relief valve.
5) Data is collected such that 1000 points are collected per shaft revolution for 14 revolutions
6) The first and last two rotations are removed from the dataset for a total of 10 complete cycles measured.
7) The oil temperature is monitored throughout experimentation so that data is only collected at oil temperatures between 22 and 23° C

A list of the transducers used and their measurements are included in Table 6.3.

TABLE 6.3 SENSORS USED FOR EXPERIMENTATION

Measurement	Sensor
Flow Rate	AW gear flow meter JVA-20KG
Shaft Position	US Digital Optical Encoder 1024 ppr
Piston Position	Allegro Microsystems A1302KUA-T Linear Hall Field Sensor
Cylinder/System Pressure	Honeywell MLH-03K-P-S-B-06-A Pressure Transducer
Inlet Pressure	Measurement Specialties U7139-050PA-5W Pressure Transducer
Temperature	AEM k-type thermocouple amplifier

6.3.3 Numerical Simulation

The piston position and inlet pressure data at each time step, in addition to the average system pressure and flowrate, are used as inputs to the model. The piston velocity is found by numerical differentiation of the position data to determine the rate of change of pumping chamber volume. The data are imported into the simulation using cubic interpolation to make the experimental and simulated time steps independent of each other. The system of ODEs are numerically integrated using the Euler method with a time step of 0.1 ms. The system of equations was programmed in matlab and then compiled into a mex file in order to reduce runtime. The model begins with the pump at a stationary state so all initial conditions are set accordingly. The numerical simulation reaches cyclic steady-state within four cycles of the ten cycles of experimental input data.

Shaft position is measured using the encoder and these data are used to define the cycle start and endpoints. After each cycle of the simulation, the average modeled system pressure is evaluated and compared to the experimental value. Additionally, the modeled cylinder pressure at the beginning of the cycle is compared to the value at the end. The

relief valve orifice area of Eqn. (6.30) is adjusted to allow the pressure at the beginning and the end of the cycle to converge. The model is considered at cyclic steady state when the average system pressure of the model is within 1% of the experiment, and the cylinder pressure of each cylinder at the beginning of the cycle is within 1% of the end.

6.4 Results

The modeled and experimentally measured PV curves for the three test conditions are shown in Figure 6.12 through Figure 6.14. These data are from the central cylinder of the pump. The measured and simulated system pressure as a function of crank angle are shown in Figure 6.15 through Figure 6.17.

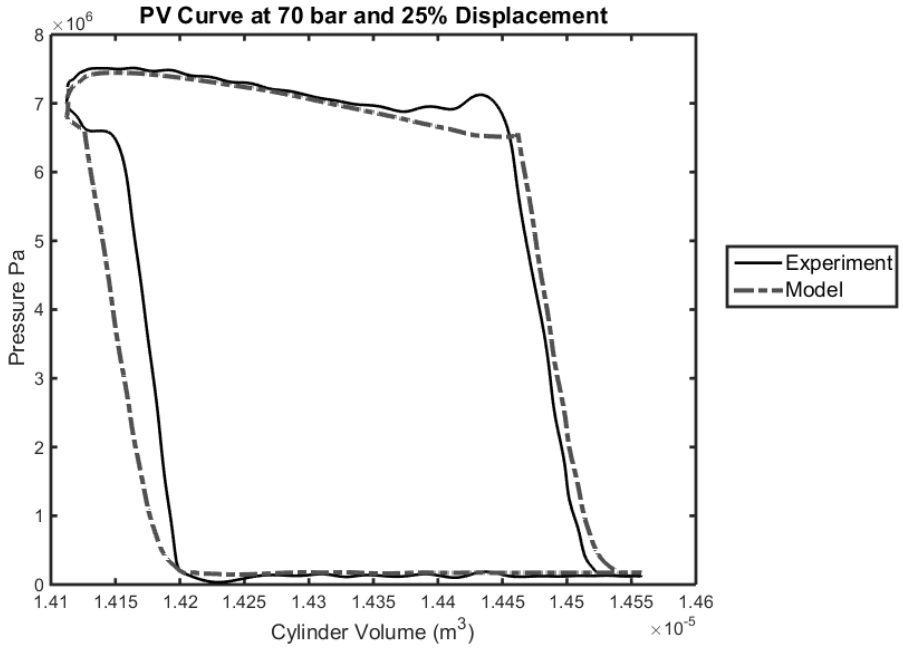

FIGURE 6.12 PV CURVE COMPARING MODEL TO EXPERIMENTAL RESULTS MEASURED AT 70 BAR AND 25% DISPLACEMENT

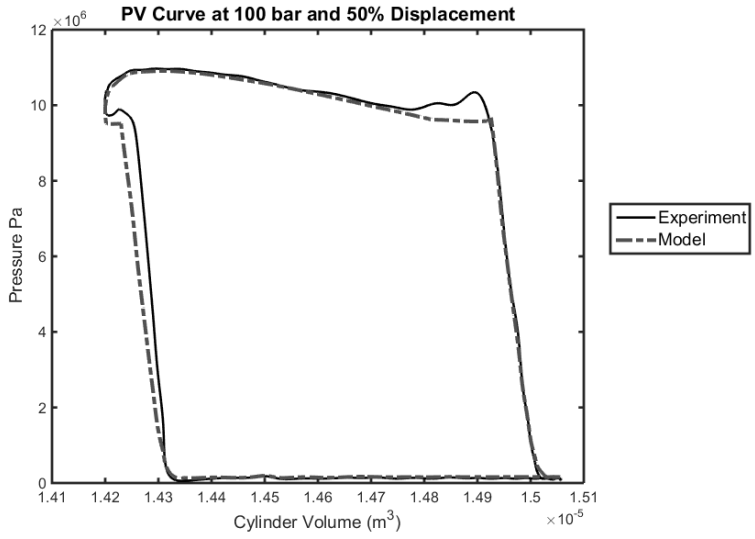

FIGURE 6.13 PV CURVE COMPARING MODEL TO EXPERIMENTAL RESULTS MEASURED AT 100 BAR AND 50% DISPLACEMENT

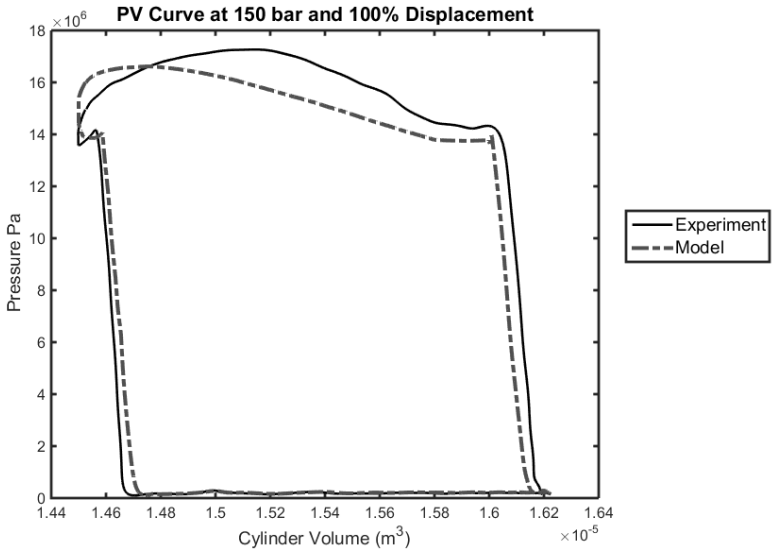

FIGURE 6.14 PV CURVE COMPARING MODEL TO EXPERIMENTAL RESULTS MEASURED AT 70 BAR AND 25% DISPLACEMENT

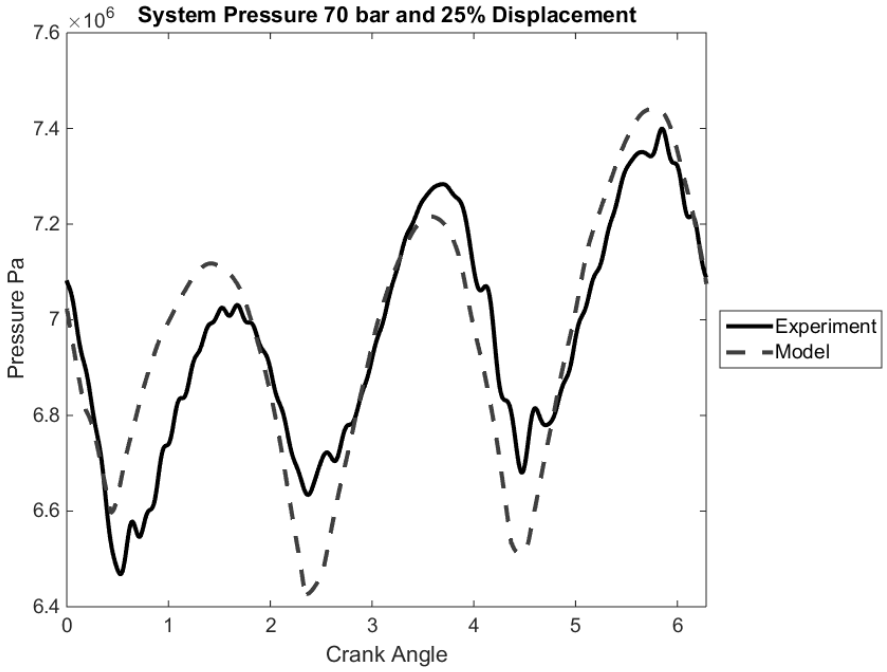

FIGURE 6.15 SYSTEM PRESSURE PLOT COMPARING MODEL TO EXPERIMENTAL RESULTS MEASURED AT 70 BAR AND 25% DISPLACEMENT

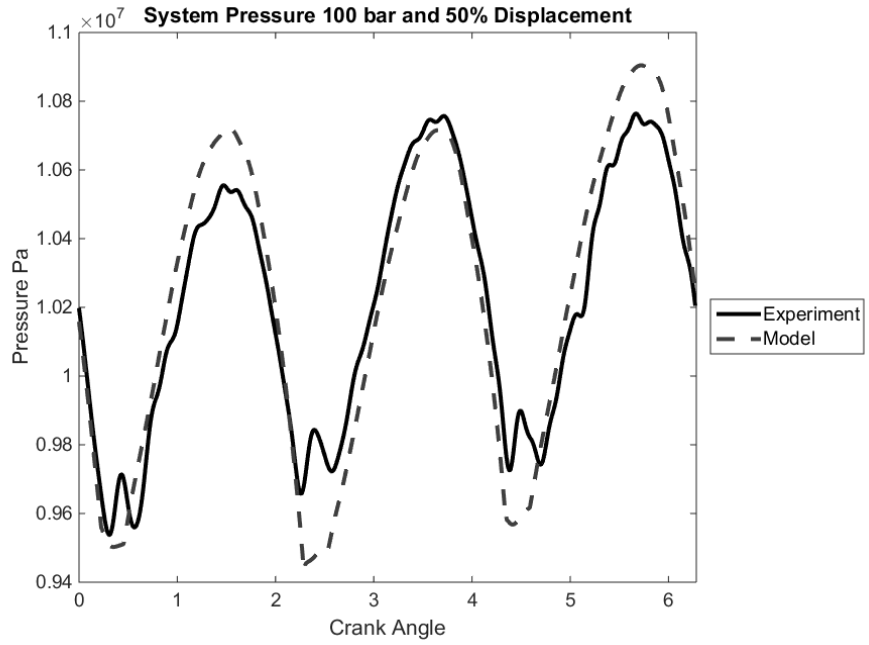

FIGURE 6.16 SYSTEM PRESSURE PLOT COMPARING MODEL TO EXPERIMENTAL RESULTS MEASURED AT 100 BAR AND 50% DISPLACEMENT

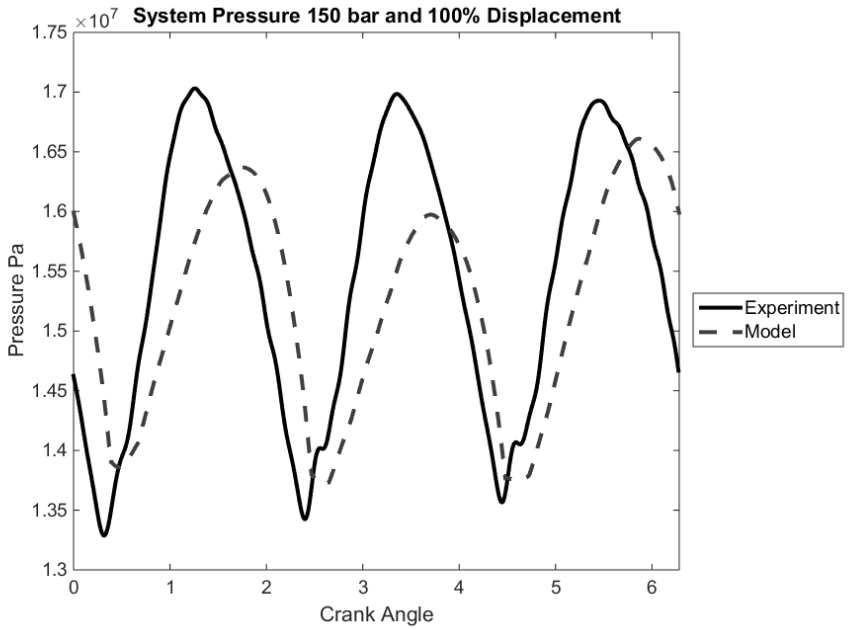

FIGURE 6.17 SYSTEM PRESSURE PLOT COMPARING MODEL TO EXPERIMENTAL RESULTS MEASURED AT 150 BAR AND 100% DISPLACEMENT

6.5 Discussion

Despite having a wide range of operating conditions, the model is able to predict experimental data fairly well for the presented cases. The largest discrepancies have to do with the closing of the discharge check valve, which occurs at the top left corner of the PV curves. Additionally, the model is not able to predict well the opening action of the discharge valve which occurs on the top right corner of the PV curves. It would seem that the model expects the valve to open almost instantly, while in reality, the valve opens slowly resulting in the initial overshoot of cylinder pressure. This discrepancy could be a result of valve sticktion which is not modeled. The sticktion force, which can be envisioned as the force to separate two sheets of glass separated with a thin liquid layer,

is inversely proportional to the cube of the gap between the poppet and its seat. This inverse cube relationship requires a minimum gap height that is challenging to accurately predict. Additionally, as soon as the valve starts to open, the sticktion force drops quickly off to zero. The effect seems to be minimal, and the evaluation arbitrary, so the added complexity does not seem justified.

Close agreement between predicted and measured system pressure is observed as well. The ripple in the experimental pressure can be attributed to the dynamics introduced by the gears of the flow meter. Additionally, the load in the system is modeled by a simple orifice, but in the experimental system a pilot operated relief valve is used. The relief valve is not explicitly modeled because not enough is known about the internal dimensions to accurately predict its behavior and considered out of the scope of the presented model. However, this valve will certainly introduce its own dynamics to the system and could also be the cause for the overshoot of the measured cylinder pressure.

However, the model captures the inlet dynamics and the fluid compression and expansion rates well. During these periods of operation, the inlet pressure is measured during fluid intake, and the pumping chamber is isolated from external influences during compression and expansion of the fluid. As a result, the boundary conditions of the model are well defined.

6.6 Conclusions

In this chapter, a dynamic model of the fluid mechanics of a passive pumping system has been developed. This model uses an arbitrary piston trajectory as an input,

making it generally applicable. The model captures the pressure dynamics of the pumping cylinder and discharge line, as well as the check valve behavior. These effects are critical for evaluating the pumps performance. The pressure dynamics have a direct influence on the loading of the mechanism. The valve dynamics aid in the prediction of reverse flows and understanding of the volumetric efficiency of the pump.

Close agreement has been shown between model and experimental results across a wide range of operating conditions. The experimental results show that the check valves permit a significant amount of reverse flow, reducing the volumetric efficiency. This reverse flow is not considered an energy loss, but results in decreased output of the pump. More work is needed to develop valves which perform well over a wider range of operating conditions.

One of the primary advantages of this model is that it does not use any empirical coefficients. All coefficients used are readily available in the literature, or are measurable properties of the pumping fluid itself. As a result, the model can be applied during the design phase of a pump allowing for optimization of dynamic pumping characteristics such as flow or pressure ripple. Another advantage is that the lumped parameter model can be evaluated quickly. With a time step as small as 0.1 ms, the Euler solver runs within five seconds on a 2.3 GHz Intel Core-i5 processor. Such a short time step is not required if experimental data is not used as the input to the model.

The optimization of the previous chapter considered the pumping behavior of the cylinders to be ideal because the pressure dynamics were not well understood. This

model provides a means of determining a realistic load to be applied to the mechanical model for more realistic optimization and simulations.

Chapter 7 Conclusions and Future Work

7.1 Thesis Review

In this thesis, a variable displacement linkage hydraulic pump was developed from mechanisms synthesis to modeling to the evaluation of a three cylinder prototype. Chapter two described the synthesis of an adjustable sixbar mechanism with a crank input and a variable stroke slider output. The described mechanism is adjusted by a movable ground pivot rather than adjusting a moving link, and is adjustable to zero stroke of the slider while maintaining constant top dead center. The synthesis process was augmented by a solution rectification technique, developed in chapter three, for the output slider dyad that limits the domain of the solution space to constructible mechanisms. Chapter four presented a mechanical energy loss model, taking into account both internal friction in the mechanism and external friction introduced by auxiliary components. A single cylinder prototype was introduced to validate the model at low powers, which used plain bearings in the revolute joints. A multi-cylinder prototype incorporating roller bearings in the joints was presented in chapter five as a demonstration of the design and optimization process, including a coupling of models to improve pumping performance. Chapter seven presented a dynamic model of the hydraulic end of the pump, creating an accurate prediction of the pumping behavior as demonstrated by comparison of the model and experimental data.

By combining these validated models, a comparison can be made between the proposed pump and a typical axial piston pump. Figure 7.1 presents the predicted efficiency of the variable displacement linkage pump described in Chapter 6 according to

the presented models without out-of-plane deflection as a function of fractional displacement as compared to that of a typical axial piston pump. The typical pump curve is developed from the Mcandlish and Dorey model of [13] with coefficients developed from experimental data which are presented in Table 7.1. There is a clear benefit to the variable displacement linkage pump with regards to efficiency.

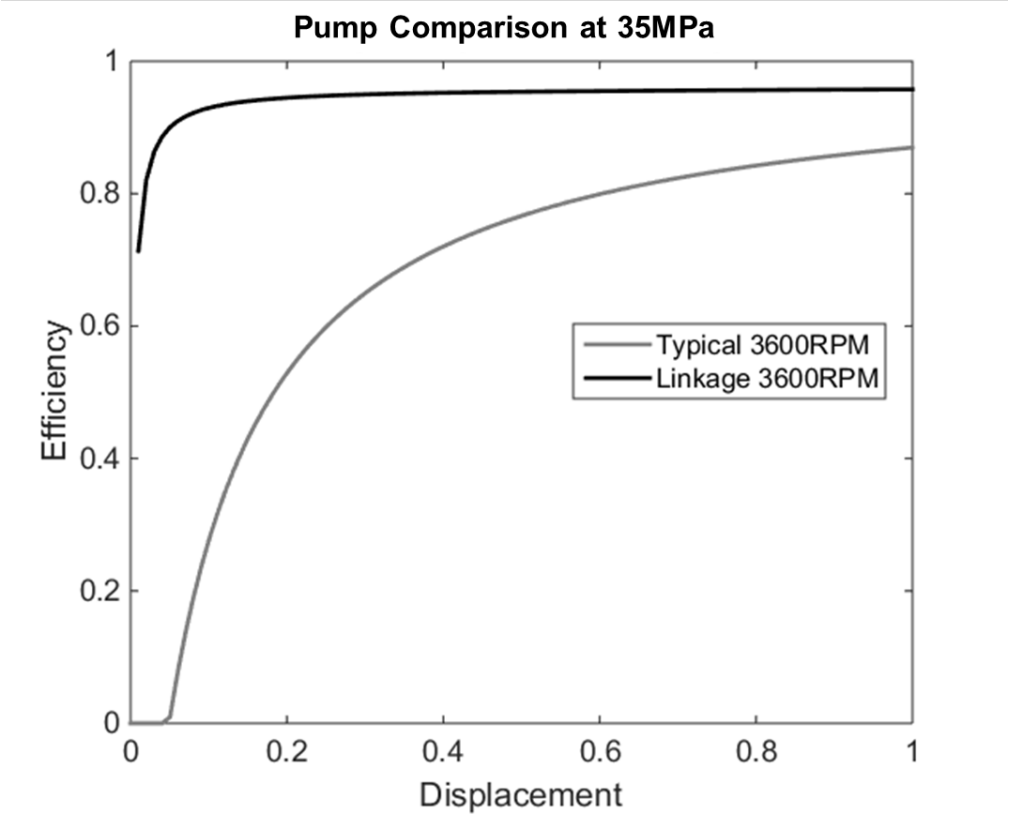

FIGURE 7.1 COMPARISON OF THE OVERALL EFFICIENCY OF THE PROPOSED LINKAGE PUMP AND AN AXIAL PISTON PUMP AS A FUNCTION OF FRACTIONAL DISPLACEMENT

TABLE 7.1 COEFFICIENCTS USED IN MCANDLISH AND DOREY MODEL FOR PUMP COMPARISON

Coefficient	Description	Value
C_v	Viscous friction coefficient	4.9098e5
C_f	Dry coefficient of friction	.024
C_s	Slip Coefficient	1.8846e-9
V_r	Volume Ratio	1.1113
ν	Dynamic Viscosity of Oil	.065 Pa s
β	Bulk Modulus of Oil	1.8e9 Pa

7.2 Conclusions of Thesis

The objective of this thesis was to develop a multi-physics model of a variable displacement linkage pump with low computational complexity for rapid design optimization. In the process, the use of an adjustable mechanism as the driver of a variable displacement pump was investigated through design, analysis, and experiment. From this work the following conclusions can be drawn:

- A linkage pump with a crosshead bearing creates the opportunity to separate the pumping fluid from the mechanism, providing the opportunity to pump non-lubricating fluids.
- At least a six bar mechanism is required to create an adjustable mechanism that does not vary the length of a moving link, the position of the input crank, or slider output.

- There are four configurations of the presented adjustable mechanism that are capable of reducing their stroke to zero while returning to the same constant top dead center position of the piston. Of these configurations, the overlapped r_{1max} configuration was found to be more compact than the other three for the same maximum stroke. However, the configuration required a link which crossed over the rest of the mechanism to connect to the piston. The extended r_{1max} configuration was found to be the most compact configuration which did not require a crossover link.
- The velocities and accelerations of the piston driven by an adjustable mechanism are on the same order as those of a fixed displacement crank slider. Furthermore, the use of a sixbar mechanism provides more design freedom with regards to the shape of these curves.
- The kineto-static force analysis can accurately predict the required shaft torque given the input speed and load on the slider. The energy loss model was able to predict the measured shaft work at powers between 6W and 900W using no experimentally determined coefficients, and provides insight to the energy loss mechanisms of the pump.
- Friction of the revolute joints is the largest contributor to energy loss in the mechanism, specifically at the input crank which rotates continuously and experiences similar loads to other joints. The crosshead friction and viscous friction are small by comparison when plain bearings are used.

- The friction at the revolute joints can be reduced by an order of magnitude when roller element bearings are used rather than plain bearings in the joints. The roller bearing energy loss of the three-cylinder prototype pump was on the same order as the shaft seal friction. It is predicted that mechanical efficiencies greater than 90% are achievable at displacements as low as 10% of the maximum.
- The major losses of the mechanism decrease as the output power decreases. As a result the efficiency of the pump can remain relatively constant at a wide range of operating conditions.
- The single shear design of the three-cylinder prototype created out of plane forces on the mechanism that caused deflection of the mechanism, reduced the pump output flow rate, and introduced additional joint friction due to thrust loads between the links. The experimentally measured deflection was shown to increase as displacement decreased and pressure increased, causing discrepancies between the measured and modeled input work at displacements below 40% of the maximum. The single shear link arrangement should be avoided in future designs, unless the joints are better designed to handle the applied torques.
- The shaft seal torque model provided by the manufacturer predicted a value four times lower than the experimentally measured shaft seal torque. The discrepancy is likely due to the surface finish of the input shaft and possibly misalignment. The coefficient of the shaft seal torque was the only experimentally determined model parameter in the thesis. However, the shaft seal torque of the input shaft is

considered external to the mechanism and does not greatly affect the usefulness of the model during the design phase of a pump.

- The dynamic model of the fluid end of the pump developed in chapter seven was shown to be able to predict the pressure dynamics of the pumping cylinders and delivery line with good agreement across a wide range of operating conditions, using no experimentally determined coefficients.
- The compressibility of the pumping fluid results in reduced volume delivered to the hydraulic load. The compressibility effects can be minimized by minimizing the dead volume of the pumping chamber, demonstrating the importance of the constant top dead center property of the linkage.
- The check valves were shown to be slow to close, resulting in reduced discharge flow. The valve operation is critical to the volumetric performance of a pump. The parameters of the check valves are included in the model and can be optimized simultaneously with the mechanism.

7.3 Recommendations for Future Work

There are a number of areas of research which would augment the work presented in this thesis. The presented model provides a framework for optimization that can be used to develop the capabilities of the mechanism. Future work could investigate optimizing the pump for minimum flow and pressure ripple with a minimum number of cylinders. Furthermore, work can be done to determine the necessity of roller bearings at specific joints in an effort to optimize a pump for compactness while achieving high efficiency. Doing so can reduce the cost and compliance of the mechanism as well as the

size. More work is necessary to increase the power density of the linkage design for use in mobile applications.

The fluid end model could be improved with a better understanding of the check valve dynamics. An improved model could be used to develop high performance check valves to reduce the lost volumetric potential. Current check valve designs used in reciprocating pumps are limited in maximum operating speed reducing the pumps potential power density. Faster responding check valves would enable high speed pump operation for increased power. Additionally, methods of active valve control could be explored allowing the pump to increase hydraulic output or operate as a motor.

The single shear linkage arrangement of the three cylinder prototype prevented the pump from demonstrating high efficiency at low piston displacements and introduced undesirable friction in the mechanism. It is recommended that future designs use a double shear arrangement to robustly demonstrate the benefits of roller bearings on mechanical efficiency at low displacements.

The movable ground pivot of the mechanism ultimately results in a two degree-of-freedom mechanism, providing many control opportunities. Combining shaft position and ground pivot location control, precision motion control could be investigated. Strategies could be explored to reduce flow and pressure ripple via displacement control. Also a pressure compensated systems that varies the displacement of the pump depending on the load demand to maintain a constant system pressure, could be explored.

The work presented here demonstrates that the variable displacement linkage pump is a viable method of delivering efficient fluid power, and provides many advantages over other architectures. The coupling of the kinematics, mechanical energy loss, and fluid end models creates a complete characterization of the variable displacement linkage pump, resulting in a predictive model that can be implemented during the early phases of pump design and optimization. The design freedom offered by the sixbar mechanism to control the piston trajectory provides an opportunity to optimize the mechanism for a variety of applications of varying requirements.

Bibliography

[1] Love, L., Lanke, E., and Alles, P., 2012, "Estimating the Impact (Energy, Emissions and Economics) of the US Fluid Power Industry," Oak Ridge National Laboratory (ORNL).
[2] Inc, E. C., 2000, "Variable Frequency Drives," No. 00-054, Easton Consultants, Inc. .
[3] Williamson, C., and Ivantysynova, M., "Pump mode prediction for four-quadrant velocity control of valveless hydraulic actutors," Proc. Symposium on Fluid Power.
[4] Wieczorek, U., and Ivantysynova, M., 2002, "Computer aided optimization of bearing and sealing gaps in hydrostatic machines- the simulation tool CASPAR," International Journal of Fluid Power, 3(1), pp. 7-20.
[5] Manring, N. D., 2003, "Valve-plate design for an axial piston pump operating at low displacements," Journal of Mechanical Design, 125(1), pp. 200-205.
[6] Inaguma, Y., and Hibi, A., 2007, "Reduction of friction torque in vane pump by smoothing cam ring surface," Proceedings of the Institution of Mechanical Engineers, Part C: Journal of Mechanical Engineering Science, 221(5), pp. 527-534.
[7] Seeniraj, G. K., and Ivantysynova, M., "Impact of valve plate design on noise, volumetric efficiency and control effort in an axial piston pump," ASME.
[8] Wang, S., 2012, "Improving the Volumetric Efficiency of the Axial Piston Pump," Journal of Mechanical Design, 134, p. 111001.
[9] Babcock, G. E., 1916, "Variable-stroke internal-combustion engine," Babcock, G.E., United States.
[10] Ivantysynova, M., "Innovations in Pump Design-What Are Future Directions," Proc. Proceedings of the 7th JFPS International Symposium on Fluid Power, pp. 59-64.
[11] Chacon, R., 2014, "Cylinder block/valve plate interface performance investigation through the introduction of micro-surface shaping," Master of Science Masters, Purdue University, West Lafayette, Indiana.
[12] Henshaw, T. L., 1987, Reciprocating pumps, New York : Van Nostrand Reinhold, New York.
[13] McCandlish, D., and Dorey, R. E., 1984, "The Mathematical Modelling of Hydrostatic Pumps and Motors," Proceedings of the Institution of Mechanical Engineers, 198, pp. 165-174.
[14] McCandlish, D., and Dorey, R., "Steady State Losses in Hydrostatic Pumps and Motors," Proc. 6th International Fluid Power Symposium, pp. 133-144.
[15] Kim, J.-K., and Jung, J.-Y., 2003, "Driving mechanism of tapered pistons in bent-axis design axial piston pumps," KSME international journal, 17(2), pp. 181-186.
[16] Shu, J. J., Burrows, C. R., and Edge, K. A., 1997, "Pressure pulsations in reciprocating pump piping systems Part 1: modelling," Proceedings of the Institution of Mechanical Engineers, Part I: Journal of Systems and Control Engineering, 211(3), pp. 229-235.
[17] McCabe, R. E., 1984, Metering pump handbook, New York, N.Y. : Industrial Press, New York, N.Y.
[18] Pierce, J., 1914, "Variable Stroke Mechanism," Pierce, Joseph, United States of America.

[19] Opitz, K., Schlücker, E., and Schade, O., "Cavitation in reciprocating positive displacement pumps," Proc. Twenty-seventh international pump users symposium, pp. 27-33.
[20] Ferguson, E. S., 1962, Kinematics of Mechanisms from the Time of Watt, Smithsonian Institution.
[21] Atkinson, J., 1887, "Gas Engine," USPTO, United States.
[22] Patton, K. J., Nitschke, R. C., and Heywood, J. B., 1989, "Development and evaluation of a friction model for spark-ignition engines," SAE Technical paper.
[23] Tao, D., 1962, "" Adjustable Four-Bar Linkages," Machine Design, 34(30), pp. 127-129.
[24] Tao, D. C., and Amos, L., 1965, "A four-bar linkage adjustable for variable straight line motions," Journal of Manufacturing Science and Engineering, 87(3), pp. 287-289.
[25] Alson, J., Barba, D., Bryson, J., Doorag, M., Haugen, D., Kargul, J., McDonald, J., Newman, K., Platte, L., and Wolcott, M., 2004, "Progress report on clean and efficient automotive technologies under development at EPA," United States Environmental Protection Agency.
[26] McGovern, J. F., and Sandor, G. N., 1973, "Kinematic synthesis of adjustable mechanisms (Part 1: Function Generation)," ASME Journal of Engineering for Industry 95(2), pp. 417–422.
[27] McGovern, J. F., and Sandor, G. N., 1973, "Kinematic synthesis of adjustable mechanisms (Part 2: Path Generation)," ASME Journal of Engineering for Industry 95(2), pp. 423–429.
[28] Handra-Luca, V., 1973, "The Study of Adjustable Oscillating Mechanisms," Journal of Engineering for Industry, 95(3), pp. 677-680.
[29] Zhou, H., and Ting, K.-L., 2002, "Adjustable slider-crank linkages for multiple path generation," Mechanism and Machine Theory, 37(5), pp. 499-509.
[30] Shoup, T. E., 1984, "The Design of an Adjustable, Three Dimensional Slider Crank Mechanism," Mechanism and Machine Theory, 19(1), pp. 107-111.
[31] Freudenstein, F., and Maki, E., 1984, "Kinematic Structure of Mechanisms for Fixed and Variable-Stroke Axial-Piston Reciprocating Machines," Journal of Mechanisms, Transmissions and Automation in Design, 106(3), pp. 355-364.
[32] Freudenstein, F., and Maki, E. R., 1983, "Development of an Optimum Variable-Stroke Internal-Combustion Engine Mechanism From the Viewpoint of Kinematic Structure," Journal of Mechanisms, Transmissions and Automation in Design, 105(2), pp. 259-266.
[33] Nelson, C. D., 1985, "Variable Stroke Engine," Nelson, Carl D., United States of America.
[34] Pouliot, H. N., Delameter, W. R., and Robinson, C. W., 1977, "A Variable Displacment Spark-Ignition Engine," No. 770114, SAE International.
[35] Yamin, J. A. A., and Dado, M. H., 2004, "Performance simulation of a four-stroke engine with variable stroke-length and compression ratio," Applied Energy, 77(4), pp. 447-463.
[36] Freudenstein, F., and Maki, E. R., 1981, "Variable displacement piston engine,"United States of America.

[37] Blendinger, S., Schlücker, E., and Schade, O., "Computational Fluid Dynamics simulation of reciprocating pumps with respect to the fluid driven valve motion," Proc. Pump Users International Forum, pp. 186-195.
[38] Iannetti, A., Stickland, M., and Dempster, W., "An investigation of the performance of a positive displacement reciprocating pump at low pressure NPSH incorporating a three phase cavitation model," Proc. 11th World Congress on Computational Mechanics, WCCMXI.
[39] Watton, J., 1989, Fluid power systems: modeling, simulation, analog and microcomputer control, Prentice-Hall.
[40] IVANTYSYNOVA, M., "A new approach to the design of sealing and bearing gaps of displacement machines," Proc. Proceedings of the JFPS International Symposium on Fluid Power, 社団法人 日本フルードパワーシステム学会, pp. 45-50.
[41] Kohmäscher, T., Rahmfeld, R., Murrenhoff, H., and Skirde, E., "Improved loss modeling of hydrostatic units: Requirement for precise simulation of mobile working machine drivelines," Proc. ASME 2007 International Mechanical Engineering Congress and Exposition, American Society of Mechanical Engineers, pp. 195-206.
[42] Bavendiek, R., 1988, "Verlustkennwertbestimmung am Beispiel von hydrostatischen Maschinen in Schrägachsenbauweise," Forschung im Ingenieurwesen, 54(3), pp. 93-93.
[43] Grandall, D. R., 2010, "The Performance and Efficiency of Hydraulic Pumps and Motors," Masters of Science, The University of Minnesota, Minneapolis, MN.
[44] Wilson, W., 1949, "Performance criteria for positive displacement pumps and fluid motors," Trans. ASME, 71(2), pp. 115-120.
[45] Ivantysyn, J., and Ivantysynova, M., 2001, "Hydrostatic pumps and motors," New Dehli: Academic Books International.
[46] Hall, S. J., 2014, "Statistical analysis of multiple hydrostatic pump flow loss models," Masters of Science, Iowa State University, Ames Iowa.
[47] Chappie, P., 1992, "Modelling of a radial-piston hydraulic motor," Proceedings of the Institution of Mechanical Engineers, Part I: Journal of Systems and Control Engineering, 206(3), pp. 171-180.
[48] Agarwal, P., Vacca, A., Wang, K., Kim, K. S., and Kim, T., 2014, "An Analysis of Lubricating Gap Flow in Radial Piston Machines," SAE Technical Paper.
[49] Adelsperger, A. C., Shang, L., Mizell, D., and Ivantysynova, M., 2014, "Modeling of Mixed Friction Interactions Occurring in Axial Piston Pumps."
[50] Pelosi, M., and Ivantysynova, M., 2012, "A geometric multigrid solver for the piston–cylinder interface of axial piston machines," Tribology Transactions, 55(2), pp. 163-174.
[51] Huhtala, K., 1996, "Modelling of hydrostatic transmission- steady-state, linear and non-linear models," Acta Polytechnica Scandinavica(123), pp. 9-101.
[52] Schenk, A., Zecchi, M., and Ivantysynova, M., "Accurate prediction of axial piston machine's performance through a thermo-elasto-hydrodynamic simulation model," Proc. ASME/BATH 2013 Symposium on Fluid Power and Motion Control, American Society of Mechanical Engineers, pp. V001T001A034-V001T001A034.
[53] Iannetti, A., Stickland, M. T., and Dempster, W. M., 2014, "A computational fluid dynamics model to evaluate the inlet stroke performance of a positive displacement

reciprocating plunger pump," Proceedings of the Institution of Mechanical Engineers, Part A: Journal of Power and Energy, p. 0957650914530295.
[54] Schloesser, W., 1961, "Mathematical model for displacement pumps and motors," Hydraulic power transmission, pp. 252-257.
[55] Zarotti, G., and Nervegna, N., 1982, "Pump efficiencies: approximation and modeling," Fluidics quarterly, 14(3), pp. 1-20.
[56] Sandoval, D., and Heywood, J. B., 2003, "An improved friction model for spark-ignition engines," SAE Technical paper.
[57] Wieczoreck, U., and Ivantysynova, M., "CASPAR-A computer aided design tool for axial piston machines," Proc. Proceedings of the power transmission motion and control international workshop, PTMC2000, Bath, UK, pp. 113-126.
[58] Kumar, S., 2010, CFD Analysis of an Axial Piston Pump, PhD Thesis from UPC, Spain.
[59] Rydberg, K.-E., 1983, On performance optimization and digital control of hydrostatic drives for vehicle applications.
[60] Kogl, C., 1996, "Verstellbare hydrostatische Verdrangereinheiten im Drehzahl-und Drehmomentregelkreis am Netz mit angepasstem Versorgungsdruck," Olhydraulik und Pneumatik, 40(6), pp. 377-377.
[61] Dasgupta, K., Mandal, S., and Pan, S., 2012, "Dynamic analysis of a low speed high torque hydrostatic drive using steady-state characteristics," Mechanism and Machine Theory, 52, pp. 1-17.
[62] Bergada, J., Kumar, S., Davies, D. L., and Watton, J., 2012, "A complete analysis of axial piston pump leakage and output flow ripples," Applied Mathematical Modelling, 36(4), pp. 1731-1751.
[63] Jeong, H.-S., 2007, "A novel performance model given by the physical dimensions of hydraulic axial piston motors: Model derivation," Journal of mechanical science and technology, 21(1), pp. 83-97.
[64] Bergada, J., Watton, J., and Kumar, S., 2008, "Pressure, flow, force, and torque between the barrel and port plate in an axial piston pump," Journal of dynamic systems, measurement, and control, 130(1), p. 011011.
[65] Zecchi, M., and Ivantysynova, M., "An investigation of the impact of micro surface shaping on the cylinder block/valve plate interface performance through a novel thermo-elastohydrodynamic model," Proc. The 7th FPNI PhD Symposium on Fluid Power.
[66] Wondergem, A. M., and Ivantysynova, M., "The Impact of the Surface Shape of the Piston on Power Losses," Proc. 8th FPNI Ph. D Symposium on Fluid Power, American Society of Mechanical Engineers, pp. V001T002A008-V001T002A008.
[67] Edge, K., Brett, P., and Leahy, J., 1984, "Digital computer simulation as an aid in improving the performance of positive displacement pumps with self-acting valves," Proceedings of the Institution of Mechanical Engineers, Part B: Journal of Engineering Manufacture, 198(4), pp. 267-274.
[68] Edge, K., and Brett, P., 1990, "The pumping dynamics of a positive displacement pump employing self-acting valves," Journal of dynamic systems, measurement, and control, 112(4), pp. 748-754.

[69] Johnston, D., Edge, K., and Vaughan, N., 1991, "Experimental investigation of flow and force characteristics of hydraulic poppet and disc valves," Proceedings of the Institution of Mechanical Engineers, Part A: Journal of Power and Energy, 205(3), pp. 161-171.
[70] Vaughan, N., Johnston, D., and Edge, K., 1992, "Numerical simulation of fluid flow in poppet valves," Proceedings of the Institution of Mechanical Engineers, Part C: Journal of Mechanical Engineering Science, 206(2), pp. 119-127.
[71] Edge, K., Boston, O., Xiao, K., Longvill, K., and Burrows, K., 1997, "Pressure pulsations in reciprocating pump piping systems Part 2: experimental investigations and model validation," Proceedings of the Institution of Mechanical Engineers, Part I: Journal of Systems and Control Engineering, 211(3), pp. 239-250.
[72] Edge, K., 1990, "The 'secondary source'method for the measurement of pump pressure ripple characteristics part 2: experimental results," Proceedings of the Institution of Mechanical Engineers, Part A: Journal of Power and Energy, 204(1), pp. 41-46.
[73] Singh, P. J., and Madavan, N., "Complete analysis and simulation of reciprocating pumps including system piping," Proc. Proceedings of Fourth International Pump Symposium, pp. 53-73.
[74] Singh, P. J., and Able, S. D., "Determination of NPSHR for Reciprocating Positive Displacement Pumps-A New Approach," Proc. PROCEEDINGS OF THE INTERNATIONAL PUMP USERS SYMPOSIUM, TEXAS A&M UNIVERSITY SYSTEM, pp. 131-142.
[75] Opitz, K., and Schlücker, E., 2010, "Detection of Cavitation Phenomena in Reciprocating Pumps using a High-Speed Camera," Chemical Engineering & Technology, 33(10), pp. 1610-1614.
[76] Norton, R. L., 2008, Design of Machinery An Introduction to the Synthesis and Analysis of Mechanisms and Machines, McGraw-Hill, Boston.
[77] Sandor, G. N., and Erdman, A. G., 1984, Advanced Mechanism Design: Analysis and Sythesis, Prentice-Hall Inc., Upper Saddle River.
[78] Alt, V. H., 1932, "The Transmission Angle and its Importance for the Design of Periodic Mechanisms," Werstattstechnik, 26, pp. 61-64.
[79] Balli, S. S., and Chand, S., 2002, "Defects in link mechanisms and solution rectification," Mechanism and Machine Theory, 37(9), pp. 851-876.
[80] Lin, C.-C., and Chang, W.-T., 2002, "The force transmissivity index of planar linkage mechanisms," Mechanism and Machine Theory, 37(12), pp. 1465-1485.
[81] Holte, J., and Chase, T., "A force transmission index for planar linkage mechanisms," Proc. Proceedings of the ASME Mechanisms Conference, pp. 377-386.
[82] He, B., Zhang, P., and Liu, L., 2014, "Simultaneous functional synthesis of mechanisms with mechanical efficiency and cost," The International Journal of Advanced Manufacturing Technology, 75(5-8), pp. 659-665.
[83] Sullivan, T. A., Northrop, W. F., and McCabe, K., 2015, "Integrated Mechanical and Thermodynamic Optimization of an Engine Linkage Using a Multi-Objective Genetic Algorithm," Journal of Mechanical Design, 137(2), p. 024501.
[84] Sullivan, T., 2013, "Multi-domain multi-objective optimization of mechanisms: a general method with two case studies," UNIVERSITY OF MINNESOTA.

[85] Cabrera, J., Simon, A., and Prado, M., 2002, "Optimal synthesis of mechanisms with genetic algorithms," Mechanism and machine theory, 37(10), pp. 1165-1177.
[86] Lin, W.-Y., 2010, "A GA–DE hybrid evolutionary algorithm for path synthesis of four-bar linkage," Mechanism and Machine Theory, 45(8), pp. 1096-1107.
[87] Lipson, H., 2008, "Evolutionary synthesis of kinematic mechanisms," Artificial Intelligence for Engineering Design, Analysis and Manufacturing, 22(03), pp. 195-205.
[88] Freudenstein, F., and Primrose, E., "The classical transmission angle problem," Proc. Proc. Conf. Mechanisms, pp. 105-110.
[89] Söylemez, E., 2002, "Classical transmission-angle problem for slider–crank mechanisms," Mechanism and machine theory, 37(4), pp. 419-425.
[90] Vadasz, A., "Design charts for slider crank mechanism with prescribed minimum transmission angle and time ratio," Proc. Proceedings of 6th Annual Applied Mechanisms Conference.
[91] Eschmann, P., 1985, Ball and Roller Bearings : Theory, Design, and Application, Wiley, New York.
[92] Miller, J. E., 1987, The reciprocating pump : theory, design, and use, New York : Wiley, New York.
[93] Merritt, H. E., 1967, Hydraulic Control Systems, John Wiley & Sons, New York.
[94] Manring, N., 2005, Hydraulic control systems, Hoboken, N.J. : John Wiley, Hoboken, N.J.
[95] Brändlein, J., 1999, Ball and roller bearings: theory, design and application, Wiley, New York.
[96] Deb, K., Pratap, A., Agarwal, S., and Meyarivan, T., 2002, "A Fast and Elitist Multiobjective Genetic Algorithm: NSGA-II," IEEE Transactions on Evolutionary Computation, 6(2), pp. 182-197.
[97] Beardmore, R., 2013, "ROYMECH Friction Factors," http://www.roymech.co.uk/Useful_Tables/Tribology/co_of_frict.htm.
[98] Kojima, E., 2003, "Development of a quieter variable-displacement vane pump for automotive hydraulic power steering system," International Journal of Fluid Power, 4(2), pp. 5-14.
[99] Johnston, D. N., and Drew, J., 1996, "Measurement of positive displacement pump flow ripple and impedance," Proceedings of the Institution of Mechanical Engineers, Part I: Journal of Systems and Control Engineering, 210(1), pp. 65-74.
[100] Manring, N. D., and Kasaragadda, S. B., 2003, "The theoretical flow ripple of an external gear pump," Journal of dynamic systems, measurement, and control, 125(3), pp. 396-404.
[101] Manring, N. D., 2000, "The discharge flow ripple of an axial-piston swash-plate type hydrostatic pump," Journal of dynamic systems, measurement, and control, 122(2), pp. 263-268.
[102] Vacca, A., and Guidetti, M., 2011, "Modelling and experimental validation of external spur gear machines for fluid power applications," Simulation Modelling Practice and Theory, 19(9), pp. 2007-2031.

[103] Johnston, D. N., 1991, "Numerical modelling of reciprocating pumps with self-acting valves," Proceedings of the Institution of Mechanical Engineers, Part I: Journal of Systems and Control Engineering, 205(2), pp. 87-96.
[104] Thorley, A., 1989, "Check valve behavior under transient flow conditions: a state-of-the-art review," Journal of Fluids Engineering, 111(2), pp. 178-183.
[105] Totten, G. E., Webster, G. M., and Yeaple, F., 2000, Physical Properties and Their Determination, Marcel Dekker, New York.
[106] Zhou, J., Vacca, A., and Manhartsgruber, B., 2013, "A novel approach for the prediction of dynamic features of air release and absorption in hydraulic oils," Journal of Fluids Engineering, 135(9), p. 091305.
[107] Gholizadeh, H., Burton, R., and Schoenau, G. J., 2011, "Fluid Bulk Modulus: a Literature Survey," International Journal of Fluid Power, 12(3), pp. 5-15.
[108] Gholizadeh, H., Burton, R., and Schoenau, G. J., 2012, "Fluid Bulk Modulus: Comparison of Low Pressure Models," International Journal of Fluid Power, 13(1), pp. 7-16.
[109] Jinghong, Y., Zhaoneng, C., and Yuanzhang, L., 1994, "The variation of oil effective bulk modulus with pressure in hydraulic systems," Journal of dynamic systems, measurement, and control, 116(1), pp. 146-150.
[110] Cho, B.-H., Lee, H.-W., and Oh, J.-S., 2002, "Estimation technique of air content in automatic transmission fluid by measuring effective bulk modulus," International journal of automotive technology, 3(2), pp. 57-61.
[111] Nykanen, T., Esque, S., and Ellman, A., 2000, "Comparison of different fluid models," Power Transmission and Motion Control, PTMC, pp. 101-110.
[112] Van de Ven, J. D., 2013, "On Fluid Compressibility in Switch-Mode Hydraulic Circuits—Part I: Modeling and Analysis," Journal of Dynamic Systems, Measurement, and Control, 135(2), p. 021013.
[113] Stone, J., 1960, "Discharge coefficients and steady-state flow forces for hydraulic poppet valves," Journal of Fluids Engineering, 82(1), pp. 144-154.

Appendix A Construction of Configurations b-d

This appendix gives the diagrams needed to construct the adjustable mechanism of configurations b, c, and d according to the methodologies of Chapter 2. All of the equations remain the same except for in cases c and d, $r_2 + r_3$ is replaced by $r_3 - r_2$, and for cases b and d, the slider is located at d_{min}.

Configuration b

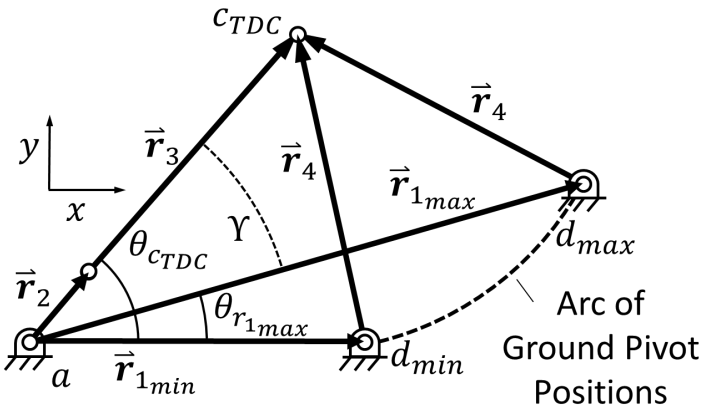

Configuration c

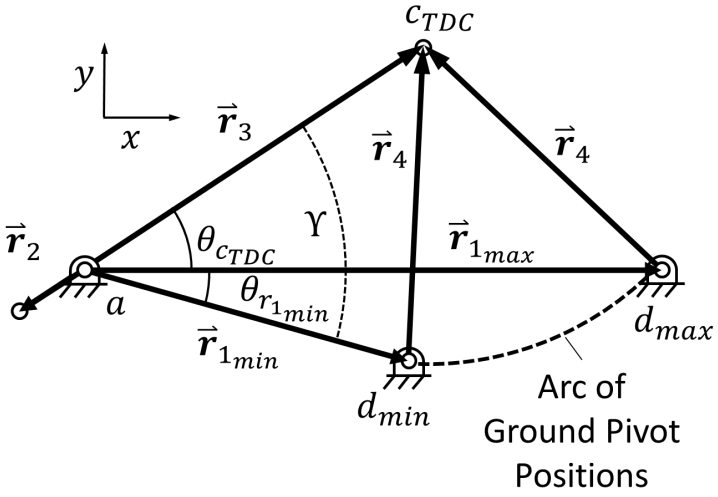

Configuration d

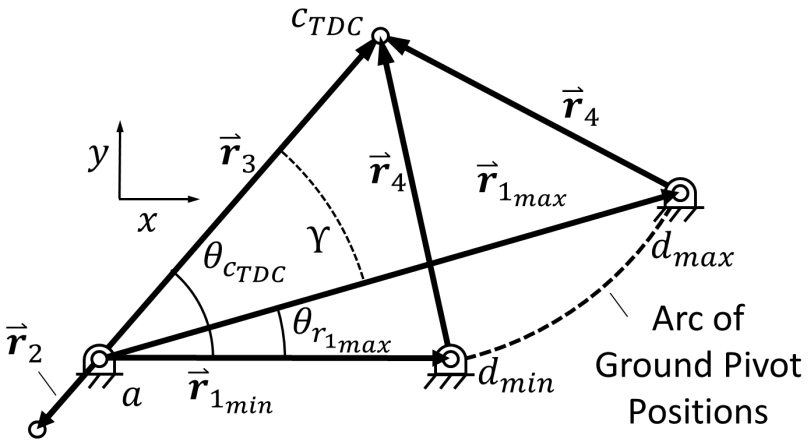

Appendix B Single Cylinder Prototype Part Drawings

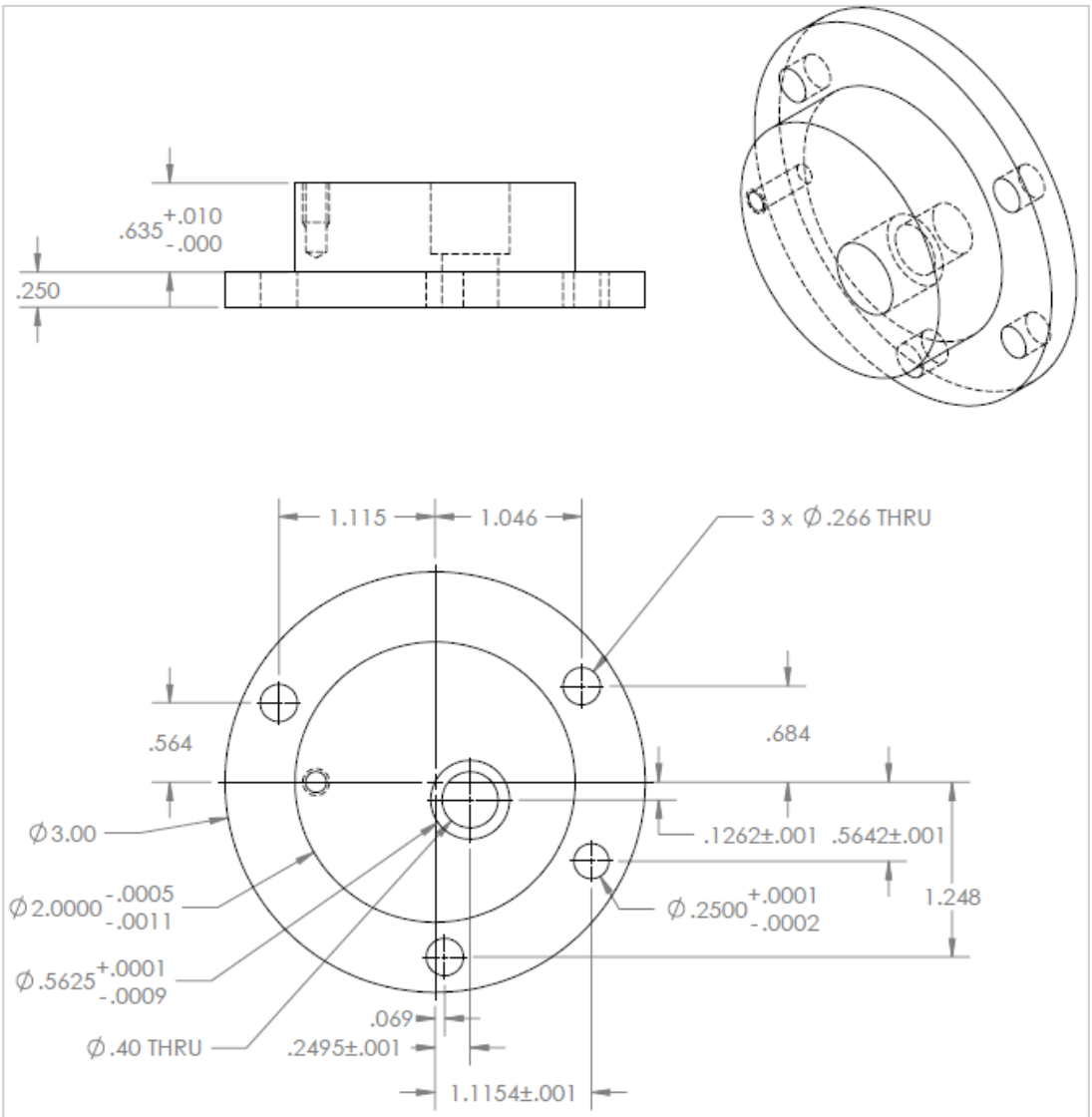

		DIMENSIONS ARE IN INCHES TOLERANCES: TWO PLACE DECIMAL ±.01 THREE PLACE DECIMAL ±.005		NAME	DATE	
			DRAWN	SW	8/4/11	
			CHECKED			
			ENG APPR.			
			MFG APPR.			
		MATERIAL SAE 863 BRONZE	Q.A.			
			COMMENTS: NO SHARP EDGES			
NEXT ASSY	USED ON	FINISH				
APPLICATION		DO NOT SCALE DRAWING				

SIZE	DWG. NO.	REV.
A	.375 Bearing Housing	
SCALE:1:1	WEIGHT:	SHEET 1 OF 1

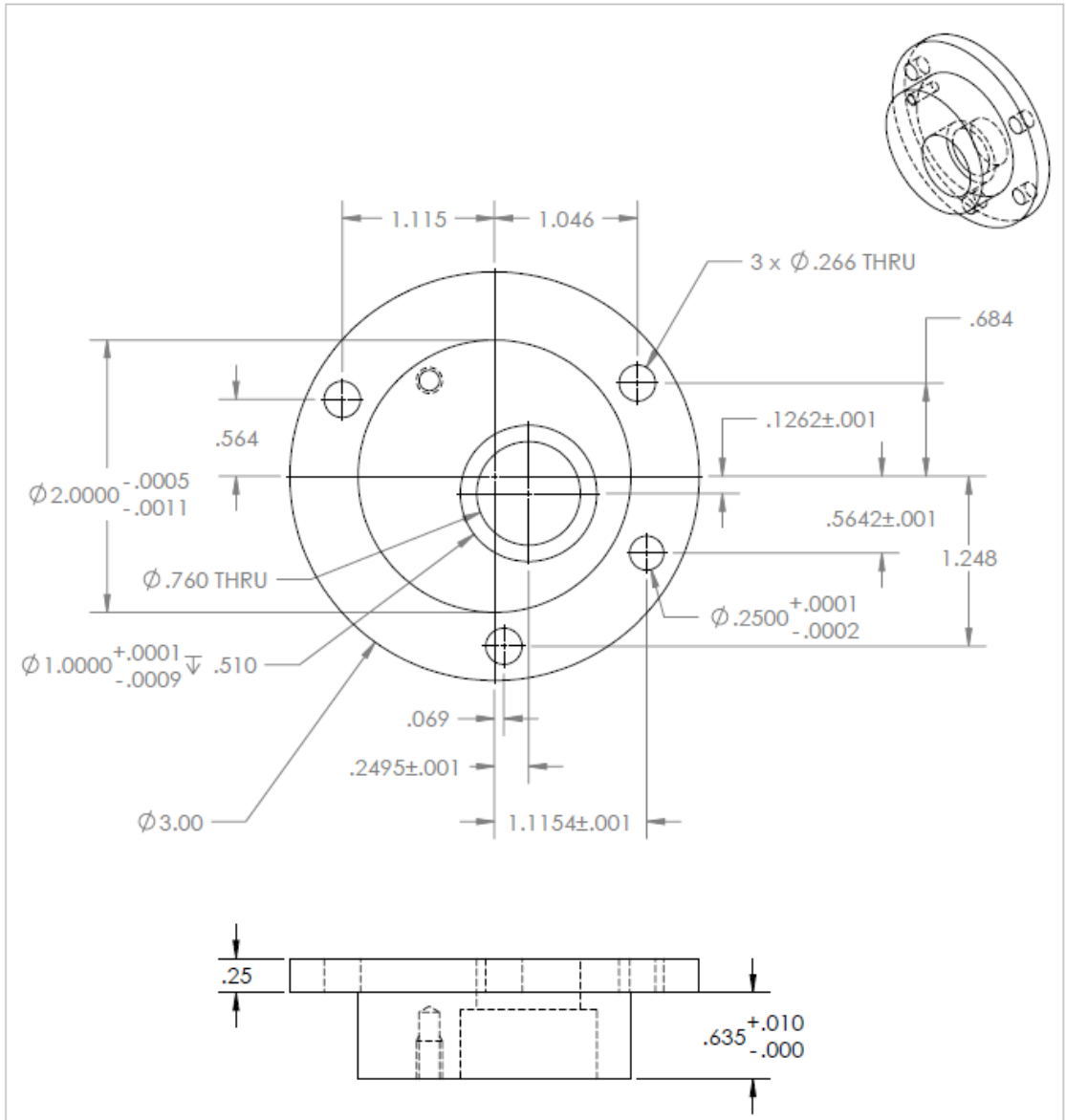

		DIMENSIONS ARE IN INCHES TOLERANCES: TWO PLACE DECIMAL ±.01 THREE PLACE DECIMAL ±.005		NAME	DATE
			DRAWN	SW	8/4/11
			CHECKED		
			ENG APPR.		
			MFG APPR.		
		MATERIAL SAE 863 BRONZE	Q.A.		
			COMMENTS: NO SHARP EDGES		
NEXT ASSY	USED ON	FINISH			
APPLICATION		DO NOT SCALE DRAWING			

SIZE	DWG. NO.	REV.
A	.75 Bearing Housing	
SCALE:1:1	WEIGHT:	SHEET 1 OF 1

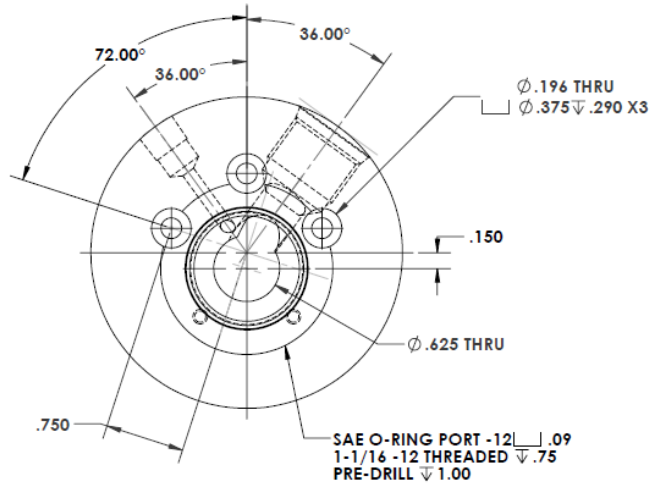

*DETAIL DRAWINGS OF ANGLED DRILL HOLE ON SHEET 2

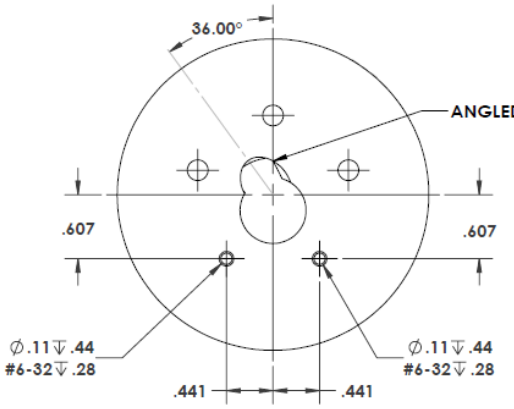

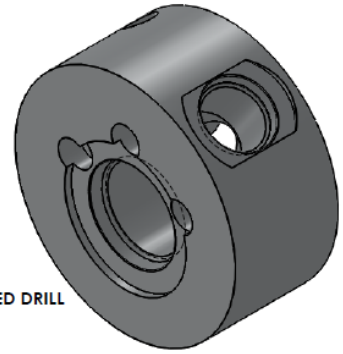

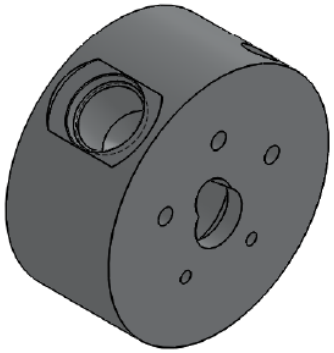

1/8-27 NPT TAPPED HOLE ↧.27
PREDRILL ↧.47
1/8 DRILL ↧1.25

*Use J1926-1 or MS16142 Porting Tool For Cutting O-Ring Boss

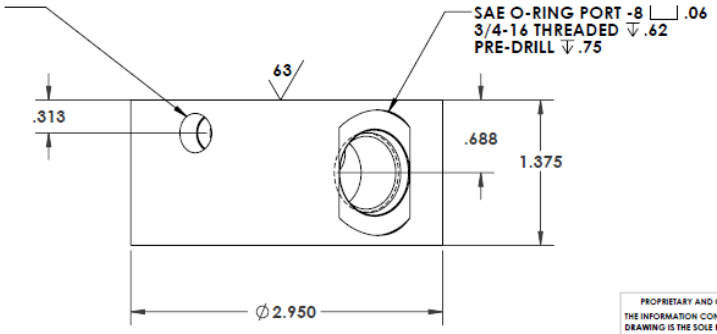

		UNLESS OTHERWISE SPECIFIED:		NAME	DATE
		DIMENSIONS ARE IN INCHES TOLERANCES:	DRAWN	SW	7/22/12
			CHECKED		
		ANGULAR: MACH ± BEND ± TWO PLACE DECIMAL ±.01 THREE PLACE DECIMAL ±.005	ENG APPR.		
			MFG APPR.		
		INTERPRET GEOMETRIC TOLERANCING PER:	Q.A.		
		MATERIAL 6061 ALUMINUM	COMMENTS: NO SHARP EDGES		
NEXT ASSY	USED ON	FINISH			
APPLICATION		DO NOT SCALE DRAWING			

TITLE:
Check Valve Adapter Porting

SIZE	DWG. NO.	REV
B		1

SCALE: 1:1 | WEIGHT: | SHEET 1 OF 2

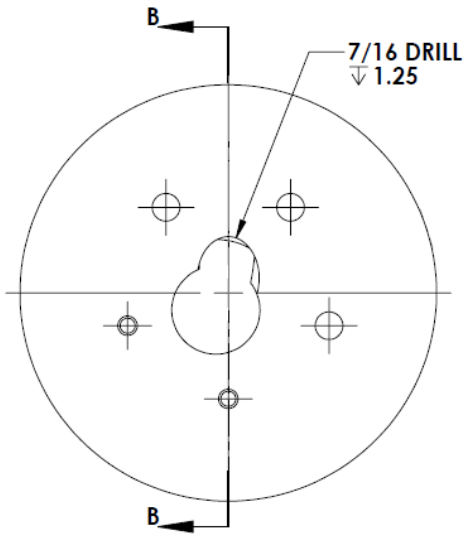

SECTION B-B

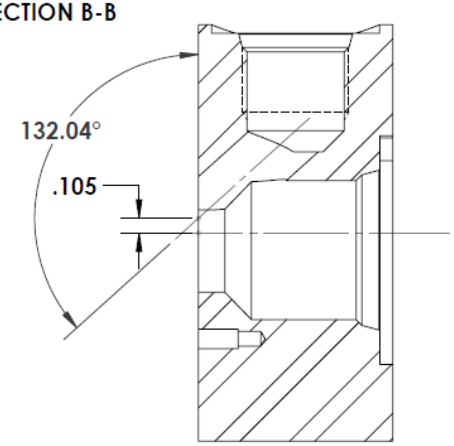

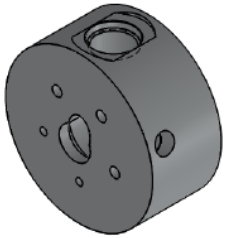

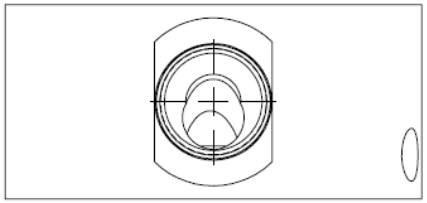

*PART ROTATED SO THAT -6 O-RING PORT IS VERTICAL AND DRILL HOLE IS CENTERED

UNLESS OTHERWISE SPECIFIED:		NAME	DATE		
DIMENSIONS ARE IN INCHES TOLERANCES: FRACTIONAL ± ANGULAR: MACH ± BEND ± TWO PLACE DECIMAL ±.01 THREE PLACE DECIMAL ±.005	DRAWN	SW	7/24/12	TITLE: ANGLED DRILL DETAIL	
	CHECKED				
	ENG APPR.				
	MFG APPR.				
INTERPRET GEOMETRIC TOLERANCING PER:	Q.A.				
MATERIAL 6061 ALUMINUM	COMMENTS:			SIZE A / DWG. NO. Check Valve Adapter Porting / REV	
FINISH				SCALE: 1:1 / WEIGHT: / SHEET 2 OF 2	
NEXT ASSY / USED ON					
APPLICATION	DO NOT SCALE DRAWING				

5 4 3 2 1

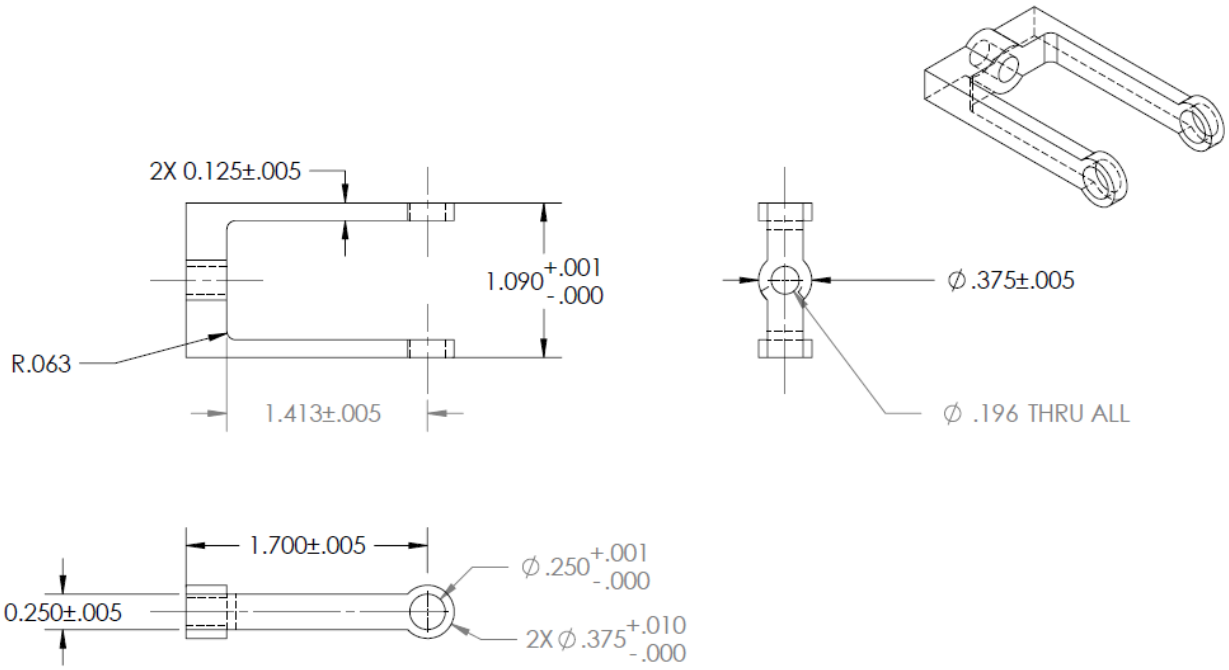

		UNLESS OTHERWISE SPECIFIED:		NAME	DATE
		DIMENSIONS ARE IN INCHES TOLERANCES: FRACTIONAL ± ANGULAR: MACH ± BEND ± TWO PLACE DECIMAL ± THREE PLACE DECIMAL ±	DRAWN	SW	8/4/11
			CHECKED		
			ENG APPR.		
			MFG APPR.		
		INTERPRET GEOMETRIC TOLERANCING PER:	Q.A.		
		MATERIAL 4340 STEEL	COMMENTS: HARDENED TO ROCKWELL 46C NO SHARP EDGES		
NEXT ASSY	USED ON	FINISH			
APPLICATION		DO NOT SCALE DRAWING			

TITLE:

SIZE	DWG. NO.	REV
A	conrod	

SCALE: 1:1	WEIGHT:	SHEET 1 OF 1

5 4 3 2 1

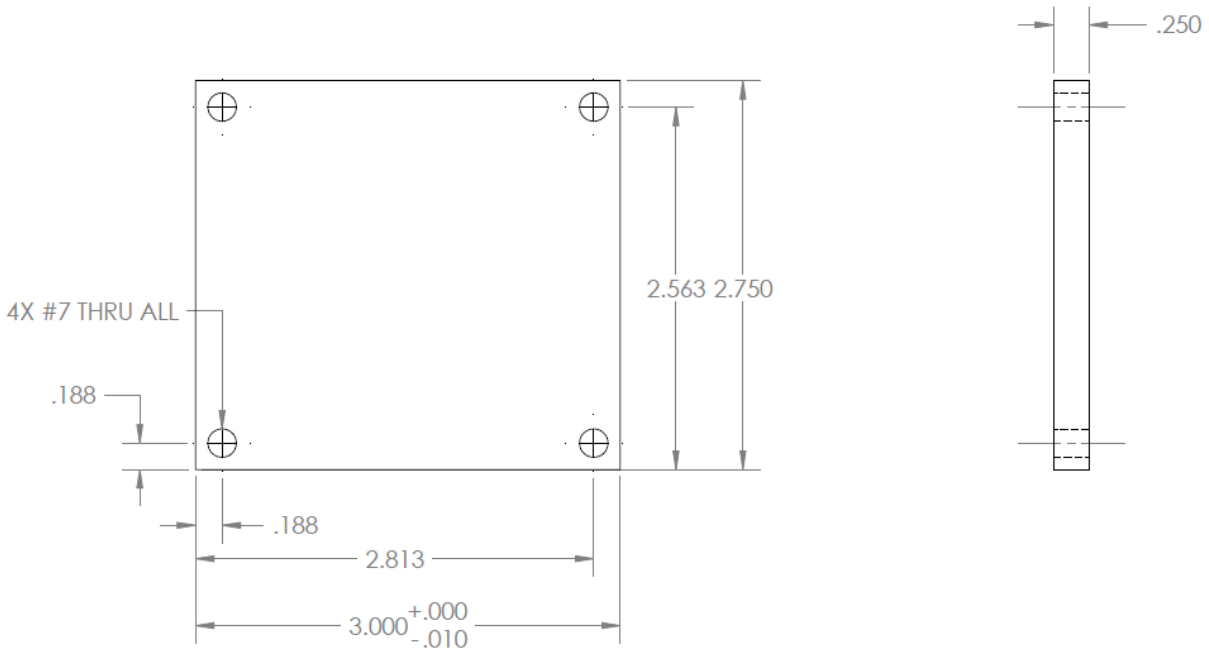

		UNLESS OTHERWISE SPECIFIED:		NAME	DATE
		DIMENSIONS ARE IN INCHES TOLERANCES: TWO PLACE DECIMAL ±.01 THREE PLACE DECIMAL ±.005	DRAWN	SW	8/4/11
			CHECKED		
			ENG APPR.		
			MFG APPR.		
		INTERPRET GEOMETRIC TOLERANCING PER:	Q.A.		
		MATERIAL 6061 ALUMINUM	COMMENTS: NO SHARP EDGES		
NEXT ASSY	USED ON	FINISH			
APPLICATION		DO NOT SCALE DRAWING			

TITLE:

SIZE	DWG. NO.	REV
A	COVER	

SCALE: 1:1	WEIGHT:	SHEET 1 OF 1

5 4 3 2 1

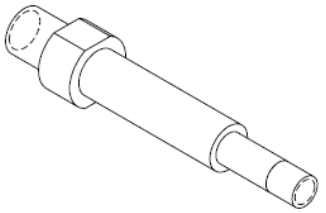

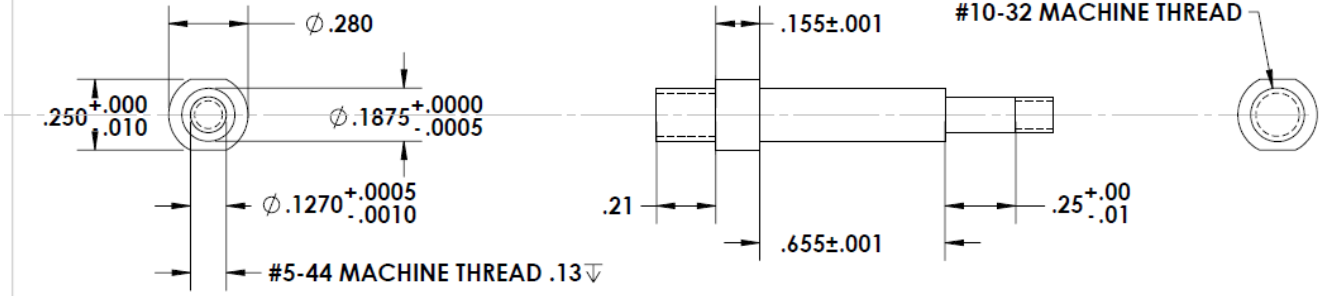

		UNLESS OTHERWISE SPECIFIED:		NAME	DATE	
		DIMENSIONS ARE IN INCHES TOLERANCES: FRACTIONAL ± ANGULAR: MACH ± BEND TWO PLACE DECIMAL ± 0.01 THREE PLACE DECIMAL ± 0.005	DRAWN			TITLE: Crank Pin
			CHECKED			
			ENG APPR.			
			MFG APPR.			
		INTERPRET GEOMETRIC TOLERANCING PER:	Q.A.			
		MATERIAL 4140 Steel	COMMENTS: NORMALIZED TO ROCKWELL 32C NO SHARP EDGES			SIZE A / DWG. NO. / REV
NEXT ASSY	USED ON	FINISH				
APPLICATION		DO NOT SCALE DRAWING				SCALE: 2:1 / WEIGHT: / SHEET 1 OF 1

5 4 3 2 1

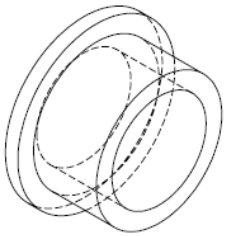

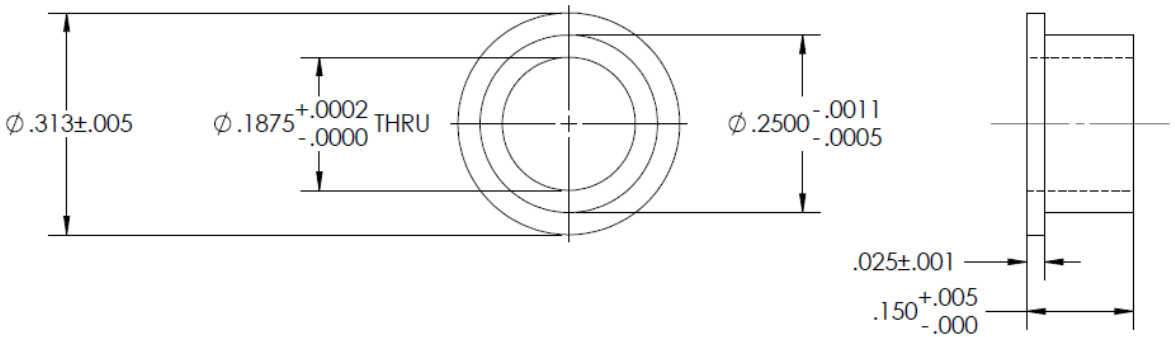

UNLESS OTHERWISE SPECIFIED:		NAME	DATE		
DIMENSIONS ARE IN INCHES TOLERANCES: FRACTIONAL ± ANGULAR: MACH ± BEND ± TWO PLACE DECIMAL ± THREE PLACE DECIMAL ±	DRAWN	SW	8/4/11	TITLE: Custom Flange Bearing	
	CHECKED				
	ENG APPR.				
	MFG APPR.				
INTERPRET GEOMETRIC TOLERANCING PER:	Q.A.				
MATERIAL SAE 863 BRONZE	COMMENTS: NO SHARP EDGES			SIZE A / DWG. NO. Custom Flange Bearing	REV
FINISH				SCALE: 5:1 / WEIGHT:	SHEET 1 OF 1
NEXT ASSY / USED ON					
APPLICATION / DO NOT SCALE DRAWING					

5 4 3 2 1

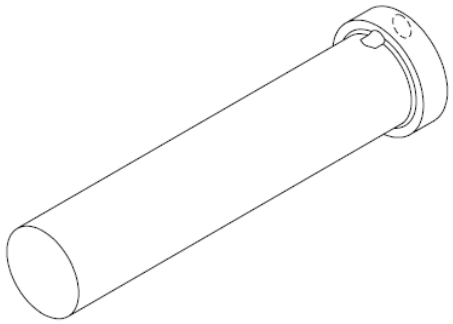

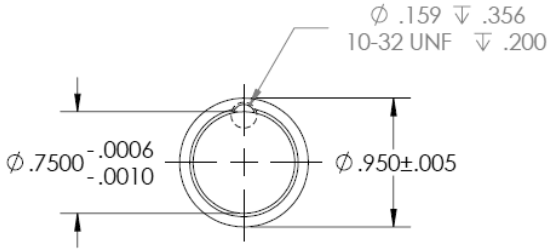

		UNLESS OTHERWISE SPECIFIED:		NAME	DATE
		DIMENSIONS ARE IN INCHES TOLERANCES: TWO PLACE DECIMAL ±.01 THREE PLACE DECIMAL ±.005	DRAWN	SW	8/3/11
			CHECKED		
			ENG APPR.		
			MFG APPR.		
		INTERPRET GEOMETRIC TOLERANCING PER:	Q.A.		
		MATERIAL 4340 STEEL	COMMENTS: HARDENED TO ROCKWELL 46C NO SHARP EDGES		
NEXT ASSY	USED ON	FINISH			
APPLICATION		DO NOT SCALE DRAWING			

TITLE:

SIZE	DWG. NO.	REV
A	FIXED END SHAFT	
SCALE: 1:1	WEIGHT:	SHEET 1 OF 1

5 4 3 2 1

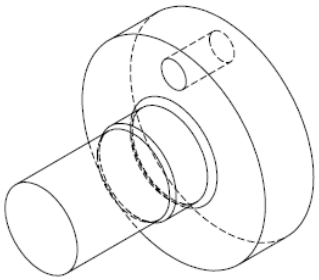

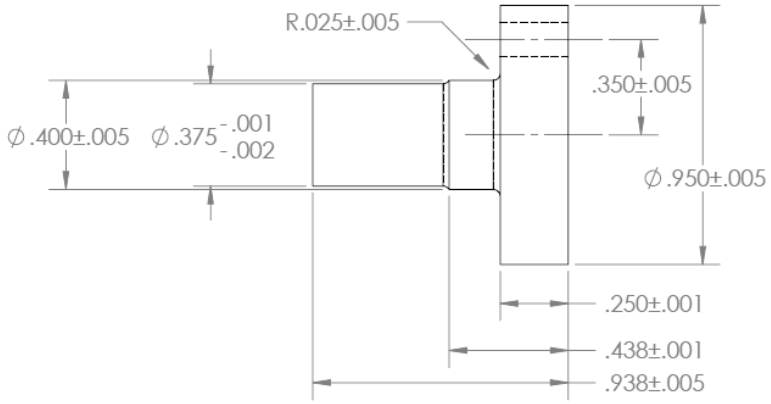

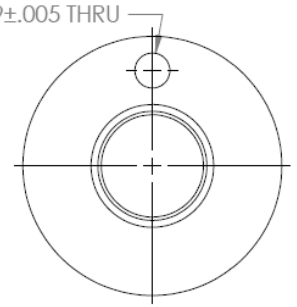

UNLESS OTHERWISE SPECIFIED:		NAME	DATE		
DIMENSIONS ARE IN INCHES TOLERANCES: ALL TOLERANCES CALLED OUT ON SHEET	DRAWN	SW	8/3/11	TITLE:	
	CHECKED				
	ENG APPR.				
	MFG APPR.				
	Q.A.				
INTERPRET GEOMETRIC TOLERANCING PER:	COMMENTS: HARDENED TO ROCKWELL 46C NO SHARP EDGES			SIZE: A	DWG. NO.: FREE END SHAFT
MATERIAL: 4340 STEEL					REV:
FINISH:				SCALE: 2:1	WEIGHT:
DO NOT SCALE DRAWING					SHEET 1 OF 1

NEXT ASSY	USED ON
APPLICATION	

5 4 3 2 1

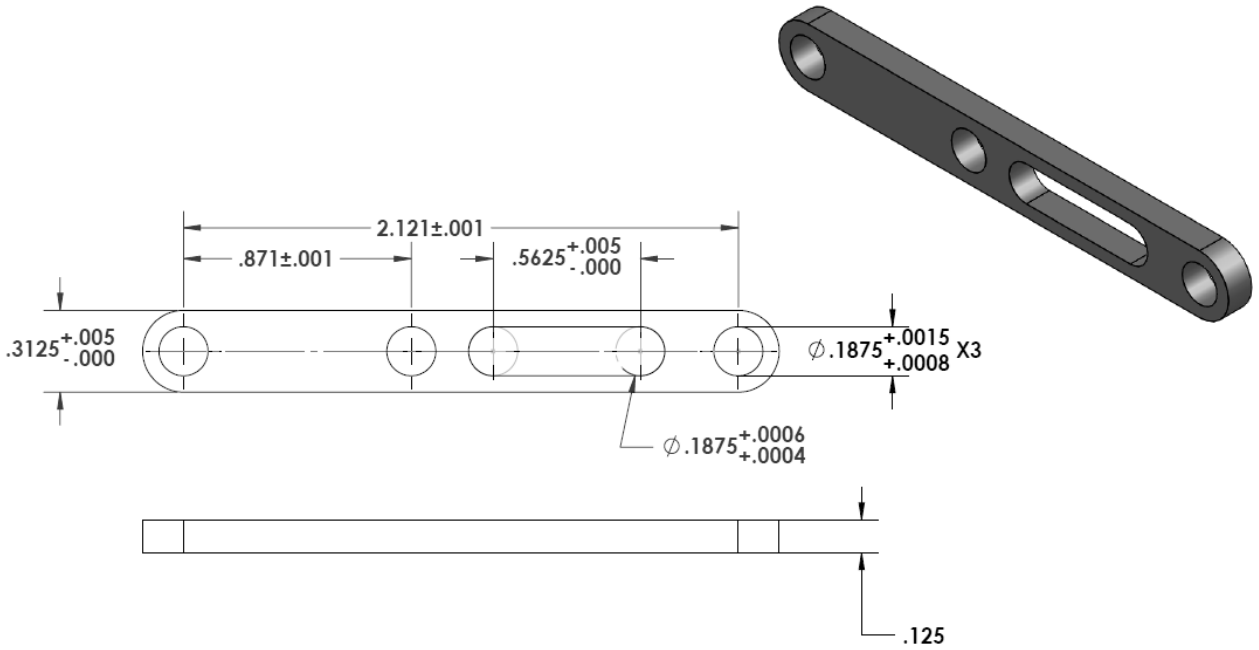

		UNLESS OTHERWISE SPECIFIED:		NAME	DATE
		DIMENSIONS ARE IN INCHES TOLERANCES: FRACTIONAL ± ANGULAR: MACH ± BEND ± TWO PLACE DECIMAL ±.01 THREE PLACE DECIMAL ±.005	DRAWN	SW	7/25/12
			CHECKED		
			ENG APPR.		
			MFG APPR.		
		INTERPRET GEOMETRIC TOLERANCING PER:	Q.A.		
		MATERIAL A2 TOOL STEEL	COMMENTS: HARDENED TO ROCKWELL C50		
NEXT ASSY	USED ON	FINISH	NO SHARP EDGES		
APPLICATION		DO NOT SCALE DRAWING			

TITLE:

SIZE	DWG. NO.	REV
A	GP	

SCALE: 2:1 | WEIGHT: | SHEET 1 OF 1

5 4 3 2 1

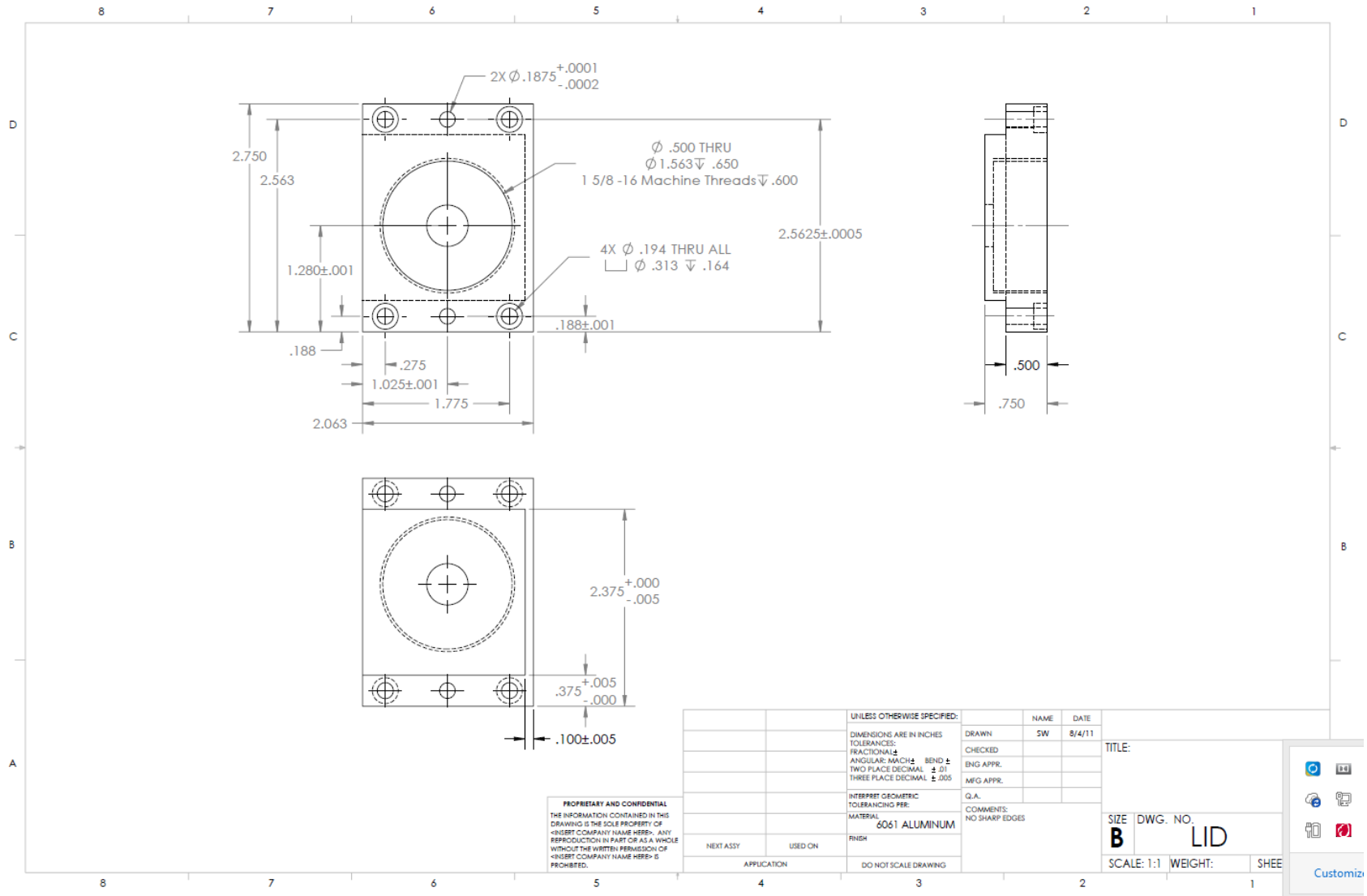
2X Ø.1875 +.0001 -.0002
Ø .500 THRU
Ø1.563↧ .650
1 5/8 -16 Machine Threads↧.600
4X Ø .194 THRU ALL
⌴ Ø .313 ↧ .164
2.750
2.563
1.280±.001
2.5625±.0005
.188±.001
.188
.275
1.025±.001
1.775
2.063
.500
.750
2.375 +.000 -.005
.375 +.005 -.000
.100±.005
PROPRIETARY AND CONFIDENTIAL
THE INFORMATION CONTAINED IN THIS DRAWING IS THE SOLE PROPERTY OF <INSERT COMPANY NAME HERE>. ANY REPRODUCTION IN PART OR AS A WHOLE WITHOUT THE WRITTEN PERMISSION OF <INSERT COMPANY NAME HERE> IS PROHIBITED.
UNLESS OTHERWISE SPECIFIED:
DIMENSIONS ARE IN INCHES
TOLERANCES:
FRACTIONAL ±
ANGULAR: MACH ± BEND ±
TWO PLACE DECIMAL ± .01
THREE PLACE DECIMAL ± .005
INTERPRET GEOMETRIC TOLERANCING PER:
MATERIAL
6061 ALUMINUM
FINISH
DO NOT SCALE DRAWING
NAME
DATE
DRAWN
SW
8/4/11
CHECKED
ENG APPR.
MFG APPR.
Q.A.
COMMENTS:
NO SHARP EDGES
NEXT ASSY
USED ON
APPLICATION
TITLE:
SIZE
B
DWG. NO.
LID
SCALE: 1:1
WEIGHT:
SHEE
Customiz

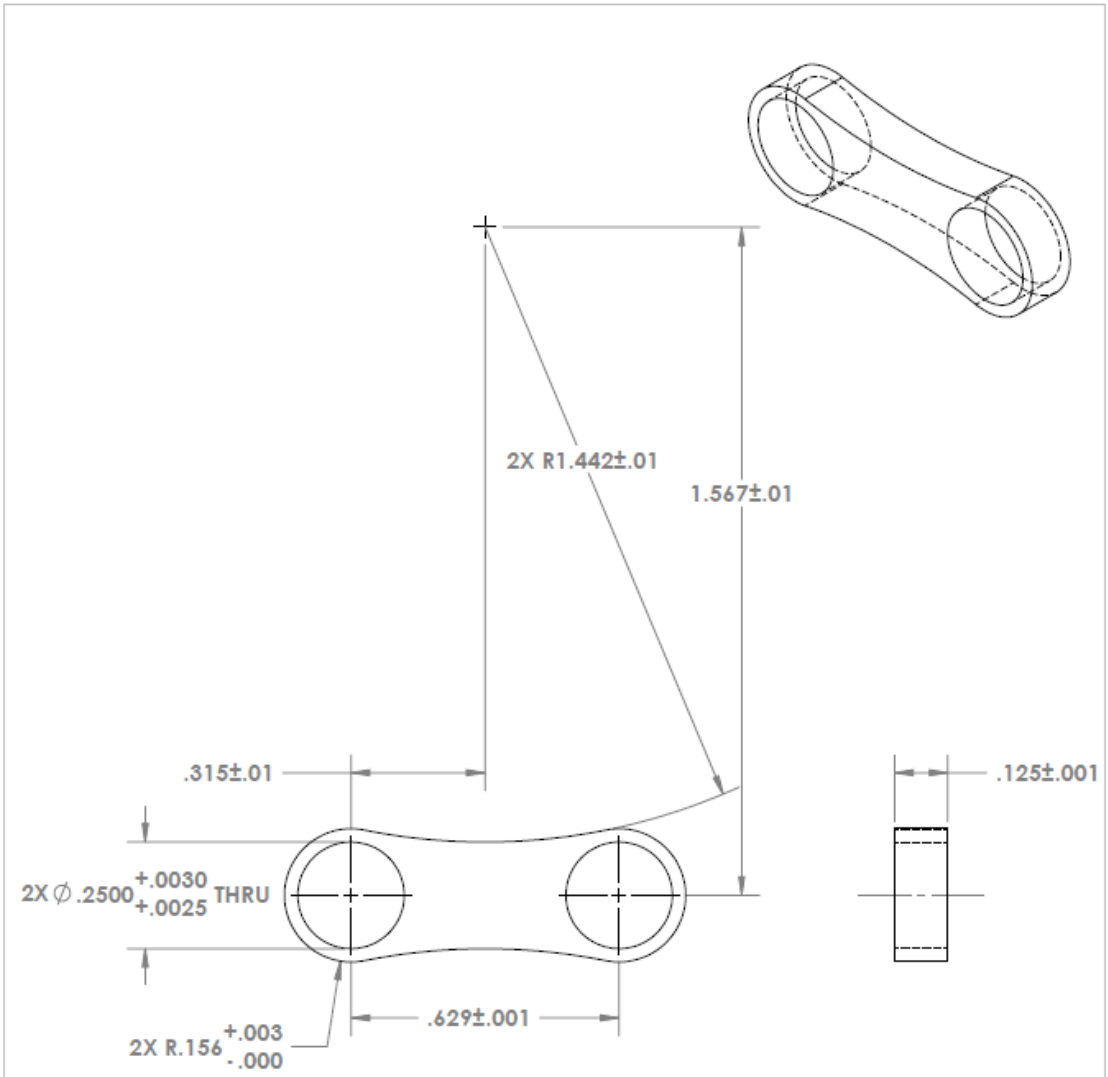

		DIMENSIONS ARE IN INCHES TOLERANCES: ALL TOLERANCES CALLED OUT ON SHEET		NAME	DATE
			DRAWN	SW	4/16/2012
			CHECKED		
			ENG APPR.		
			MFG APPR.		
		MATERIAL 4140 STEEL	Q.A.		
NEXT ASSY	USED ON	FINISH	COMMENTS: NORMALIZED TO ROCKWELL 32C NO SHARP EDGES		
APPLICATION		DO NOT SCALE DRAWING	SIZE A	DWG. NO. Link 3	REV.
			SCALE:3:1	WEIGHT:	SHEET 1 OF 1

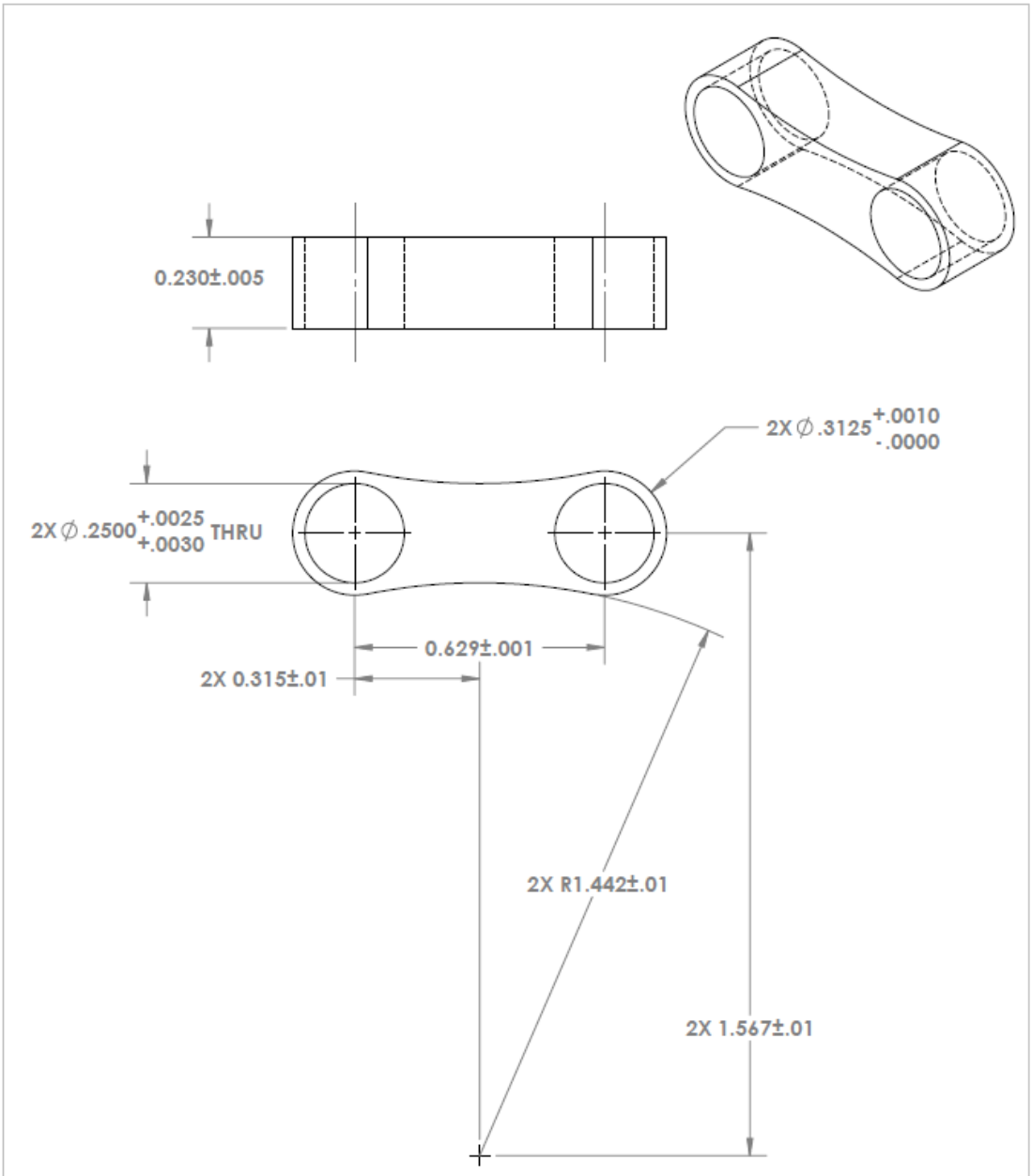

		DIMENSIONS ARE IN INCHES TOLERANCES: ALL TOLERANCES CALLED OUT ON SHEET		NAME	DATE	
			DRAWN	SW	4/16/2012	
			CHECKED			
			ENG APPR.			
			MFG APPR.			
		MATERIAL 4140 STEEL	Q.A.			
		FINISH	COMMENTS: NORMALIZED TO ROCKWELL 32C NO SHARP EDGES			SIZE A; DWG. NO. LINK 4; REV.
NEXT ASSY	USED ON					SCALE:3:1; WEIGHT:; SHEET 1 OF 1
APPLICATION		DO NOT SCALE DRAWING				

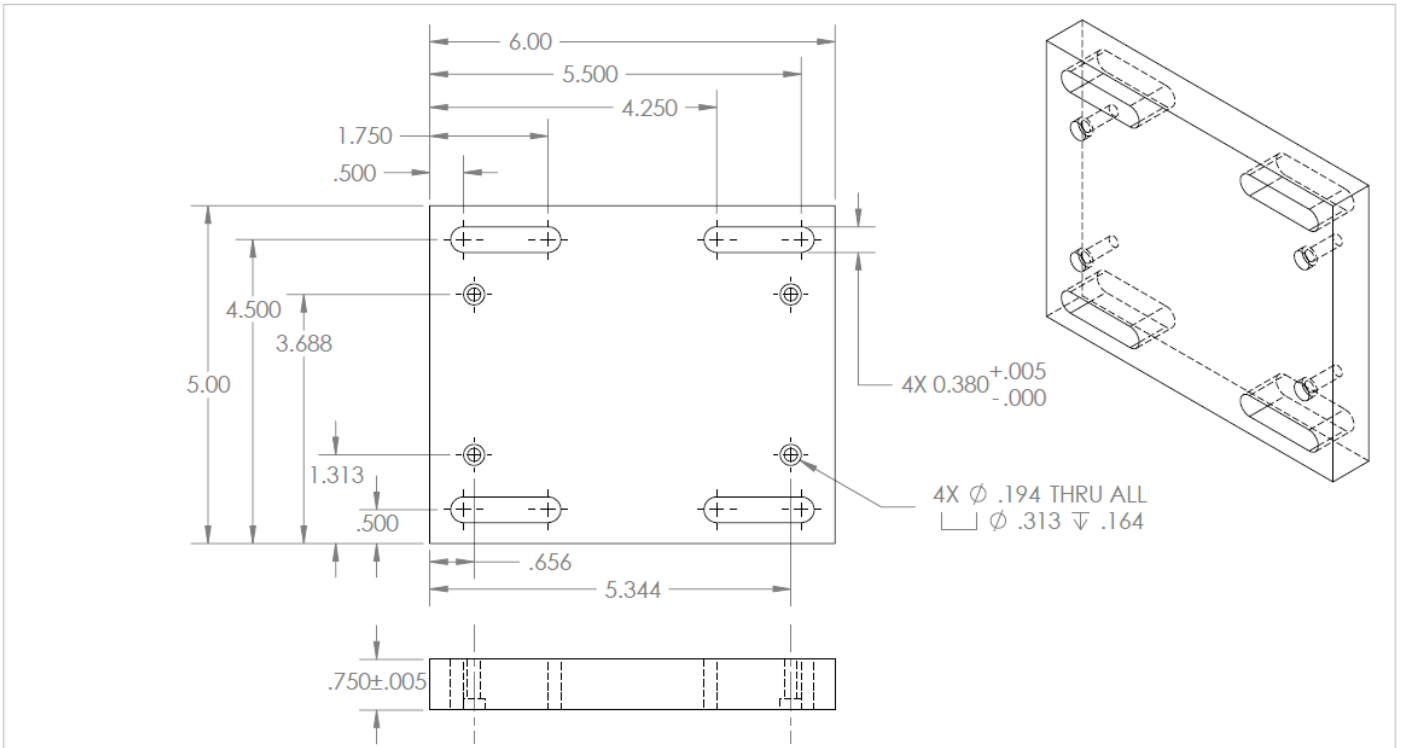

		UNLESS OTHERWISE SPECIFIED:		NAME	DATE
		DIMENSIONS ARE IN INCHES TOLERANCES:	DRAWN	SW	8/4/11
			CHECKED		
		TWO PLACE DECIMAL ±.01 THREE PLACE DECIMAL ±.005	ENG APPR.		
			MFG APPR.		
		INTERPRET GEOMETRIC TOLERANCING PER:	Q.A.		
		MATERIAL 6061 ALUMINUM	COMMENTS: NO SHARP EDGES		
NEXT ASSY	USED ON	FINISH			
APPLICATION		DO NOT SCALE DRAWING			

TITLE:

SIZE A | DWG. NO. MOUNTING PLATE | REV

SCALE: 1:2 | WEIGHT: | SHEET 1 OF 1

5 4 3 2 1

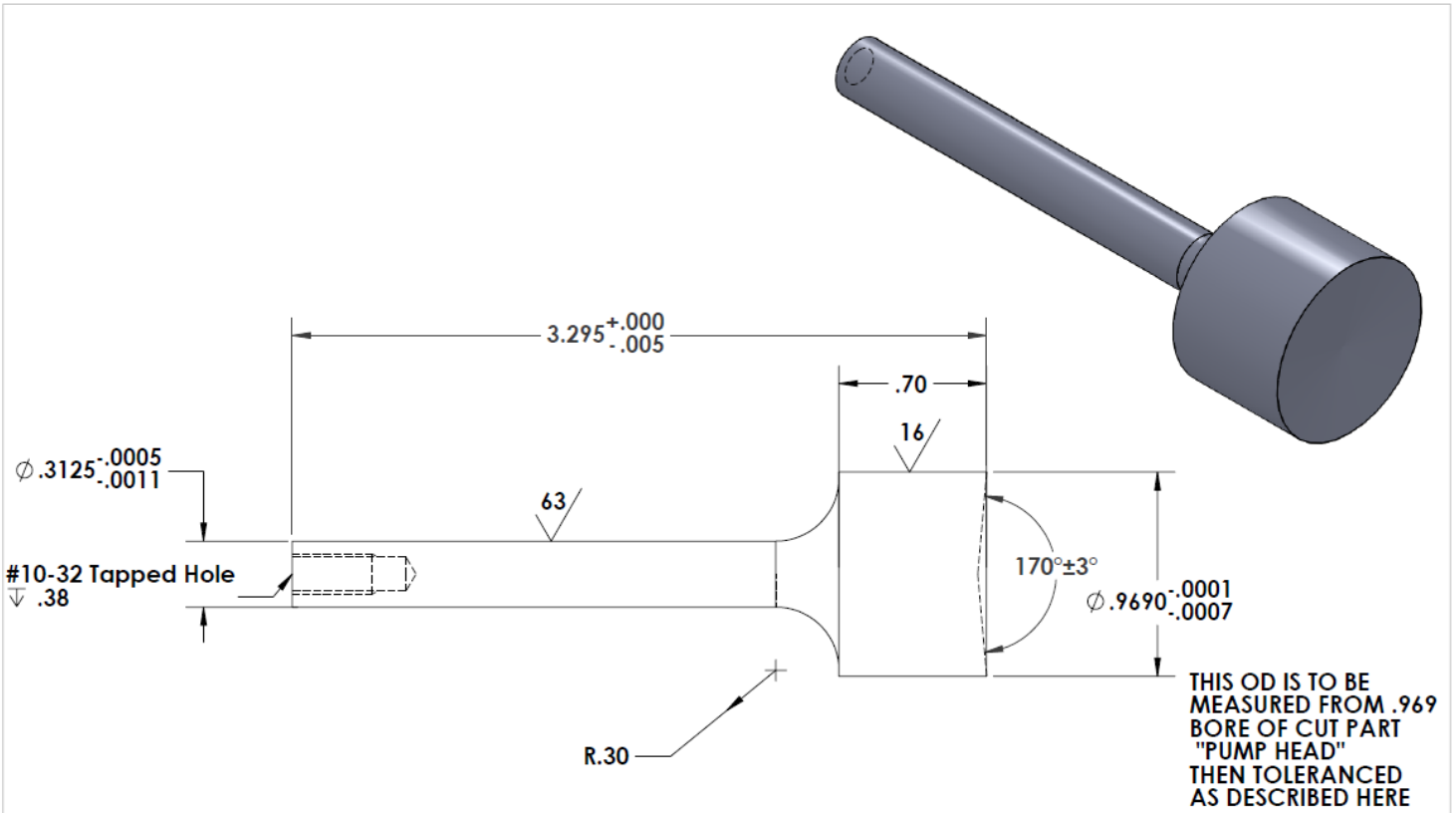

UNLESS OTHERWISE SPECIFIED:		NAME	DATE		
DIMENSIONS ARE IN INCHES TOLERANCES: TWO PLACE DECIMAL ±0.01 THREE PLACE DECIMAL ±.005	DRAWN	SW	7/22/12	TITLE:	
	CHECKED				Piston
	ENG APPR.				
	MFG APPR.				
INTERPRET GEOMETRIC TOLERANCING PER:	Q.A.			SIZE A	DWG. NO. REV 1
MATERIAL 52100 STEEL	COMMENTS: HARDENED TO ROCKWELL C60			SCALE: 1.5:1	WEIGHT: SHEET 1 OF 1
FINISH	NO SHARP EDGES				
NEXT ASSY / USED ON					
APPLICATION	DO NOT SCALE DRAWING				

5 4 3 2 1

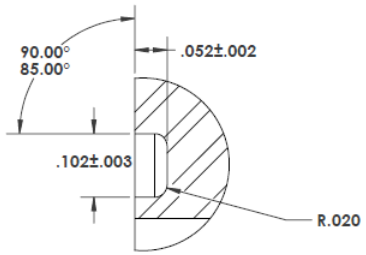

DETAIL C
SCALE 6 : 1

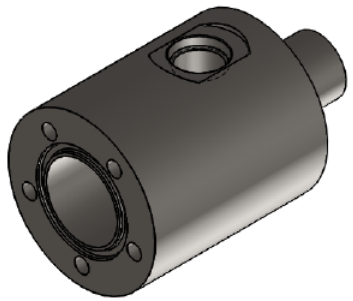

*Use J1926-1 or MS16142 Porting Tool For Cutting O-Ring Boss

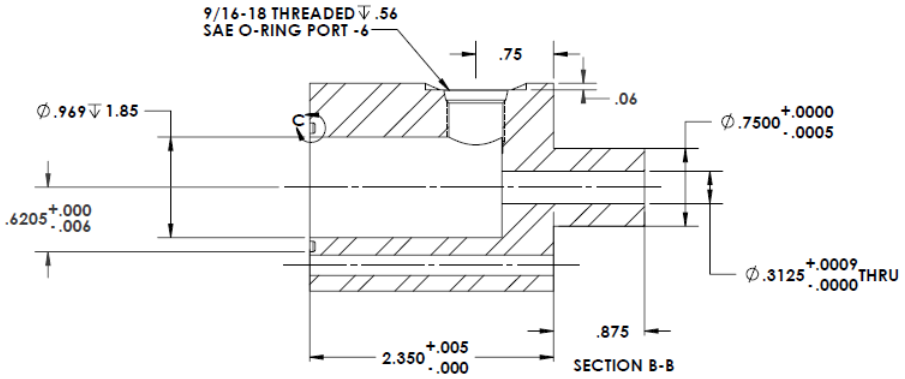

SECTION B-B

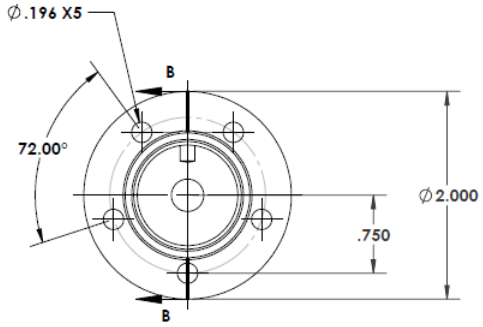

		UNLESS OTHERWISE SPECIFIED:		NAME	DATE
		DIMENSIONS ARE IN INCHES TOLERANCES: ANGULAR: MACH ± BEND ± TWO PLACE DECIMAL ±.01 THREE PLACE DECIMAL ±.005	DRAWN	SW	7/24/12
			CHECKED		
			ENG APPR.		
			MFG APPR.		
		INTERPRET GEOMETRIC TOLERANCING PER:	Q.A.		
		MATERIAL 52100 STEEL	COMMENTS: NO SHARP EXTERNAL EDGES HARDENED TO ROCKEWLL C60		
NEXT ASSY	USED ON	FINISH			
APPLICATION		DO NOT SCALE DRAWING			

TITLE: **Pump head**

SIZE	DWG. NO.	REV
B		
SCALE: 1:1	WEIGHT:	SHEET 1 OF 1

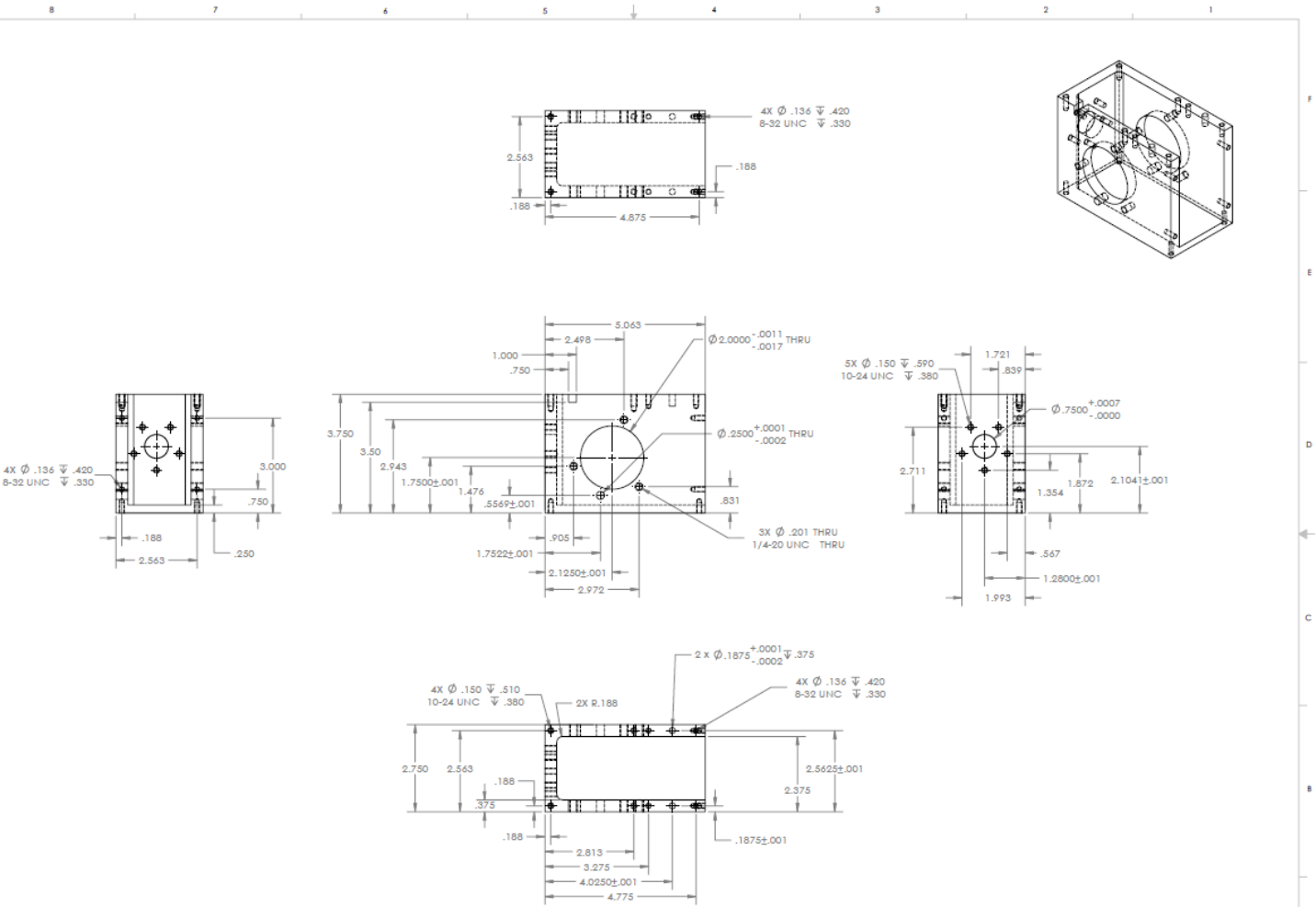

		UNLESS OTHERWISE SPECIFIED:		NAME	DATE
		DIMENSIONS ARE IN INCHES	DRAWN	SW	11/4/11
		TOLERANCES:	CHECKED		
		TWO PLACE DECIMAL ±.01	ENG APPR.		
		THREE PLACE DECIMAL ±.002	MFG APPR.		
		INTERPRET GEOMETRIC TOLERANCING PER:	Q.A.		
		MATERIAL: 6061ALUMINUM	COMMENTS: NO SHARP EDGES		
		FINISH			
NEXT ASSY	USED ON				
APPLICATION					

PROPRIETARY AND CONFIDENTIAL
THE INFORMATION CONTAINED IN THIS DRAWING IS THE SOLE PROPERTY OF <INSERT COMPANY NAME HERE>. ANY REPRODUCTION IN PART OR AS A WHOLE WITHOUT THE WRITTEN PERMISSION OF <INSERT COMPANY NAME HERE> IS PROHIBITED.

TITLE:

SIZE	DWG. NO.	REV
C	PUMP BODY	
SCALE: 1:2	WEIGHT:	SHEET 1 OF 1

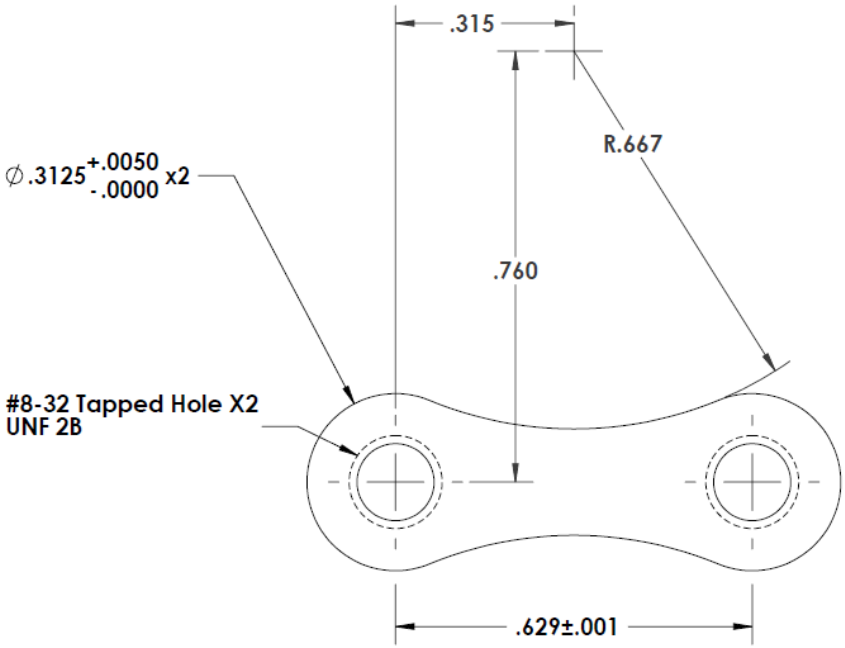

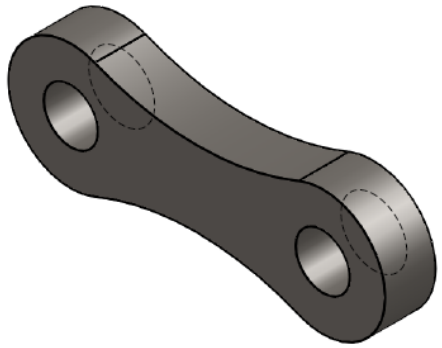

		UNLESS OTHERWISE SPECIFIED:		NAME	DATE
		DIMENSIONS ARE IN INCHES TOLERANCES: TWO PLACE DECIMAL ±.01 THREE PLACE DECIMAL ±.005	DRAWN		
			CHECKED		
			ENG APPR.		
			MFG APPR.		
		INTERPRET GEOMETRIC TOLERANCING PER:	Q.A.		
		MATERIAL A2 TOOL STEEL	COMMENTS: HARDENED TO ROCKWELL 46C NO SHARP EDGES		
NEXT ASSY	USED ON	FINISH			
APPLICATION		DO NOT SCALE DRAWING			

TITLE:

r5 dogbone redesign

SIZE	DWG. NO.	REV
A		

SCALE: 4:1	WEIGHT:	SHEET 1 OF 1

5 4 3 2 1

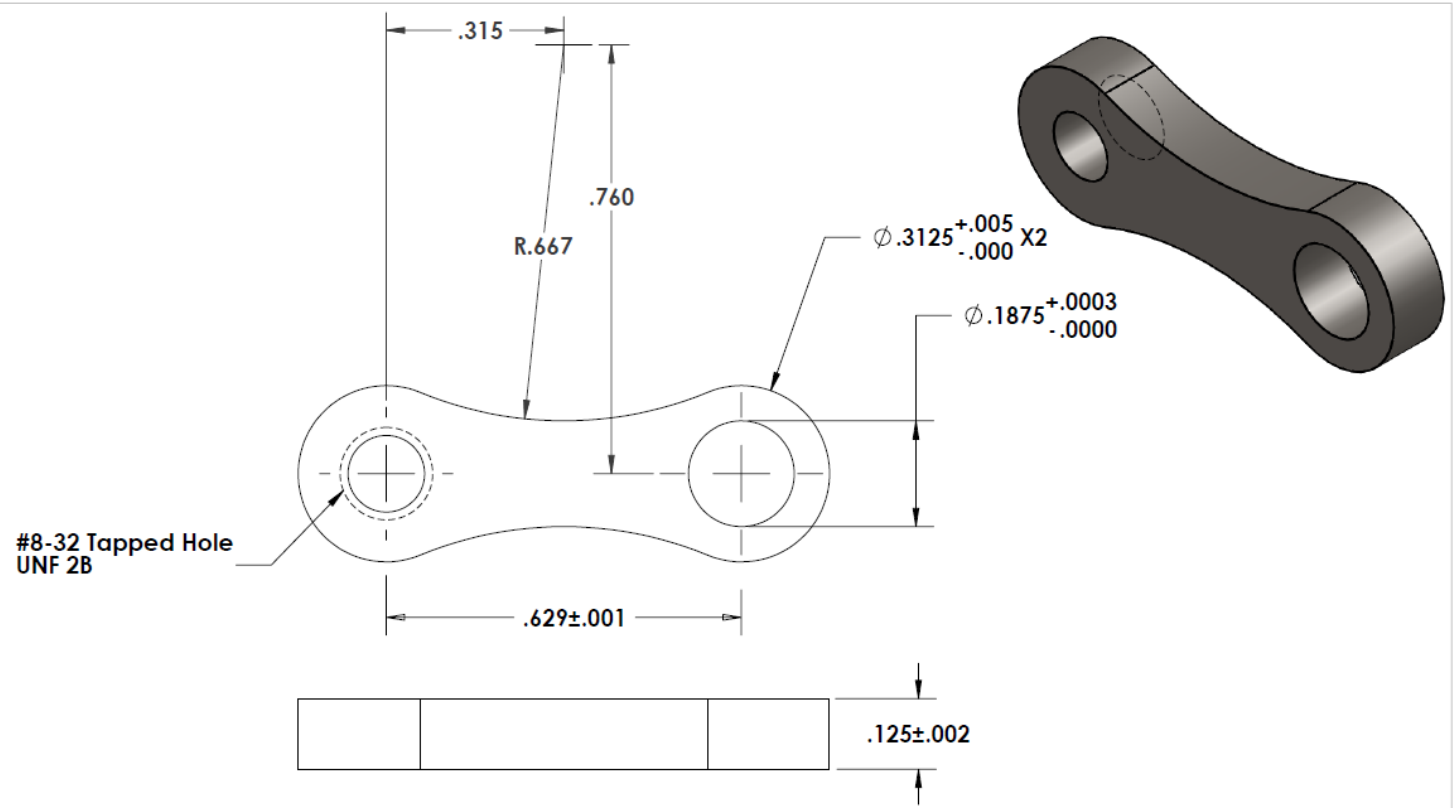

		UNLESS OTHERWISE SPECIFIED:		NAME	DATE	
		DIMENSIONS ARE IN INCHES TOLERANCES:	DRAWN			TITLE:
			CHECKED			r5 dogbone redesign 2
		TWO PLACE DECIMAL ±.01 THREE PLACE DECIMAL ±.005	ENG APPR.			
			MFG APPR.			
		INTERPRET GEOMETRIC TOLERANCING PER:	Q.A.			
		MATERIAL A2 TOOL STEEL	COMMENTS: HARDENED TO ROCKWELL C46 NO SHARP EDGES			SIZE A / DWG. NO. / REV
NEXT ASSY	USED ON	FINISH				
APPLICATION		DO NOT SCALE DRAWING				SCALE: 4:1 / WEIGHT: / SHEET 1 OF 1

5 4 3 2 1

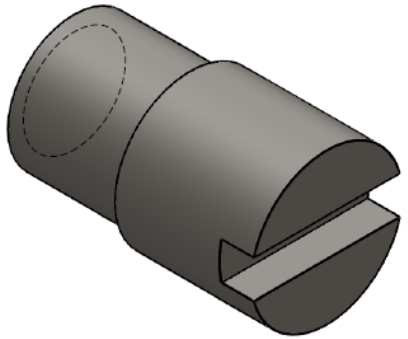

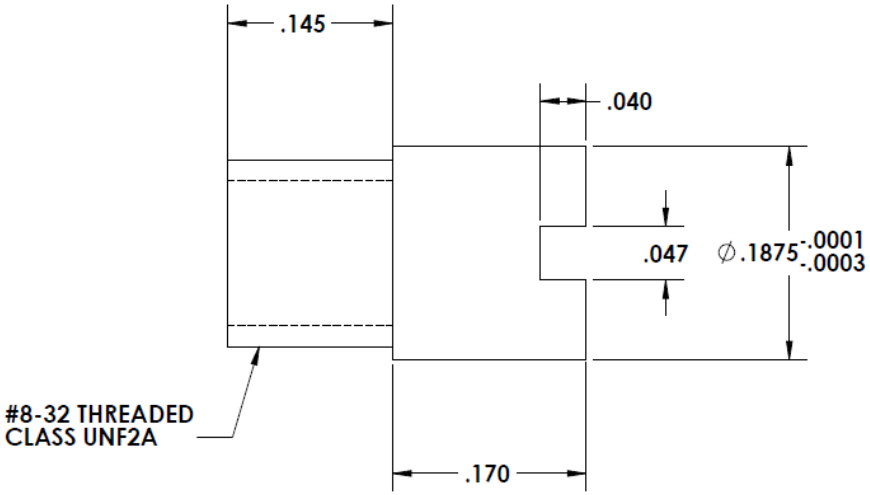

		UNLESS OTHERWISE SPECIFIED:		NAME	DATE	
		DIMENSIONS ARE IN INCHES TOLERANCES: FRACTIONAL ± ANGULAR: MACH ± BEND ± TWO PLACE DECIMAL ±.01 THREE PLACE DECIMAL ±.005	DRAWN			TITLE: R5 threaded pin
			CHECKED			
			ENG APPR.			
			MFG APPR.			
		INTERPRET GEOMETRIC TOLERANCING PER:	Q.A.			
PROPRIETARY AND CONFIDENTIAL THE INFORMATION CONTAINED IN THIS DRAWING IS THE SOLE PROPERTY OF <INSERT COMPANY NAME HERE>. ANY REPRODUCTION IN PART OR AS A WHOLE WITHOUT THE WRITTEN PERMISSION OF <INSERT COMPANY NAME HERE> IS PROHIBITED.		MATERIAL A2 Tool Steel	COMMENTS: HARDENED TO ROCKWELL C46			SIZE A | DWG. NO. | REV
NEXT ASSY	USED ON	FINISH				
APPLICATION		DO NOT SCALE DRAWING				SCALE: 8:1 | WEIGHT: | SHEET 1 OF 1

5 4 3 2 1

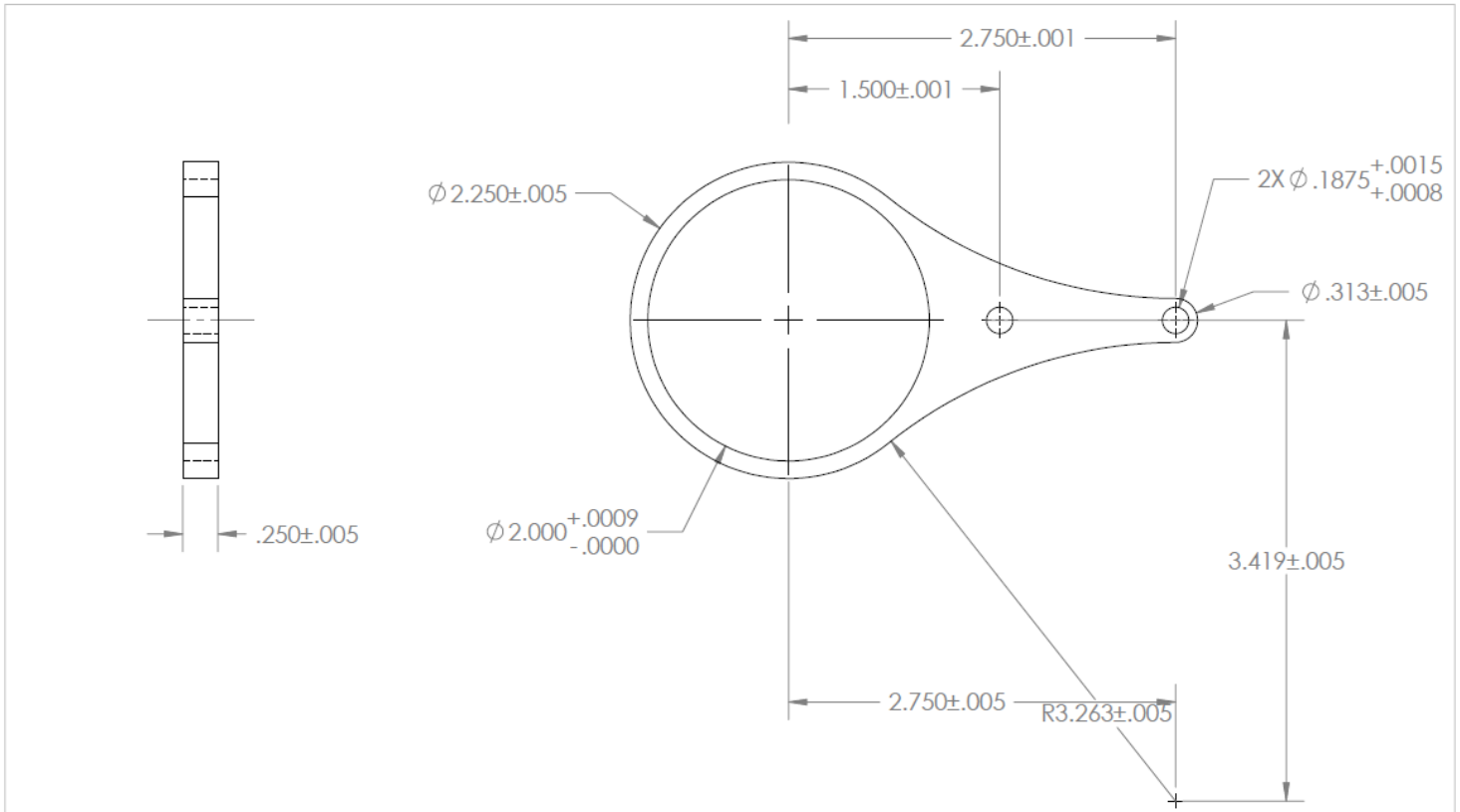

		UNLESS OTHERWISE SPECIFIED:		NAME	DATE
		DIMENSIONS ARE IN INCHES TOLERANCES: ALL TOLERANCES CALLED OUT ON SHEET	DRAWN	SW	8/3/11
			CHECKED		
			ENG APPR.		
			MFG APPR.		
		INTERPRET GEOMETRIC TOLERANCING PER:	Q.A.		
		MATERIAL 4340 STEEL	COMMENTS: HARDENED TO ROCKWELL 46C NO SHARP EDGES		
NEXT ASSY	USED ON	FINISH			
APPLICATION		DO NOT SCALE DRAWING			

TITLE:

SIZE	DWG. NO.	REV
A	Swimgarm	
SCALE: 1:1	WEIGHT:	SHEET 1 OF 1

5 4 3 2 1

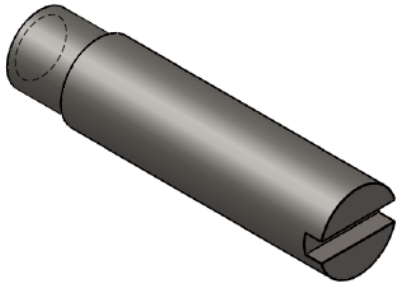

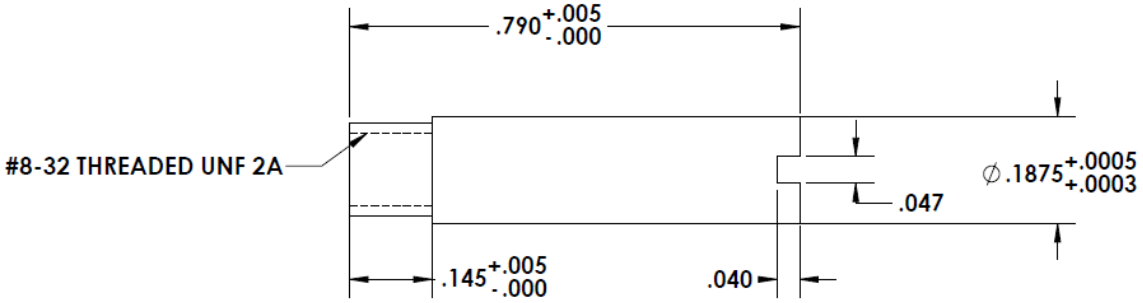

		UNLESS OTHERWISE SPECIFIED:		NAME	DATE
		DIMENSIONS ARE IN INCHES TOLERANCES: FRACTIONAL ± ANGULAR: MACH ± BEND ± TWO PLACE DECIMAL ±.01 THREE PLACE DECIMAL ±.005	DRAWN	SW	7/25/12
			CHECKED		
			ENG APPR.		
			MFG APPR.		
		INTERPRET GEOMETRIC TOLERANCING PER:	Q.A.		
		MATERIAL A2 TOOL STEEL	COMMENTS: HARDENED TO ROCKWELL C46		
NEXT ASSY	USED ON	FINISH			
APPLICATION		DO NOT SCALE DRAWING			

TITLE:

SIZE	DWG. NO.	REV
A	Ternary Pin	

SCALE: 4:1	WEIGHT:	SHEET 1 OF 1

5 4 3 2 1

Appendix C Three Cylinder Prototype Part Drawings

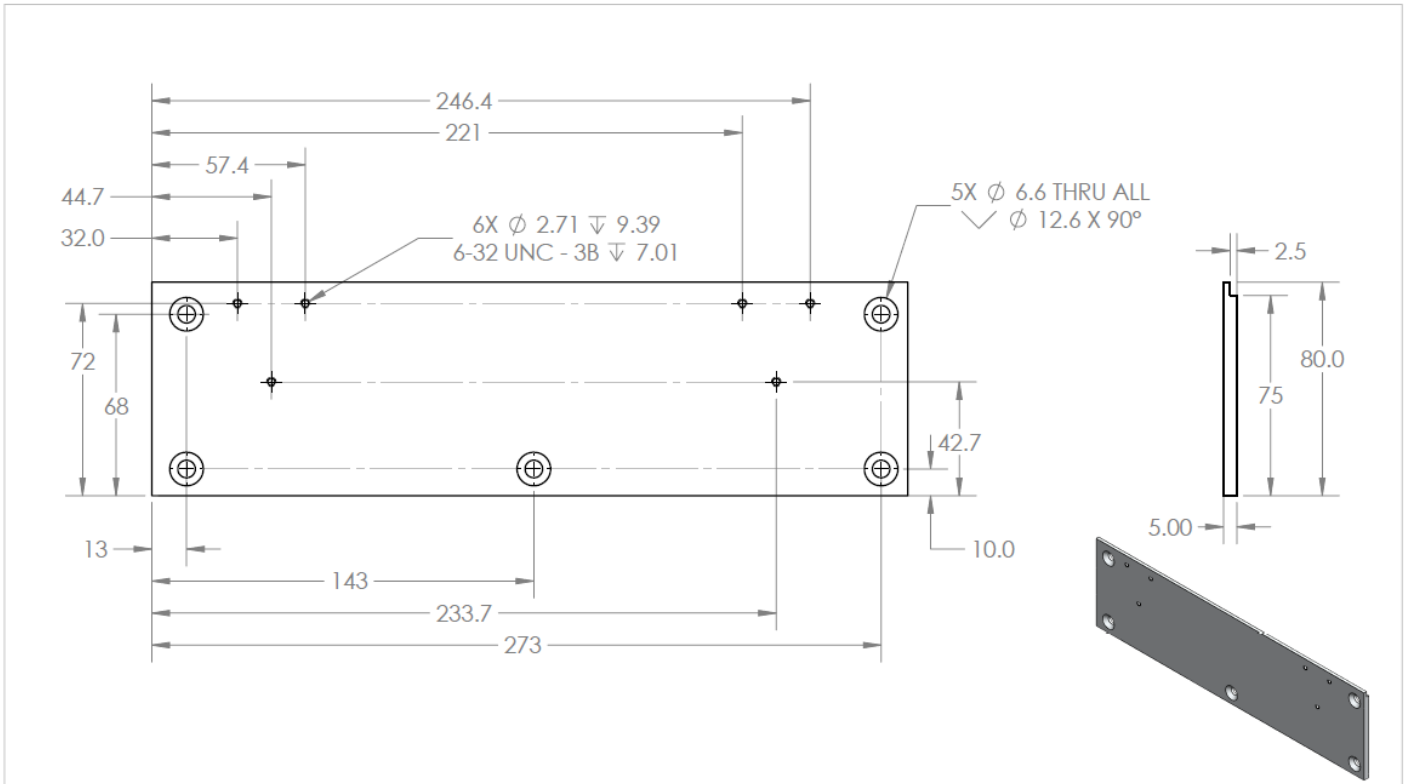

		UNLESS OTHERWISE SPECIFIED:		NAME	DATE
		DIMENSIONS ARE IN mm TOLERANCES: ZERO PLACE DECIMAL ± .25 ONE PLACE DECIMAL ± .12 TWO PLACE DECIMAL ± .05	DRAWN	SW	12-3-13
			CHECKED		
			ENG APPR.		
			MFG APPR.		
		INTERPRET GEOMETRIC TOLERANCING PER:	Q.A.		
		MATERIAL 6061 ALUMINUM	COMMENTS: -		
NEXT ASSY	USED ON	FINISH			
APPLICATION		DO NOT SCALE DRAWING			

TITLE:

Back Plate Lower

SIZE	DWG. NO.	REV
A	GP14	1

SCALE: 1:2 | WEIGHT: | SHEET 1 OF 1

5 4 3 2 1

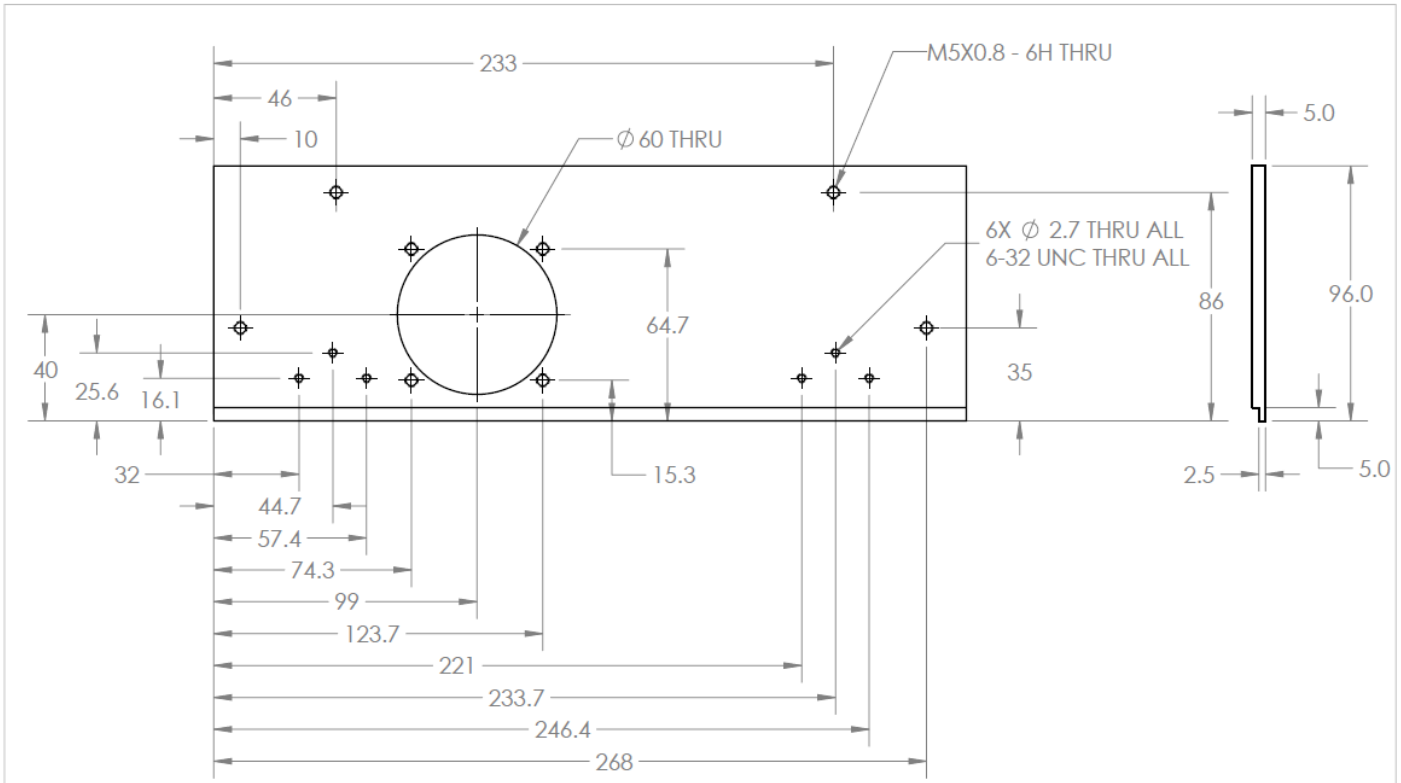

		UNLESS OTHERWISE SPECIFIED:		NAME	DATE
		DIMENSIONS ARE IN mm TOLERANCES: ZERO PLACE DECIMAL ± .12 ONE PLACE DECIMAL ± .08 TWO PLACE DECIMAL ± .04	DRAWN	SW	12-3-13
			CHECKED		
			ENG APPR.		
			MFG APPR.		
			Q.A.		
		INTERPRET GEOMETRIC TOLERANCING PER:	COMMENTS:		
		MATERIAL 6061 ALUMINUM	-		
NEXT ASSY	USED ON	FINISH			
APPLICATION		DO NOT SCALE DRAWING			

TITLE: Back Plate Upper

SIZE	DWG. NO.	REV
A	CB4	1

SCALE: 1:2 | WEIGHT: | SHEET 1 OF 1

5 4 3 2 1

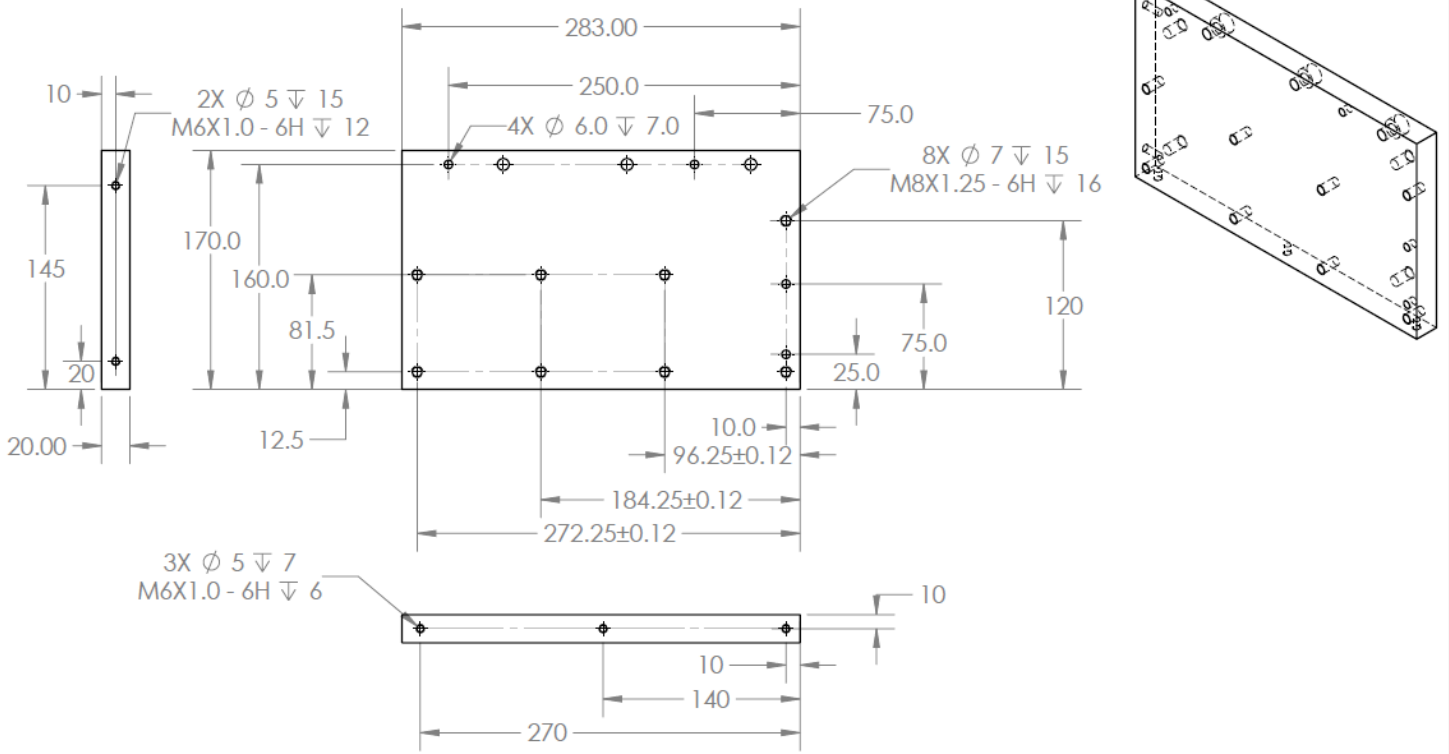

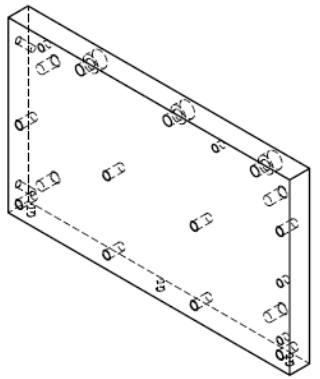

		UNLESS OTHERWISE SPECIFIED:		NAME	DATE
		DIMENSIONS ARE IN mm TOLERANCES: ZERO PLACE DECIMAL ± .12 ONE PLACE DECIMAL ± .08 TWO PLACE DECIMAL ± .03	DRAWN	SW	12-3-13
			CHECKED		
			ENG APPR.		
			MFG APPR.		
		INTERPRET GEOMETRIC TOLERANCING PER:	Q.A.		
		MATERIAL 7075-T6 ALUMINUM	COMMENTS: -		
NEXT ASSY	USED ON	FINISH			
APPLICATION		DO NOT SCALE DRAWING			

TITLE:

Base Plate

SIZE	DWG. NO.	REV
A	GP13	1

SCALE: 1:4 | WEIGHT: | SHEET 1 OF 2

5 4 3 2 1

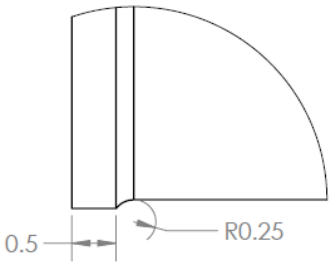

DETAIL B
SCALE 16 : 1

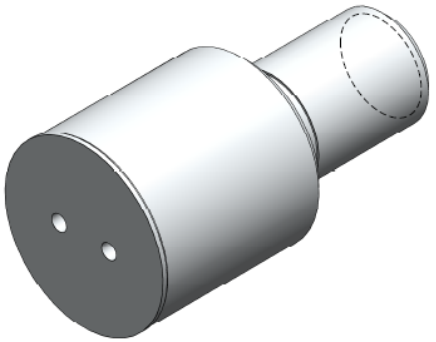

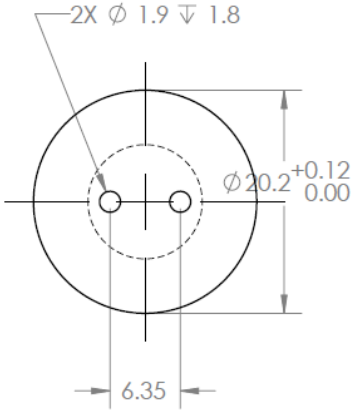

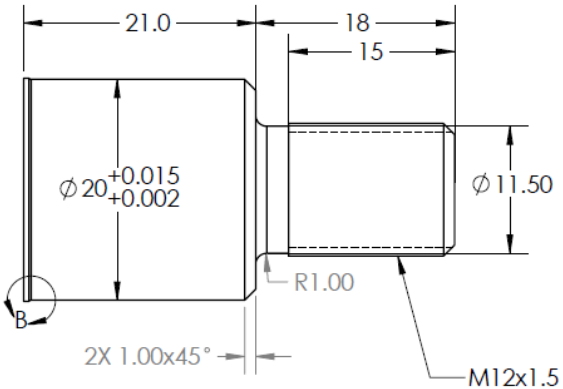

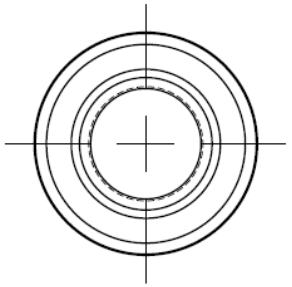

		UNLESS OTHERWISE SPECIFIED:		NAME	DATE
		DIMENSIONS ARE IN mm TOLERANCES: ZERO PLACE DECIMAL ± .12 ONE PLACE DECIMAL ± .08 TWO PLACE DECIMAL ± .03	DRAWN	SW	12-3-13
			CHECKED		
			ENG APPR.		
			MFG APPR.		
		INTERPRET GEOMETRIC TOLERANCING PER:	Q.A.		
		MATERIAL 4140 STEEL	COMMENTS: -		
NEXT ASSY	USED ON	FINISH			
APPLICATION		DO NOT SCALE DRAWING			

TITLE:
CONTROL LINK BOLT

SIZE	DWG. NO.	REV
A	CLR3	1

SCALE: 2:1	WEIGHT:	SHEET 1 OF 1

5 4 3 2 1

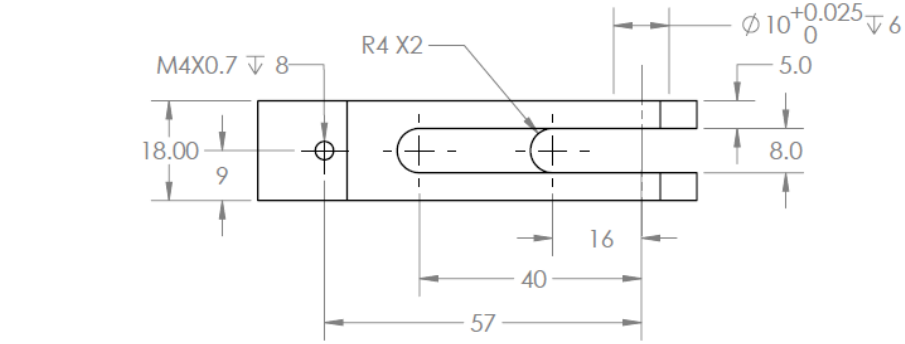

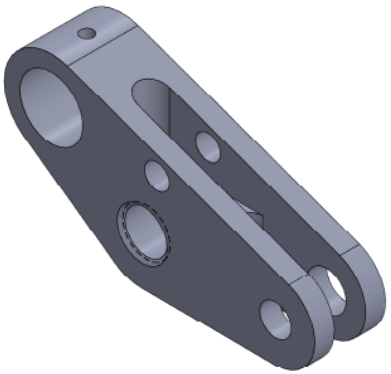

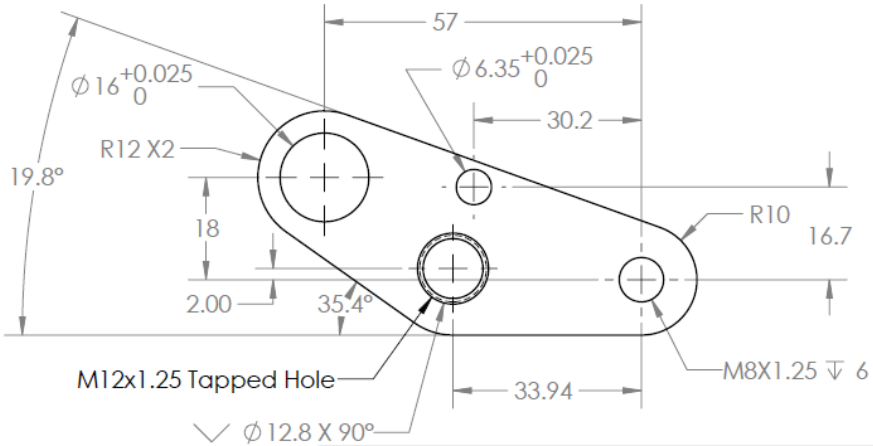

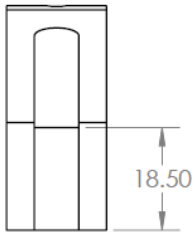

		UNLESS OTHERWISE SPECIFIED:		NAME	DATE	
		DIMENSIONS ARE IN mm TOLERANCES: ZERO PLACE DECIMAL ± .12 ONE PLACE DECIMAL ± .08 TWO PLACE DECIMAL ± .03	DRAWN	SW	12-14-13	TITLE: ADJUSTOR ARM
			CHECKED			
			ENG APPR.			
			MFG APPR.			
		INTERPRET GEOMETRIC TOLERANCING PER:	Q.A.			
		MATERIAL 7075-T6 ALUMINUM	COMMENTS: -			SIZE A / DWG. NO. CLR1 / REV 1
NEXT ASSY	USED ON	FINISH				
APPLICATION		DO NOT SCALE DRAWING				SCALE: 1:1 / WEIGHT: / SHEET 1 OF 1

5 4 3 2 1

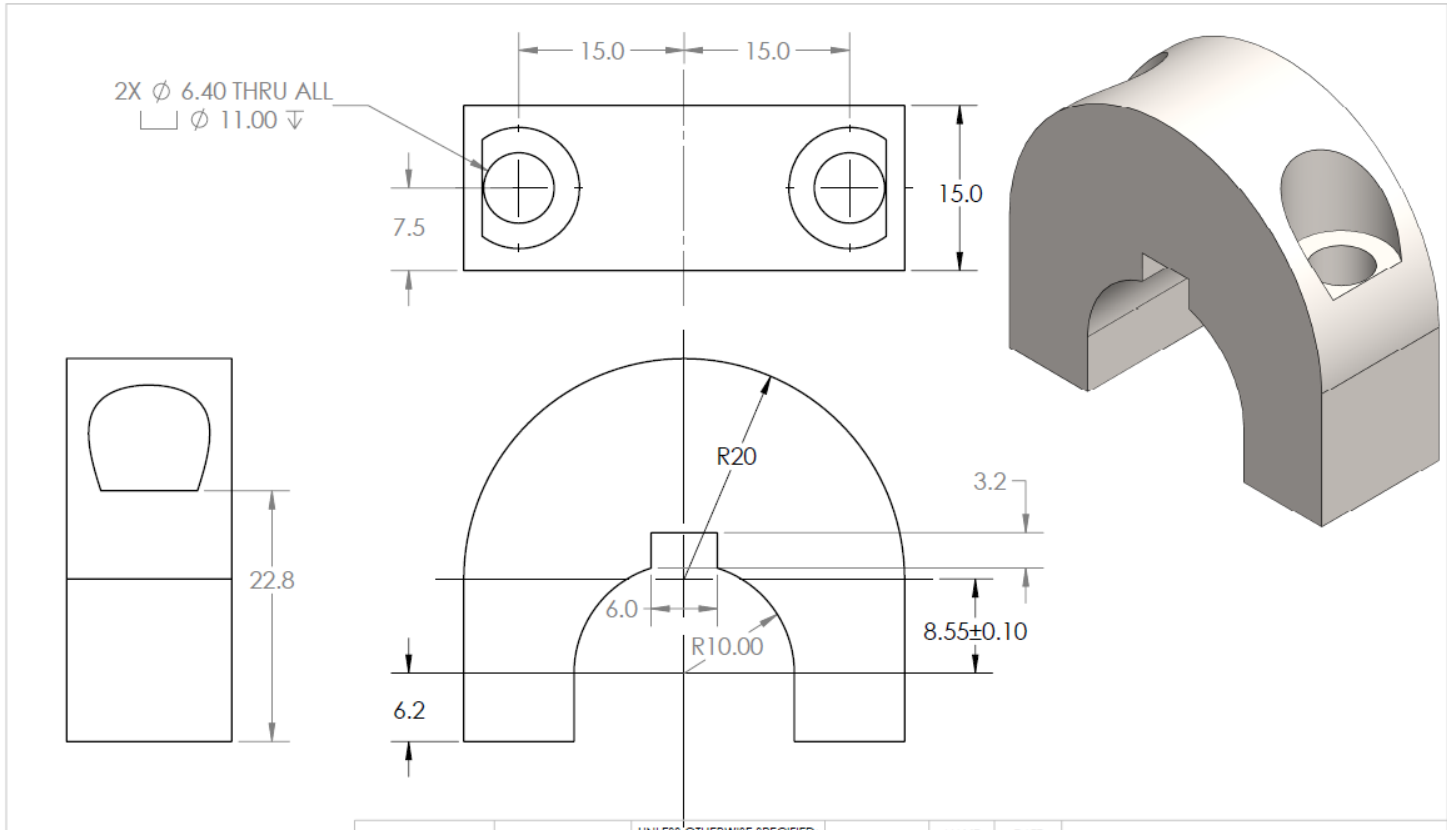

		UNLESS OTHERWISE SPECIFIED:		NAME	DATE
		DIMENSIONS ARE IN mm TOLERANCES: ZERO PLACE DECIMAL ± .12 ONE PLACE DECIMAL ± .08 TWO PLACE DECIMAL ± .03	DRAWN	SW	12-3-13
			CHECKED		
			ENG APPR.		
			MFG APPR.		
		INTERPRET GEOMETRIC TOLERANCING PER:	Q.A.		
		MATERIAL PLAIN CARBON STEEL	COMMENTS: -		
NEXT ASSY	USED ON	FINISH			
APPLICATION		DO NOT SCALE DRAWING			

TITLE:

COUNTER WEIGHT

SIZE	DWG. NO.	REV
A	CS5	1

SCALE: 2:1	WEIGHT:	SHEET 1 OF 1

5 4 3 2 1

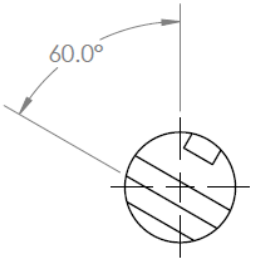

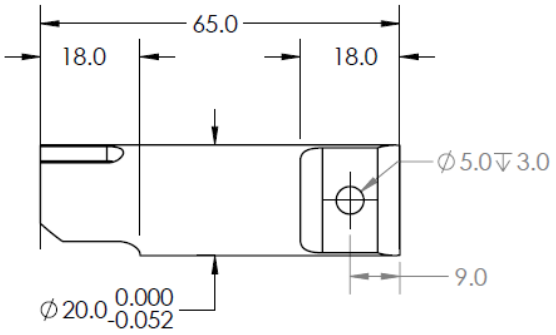

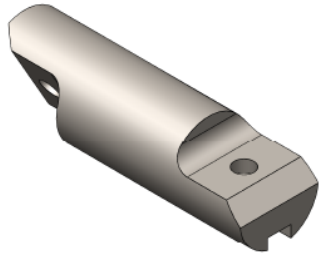

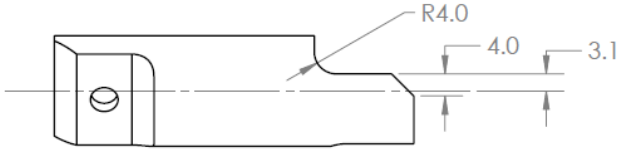

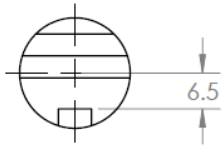

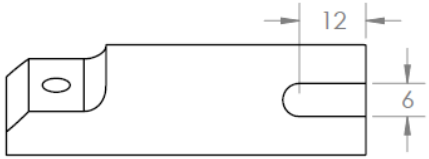

THE TWO FEATURES ON EITHER END OF THE SHAFT ARE IDENTICAL BUT OFFSET BY 60 RELATIVE TO THE SHAFT CENTER

		UNLESS OTHERWISE SPECIFIED:		NAME	DATE
		DIMENSIONS ARE IN mm TOLERANCES: ZERO PLACE DECIMAL ± .12 ONE PLACE DECIMAL ± .08 TWO PLACE DECIMAL ± .03	DRAWN	SW	12-3-13
			CHECKED		
			ENG APPR.		
			MFG APPR.		
			Q.A.		
		INTERPRET GEOMETRIC TOLERANCING PER:	COMMENTS:		
		MATERIAL 4140 STEEL	MADE FROM McMASTER pn 8927K89		
NEXT ASSY	USED ON	FINISH			
APPLICATION		DO NOT SCALE DRAWING			

TITLE: CRANK SHAFT COUPLER

SIZE	DWG. NO.	REV
A	CS2	1

SCALE: 1:1	WEIGHT:	SHEET 1 OF 1

5 4 3 2 1

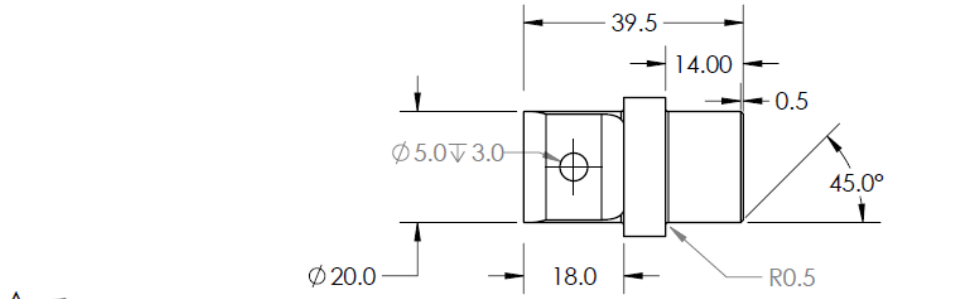

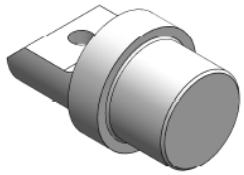

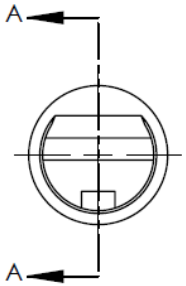

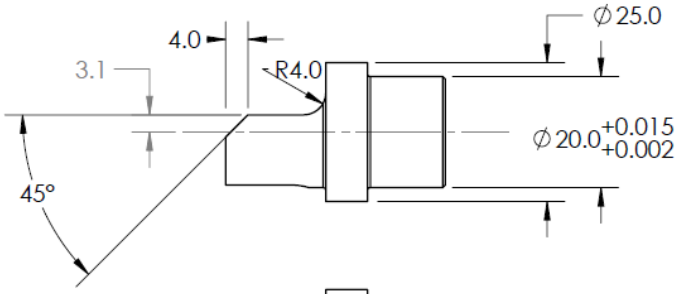

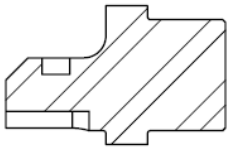

SECTION A-A

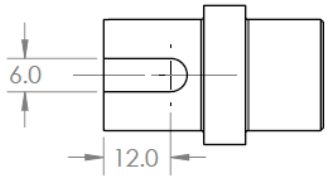

		UNLESS OTHERWISE SPECIFIED:		NAME	DATE
		DIMENSIONS ARE IN mm TOLERANCES: ZERO PLACE DECIMAL ± .12 ONE PLACE DECIMAL ± .08 TWO PLACE DECIMAL ± .03	DRAWN	SW	12-3-13
			CHECKED		
			ENG APPR.		
			MFG APPR.		
		INTERPRET GEOMETRIC TOLERANCING PER:	Q.A.		
		MATERIAL 4140 STEEL	COMMENTS: MADE FROM McMASTER pn 8927K91		
NEXT ASSY	USED ON	FINISH			
APPLICATION		DO NOT SCALE DRAWING			

TITLE:

CRANK SHAFT END

SIZE	DWG. NO.	REV
A	CS3	1

SCALE: 1:1	WEIGHT:	SHEET 1 OF 1

5 4 3 2 1

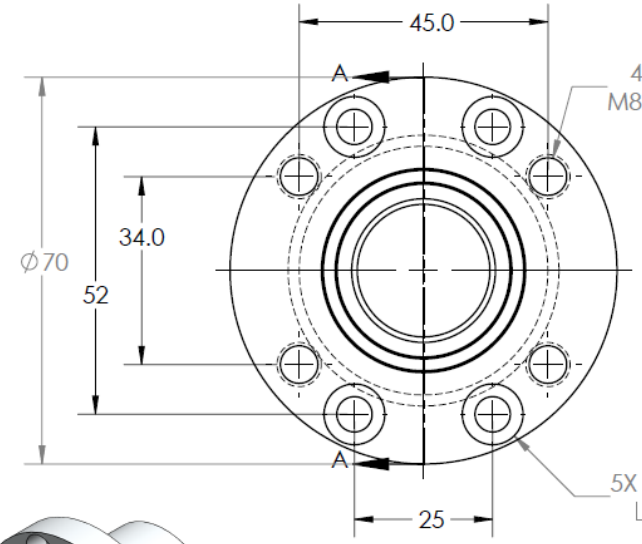

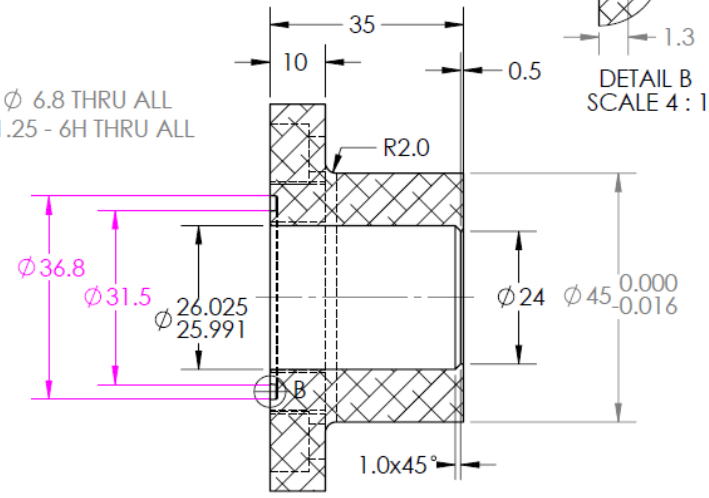

SECTION A-A

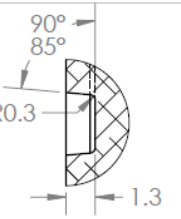

DETAIL B
SCALE 4 : 1

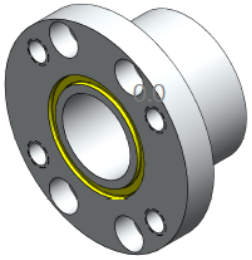

			NAME	DATE
UNLESS OTHERWISE SPECIFIED:		DRAWN	SW	12-3-13
DIMENSIONS ARE IN mm TOLERANCES: ZERO PLACE DECIMAL ± .12 ONE PLACE DECIMAL ± .08 TWO PLACE DECIMAL ± .03		CHECKED		
		ENG APPR.		
		MFG APPR.		
INTERPRET GEOMETRIC TOLERANCING PER:		Q.A.		
MATERIAL 6061 ALUMINUM		COMMENTS: -		
FINISH				
NEXT ASSY	USED ON			
APPLICATION	DO NOT SCALE DRAWING			

TITLE:

CYLINDER RETAINER

SIZE	DWG. NO.	REV
A	PH2	1
SCALE: 1:1	WEIGHT:	SHEET 1 OF 1

5 4 3 2 1

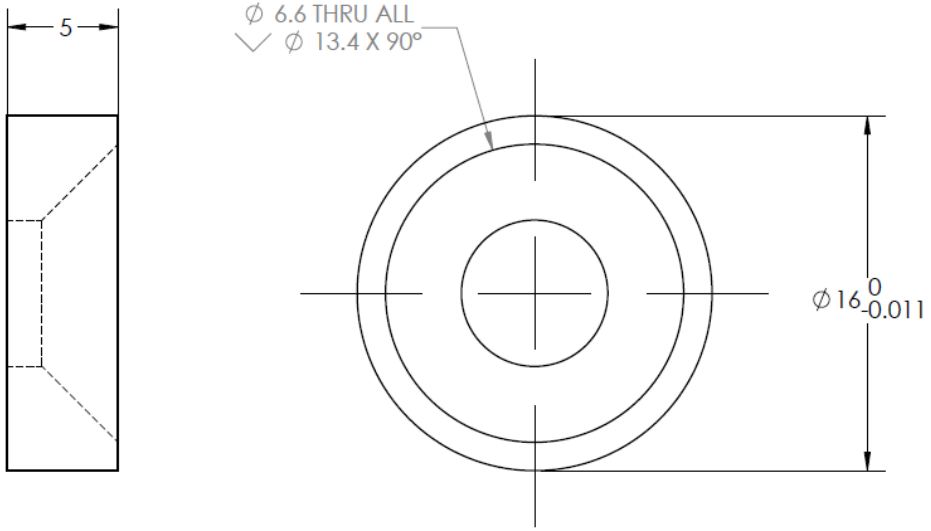

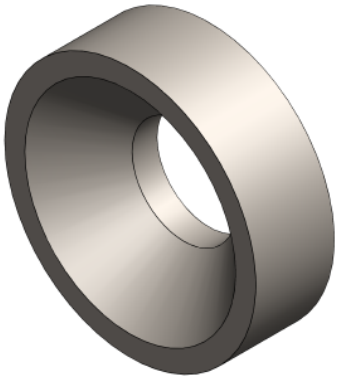

		UNLESS OTHERWISE SPECIFIED:		NAME	DATE
		DIMENSIONS ARE IN mm TOLERANCES: ZERO PLACE DECIMAL ± .12 ONE PLACE DECIMAL ± .08 TWO PLACE DECIMAL ± .03	DRAWN	SW	12-3-13
			CHECKED		
			ENG APPR.		
			MFG APPR.		
		INTERPRET GEOMETRIC TOLERANCING PER:	Q.A.		
		MATERIAL 1055 STEEL	COMMENTS: MADE FROM MCMASTER 6117K107 STOCK OD		
NEXT ASSY	USED ON	FINISH			
APPLICATION		DO NOT SCALE DRAWING			

TITLE:
CYLINDER SUPPORT PIN

SIZE	DWG. NO.	REV
A	CLR8	1
SCALE: 4:1	WEIGHT:	SHEET 1 OF 1

5 4 3 2 1

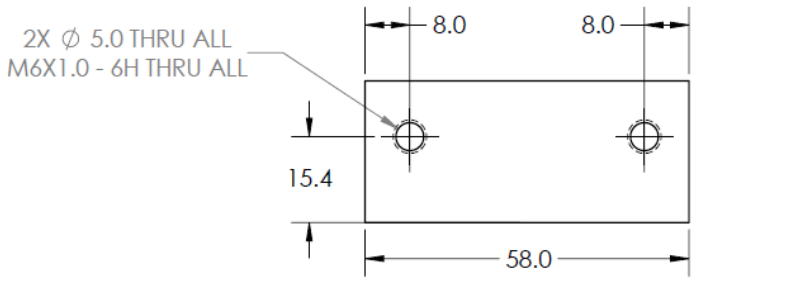

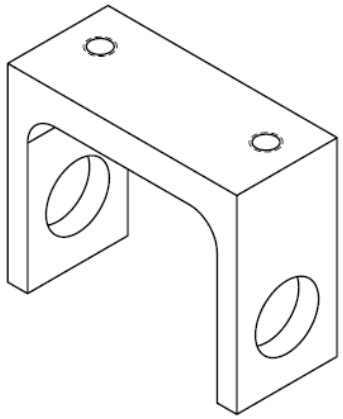

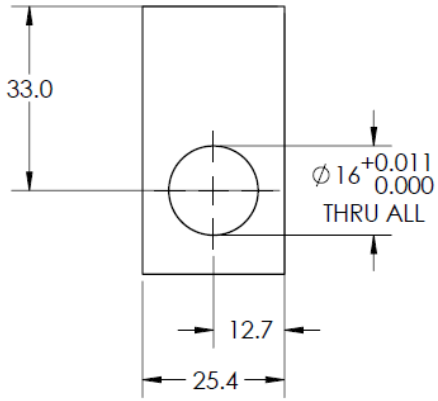

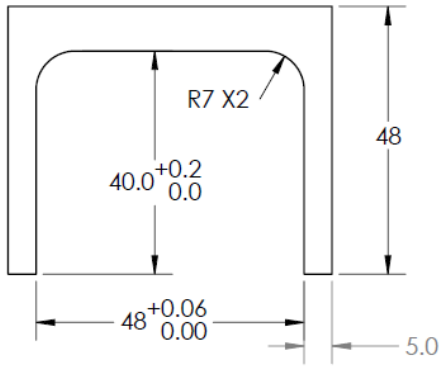

		UNLESS OTHERWISE SPECIFIED:		NAME	DATE
		DIMENSIONS ARE IN mm TOLERANCES: ZERO PLACE DECIMAL ± .12 ONE PLACE DECIMAL ± .08 TWO PLACE DECIMAL ± .03	DRAWN	SW	12-3-13
			CHECKED		
			ENG APPR.		
			MFG APPR.		
		INTERPRET GEOMETRIC TOLERANCING PER:	Q.A.		
		MATERIAL 4130 STEEL	COMMENTS: HARDENED TO ROCKWEL C59 CAN BE MADE FROM MCMASTER PN 89715K977		
NEXT ASSY	USED ON	FINISH			
APPLICATION		DO NOT SCALE DRAWING			

TITLE:

CYLINDER SUPPORT

SIZE	DWG. NO.	REV
A	CLR7	1
SCALE: 1:1	WEIGHT:	SHEET 1 OF 1

5 4 3 2 1

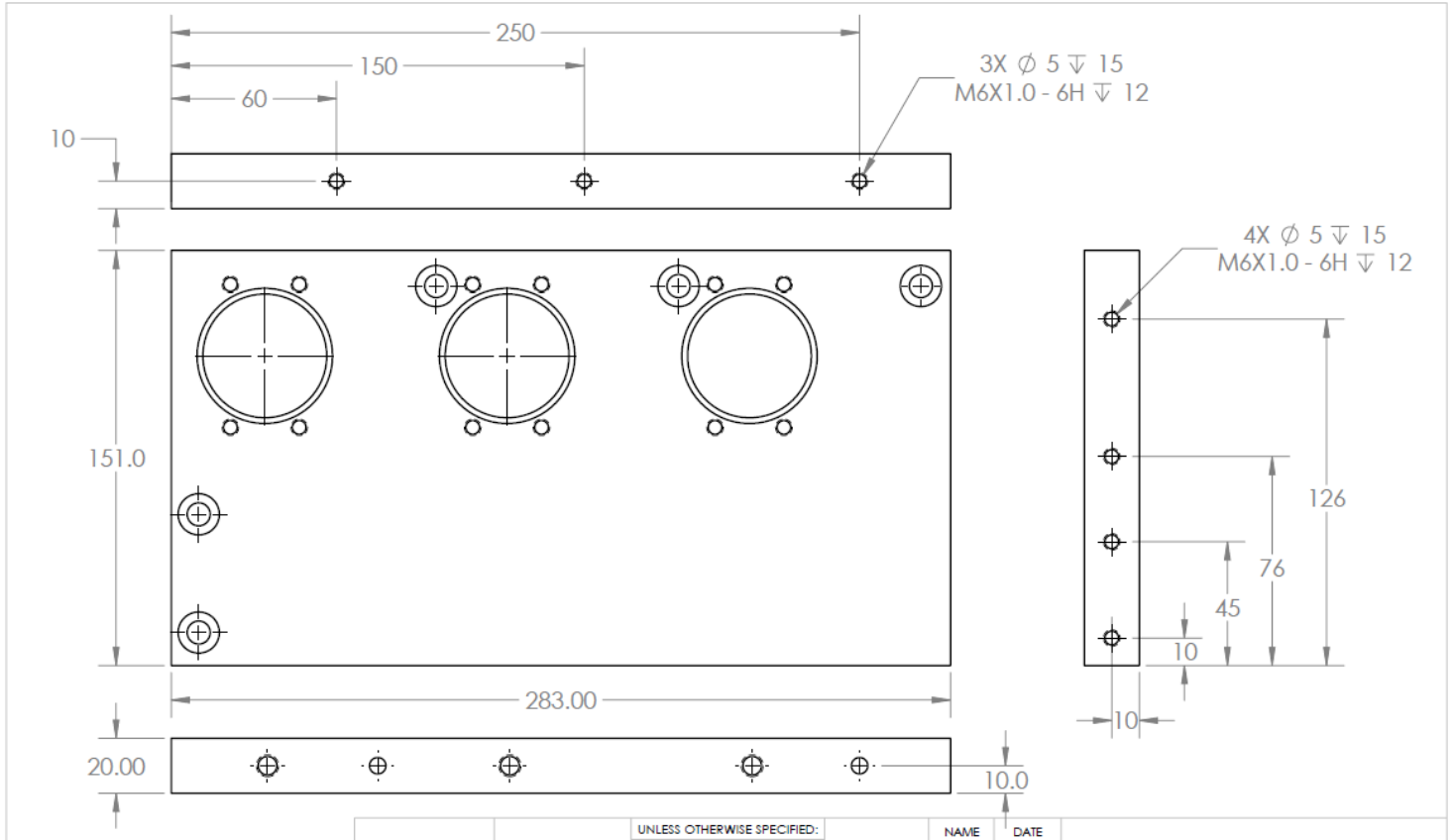

		UNLESS OTHERWISE SPECIFIED:		NAME	DATE
		DIMENSIONS ARE IN mm TOLERANCES: ZERO PLACE DECIMAL ± .12 ONE PLACE DECIMAL ± .08 TWO PLACE DECIMAL ± .03	DRAWN	SW	12-3-13
			CHECKED		
			ENG APPR.		
			MFG APPR.		
		INTERPRET GEOMETRIC TOLERANCING PER:	Q.A.		
		MATERIAL 6061 ALUMINUM	COMMENTS: -		
NEXT ASSY	USED ON	FINISH			
APPLICATION		DO NOT SCALE DRAWING			

TITLE:

Front Plate

SIZE	DWG. NO.	REV
A	PH4	1

SCALE: 1:2 | WEIGHT: | SHEET 1 OF 3

5 4 3 2 1

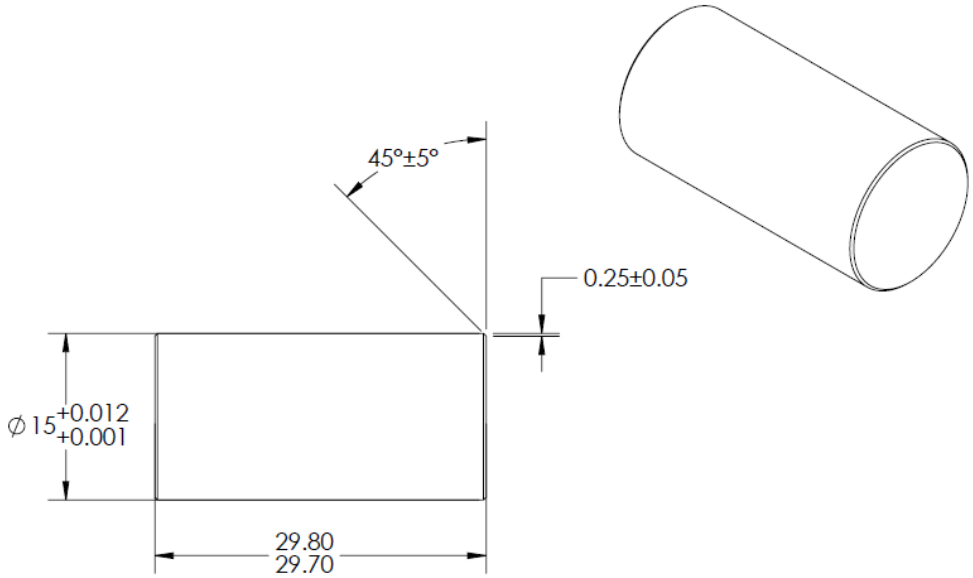

		UNLESS OTHERWISE SPECIFIED:		NAME	DATE
		DIMENSIONS ARE IN mm TOLERANCES: ZERO PLACE DECIMAL ± .1 ONE PLACE DECIMAL ± .05 TWO PLACE DECIMAL ± .01	DRAWN	SW	12-3-13
			CHECKED		
			ENG APPR.		
			MFG APPR.		
		INTERPRET GEOMETRIC TOLERANCING PER:	Q.A.		
		MATERIAL A2 Tool Steel	COMMENTS: Hardened to Rockwell C59		
NEXT ASSY	USED ON	FINISH			
APPLICATION		DO NOT SCALE DRAWING			

TITLE:

Gungeon Pin

SIZE	DWG. NO.	REV
A	SGL8	1

SCALE: 2:1	WEIGHT:	SHEET 1 OF 1

5 4 3 2 1

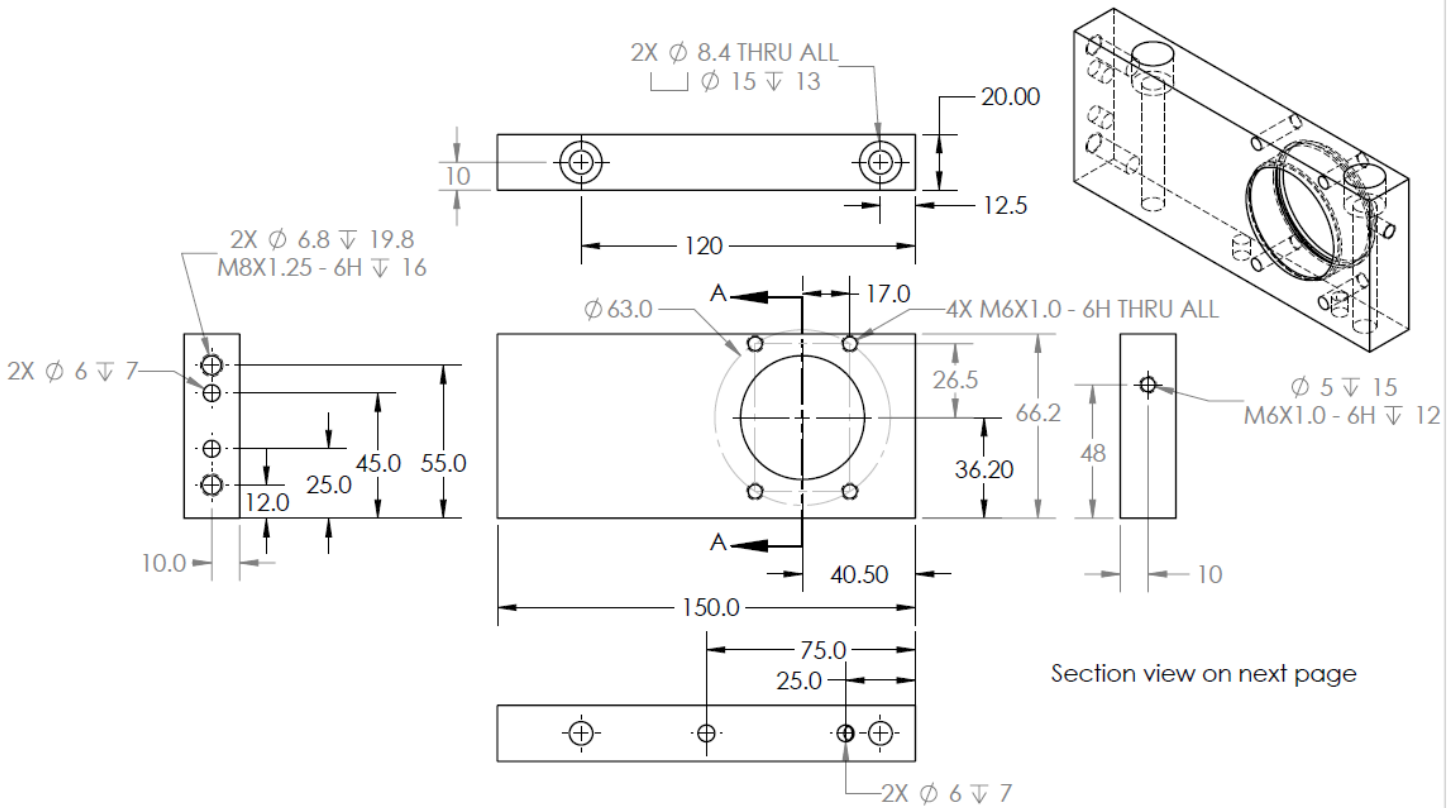

Section view on next page

		UNLESS OTHERWISE SPECIFIED:		NAME	DATE
		DIMENSIONS ARE IN mm TOLERANCES: ZERO PLACE DECIMAL ± .12 ONE PLACE DECIMAL ± .08 TWO PLACE DECIMAL ± .03	DRAWN	SW	12-3-13
			CHECKED		
			ENG APPR.		
			MFG APPR.		
		INTERPRET GEOMETRIC TOLERANCING PER:	Q.A.		
		MATERIAL 7075-T6 ALUMINUM	COMMENTS: -		
NEXT ASSY	USED ON	FINISH			
APPLICATION		DO NOT SCALE DRAWING			

TITLE:

INPUT PILLOW BLOCK

SIZE	DWG. NO.	REV
A	GP11	1
SCALE: 1:2	WEIGHT:	SHEET 1 OF 2

5 4 3 2 1

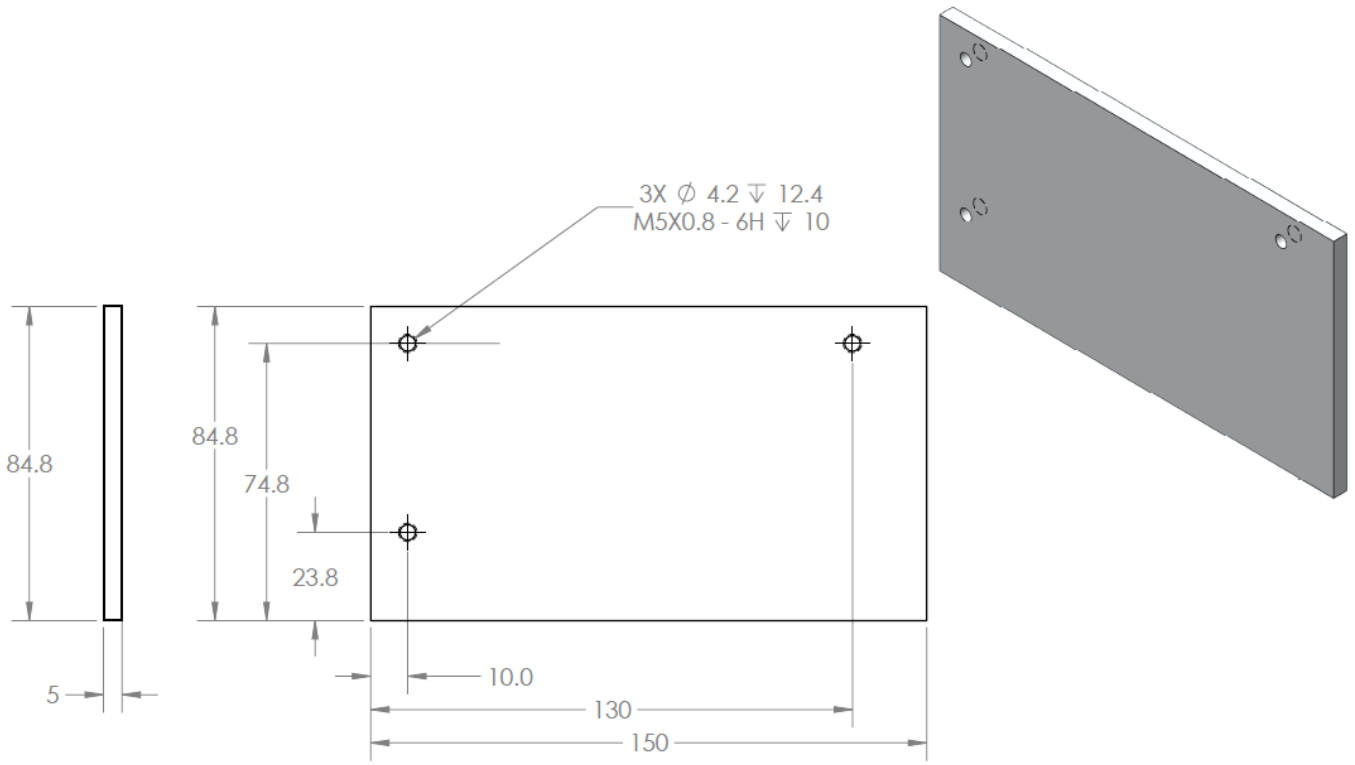

		UNLESS OTHERWISE SPECIFIED:		NAME	DATE
		DIMENSIONS ARE IN mm TOLERANCES: ZERO PLACE DECIMAL ± .12 ONE PLACE DECIMAL ± .08 TWO PLACE DECIMAL ± .04	DRAWN	SW	12-3-13
			CHECKED		
			ENG APPR.		
			MFG APPR.		
		INTERPRET GEOMETRIC TOLERANCING PER:	Q.A.		
		MATERIAL 6061ALUMINUM	COMMENTS: -		
NEXT ASSY	USED ON	FINISH			
APPLICATION		DO NOT SCALE DRAWING			

TITLE:

Input plate Upper

SIZE	DWG. NO.	REV
A	CB1	1
SCALE: 2:3	WEIGHT:	SHEET 1 OF 1

5 4 3 2 1

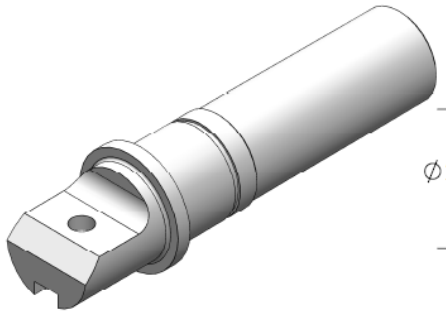

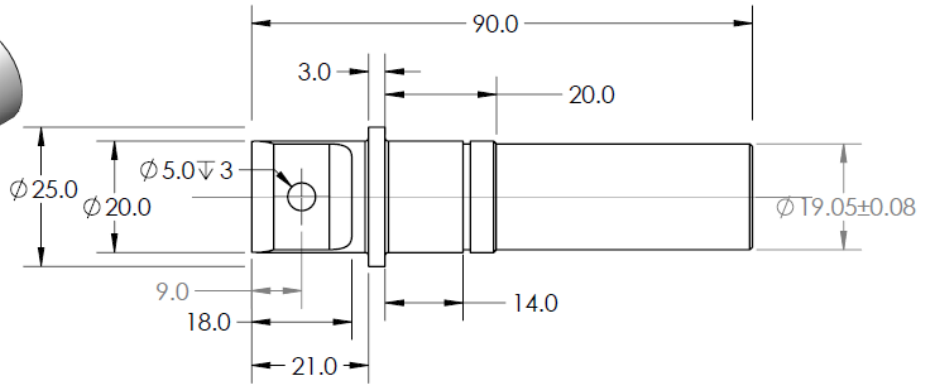

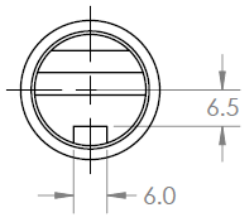

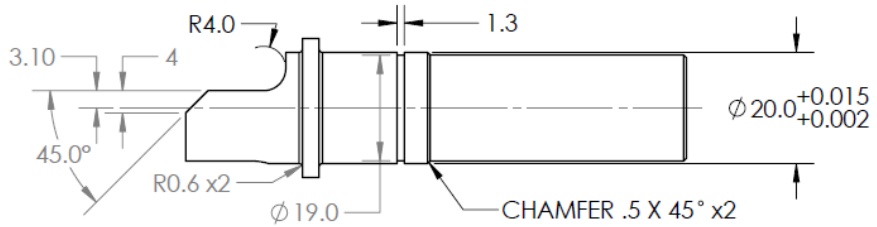

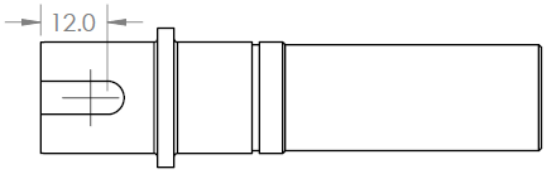

		UNLESS OTHERWISE SPECIFIED:		NAME	DATE
		DIMENSIONS ARE IN mm TOLERANCES: ZERO PLACE DECIMAL ± .12 ONE PLACE DECIMAL ± .08 TWO PLACE DECIMAL ± .03	DRAWN	SW	1-5-14
			CHECKED		
			ENG APPR.		
			MFG APPR.		
		INTERPRET GEOMETRIC TOLERANCING PER:	Q.A.		
		MATERIAL 4140 STEEL	COMMENTS: MADE FROM McMASTER pn 8927K91		
NEXT ASSY	USED ON	FINISH			
APPLICATION		DO NOT SCALE DRAWING			

TITLE:

INPUT SHAFT

SIZE	DWG. NO.	REV
A	CS1	1

SCALE: 1:1	WEIGHT:	SHEET 1 OF 1

5 4 3 2 1

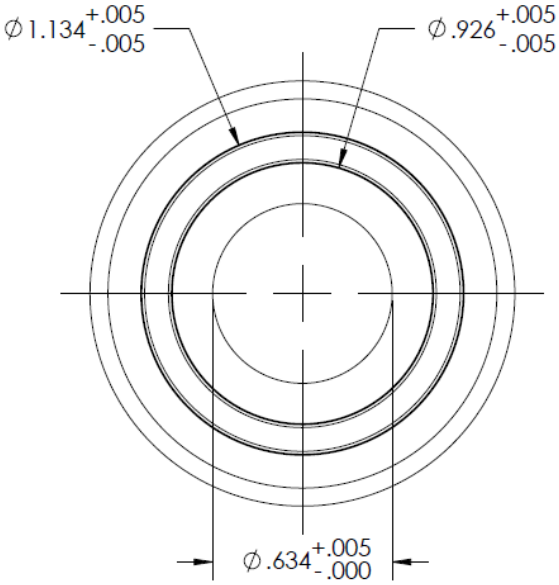

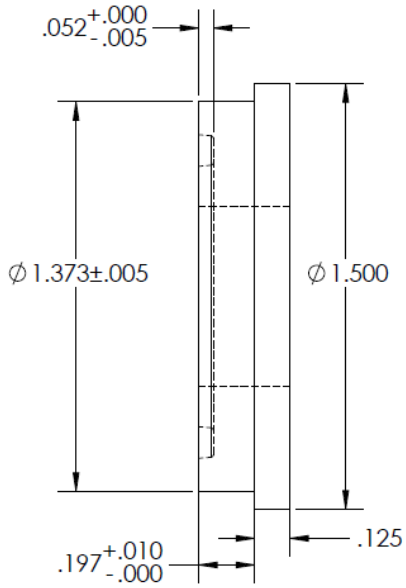

3 needed.
Aluminum would be great. critical dimensions are circled and tolerances given

		UNLESS OTHERWISE SPECIFIED:		NAME	DATE
		DIMENSIONS ARE IN INCHES TOLERANCES: FRACTIONAL± ANGULAR: MACH± BEND ± TWO PLACE DECIMAL ± THREE PLACE DECIMAL ±	DRAWN		
			CHECKED		
			ENG APPR.		
			MFG APPR.		
		INTERPRET GEOMETRIC TOLERANCING PER:	Q.A.		
		MATERIAL	COMMENTS:		
NEXT ASSY	USED ON	FINISH			
APPLICATION		DO NOT SCALE DRAWING			

TITLE:

SIZE	DWG. NO.	REV
A	Oil spacer	
SCALE: 2:1	WEIGHT:	SHEET 1 OF 1

5 4 3 2 1

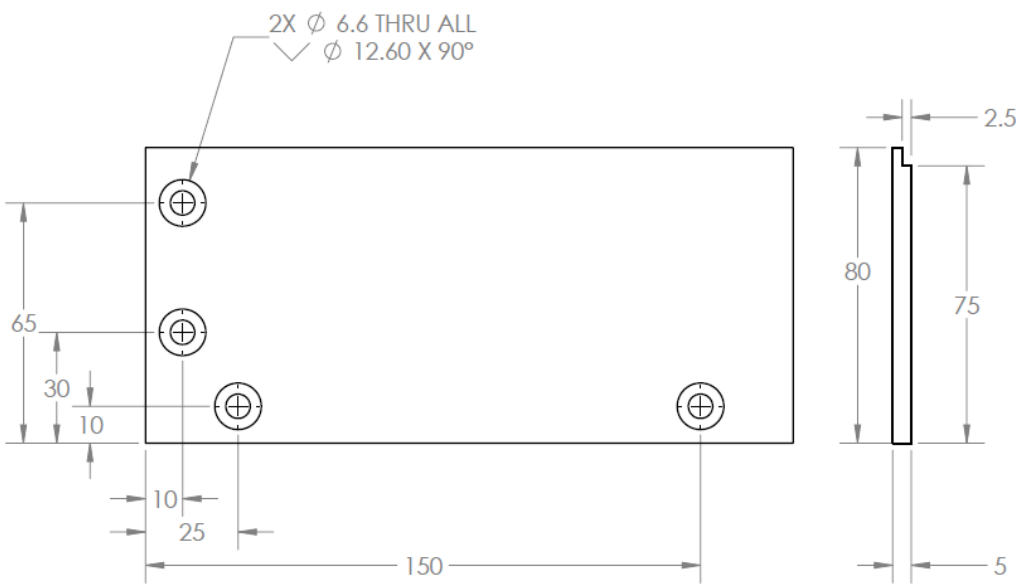

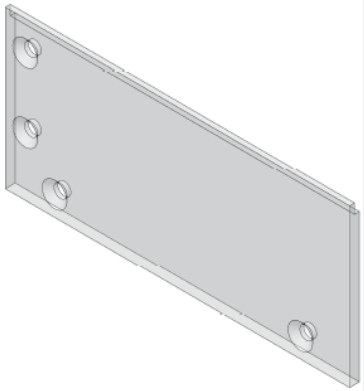

		UNLESS OTHERWISE SPECIFIED:		NAME	DATE
		DIMENSIONS ARE IN mm TOLERANCES: ZERO PLACE DECIMAL ± .12 ONE PLACE DECIMAL ± .08 TWO PLACE DECIMAL ± .04	DRAWN	SW	12-3-13
			CHECKED		
			ENG APPR.		
			MFG APPR.		
		INTERPRET GEOMETRIC TOLERANCING PER:	Q.A.		
		MATERIAL 6061 ALUMINUM	COMMENTS: -		
NEXT ASSY	USED ON	FINISH			
APPLICATION		DO NOT SCALE DRAWING			

TITLE:

Output Plate Lower

SIZE	DWG. NO.	REV
A	GP15	1

SCALE: 2:3	WEIGHT:	SHEET 1 OF 1

5 4 3 2 1

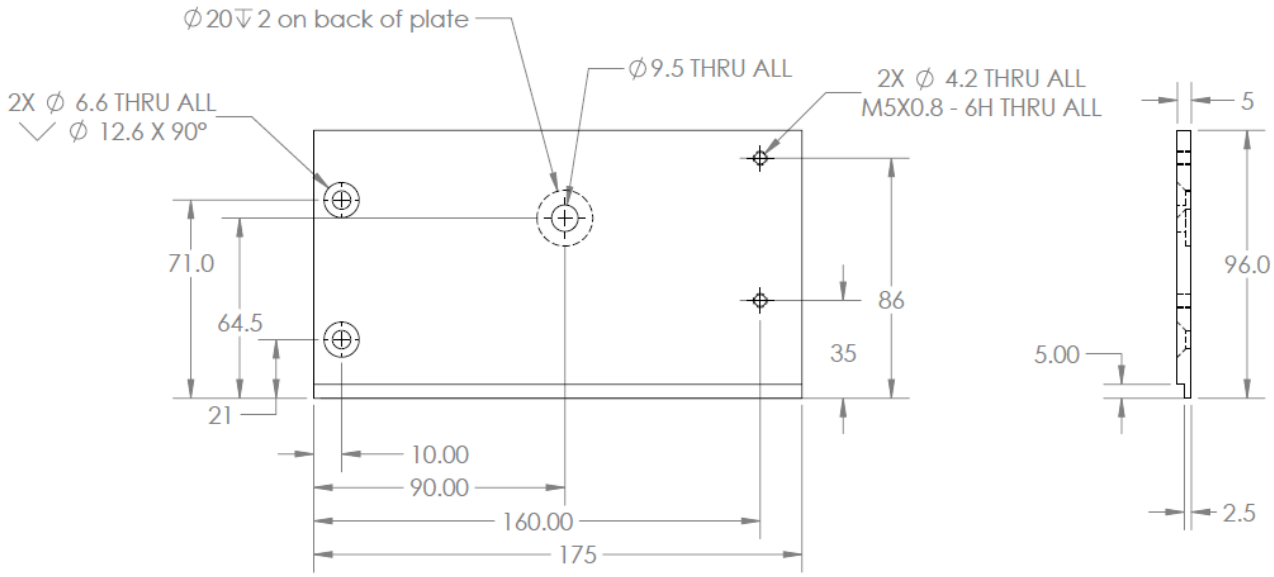

		UNLESS OTHERWISE SPECIFIED:		NAME	DATE
		DIMENSIONS ARE IN mm TOLERANCES: ZERO PLACE DECIMAL ± .12 ONE PLACE DECIMAL ± .08 TWO PLACE DECIMAL ± .04	DRAWN	SW	12-3-13
			CHECKED		
			ENG APPR.		
			MFG APPR.		
		INTERPRET GEOMETRIC TOLERANCING PER:	Q.A.		
		MATERIAL 6061 ALUMINUM	COMMENTS: -		
NEXT ASSY	USED ON	FINISH			
APPLICATION		DO NOT SCALE DRAWING			

TITLE:

Output Plate Upper

SIZE	DWG. NO.	REV
A	CB2	1

SCALE: 1:2	WEIGHT:	SHEET 1 OF 1

5 4 3 2 1

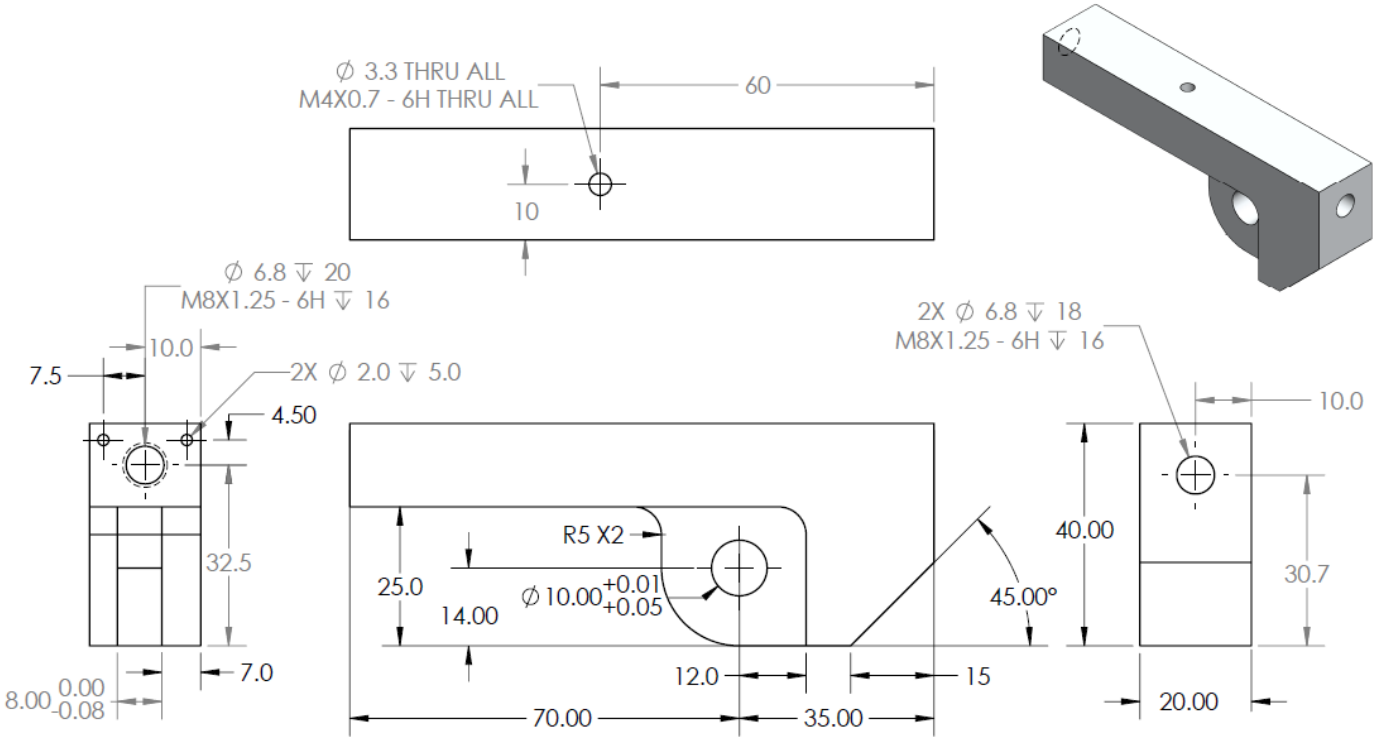

		UNLESS OTHERWISE SPECIFIED:		NAME	DATE
		DIMENSIONS ARE IN mm TOLERANCES: ZERO PLACE DECIMAL ± .12 ONE PLACE DECIMAL ± .08 TWO PLACE DECIMAL ± .03	DRAWN	SW	12-3-13
			CHECKED		
			ENG APPR.		
			MFG APPR.		
		INTERPRET GEOMETRIC TOLERANCING PER:	Q.A.		
		MATERIAL 7075-T6 ALUMINUM	COMMENTS: -		
NEXT ASSY	USED ON	FINISH			
APPLICATION		DO NOT SCALE DRAWING			

TITLE:

MODIFIED PIVOT LOCATOR

SIZE	DWG. NO.	REV
A	GLR2-2	1

SCALE: 1:1	WEIGHT:	SHEET 1 OF 1

5 4 3 2 1

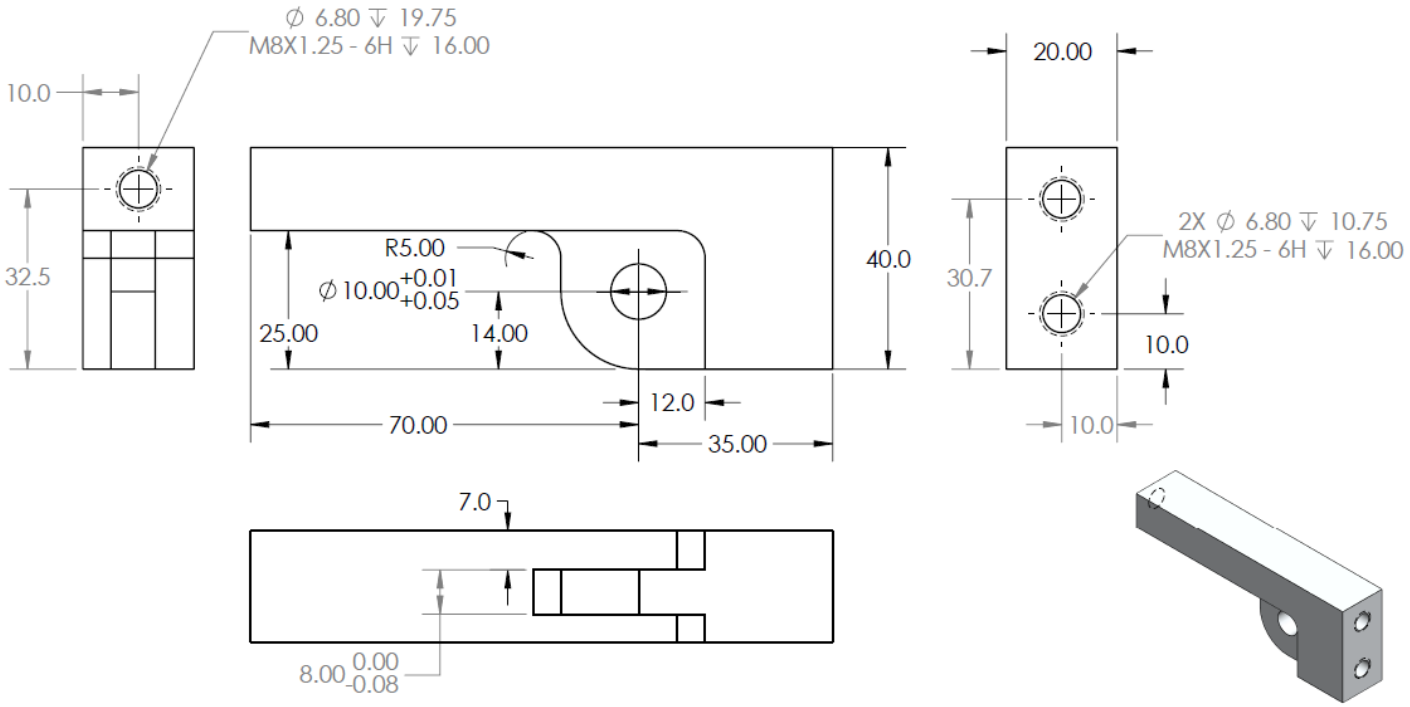

		UNLESS OTHERWISE SPECIFIED:		NAME	DATE
		DIMENSIONS ARE IN mm TOLERANCES: ZERO PLACE DECIMAL ± .12 ONE PLACE DECIMAL ± .08 TWO PLACE DECIMAL ± .03	DRAWN	SW	12-3-13
			CHECKED		
			ENG APPR.		
			MFG APPR.		
		INTERPRET GEOMETRIC TOLERANCING PER:	Q.A.		
		MATERIAL 7075-T6 ALUMINUM	COMMENTS: -		
NEXT ASSY	USED ON	FINISH			
APPLICATION		DO NOT SCALE DRAWING			

TITLE:

P PIVOT LOCATOR

SIZE	DWG. NO.	REV
A	GLR2-1	1
SCALE: 1:1	WEIGHT:	SHEET 1 OF 1

5 4 3 2 1

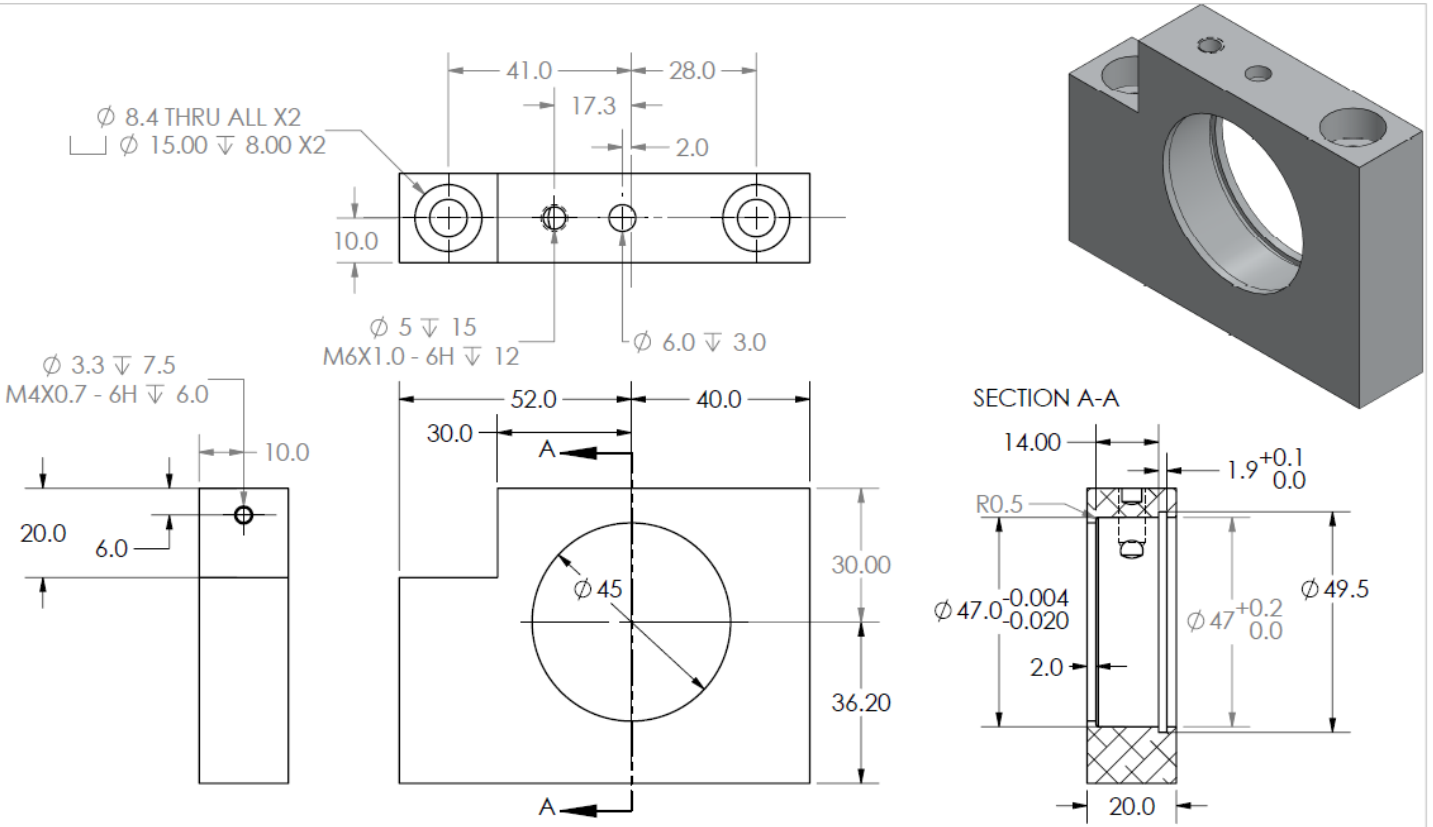

		UNLESS OTHERWISE SPECIFIED:		NAME	DATE
		DIMENSIONS ARE IN mm TOLERANCES: ZERO PLACE DECIMAL ± .12 ONE PLACE DECIMAL ± .08 TWO PLACE DECIMAL ± .03	DRAWN	SW	1-5-14
			CHECKED		
			ENG APPR.		
			MFG APPR.		
		INTERPRET GEOMETRIC TOLERANCING PER:	Q.A.		
		MATERIAL 7075-T6 ALUMINUM	COMMENTS: -		
NEXT ASSY	USED ON	FINISH			
APPLICATION		DO NOT SCALE DRAWING			

TITLE:

PILLOW BLOCK

SIZE	DWG. NO.	REV
A	CS4	1
SCALE: 1:1.25	WEIGHT:	SHEET 1 OF 1

5 4 3 2 1

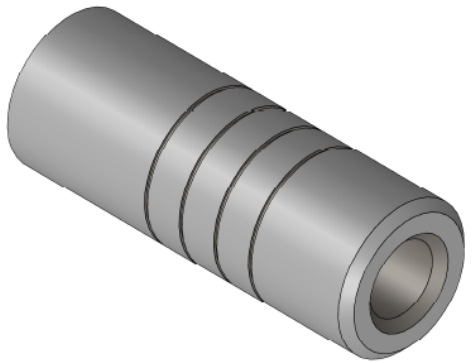

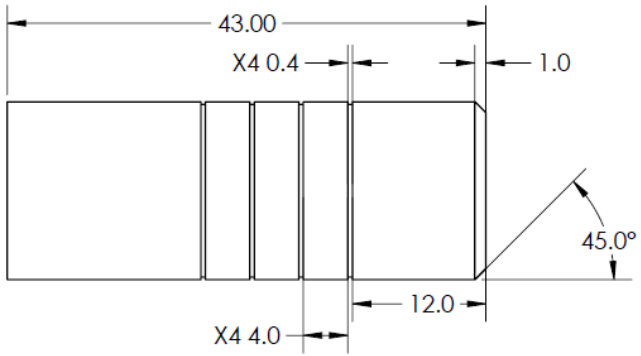

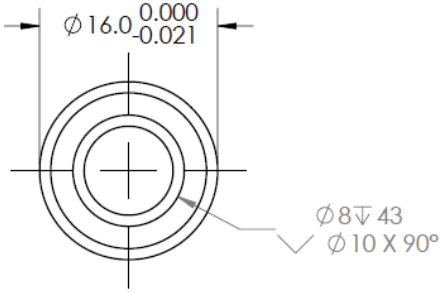

		UNLESS OTHERWISE SPECIFIED:		NAME	DATE
		DIMENSIONS ARE IN mm TOLERANCES: ZERO PLACE DECIMAL ± .12 ONE PLACE DECIMAL ± .08 TWO PLACE DECIMAL ± .03	DRAWN	SW	1-5-13
			CHECKED		
			ENG APPR.		
			MFG APPR.		
		INTERPRET GEOMETRIC TOLERANCING PER:	Q.A.		
		MATERIAL 1055 STEEL	COMMENTS: MADE FROM MCMASTER PN 5964K31 WITH STOCK OD		
NEXT ASSY	USED ON	FINISH			
APPLICATION		DO NOT SCALE DRAWING			

TITLE:

PISTON

SIZE	DWG. NO.	REV
A	PH1	1

SCALE: 2:1	WEIGHT:	SHEET 1 OF 1

5 4 3 2 1

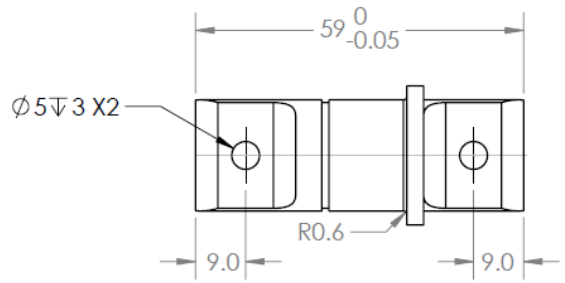

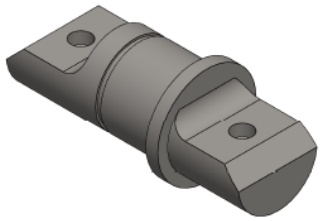

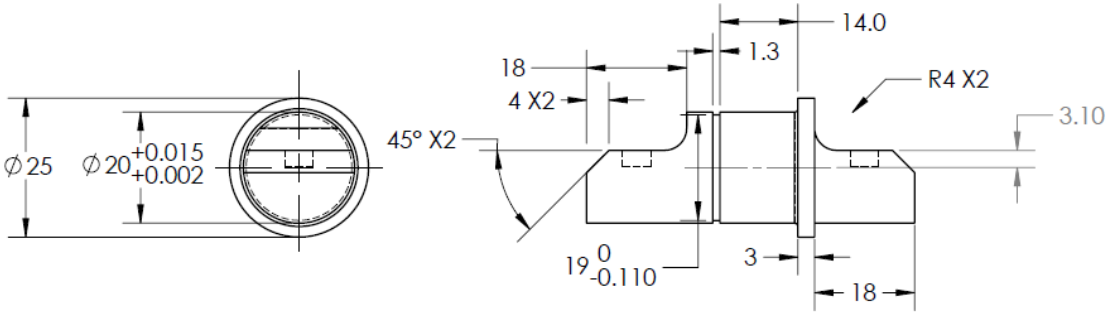

		UNLESS OTHERWISE SPECIFIED:		NAME	DATE
		DIMENSIONS ARE IN mm TOLERANCES: ZERO PLACE DECIMAL ± .12 ONE PLACE DECIMAL ± .08 TWO PLACE DECIMAL ± .03	DRAWN	SW	12-3-13
			CHECKED		
			ENG APPR.		
			MFG APPR.		
		INTERPRET GEOMETRIC TOLERANCING PER:	Q.A.		
		MATERIAL 4140 STEEL	COMMENTS: MADE FROM McMASTER P/N 8927K91		
NEXT ASSY	USED ON	FINISH			
APPLICATION		DO NOT SCALE DRAWING			

TITLE:

INPUT PIN

SIZE	DWG. NO.	REV
A	SGL2	1
SCALE: 1:1	WEIGHT:	SHEET 1 OF 1

5 4 3 2 1

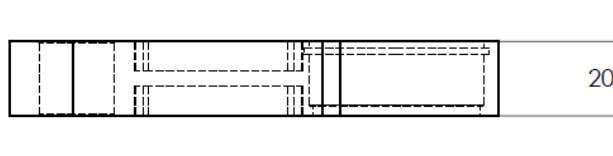

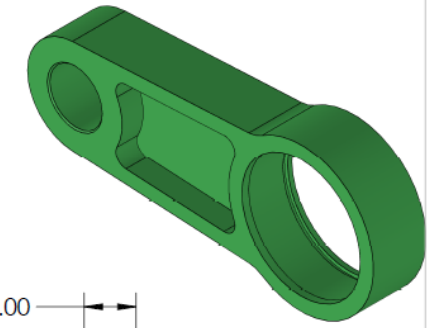

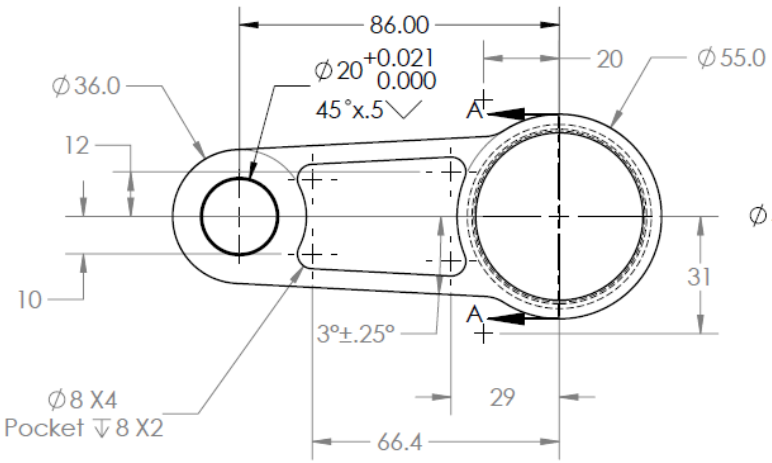

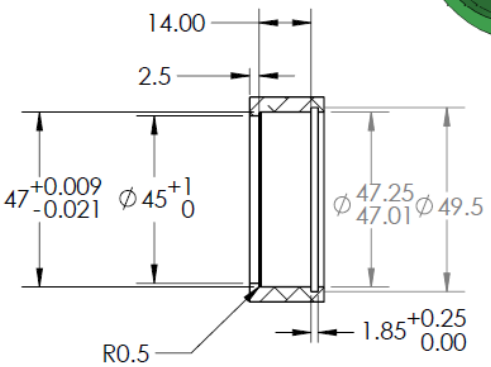

SECTION A-A

		UNLESS OTHERWISE SPECIFIED:		NAME	DATE
		DIMENSIONS ARE IN mm TOLERANCES: ZERO PLACE DECIMAL ± .12 ONE PLACE DECIMAL ± .08 TWO PLACE DECIMAL ± .04	DRAWN	SW	12-3-13
			CHECKED		
			ENG APPR.		
			MFG APPR.		
		INTERPRET GEOMETRIC TOLERANCING PER:	Q.A.		
		MATERIAL 7075-T6 ALUMINUM	COMMENTS: -		
NEXT ASSY	USED ON	FINISH			
APPLICATION		DO NOT SCALE DRAWING			

TITLE:

R3

SIZE	DWG. NO.	REV
A	SGL3	1

SCALE: 2:3	WEIGHT:	SHEET 1 OF 1

5 4 3 2 1

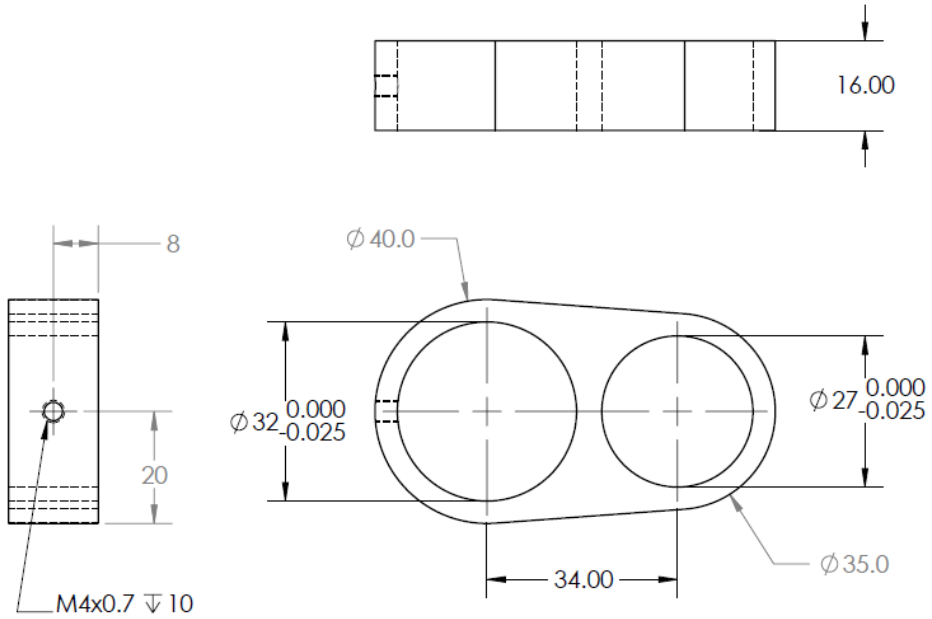

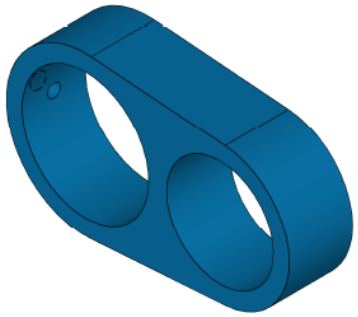

		UNLESS OTHERWISE SPECIFIED:		NAME	DATE	
		DIMENSIONS ARE IN mm TOLERANCES: ZERO PLACE DECIMAL ± .12 ONE PLACE DECIMAL ± .08 TWO PLACE DECIMAL ± .03	DRAWN	SW	12-3-13	TITLE: R4
			CHECKED			
			ENG APPR.			
			MFG APPR.			
		INTERPRET GEOMETRIC TOLERANCING PER:	Q.A.			
		MATERIAL 7075-T6 ALUMINUM	COMMENTS: -			SIZE A / DWG. NO. SGL4 / REV 1
NEXT ASSY	USED ON	FINISH				
APPLICATION		DO NOT SCALE DRAWING				SCALE: 1:1 / WEIGHT: / SHEET 1 OF 1

5 4 3 2 1

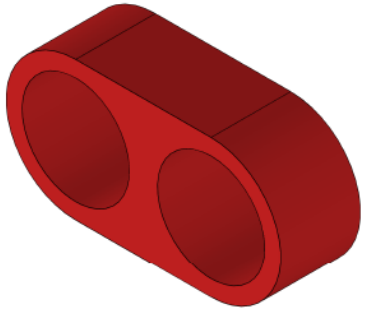

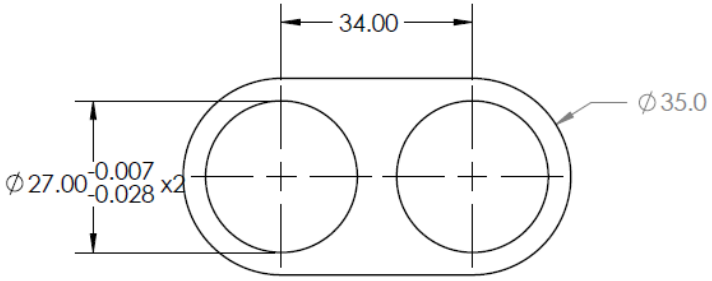

		UNLESS OTHERWISE SPECIFIED:		NAME	DATE
		DIMENSIONS ARE IN mm TOLERANCES: ZERO PLACE DECIMAL ± .12 ONE PLACE DECIMAL ± .08 TWO PLACE DECIMAL ± .03	DRAWN	SW	12-3-13
			CHECKED		
			ENG APPR.		
			MFG APPR.		
		INTERPRET GEOMETRIC TOLERANCING PER:	Q.A.		
		MATERIAL 7075-T6 ALUMINUM	COMMENTS:		
NEXT ASSY	USED ON	FINISH			
APPLICATION		DO NOT SCALE DRAWING			

TITLE:

R5

SIZE	DWG. NO.	REV
A	SGL5	

SCALE: 1:1	WEIGHT:	SHEET 1 OF 1

5 4 3 2 1

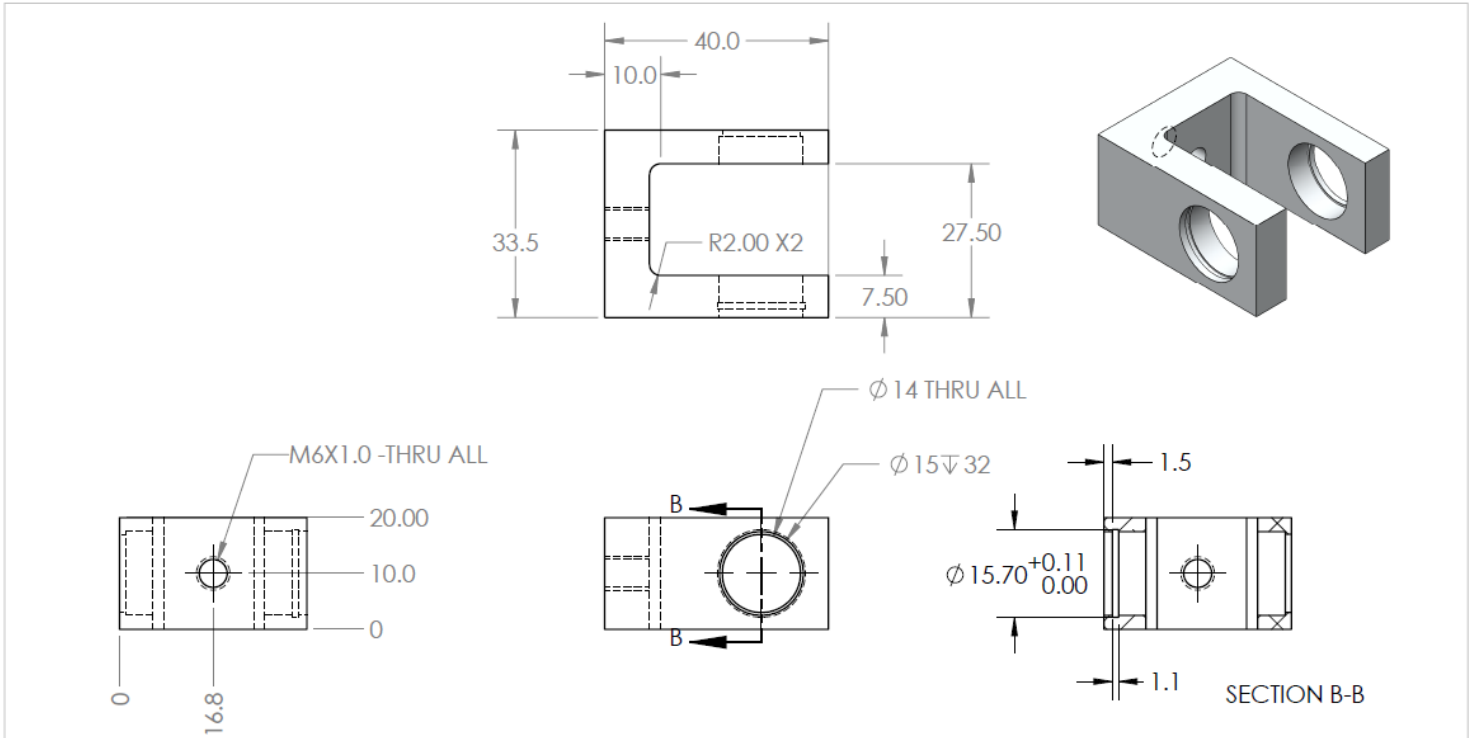

		UNLESS OTHERWISE SPECIFIED:		NAME	DATE
		DIMENSIONS ARE IN mm TOLERANCES: ZERO PLACE DECIMAL ± .12 ONE PLACE DECIMAL ± .08 TWO PLACE DECIMAL ± .03	DRAWN	SW	12-3-13
			CHECKED		
			ENG APPR.		
			MFG APPR.		
		INTERPRET GEOMETRIC TOLERANCING PER:	Q.A.		
		MATERIAL 7075-T6 ALUMINUM	COMMENTS: -		
NEXT ASSY	USED ON	FINISH			
APPLICATION		DO NOT SCALE DRAWING			

TITLE: R6

SIZE	DWG. NO.	REV
A	SGL6	1

SCALE: 1:1	WEIGHT:	SHEET 1 OF 1

5 4 3 2 1

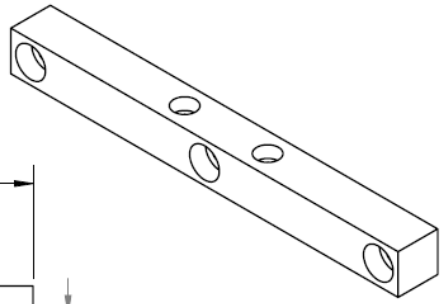

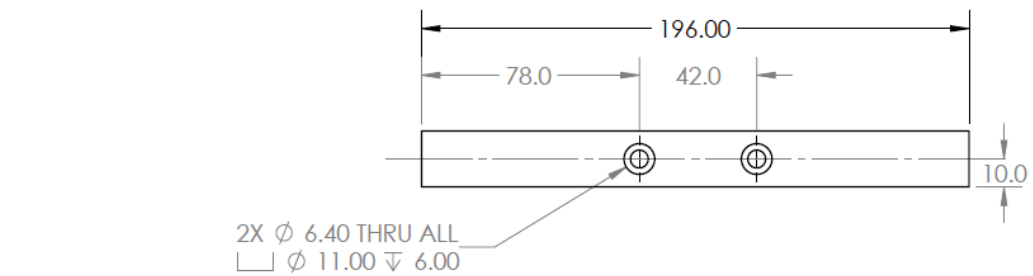

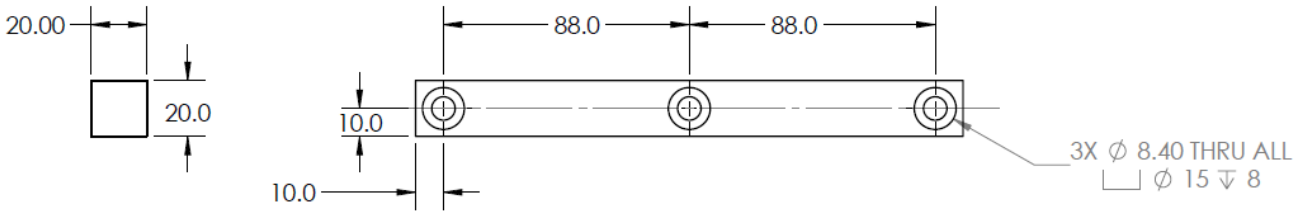

		UNLESS OTHERWISE SPECIFIED:		NAME	DATE
		DIMENSIONS ARE IN mm TOLERANCES: ZERO PLACE DECIMAL ± .12 ONE PLACE DECIMAL ± .08 TWO PLACE DECIMAL ± .03	DRAWN	SW	12-3-13
			CHECKED		
			ENG APPR.		
			MFG APPR.		
		INTERPRET GEOMETRIC TOLERANCING PER:	Q.A.		
		MATERIAL 4130 STEEL	COMMENTS: -		
NEXT ASSY	USED ON	FINISH			
APPLICATION		DO NOT SCALE DRAWING			

TITLE:

PIVOT SUPPORT BEAM

SIZE	DWG. NO.	REV
A	CLR5	1

SCALE: 1:2	WEIGHT:	SHEET 1 OF 1

5 4 3 2 1

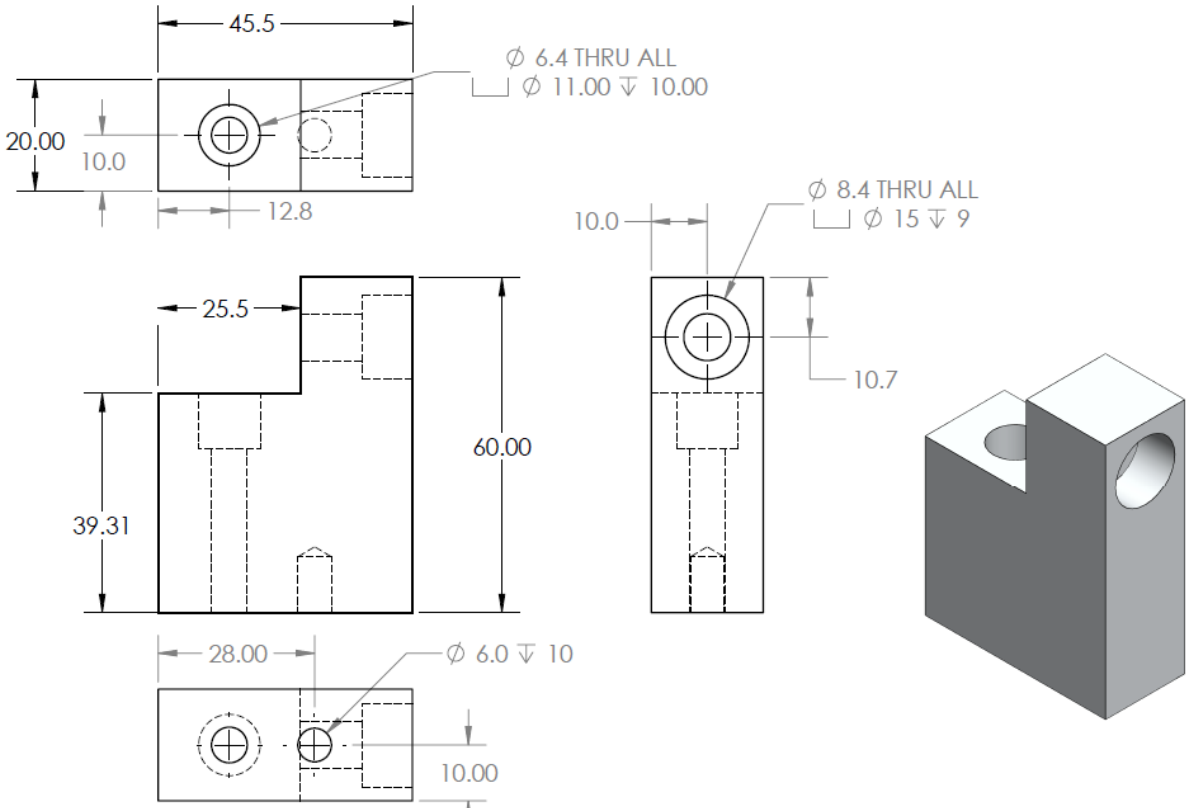

		UNLESS OTHERWISE SPECIFIED:		NAME	DATE
		DIMENSIONS ARE IN mm TOLERANCES: ZERO PLACE DECIMAL ± .12 ONE PLACE DECIMAL ± .08 TWO PLACE DECIMAL ± .03	DRAWN	SW	12-3-13
			CHECKED		
			ENG APPR.		
			MFG APPR.		
		INTERPRET GEOMETRIC TOLERANCING PER:	Q.A.		
		MATERIAL 7075-T6 ALUMINUM	COMMENTS: -		
NEXT ASSY	USED ON	FINISH			
APPLICATION		DO NOT SCALE DRAWING			

TITLE:

PIVOT SUPORT COLUMN

SIZE	DWG. NO.	REV
A	CLR6	1

SCALE: 1:1	WEIGHT:	SHEET 1 OF 1

5 4 3 2 1

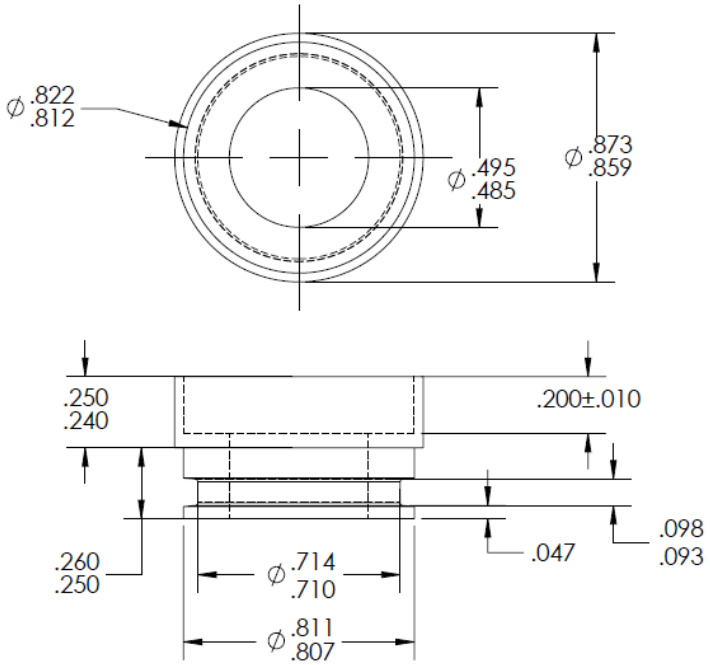

		UNLESS OTHERWISE SPECIFIED:		NAME	DATE
		DIMENSIONS ARE IN INCHES TOLERANCES: FRACTIONAL ± ANGULAR: MACH ± BEND ± TWO PLACE DECIMAL ± THREE PLACE DECIMAL ±	DRAWN		
			CHECKED		
			ENG APPR.		
			MFG APPR.		
		INTERPRET GEOMETRIC TOLERANCING PER:	Q.A.		
		MATERIAL	COMMENTS:		
NEXT ASSY	USED ON	FINISH			
APPLICATION		DO NOT SCALE DRAWING			

TITLE:

SIZE	DWG. NO.	REV
A	splitter2	
SCALE: 2:1	WEIGHT:	SHEET 1 OF 1

5 4 3 2 1

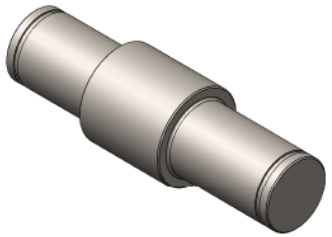

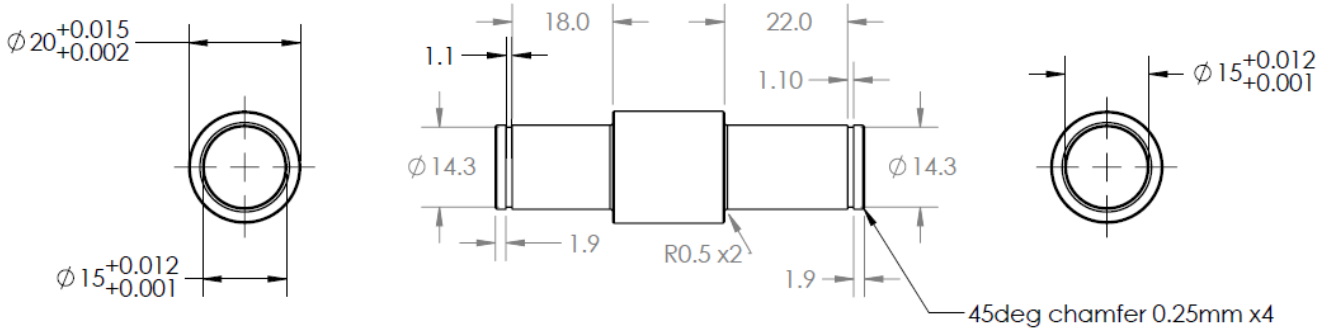

		UNLESS OTHERWISE SPECIFIED:		NAME	DATE
		DIMENSIONS ARE IN mm TOLERANCES: ZERO PLACE DECIMAL ± .12 ONE PLACE DECIMAL ± .08 TWO PLACE DECIMAL ± .02	DRAWN	SW	12-3-13
			CHECKED		
			ENG APPR.		
			MFG APPR.		
		INTERPRET GEOMETRIC TOLERANCING PER:	Q.A.		
		MATERIAL A2 Tool Steel	COMMENTS: Hardened to Rockwell C59		
NEXT ASSY	USED ON	FINISH			
APPLICATION		DO NOT SCALE DRAWING			

TITLE:

TERNARY PIN

SIZE	DWG. NO.	REV
A	SGL7	1

SCALE: 1:1	WEIGHT:	SHEET 1 OF 1

5 4 3 2 1

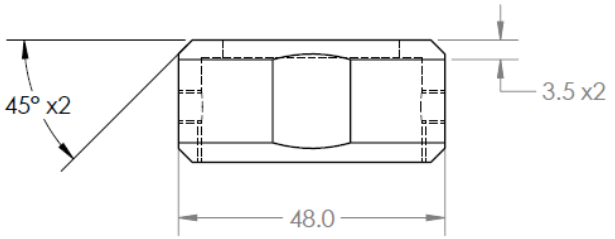

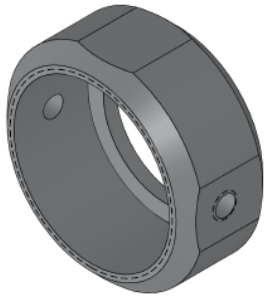

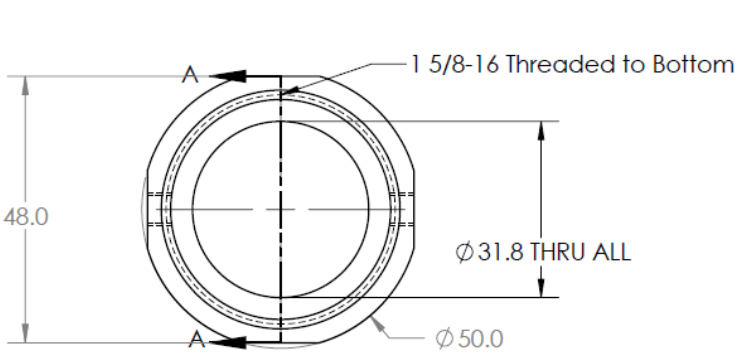

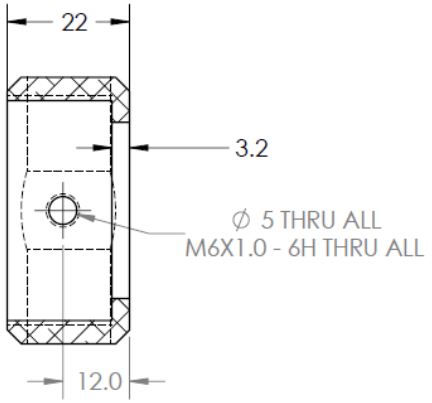

SECTION A-A

		UNLESS OTHERWISE SPECIFIED:		NAME	DATE
		DIMENSIONS ARE IN mm TOLERANCES: ZERO PLACE DECIMAL ± .12 ONE PLACE DECIMAL ± .08 TWO PLACE DECIMAL ± .03	DRAWN	SW	1-3-13
			CHECKED		
			ENG APPR.		
			MFG APPR.		
		INTERPRET GEOMETRIC TOLERANCING PER:	Q.A.		
		MATERIAL 6061 ALUMINUM	COMMENTS: -		
NEXT ASSY	USED ON	FINISH			
APPLICATION		DO NOT SCALE DRAWING			

TITLE:

Thread-in Cylinder Mount

SIZE	DWG. NO.	REV
A	CLR9	1
SCALE: 1:1	WEIGHT:	SHEET 1 OF 1

5 4 3 2 1

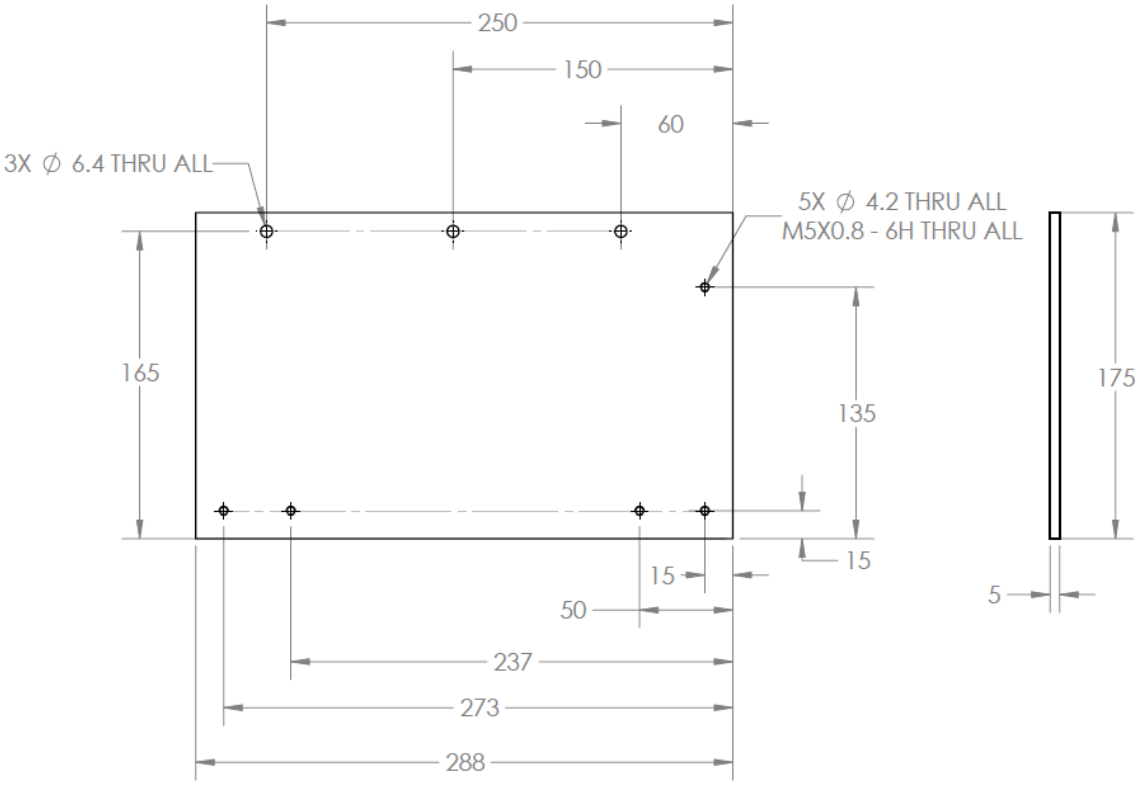

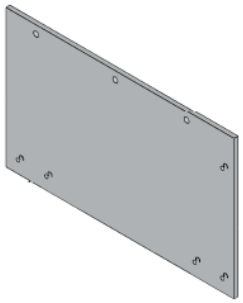

		UNLESS OTHERWISE SPECIFIED:		NAME	DATE
		DIMENSIONS ARE IN mm TOLERANCES: ZERO PLACE DECIMAL ± .12 ONE PLACE DECIMAL ± .08 TWO PLACE DECIMAL ± .04	DRAWN	SW	12-3-13
			CHECKED		
			ENG APPR.		
			MFG APPR.		
		INTERPRET GEOMETRIC TOLERANCING PER:	Q.A.		
		MATERIAL 6061 ALUMINUM	COMMENTS:		
NEXT ASSY	USED ON	FINISH			
APPLICATION		DO NOT SCALE DRAWING			

TITLE:

Top Plate

SIZE	DWG. NO.	REV
A	CB3	1

SCALE: 1:3 | WEIGHT: | SHEET 1 OF 1

5 4 3 2 1

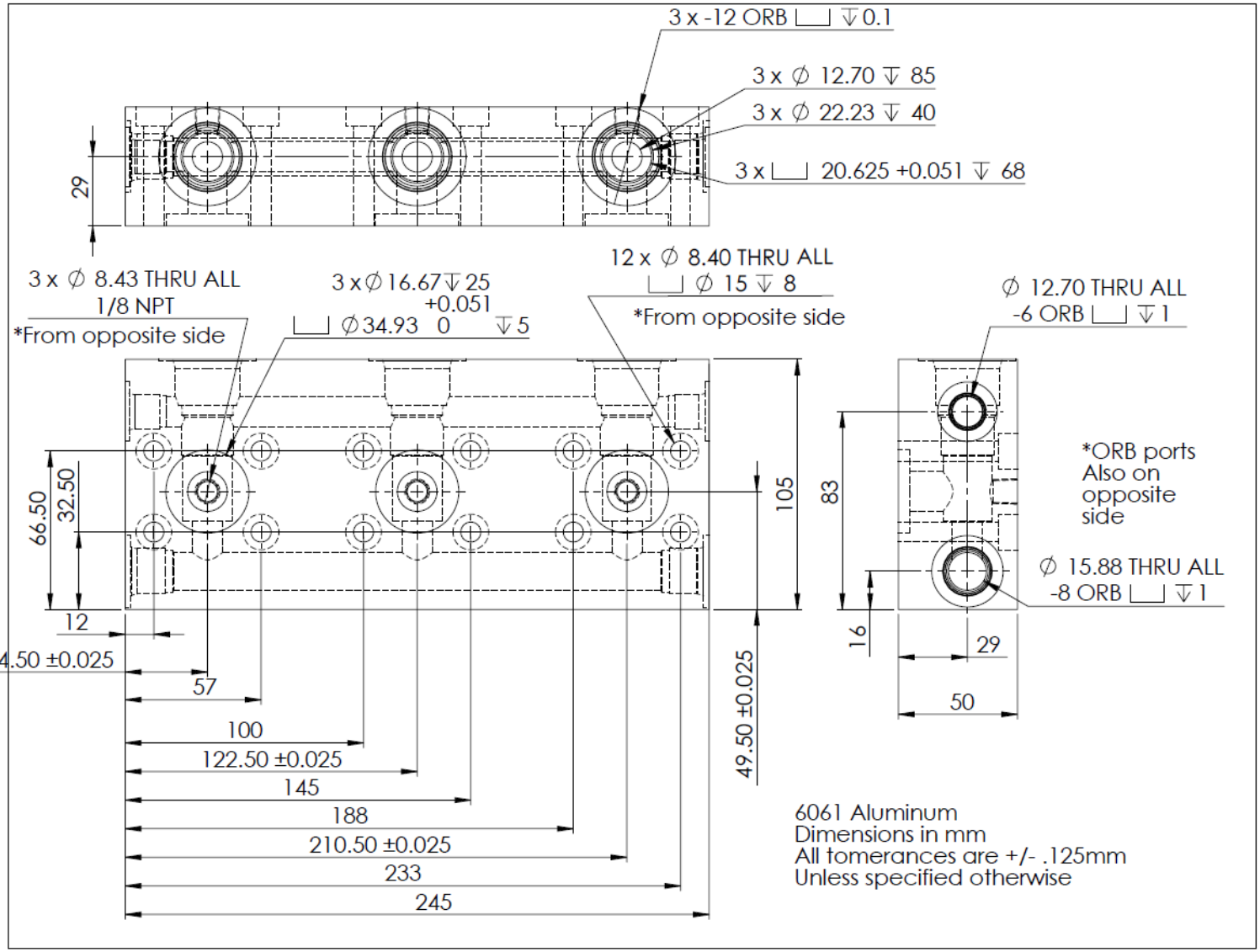
3 x -12 ORB ⌴ ↧0.1
3 x ∅ 12.70 ↧ 85
3 x ∅ 22.23 ↧ 40
3 x ⌴ 20.625 +0.051 ↧ 68
29
3 x ∅ 8.43 THRU ALL
1/8 NPT
*From opposite side
3 x∅16.67↧25 +0.051
⌴ ∅34.93 0 ↧5
12 x ∅ 8.40 THRU ALL
⌴ ∅ 15 ↧ 8
*From opposite side
∅ 12.70 THRU ALL
-6 ORB ⌴ ↧1
*ORB ports
Also on
opposite
side
∅ 15.88 THRU ALL
-8 ORB ⌴ ↧1
66.50
32.50
12
34.50 ±0.025
57
100
122.50 ±0.025
145
188
210.50 ±0.025
233
245
105
49.50 ±0.025
83
16
29
50
6061 Aluminum
Dimensions in mm
All tomerances are +/- .125mm
Unless specified otherwise

Appendix D Chapter 5 Model Inputs

PROTOTYPE DESIGN TABLE

Symbol	Description	Value	Unit
d_p	Piston Diameter	0.016	$[m]$
h	Piston Cylinder Gap Height	6.00	$[\mu m]$
h_s	Distance to axis of slide from x axis	76.4	$[mm]$
l_p	Length of Piston Sealing Surface	28	$[mm]$
m_2	Mass of link 2	830	$[gram]$
m_3	Mass of link 3	239	$[gram]$
m_4	Mass of link 4	57	$[gram]$
m_5	Mass of link 5	70	$[gram]$
m_s	Mass of slider link	127	$[gram]$
r_2	Length of Link 2	6.2	$[mm]$
r_3	Length of Link 3	86	$[mm]$
r_4	Length of Link 4	34	$[mm]$
r_5	Length of Link 5	34	$[mm]$
r_a	Pin radius at joint a	10	$[mm]$
r_b	Pin radius at joint b	10	$[mm]$
r_{c4}	Pin radius at joint c4	17	$[mm]$
r_{c5}	Pin radius at joint c5	17	$[mm]$
r_d	Pin radius at joint d	13.2	$[mm]$
r_e	Pin radius at joint e	17	$[mm]$
r_{g2}	Distance to Cg of Link 2	-1.24 (overbalanced)	$[mm]$
r_{g3}	Distance to Cg of Link 3	64.5	$[mm]$
r_{g4}	Distance to Cg of Link 4	15.98	$[mm]$
r_{g5}	Distance to Cg of Link 5	16	$[mm]$
θ_{min}	Minimum linkage transmission angle	.8334	$[rad]$
μ_d	Coefficient of dynamic viscosity*	0.065*	$[Pa\ s]$
μ_{k_c}	Coefficient of friction for crosshead bearing	0.12	$[unitless]$
$\mu_{k_{rb}}$	Coefficient of friction for roller bearing [91]	.0025	$[unitless]$

***Based on ISO grade 46 Hydraulic Oil at 22°C**